Development of Antimony-based Robust Electrocatalysts for Low-pH Water Oxidation

Submitted in partial fulfillment of the requirements

of the degree of

Doctor of Philosophy

of the
Indian Institute of Technology Bombay, India
and
Monash University, Australia

by

Sibimol Luke

Supervisors:

Prof. Aswani Yella (IIT Bombay)

Prof. Akshat Tanksale (Monash University)

Dr. Alexandr N. Simonov (Monash University)

The course of study for this award was developed jointly by
Monash University, Australia and the Indian Institute of Technology Bombay, India
and was given academic recognition by each of them.
The programme was administrated by the IITB-Monash Research Academy.

(Year 2021)

Thesis Approval

This thesis entitled **Development of Antimony-based Robust Electrocatalysts for Low-pH Water Oxidation** by Sibimol Luke is approved for the degree of Doctor of Philosophy.

Prof. Lianzhou Wang	**Prof. Dipti Gupta**
External Examiner	Internal Examiner
Prof. Aswani Yella	**Prof. Akshat Tanksale**
IITB Supervisor	Monash Supervisor
Dr. Alexandr N. Simonov	**Prof. Anindya Dutta**
Monash Supervisor	Chairman

Place: IITB-Monash Research Academy, IIT Bombay, Mumbai, India

Date: 30 June 2021

To,

Jesus and my family

Copyright notice

Abstract

The perception of the “hydrogen economy” has progressively changed from a blue-sky hypothesis to a viable concept reinforced by robust technologies, catalyst development and energy policies around the world and gained momentum as a means of global energy transition over the recent years. Electrolytic water splitting with renewable sources is among the most feasible methods to produce “green” H_2 fuel as a versatile means of storage and transportation of energy, especially the energy derived from the renewable sources. Proton-exchange membrane (PEM) electrolyte based electrochemical water splitting provides many advantages over other modes of electrolysis to produce high-purity hydrogen in an energy-efficient and sustainable way for different applications. However, the current PEM water electrolysis is mostly relying on high loadings of expensive and scarce iridium at the anodes, which are also often inadequately stable in operation during the oxygen evolution reaction (OER), *i.e.* four-electron electrooxidation of water. Thus, reduction of the precious metal content with more earth abundant metals and enhancing the durability of these electrocatalysts is a high priority for the commercialization of this critically important technology. The present PhD thesis aims to address the performance issues encountered by the currently known OER catalysts under the harsh acidic conditions of the PEM water electrolysis anodes. The work aims to point to potential solutions to enhance the stability and electrocatalytic performance of the catalysts for the low pH oxygen evolution reaction at ambient and elevated temperatures.

Chapter 1 discusses the progress of the renewable energy technologies focusing on the importance and need of hydrogen and its prospects that can revolutionize the energy industry.

This chapter also highlights the challenges and limitations of the presently available OER catalysts for the low pH applications and new design concepts which can possibly lead to the development of low-cost, robust electrocatalysts that can aid low-potential water oxidation under industrial conditions.

Chapter 2 summarizes the experimental methods including the materials synthesis procedures, characterization techniques, electrocatalytic testing and theoretical methods employed in the work. In particular, this chapter describes a simple and potentially scalable solution processing technique for the synthesis of antimony-based oxide OER electrocatalysts.

In chapter 3, the electrocatalytic performance of a range of mixed antimony-metal (Co, Mn, Ni, Fe, Ru) oxides synthesized as thin films on flat electrodes by a simple solution-based method for the oxygen evolution reaction in aqueous 0.5 M H_2SO_4 is scrutinized. Among noble-metal free materials, only cobalt-antimony and manganese-antimony oxides demonstrate reasonable stability over 24 h and activity at 24 ± 2 °C, with 10 mA $cm^{-2}_{geom.}$ current density achieved at overpotentials of 0.769 ± 0.010 and 0.677 ± 0.008 V, respectively. When tested at elevated temperatures, manganese-antimony oxides slowly lose their initial activity at a rate of approximately 0.001-0.002 V h^{-1}. In contrast, the ruthenium-antimony oxide system was found to be highly active, requiring an overpotential of only 0.39 ± 0.03 and 0.34 ± 0.01 V to achieve a current density of 10 mA cm^{-2} at 24 ± 2 and 80 °C, respectively, and most importantly, remaining stable during one-week tests at 80 °C. Density functional theory analysis suggests that the improved stability of the metal-antimony oxides during the OER is arising from the enhanced hybridization of the oxygen p- and metal d-orbitals induced by the presence of Sb. Comprehensive physical characterization and electrochemical studies along with the theoretical

density functional theory analysis demonstrate that high stability of the metal-antimony oxide systems can be achieved through either the formation of the new mixed phases or the intimate intermixing of the discrete metal and antimony oxide crystallites at the nanoscale.

Chapter 4 explores the possibility of improving the performance of the promising manganese antimonate catalysts through mixing with elements to endow the resulting materials with superior activity and stability in operation. A simple solution-based synthesis method was demonstrated to be suitable for the preparation of a set of multi-metallic manganese antimonates $[MnM+Sb]O_x$, where M = Ru, Co, Pb and Cr. Physical characterization of the materials revealed that the introduction of Co and Cr does not change the trirutile crystal structure of the parent manganese antimonate oxide, but modification with Pb and Ru induces the formation of a new pyrochlore-related antimonate phase. All additional metals examined were found to notably increase the initial catalytic activity of $[Mn+Sb]O_x$ towards the oxygen evolution reaction in 0.5 M H_2SO_4 at ambient temperature. The most significant improvements were found for Cr (0.61 ± 0.01 V improvement in overpotential at 10 mA $cm^{-2}_{geom.}$ with respect to $[Mn+Sb]O_x$) and Ru (0.53 ± 0.03 V improvement), but both were found to be unstable even at 24 ± 2 °C. In contrast, $[MnCo+Sb]O_x$, $[MnPb+Sb]O_x$ and $[MnCoPb+Sb]O_x$ maintained high stability on a timescale of one day with an overpotential improvement of 0.64 ± 0.01, 0.6 ± 0.03 and 0.63 ± 0.01 V, respectively. However, when tested at elevated temperatures of 60 and 80 °C all materials slowly lost their activity due to corrosion, similar to the unmodified $[Mn+Sb]O_x$. This loss of activity was irreversible at 80 °C for all materials examined except for the $[MnCo+Sb]O_x$ system, which has suffered partial degradation over the initial 48 h but then achieved a quasi-stable state and operated without any losses in activity for at least 144 h supported through a self-healing mechanism. These results indicate that the new antimony-based materials introduced

herein might be designed into robust OER catalysts operating at elevated temperatures at low pH if appropriate self-healing conditions are provided.

Chapter 5 investigates the effects of interfacial layers on the electrocatalytic performance of the manganese antimonate low pH water oxidation electrocatalyst as a new strategy for improving the catalytic activity. The specific focus is on the modification of manganese-antimony oxide material with over- and underlayer of catalytically inactive oxides of tin(IV), silicon(IV), cerium(IV), alumina(III) and titanium(IV). When applied both over and under the catalytic $[Mn+Sb]O_y$ thin film, these oxide layers induce a notable enhancement in the water oxidation electrocatalytic activity of the catalyst without compromising its stability in aqueous 0.5 M H_2SO_4. The most significant enhancement in the overpotential is achieved with SnO_2 overlayers and it required an overpotential of 0.58 ± 0.001 V to achieve the reaction rate of 10 mA cm^{-2}_{geom}. *Ex situ* soft X-ray absorption and X-ray photoelectron spectroscopic analysis suggests that the introduction of overlayers suppresses both the loss of manganese from the catalytic surface and the oxidation of manganese within the $[Mn+Sb]O_y$ catalyst during the OER. In the case of underlayers, the enhancement in the performance is likely originating from the enhanced electrochemically active surface area of the catalyst. This chapter emphasizes the importance of the surface, bulk, and substrate engineering of the electrocatalysts to improve the performance of common catalysts.

The final chapter 6 provides a summary of the major conclusions and outputs of the PhD thesis as well as an outlook for future work towards solving the challenges in the development of the sustainable hydrogen generation technologies *via* PEM water electrolysis.

Declaration

This thesis is an original work of my research and contains no material which has been accepted for the award of any other degree or diploma at any university or equivalent institution and that, to the best of my knowledge and belief, this thesis contains no material previously published or written by another person, except where due reference is made in the text of the thesis.

Signature: ----------

Name: Sibimol Luke

Date: 15 Feb 2021

Acknowledgements

My PhD studies gave me a unique opportunity to simultaneously work with outstanding people in energy research in India and Australia. I am most grateful to my supervisors Dr. Aswani Yella and Dr. Akshat Tanksale for giving me an opportunity to pursue this joint PhD in IIT Bombay and Monash University. Though there were changes in the initial plan and the topic of my project during the study, they persisted in their encouragement of me and provided me with full support and facilities for my research. I am obliged to Dr. Alexandr N. Simonov for welcoming me into his group in my time of dire need without much prior knowledge about me. He provided me with facilities and a new direction to work, and he was willing to be my supervisor which was truly wonderful. He taught me to research the subject of electrocatalysis and write down my findings. It was great learning to work with him. He encouraged me to strive for excellence in everything and to pay attention to detail. I am thankful to all my three supervisors for their encouragement, wisdom, guidance, and every kind of support, which were truly remarkable.

I can never forget my group members from both Universities. I was lucky to be a part of three big groups that worked in different areas. They played a role in broadening my scientific knowledge and understanding of the broad areas of research in renewable energy and catalysis. I am thankful to them for their valuable friendship and assistance; they have made these years memorable. They were very cooperative whenever I needed to perform repetitive experiments over long durations in limited facilities. I would like to specifically thank Dr. Maxime Fournier for teaching me the basics of electrocatalysis, performing experiments, and patiently answering my possibly trivial questions. I also want to acknowledge Dr. Manjunath Chatti for repeating my

experiments, performing the necessary characterizations in Monash, and his contributions to my research.

The technicians and operators of the various research facilities and equipment that I used for my work in IIT Bombay were very gracious and willing to help me in getting slots and characterizations for a large number of samples. I extend my appreciation to the various research facility centers and collaborators in IIT Bombay and Monash for their assistance in enabling me to gain a greater understanding of my research. I would like to thank, specifically,

- Dr. Asha Yadav, Dr. Jiban Kangsabanik, and Dr. Aftab Alam from the Dept. of Physics, IIT Bombay for performing the computational studies for my work.
- Mr. Hitesh Takur (X-Ray Diffraction), Mrs. Anjum Ahmad (X-Ray Photoelectron Spectroscopy,) and Mrs. Monika Bhagat (Scanning Electron Microscopy) from IIT Bombay for their assistance in collecting data.
- Dr. Ronny Golnak and Dr. Jie Xiao from Helmholtz Zentrum Berlin for the instrumental support during the beamtime and the collection of the soft X-ray absorption spectroscopy (XAS) data at the LiXEdrom beamline at the BESSY II synchrotron facility (Berlin).
- Dr. Shannon A. Bonke and Dr. Marc Tech from MPI-CEC Mulheim, and Mr. Darcy Simondson from Monash University for the collection, processing, and analysis of the soft-XAS data.
- Ms. Brittany V. Kerr and Dr. Rosalie K. Hocking from Swinburne University of Technology, and Dr. Bernt Johannessen from Australian Synchrotron for recording, analyzing, and interpreting the XAS data.

- Dr. Tim Williams from Monash Centre for Electron Microscopy for the collection and interpretation of Transmission Electron Microscopy data; Dr. Pavel V. Cherepanov for the collection and analysis of the XPS data; and Prof. Douglas R. MacFarlane for his valuable assistance in data interpretation.

I acknowledge BESSY II synchrotron facility, XAS beamline of the Australian Synchrotron, Monash Centre for Electron Microscopy, Monash X-ray platform, Indian National Centre for Photovoltaic Research and Education (NCPRE), Sophisticated Analytical Instrument Facility (SAIF), and Central Surface Analytical Facility of IIT Bombay for granting access to their facilities. In addition, I am grateful to MNRE Government of India (NCPRE-Phase II, IIT Bombay, Aswani Yella), Early Career Research Award, Science and Engineering Research Board, Government of India (ECR/2016/000550 to Aswani Yella) for funding my research. IITB-Monash Research Academy facilitated this great collaboration between India and Australia through prominent universities in the respective countries and granted me the scholarship. I am thankful to the entire team for their timely support and interventions in resolving issues to make this a smooth journey.

I cannot thank all my teachers and friends enough in all the places where I did my education. I thank also my well-wishers whom God used to support me during different stages of my life. The one person I owe much to is Late Dr. S. K. Sudheer, Assistant Professor, Dept. of Optoelectronics, University of Kerala. He believed in me much, and always saw something unique in me. I am thankful to him for diverting me toward research.

I have no words to express my sincere gratitude toward my family. What I am is because of my parents, their sacrifices, and tears. Their boundless love, support, efforts, encouragements, and

prayers were my pillars to hold on to during my difficult times, which motivated me to never give up. I thank also Danny, my younger brother, who always inspires me to dream big and attempt new things. Above all, I thank Almighty God for His grace and mercy that has sustained me and brought me thus far in life.

Sibimol Luke

Publications and Conferences

1. ***Mixed metal-antimony oxide nanocomposites: low pH water oxidation electrocatalysts with outstanding durability at ambient and elevated temperatures***

   Sibimol Luke, Manjunath Chatti, Asha Yadav, Brittany V. Kerr, Jiban Kangsabanik, Tim Williams, Pavel V. Cherepanov, Akshat Tanksale, Bernt Johannessen, Douglas R. MacFarlane, Rosalie K. Hocking, Aftab Alam, Aswani Yella, Alexandr N. Simonov
   (Submitted to Advanced Energy Materials)

2. ***Performance of manganese antimonate electrocatalysts modified with different metal oxides for the acidic water oxidation at ambient and elevated temperatures***

   Sibimol Luke, Manjunath Chatti, Brittany Kerr, Bernt Johannessen, Akshat Tanksale, Douglas R. MacFarlane, Rosalie K. Hocking, Aswani Yella, Alexandr N. Simonov
   (Manuscript in preparation)

3. ***Modification of manganese antimonate low-pH water electrooxidation catalyst with interfacial oxide layers for the enhanced performance***

   Sibimol Luke, Manjunath Chatti, Rupan Bera, Akshat Tanksale, Douglas R. MacFarlane, Aswani Yella, Alexandr N. Simonov
   (Manuscript in preparation)

4. ***Catalyst in a stable matrix: engineering robust water splitting anodes for long term operation at high temperature in acidic media***

   Sibimol Luke, Manjunath Chatti, Asha Yadav, Jiban Kangsabanik, Akshat Tanksale, Aftab Alam, Aswani Yella, Alexandr N Simonov

   Online nanoGe Fall Meeting 2020, 20th – 23rd October 2020 (Oral presentation)

   https://www.nanoge.org/proceedings/OnlineNFM20/5f5fac1745c1ae491df6f05a

5. ***Mixed metal antimonates as efficient electrocatalysts for OER in acidic medium***

   Sibimol Luke, Alexandr N. Simonov, Aswani Yella and Akshat Tanksale

   17th International Congress on Catalysis, 14th – 19th June 2020 (Abstract accepted for oral presentation)

   https://nam.confex.com/nam/2020icc/meetingapp.cgi/Paper/23835

6. ***Enhancing the activity of electrocatalyst by mesoporous over layers***

   Sibimol Luke, Aswani Yella, Akshat Tanksale, Alexandr N Simonov

   7th International Conference on Advances in Energy Research, 10th – 12th December 2019 (Poster presentation)

   https://www.ese.iitb.ac.in/icaer2019/assets/files/Programme%20booklet%20-%20ICAER%202019%20-%2002.pdf

Table of Contents

Chapter 1

Renewable Energy: Hydrogen Economy and Water Oxidation Electrocatalysts

1.1 THE CURRENT ENERGY SCENARIO

"Energy is the golden thread that connects economic growth, social equity, and environmental sustainability. We must find a way to end energy poverty. We can no longer burn our way to prosperity." These are the words of Ban Ki-moon, former UN Secretary-General, who said this in the context of the 'Sustainable Energy for All' initiative, which aimed to guarantee universal access to modern energy services. The goal of this initiative is to double the global rate of improvement in energy efficiency and to double the share of renewable energy in the global energy mix by 2030.[1] Secure, reliable, affordable, clean, and equitable energy supply is fundamental to global economic growth and human development, and it is a great challenge because energy poverty affects about half of the world's population.[2]

Due to improved health facilities and awareness, the global population is projected to reach its peak early at a total of 9.7 billion by 2050.[3] The global primary energy consumption grows even more rapidly; for example, it was almost two-fold higher in 2018 than a previous ten-year average.[4] Eighty percent of the present global primary energy demand is met by fossil fuels (Figure 1.1).[4] Dependability, high energy density, and well-established storage and transportation technologies make fossil fuels the most convenient source of energy currently, although it is

clear that their reserves are limited[5] and cannot support the sustainable energy needs of the future. Moreover, the extraction and the use of the fossil fuels are responsible for large amounts of local air pollution, which leads to at least five million premature deaths each year.[6]

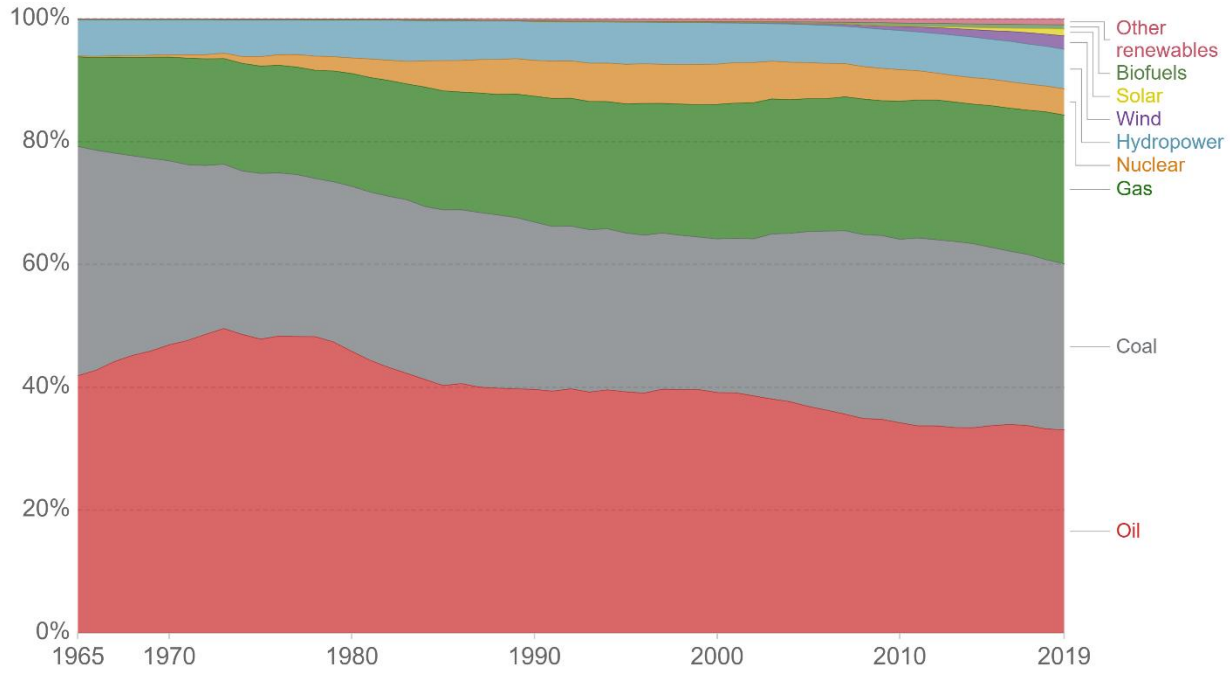

Figure 1.1. Primary world energy consumption by source according to BP Statistical Review of World Energy 2019.[4] 'Other renewables' includes geothermal, biomass and waste energy. Figure adapted.[7]

Approximately two-thirds of global CO_2 emissions come from fossil fuels, which is another major concern.[8] Despite the global growth in the demand for renewables and the increase in their usage, global carbon emissions, which are the primary drivers of global climate change, continue to grow.[9] To achieve the goal of the Paris Agreement to limit the average global temperature increase to 1.5 °C, global greenhouse gas emissions should fall by 7.6 percent each year between 2020 and 2030.[10] With the present climate policies, the world is making slow progress in

reducing emissions, which is not good enough to meet the global target. The use of renewable energy and fundamental improvements in the efficiency of energy generation and consumption provide optimal pathways to deliver most of the needed emission cuts at the necessary speed and to eliminate damage to the environment.

Moreover, the energy sector has been severely affected by the coronavirus (Covid-19), which has slowed transport, trade, and economic activity across the globe. According to Global Energy Review 2020, countries are experiencing a sharp decline in the demand for energy per week along with an unprecedented decline of 57 % in the global demand for oil.[11] This implies that energy security is a keystone in the reviving of the economy during these difficult times. Clean energy transitions that reduce interdependence at a global scale are essential for electricity security and resilient energy systems.[11,12]

Since the developments in renewable power are faster than before along with reductions in costs, the promise of a clean energy future can be foreseen as reality. For example, the installed power capacity of renewable energy increased to more than 200 gigawatts (GW) in 2019.[13] Capacity installations and investment in the renewable energy sector continues to increase all over the world. This opens the prospect of electricity access for households in developing and emerging countries with distributed renewable energy systems. Net additions of renewable power generation capacity are now outgrowing net installations of the combined power capacity of fossil fuels and nuclear power plants.[13] Electricity production from wind turbines and solar photovoltaics (PV) is now more cost-effective than its generation from new coal-fired power plants in many countries.[14] Cities are becoming key players in renewable energy transition because there is a growing movement to source their electricity completely from renewables.[15]

Although this progress is exciting and promising, certain barriers still need to be tackled. The share of renewables in the total energy demand in the heating, cooling, and transport sectors, which are responsible for over 80 % of the global energy demand, is increasing slowly in comparison to the power sector.[16] Unfortunately, renewable energy remains non-competitive in some countries in which fossil fuels are still heavily subsidized and funded. The provision of cheap and easily available energy to humankind is the current most important goal to stop the vicious cycle of poverty.

Making the transition to renewables as one of the dominant sources of our energy is possible and ecumenically feasible only if the excess generation of energy from renewables can be converted and stored in other forms of energy. This is because renewable systems are vulnerable, given that they often rely on the weather for energy production. In addition, renewable sources are mostly available in specific spots, and solar energy is available during the day only. Due to intermittent nature of solar and wind, the ability to backup energy is required to meet the demand for continuous reliable supply. Matching the output to grid demand beyond about 20 % of the total supply is very difficult with intermittent renewables, which is yet another issue.[17] Moreover for solar- and wind-generated electricity to be used in an off-grid stand-alone system, it needs to be complemented with a battery or some other kind of storage system. The demand growth that is associated with renewable energy, as well as the battery bottlenecks that are caused by lack of access to lithium and cobalt which are the critical elements in Lithium-ion batteries pose big challenges in the development of storage devices.[18] A flexible solution, that is, the storing of renewable energy in the form of a fuel by electrosynthesis, is required to manage the intermittency of these energy sources. Hydrogen is the most convenient of all fuels that can be

produced by electrosynthesis.[19] Hydrogen as a green fuel emerges as a leading contender in providing flexibility, while carrying energy to all sectors across the energy landscape.

Due to the many advantages of hydrogen, such as its versatility, cleanness, and safety as an energy carrier, it can be used as a fuel or a as a reductant in the industry. It has the potential to replace natural gas in heating and electricity generation. Electricity can be produced directly on electric vehicles or in remote areas that are not connected to a power grid by combining hydrogen with a fuel cell. If renewable sources are used to generate electricity to make hydrogen, they can be utilized fully whenever they are available. Moreover, the output during the off-peak periods can be used to make hydrogen for maximum efficiency of the nuclear power plants. These possibilities show that hydrogen has enormous potential to meet the growing global demand for clean and sustainable energy if research can overcome the hurdles in its efficient and safe production, storage, and use in fuel cell vehicles. Hydrogen is discussed in detail in the next section.

1.2 HYDROGEN: THE PRESENT AND THE FUTURE

The global demand for hydrogen has been growing steadily over the past 50 years and is around 70 Mt per year today (Figure 1.2). It is used to a great extent in the refining of oil and production of ammonia.[20] Currently, hydrogen is almost entirely derived from fossil fuels along with 6 % of the global natural gas and 2 % of the global coal extracted which is accompanied by massive amounts of CO_2 emissions.[21] There is a rapid increase in the number of hydrogen generation projects and the capacity of installed water electrolyzers, which increased from less than 1 MW in 2010 to more than 25 MW in 2019 of hydrogen production in the last decade.[22]

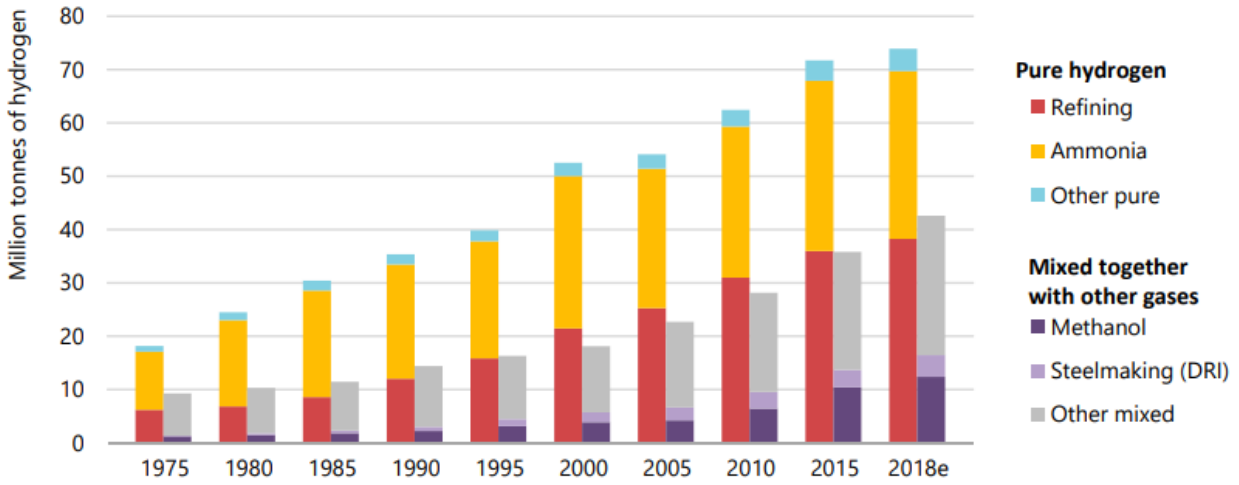

Figure 1.2. Global hydrogen demand according to International Energy Agency (2019).[20]

One of the current challenges of hydrogen technologies such as electrolyzers, fuel cells, and hydrogen production along with carbon capture, utilization and storage (CCUS) is the further reduction in cost through scaling of technologies to produce and use clean hydrogen.[22,23] There are currently only a few applications in which pure hydrogen is a cost-effective fuel or feedstock. Therefore, addressing wider markets for hydrogen use in new applications can play a role in bringing down the cost.[24] The development of robust policies and regulations can incentivize private sector investment in low-carbon hydrogen, which would raise both supply and demand and eventually enabling it financially self-sustaining in a greater number of sectors and countries.[25] Encouraging refining and chemical production plants to shift to cleaner hydrogen production would drive down overall costs.[20] Building on existing infrastructure by introducing clean hydrogen to replace merely 5 % of the volume of the natural gas supplies of different countries would significantly boost the demand for hydrogen and reduce costs.[20] Policies that create sustainable markets for clean hydrogen and a role for hydrogen in long-term energy strategies are also essential to scale up the production of hydrogen.[26]

1.2.1 Industrial importance of H_2

Of all energy utilizing sectors, industrial sector has the highest demand for hydrogen. Hydrogen is a strategically important commodity, both as a primary feedstock to the refining, fertilizer, and chemical industries and as a by-product in other industrial processes.[27] Hydrogen is a fundamental building block in the manufacture of ammonia and, hence, of fertilizers[28] and methanol, which are used in the production of many polymers.[29] About 55 % of the hydrogen produced globally is used in the synthesis of ammonia, of which 25 % is used in refineries and about 10 % in methanol production (Figure 1.3).[30]

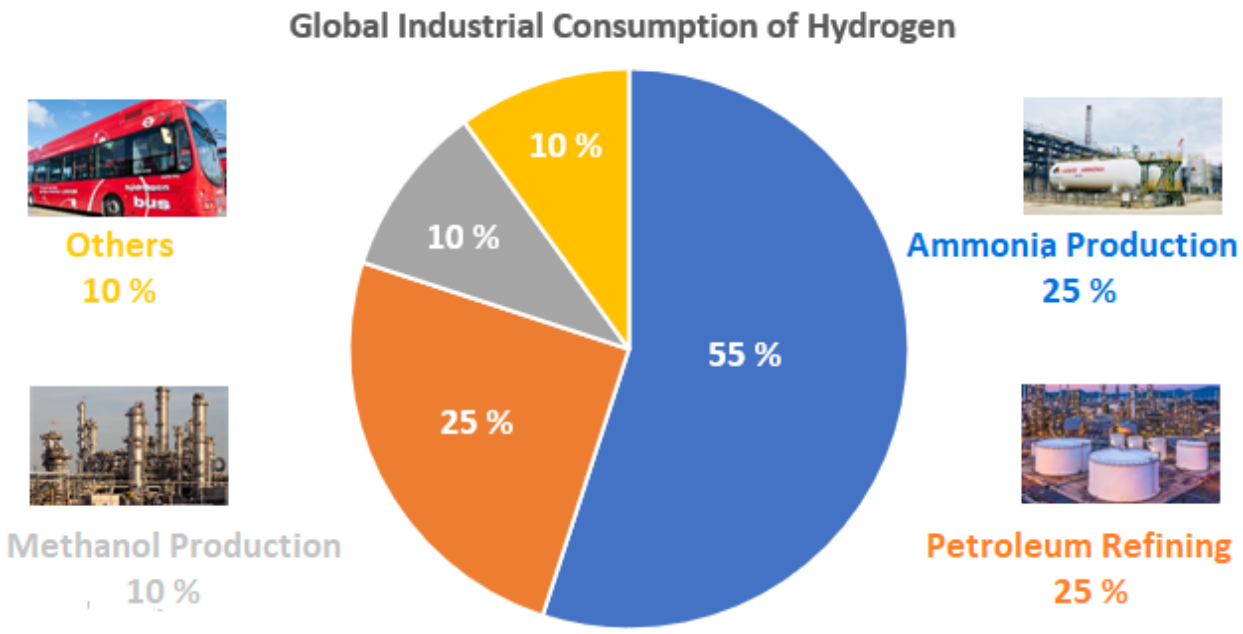

Figure 1.3. Global hydrogen consumption by industry (Data from Hydrogen Europe).[31]

Other applications worldwide account for only about 10 % of the global production of hydrogen.[30] It is also used in the production of carbon steels, special metals, and

semiconductors.[32] It is widely used as a reducing agent in electronics and the metallurgical industry.[33] Hydrogen is also used to produce refined fuels from crude oil and to eliminate contaminants such as sulfur from fuels.[34]

The Power-to-X conversion of renewable power into various forms of chemical energy carriers shows the potential use of hydrogen in various industries and its use in different applications (Figure 1.4).[35] This shows that hydrogen is not only useful in oil refineries, which may not last another 50 years, but in many other irreplaceable processes (most importantly, in the production of NH_3). Ammonia is currently the largest application of hydrogen. The Haber–Bosch process is the main industrial procedure that is used to produce ammonia today, and it involves the direct combination of hydrogen and nitrogen under pressure and temperature in the presence of a metal catalyst.[36–38] The nitrogen that is used in this process is obtained by low-temperature separation of air, and the hydrogen is obtained from natural gas steam reforming, which releases CO_2 into the environment.[39] Almost 90 % of ammonia goes into fertilizer production.[40] About 50 % of the world's food production relies on ammonia fertilizer.[41] Owing to its high energy of evaporation, ammonia is also used in refrigeration plants as an environment-friendly and inexpensively produced refrigerant that is known as R-717.[42] To replace the traditional technology and for a clean and efficient ammonia process, electrochemical methods to produce ammonia are currently explored . However, the most realistic approaches, such as the coupling of Haber–Bosch plants and water electrolysis still require H_2.[43–45] In addition to hydrogen, ammonia provides the only carbon-free chemical energy carrier solution for the transportation sector.[46] Since a highly developed ammonia infrastructure is already in existence, Ammonia is also considered an ideal hydrogen carrier.[47]

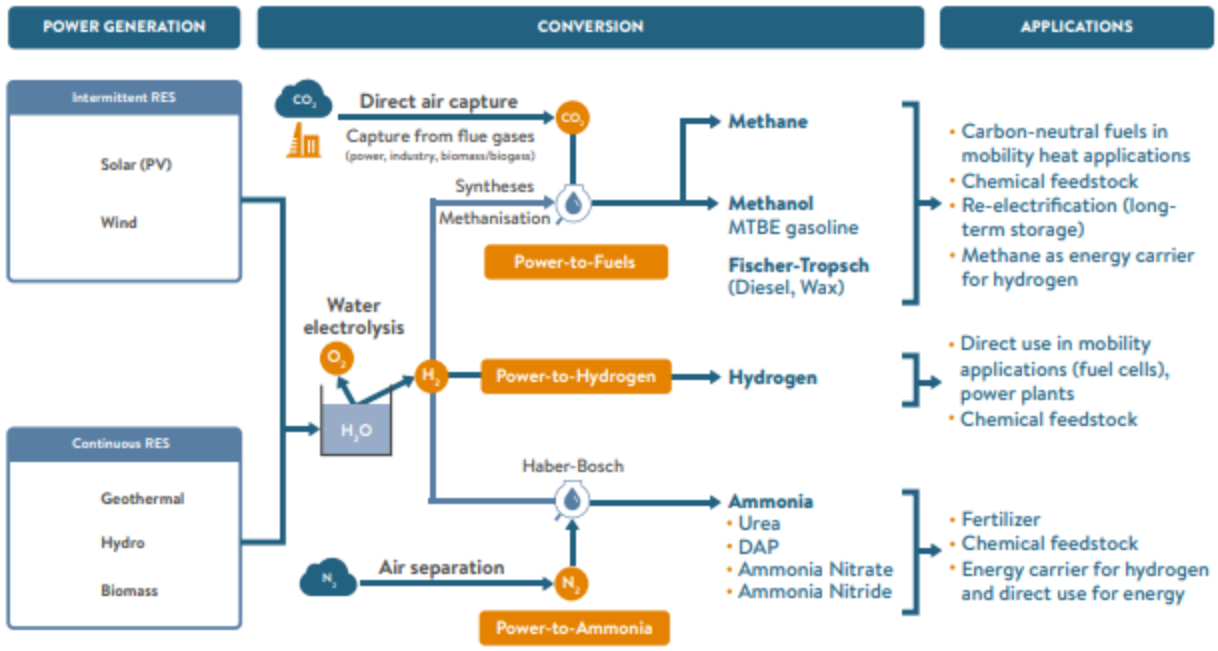

Figure 1.4. Conversion of renewable power into various forms of chemical energy carriers based on Siemens.[35]

Hydrogen is used to process crude oil into refined fuels such as gasoline and diesel and to remove contaminants such as Sulfur from these fuels.[48] Approximately 75 % of the hydrogen that is currently consumed worldwide by oil refineries is supplied by large hydrogen plants that generate hydrogen from natural gas or other hydrocarbon fuels.[49] Hydrogen is also an important basic substance in the production of methanol (CH_3OH). Methanol is produced by means of the catalytic hydrogenation of carbon monoxide.[50] Methanol is primarily used in chemical synthesis and as antifreeze; it can be used directly as a fuel in internal combustion engines.[51] It is also used in direct methanol fuel cells or, after reforming, in polymer exchange membrane (PEM) fuel cells.[52] Fuel additives are produced from methanol, and they are used to trans-esterify vegetable oils to form methyl esters (biodiesel).[53]

Since many of the industries mentioned above use high-carbon hydrogen for their processes, replacing it with low-carbon hydrogen would be an ideal opportunity to increase demand while decreasing greenhouse gas emissions in the short term.[54] Electrolytic hydrogen is gaining momentum in steelmaking, oil refining, and methanol and ammonia production.[55–58] Renewable hydrogen can simplify the value chain for many industries, and it can be used as a feedstock in the production of methane, clean chemicals, and fertilizers.[59,60] To achieve the decarbonization target, building heating can use hydrogen as a fuel, leverage hydrogen technologies, or use a combination of both, which would offer high efficiency to the generation of heat and power.[61] In homes, hydrogen could be used to power fuel cell micro-combined heat and power systems, direct flame combustion boilers, catalytic boilers, and gas-powered heat pumps.[61,62]

1.2.2 Hydrogen as an energy carrier

It is important to note that hydrogen is not an energy source but an energy carrier, and it has the potential to deliver or store a tremendous amount of energy per unit mass. Hydrogen as an energy carrier offers the best solutions to challenges in transitioning to renewable energy, if issues of storage are resolved. Hydrogen can be used as a fuel and converted back to electrical energy by fuel cells with high efficiency. Such an approach, in particular, can be implemented to stabilize the electrical grid by providing constant power when the renewable source is unavailable.[63,64] Hydrogen can provide a cost-effective, and clean energy infrastructure to distribute energy in any region of the world.[65] Wherever technological and/or economic obstacles prevent direct electrification, hydrogen offers a viable solution especially to the transport sector.[66]

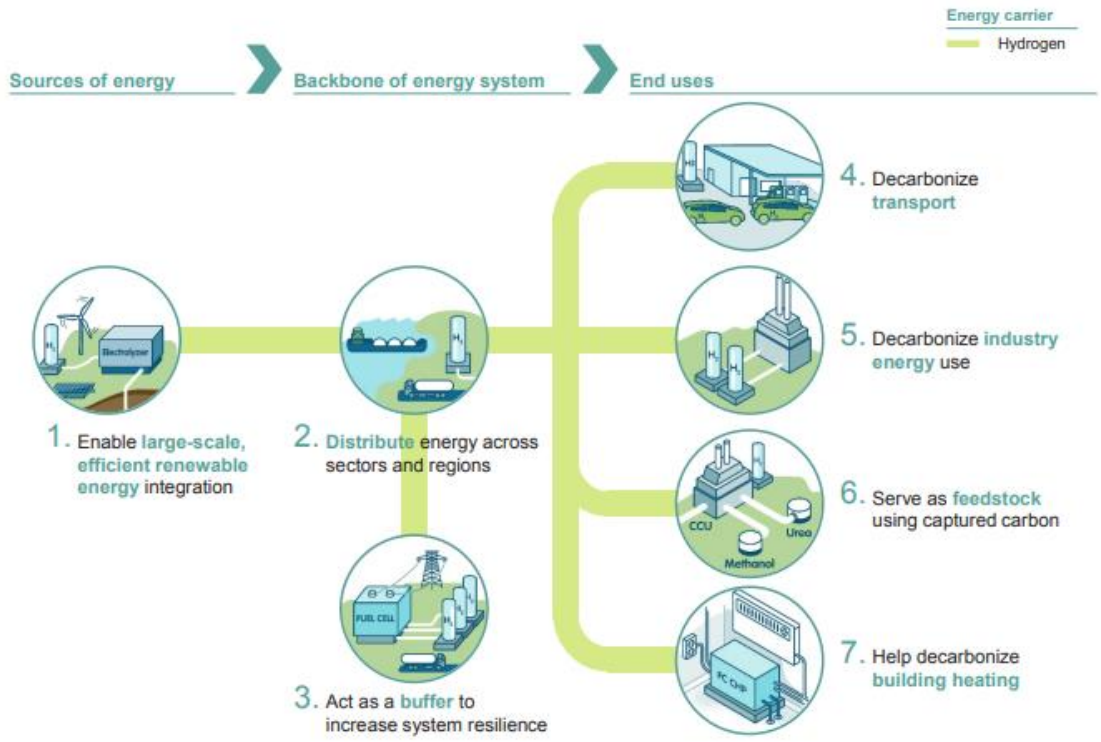

Figure 1.5. Seven roles of hydrogen in decarbonizing the major sectors of economy according to Hydrogen Council (2017).[67]

Hydrogen as an energy carrier could offer a climate-friendly solution in the decarbonizing industry; its seven major roles are shown in Figure 1.5. Hydrogen can be injected into the natural gas distribution grid to support the distribution of a clean gas for domestic and industrial heating, which would, at the same time, reduce emissions.[68,69] Blending sustainably sourced hydrogen at up to 20 % on a volumetric basis with the gas grid requires minimal or potentially no modifications to the infrastructure of the grid or to domestic end-user appliances.[70,71] This is an intermittent solution, which should be eventually applied in its entirety. However, injecting hydrogen into the gas transmission grid is more challenging due to material incompatibilities at high pressures and a lower hydrogen concentration tolerance in the blending, which industrial

users can accept.[72,73] Although challenges exists, solutions are currently being developed. However, a growing number of countries is interested in gas grid hydrogen-blending because of the increase in the use of variable renewable electric generation. Another potential application of hydrogen is heating in industry and building as a zero-emission alternative since it can be combusted in hydrogen burners or be used in fuel cells.[74,75] In addition, in carbon capture and utilization (CCU) technology, green hydrogen is required to convert the captured carbon into usable chemicals such as methanol, methane, formic acid, or urea.[76,77]

Converting renewable electricity through hydrogen into other energy carriers such as gases, liquids and heat, and into chemical feedstocks is a process known as "Power-to-X" (PtX or P2X), which is shown in Figure 1.4. The global excess in renewable power generation combined with improvements in utility-scale electrolysis are paving the way for domestic and fledgling self-organized regional power-to-X markets.[35] P2X allows the decoupling of the direct use of power from the electricity sector for use in other sectors such as transport or chemicals. It also provides the opportunity to replace conventional fossil fuels with "downstream derivates" of hydrogen such as synthetic methane, synthetic diesel, methanol, and ammonia, which has its own value-chains.[78] Even the synthetic methane that can be produced through a power-to-methane process can be injected into the natural gas grid.

The main drawbacks of this route are low renewables penetration, the high cost of current water electrolyzers in hydrogen production, and low electrolyzer efficiency.[79] Continued deployment of low-cost renewable energy generation and continued reduction in electrolyzer costs as well as efficiency are key elements in the success of P2X. Currently, over 70 projects are operational globally, with scales ranging from 250kW to 6,300kW of electrolyzer capacity.[27] The size of

P2X installations is growing, and electrolyzer units have reached capacities of 50+MW under deployment.[80] However, these are not sufficient to satisfy the already existing demand for sustainable hydrogen and to develop future technologies. Breakthroughs in H_2 production technologies are required, which are discussed in further sections.

1.2.3 Hydrogen production

Hydrogen can be produced from almost all energy resources in several different ways. Natural gas comprises 48 % of the global hydrogen production, which is followed by 30 % from oil, 18 % from coal, and 4 % by electrolysis.[61] Based on whether the energy resource is renewable or not, it is classified as a sustainable or a non-sustainable production process, respectively (Figure 1.6).

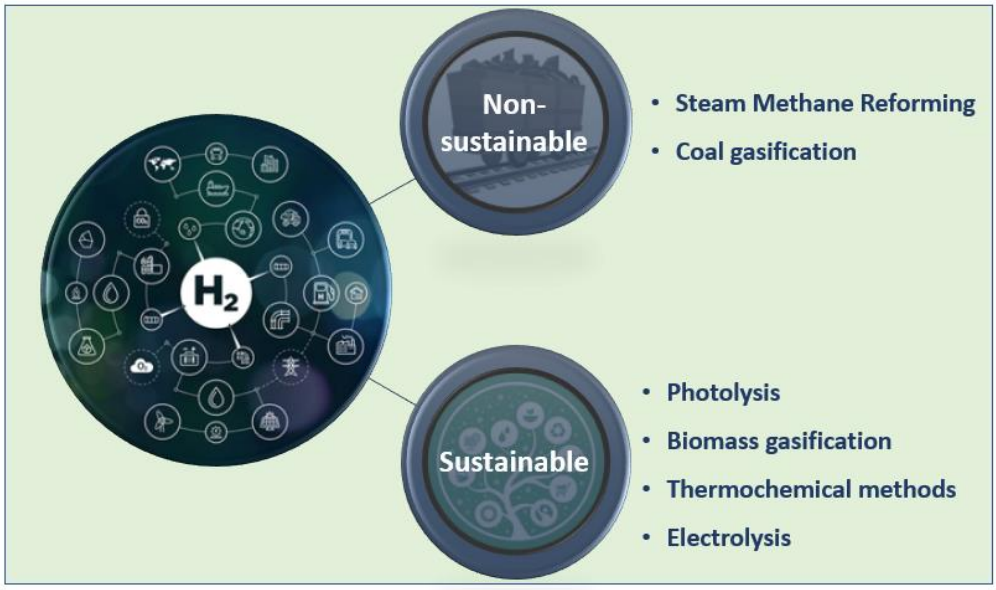

Figure 1.6. Production of hydrogen: non-sustainable and sustainable technologies.

The dominant source of industrial hydrogen is fossil fuels. Hydrogen that is produced from fossil fuels such as natural gas and coal are considered non-sustainable, since these are depleting resources, and their processing produces significant emissions. Hydrogen can also be produced from renewable sources. The latter includes the gasification of biomass, which is still a CO_2-emitting but formally carbon-neutral process,[81] and various methods of splitting water into oxygen and hydrogen (Figure 1.6). The latter can be achieved thermochemically,[82] photochemically,[83] or electrochemically.[84]

1.2.3.1 Non-sustainable technologies

Methane is the most widely used source of hydrogen and this methane comes mainly from natural gas, which is used to produce hydrogen in hydrogen plants and petroleum refineries. To produce hydrogen, Steam-methane reforming (SMR) is the most widely used method today. This is a well-established technology in which natural gas that contains methane (CH_4) is used to produce hydrogen by using thermal processes such as steam-methane reformation and partial oxidation.[85,86] It provides almost a half of all the hydrogen that is produced globally.[87] In an SMR reaction, methane reacts with water under 3–25 bar pressure at 1300–1800 °F in the presence of a nickel catalyst to produce hydrogen and carbon monoxide; this is followed be a water-gas shift reaction, which involves the reaction of CO with H_2O to generate more hydrogen and CO_2.[88] It is also used to produce hydrogen from other fuels such as ethanol, propane, or even gasoline.[89] In the partial oxidation method, the natural gas reacts with a limited amount of oxygen, which is followed by the water-gas shift reaction that produces hydrogen.[90,91]

Coal gasification can produce power, liquid fuels, chemicals, and hydrogen. Hydrogen is produced at pressures below 10 MPa and temperatures above 750 °C by first causing coal to

react with oxygen and steam to form synthesis gas, which further reacts with steam through the water-gas shift reaction to produce hydrogen.[92] Coal gasification can produce large quantities of hydrogen, which leads to economical production of electricity. However, the reserves-to-production ratio for coal is less than 150 years,[93] and the energy required for the necessary sequestration of CO_2 would increase the rate at which coal reserves are depleted.[94,95] Coupling conventional technologies with carbon capture, utilization, and storage (CCUS) is still the main route for low-carbon hydrogen production, since production costs are lower in CCUS than in other low-carbon technologies such as electrolysis.[23]

1.2.3.2 Sustainable production of hydrogen

Hydrogen production pathways that use naturally occurring energy that is essentially perpetual on the timescale of humanity, such as solar irradiation, wind, geothermal heat, and water as the only source of hydrogen are considered truly sustainable.

Photolysis directly utilizes the energy of solar irradiation to split water. Arguably, this method might be considered the most sustainable mode of hydrogen production. This could comprise photocatalytic, photoelectrochemical, or photobiological water splitting processes. Photocatalytic water splitting uses particulate semiconductor materials for water splitting, which combines photoelectric conversion and catalyst functions in a single particle.[96] On the other hand, photoelectrochemical water splitting uses semiconductor photoelectrodes. Combining photovoltaic systems with an external electrocatalyst is an indirect route of photolysis for fuel production. A simple system, inexpensive basic materials, and low-cost processing are the advantages of direct photolysis.[92,93] However, photostability issues and stringent requirements for photocatalysts limit the improvements in this field.[94] In spite of these challenges and low

solar-to-hydrogen (STH) energy conversion efficiency,[97] pilot solar hydrogen plants in Japan under the Japan Technological Research Association of Artificial Photosynthetic Chemical Process (ARPChem) project report significant hydrogen production, which indicates the feasibility of this technique in sustainable hydrogen production.[98] In photobiological water splitting or biophotolysis, microorganisms are used for oxygenic photosynthesis and splitting of water to produce hydrogen.[99] Though this technology is in its nascent stages, it has the potential to develop into one of the most cost-effective ways to produce hydrogen from renewable energy.

Artificially created biomass has enormous potential to hasten the realization of hydrogen as a major fuel of the future. Biomass is renewable, and it has low net CO_2 impact on fossil fuels since it consumes atmospheric CO_2 during growth. However, not every biomass is useful, and green algae that grow fast are required. Biomass can easily be converted into several liquid fuels such as methanol, ethanol, biodiesel, and pyrolysis oil, which could be used to generate hydrogen.[100,101] In comparison to chemical and biochemical methods, the thermochemical method yields a simpler route to the production of hydrogen from biomass and usually needs no chemical addition. It can also convert a variety of wet biomass and use the entire biomass-derived feedstock with comparatively high efficiency.[102] The inherent limitations of this process are low yield of hydrogen, low energy content in the biomass, and the greater amount of time that is required to grow the biomass, which is naturally slower than gasification and use of fuel, even for algae.[103,104]

Thermochemical water splitting is a carbon-free high temperature (500–2000 °C) hydrogen production technique that uses concentrated solar power or waste heat from nuclear reactors by consuming only water.[105–107] However, direct thermal splitting of water requires temperatures of

at least 2000 °C, which leads to technological problems such as the mixing of hydrogen and oxygen. To address this, a number of thermal chemical processes such as S–I, S–Br, Fe–Cl, Hg–Br, and Cu–Cl cycles have been identified; all of these use temperatures below 1000 °C and produce H_2 and O_2 in separate steps.[108–112] The Sulfur–Iodine cycle, which is a promising route for mass hydrogen production because of its high efficiency, has been the most studied.[113] This process is a closed cycle operation that comprises three major reaction steps. The first reaction is the Bunsen reaction, which involves a reaction between iodine, sulfur dioxide, and water to form hydroiodic (HI) and sulfuric acids (H_2SO_4). It is followed by the HI decomposition reaction and the sulfuric acid decomposition reaction.[114] Most of the input heat is used for the dissociation of sulfuric acid. All the reagents are recycled, which leaves no effluents.[115] The S-I cycle requires moderate temperatures of 800–900 °C and offers the prospect of high efficiency in the conversion of heat to hydrogen. However, this process is very demanding on materials, which are exposed to very corrosive species at elevated temperatures (up to 1000 °C) and pressures.[113,116] So, the design of materials for the process apparatus with sufficient corrosion resistance under these conditions is required.[117,118] Since iodine is comparatively less abundant and more expensive, the economic viability of the cycle is also a challenge.[119] It is reported that concentrated solar thermal systems could also be used to drive such thermal chemical cycles.[120,121]

Finally, an approach that probably attracts the maximum attention at the moment is water electrolysis, which quite ironically, is also the oldest known method of sustainable H_2 production.[122] Compared to other techniques, water electrolysis is a relatively technologically simple process in which an electrical current flowthrough two electrodes and an electrolyte to induce decomposition of water into hydrogen and oxygen molecules. When electricity is sourced

from renewable source, electrolysis produces zero greenhouse gas emissions. In fact, any technology that produces electricity can drive a water electrolyzer to produce hydrogen. Because of the enormous potential and surplus clean energy produced by solar, wind, or nuclear technologies, water electrolysis is considered an excellent potential technique for the mass production of hydrogen; it will also enable greater integration of renewables.[61,123,124] Currently, only 4 % of the H_2 that is produced is obtained by means of water electrolysis. This is still a higher percentage than that for any other sustainable approach, and it is expected to increase with further efforts in cost reduction.[125] When compared to other techniques, water electrolysis produces very pure hydrogen (>99.9%), which is ideal for high value-added processes in different industries.[126] Since water electrolysis is a pure hydrogen production route, it is the major focus of the present PhD project and is discussed in further detail below.

1.3 PRINCIPLES OF WATER ELECTROLYSIS

Water electrolysis, an electrochemical process was first demonstrated in 1789 and is now a well-established technology for the production of hydrogen that has a high level of purity.[127] Although there are different water electrolysis technologies depending on operating conditions such as the temperature and the nature of the electrolyte, the simplest water electrolysis unit consists of an anode and a cathode that is separated by a membrane in an electrolyte solution and connected to a power supply (Figure 1.7).

An overall water splitting reaction can be written as

$$2H_2O \rightleftarrows 2H_2 + O_2 \qquad \text{Eq 1.1}$$

Water splitting is described by two half-reactions: the hydrogen evolution reaction (HER) as the reduction reaction at the cathode where H_2 evolves, and the oxygen evolution reaction (OER) as the oxidation reaction at the anode where O_2 is produced. Depending on the chemical nature of the electrolyte, that is, of the species that supports ionic conductivity, the half-reactions differ at both electrodes and can be described by following equations:[128]

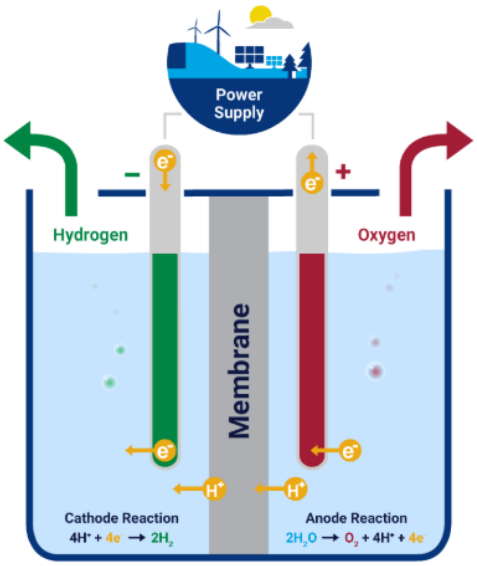

Figure 1.7. A schematic of basic water electrolysis cell

In an acidic medium:

OER: $2H_2O \rightleftarrows O_2 + 4e^- + 4H^+$ Eq. 1.2

HER: $4H^+ + 4e^- \rightleftarrows 2H_2$ Eq. 1.3

In an alkaline medium:

OER: $4OH^- \rightleftarrows O_2 + 4e^- + 2H_2O$ Eq. 1.4

HER: $4H_2O + 4e^- \rightleftarrows 2H_2 + 4OH$ Eq. 1.5

The water splitting reaction is an endothermic process, which is characterized by Gibbs free energy (ΔG^0) and enthalpy (ΔH^0) of 237 and 286 $kJmol^{-1}$, respectively, under standard conditions of 298 K and 1 bar of pressure.[129,130] This corresponds to a thermodynamic potential difference of 1.23 V. However, in practice, a significantly higher potential difference is required due to various losses. The overall cell potential that is needed to drive water electrolysis is as follows:[131,132]

$$E(I) = \Delta E_0 + \eta_a(I) + \eta_c(I) + IR \qquad \text{Eq. 1.6}$$

where E(i) is the voltage that should be supplied to the cell for water electrolysis to occur at a specified current, *I*; E_0 is the standard OER-HER electrode difference (1.23 V under standard conditions;) η_a and η_c are the overpotentials that are associated with the anodic and cathodic reactions, respectively; and *R* is the total resistance of the electrolyzer that gives rise to the ohmic drop, which is calculated as *IR*. The resistance is contributed by the nature and dimensions of the materials that are used as the electrode, the electrical conductivity of various components and the connections in the electric circuits, and the ionic transport in the electrolyte.[122,133] In this study, reversible hydrogen electrode (RHE) is used as a reference for all measured OER potentials, because the potential of RHE is independent of pH.

The most important parameter of an electrolyzer is its efficiency. The efficiency of an electrolyzer is defined based on the extent of the efficiency of an electrolyzer in converting electricity into hydrogen. It is calculated by the energy content (higher heating value) of the hydrogen, which is divided by the electricity that is consumed per kilogram of hydrogen produced.[134]

1.3.1 Modes of electrolysis

Based on the nature of the electrolyte and the operating conditions of the process, water electrolysis techniques can be classified mainly into three types: alkaline water electrolysis (AWE), solid oxide electrolysis (SOE), and PEM water electrolysis;[135,136] the schematic is shown in Figure 1.8. A comparison of these technologies is presented in Table 1.1.

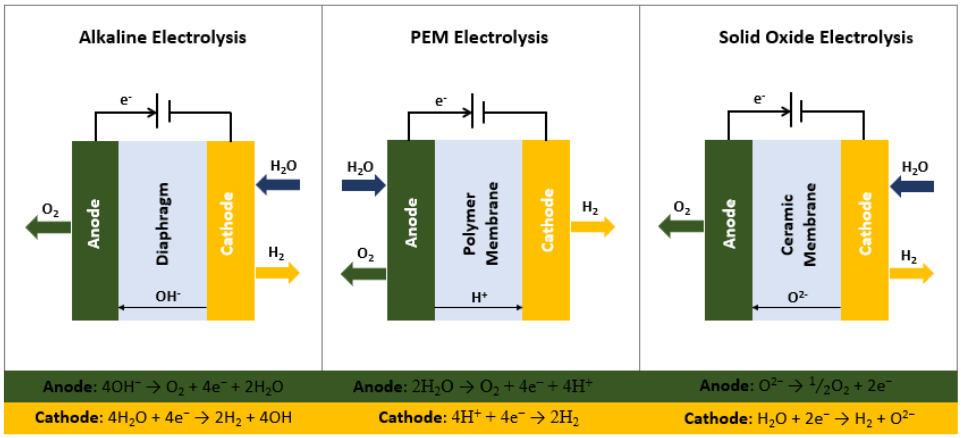

Figure 1.8. Schematic presentation of basic modes of operation of different water electrolyzers

Alkaline water electrolysis is the most mature water electrolysis technology to produce hydrogen, which can be implemented commercially at a large scale. The electrolyte is an aqueous solution that contains either NaOH or KOH, and it typically achieves an efficiency of 50–70 %;[130] a main disadvantage is its corrosive nature.[137] The compactness of PEM water electrolyzers offers many advantages over well-established alkaline water electrolysis.[125] One of the biggest advantages is that the PEM electrolyzers can be operated at high current densities even at moderate temperatures due to the increase in conductivity in an acidic electrolyte, which reduces the operational cost.[138] The ability of PEM electrolyzers to produce high purity hydrogen

by minimizing the gas crossover rate and withstanding high pressures makes them different from other parallel technologies.[139] The ohmic losses are also less because of the use of a thin layer membrane in this electrolyzer.[138] The absence of a corrosive electrolyte, a high hydrogen production rate, low maintenance and safeness render PEM electrolyzer promising and preferable to other electrolyzers.[140] A major drawback is the use of an acidic environment, which has restricted its catalysts to noble metals thus far.[141] PEM is the most desirable method to produce hydrogen by electrolysis, and it can have high efficiencies of 60–80 %. However, it still needs further optimization to reduce the cost of expensive components.[142] Anion Exchange Membrane (AEM) water electrolysis, which combines the advantages of alkaline and PEM-based water electrolysis, is promising in hydrogen production; however, issues such as stability and conductivity pose challenges.[143,144] SOEs are operated at high temperatures, which results in favorable thermodynamics and kinetics.[145] This leads to higher efficiencies of 85–90 % in comparison to other electrolyzers.[146] Currently, this technology is at the research and development stage and it can use nuclear reactors as heat source.[145] Although this technology seems to have long-term potential, the challenges in safety need to be addressed for its implementation.

Many new projects are now opting for PEM designs over alkaline electrolyzers, which are generally implemented in large-scale projects.[147,148] PEM electrolyzers are at an earlier stage of development than alkaline electrolyzers. However, they can operate more flexibly and are, therefore, more compatible with variable renewable electricity generation; they are also widely recommended.[149] This thesis focuses on developing catalysts that can solve stability issues with expensive noble-metal catalysts and alternate non-noble-metal electrocatalysts for PEM electrolyzers.

Table 1.1 Comparison of three major water electrolysis technologies.[130,145,146,150]

Electrolyser	Operating temperature and pressure	Advantages	Disadvantages
Alkaline	< 80°C < 30 bar	Long term durability Less expensive catalysts	Complicated maintenance Corrosive electrolyte Low current densities Slow ionic transport
PEM	80-100°C < 200 bar	High purity gas High current densities Compact design Compatible to variable power loads Fast start up	Expensive membranes Expensive electrodes Noble metal catalysts
SOEC	600-1000°C < 25 bar	High operational efficiency Increased kinetics Non-corrosive Less expensive catalysts	Limited stability High investment cost Safety concerns Bulk design

1.4 ELECTROCATALYSIS OF THE OXYGEN EVOLUTION REACTION

Oxygen Evolution Reaction (OER), a four-electron-transfer reaction is considered a rate-limiting step in water splitting.[151] The slow kinetics of the OER due to multi-proton/electron-coupled kinetics reduces the process efficiency of the entire system, which results in higher overpotential at the anode than the cathode even with the best available catalysts in an acidic medium.[152] Therefore, water oxidation is considered a bottleneck in the commercialization of hydrogen in the market. This shows that electrocatalysts are required to increase the efficiency of energy conversion and to reduce the amount of energy that is consumed in this process by lowering the kinetic barriers for OER. A fundamental understanding of OER is very crucial in developing

suitable catalyst materials to ease the reaction. The mechanism of the water splitting half reaction with electrocatalysts involves the following steps. One of these steps in the process acts as the rate-determining step for the entire reaction.

(i) Diffusion of species from the electrolyte solution to the catalyst surface.

(ii) Physio-chemical interactions, which leads to adsorption of these reactive species on the catalyst.

(iii) Charge transfer reactions and diffusion of species across the surface of the electrode.

(iv) Desorption of molecular species as products to the electrolyte from the surface of the catalyst.

Several hypotheses are proposed for the possible mechanism of the OER on heterogenous catalysts that are based on a density functional theory (DFT) analysis, and in situ spectroscopic and kinetic studies.[153–157] However, none of the mechanisms proposed thus far fully explains the experimental results that were obtained by using different heterogeneous catalysts. A significant contribution in this field has been made by Bockris, who proposed different kinetic models (discussed below) based on the Tafel slope analysis.[156] M in the following reactions represents an active site on the surface of a metal oxide catalyst.

I. Oxide pathway

1. $H_2O + M \rightarrow M\text{-}OH + H^+ + e^-$ Eq. 1.7

2. $2M\text{-}OH \rightarrow M\text{-}O + M + H_2O$ Eq. 1.8

3. $2M\text{-}O \rightarrow 2M + O_2$ Eq. 1.9

II. Electrochemical oxide pathway

1. $H_2O + M \rightarrow M\text{-}OH + H^+ + e^-$ Eq. 1.10

2. $M\text{-}OH \rightarrow M\text{-}O + H^+ + e^-$ Eq. 1.11

3. $2M\text{-}O \rightarrow 2M + O_2$ Eq. 1.12

III. Electrochemical Metal peroxide pathway

1. $H_2O + M \rightarrow M\text{-}OH + H^+ + e^-$ Eq. 1.13

2. $2M\text{-}OH \rightarrow M\text{-}O + M + H_2O$ Eq. 1.14

3. $H_2O + M\text{-}O \rightarrow M\text{-}O\text{-}OH + H^+ + e^-$ Eq. 1.15

4. $2M\text{-}O\text{-}OH \rightarrow M\text{-}O + H_2O + O_2 + M$ Eq. 1.16

However, since the Tafel slope is not a reliable measure since it depends on various underlying factors, these mechanisms fail to provide an unambiguous pathway for OER.[158,159] Another plausible pathway is proposed by Rossmeisl based on a thermochemical analysis and adsorption energies of reaction intermediates.[155]

IV. DFT-predicted peroxide pathway

1. $H_2O + M \rightarrow M\text{-}OH + H^+ + e^-$ Eq. 1.17

2. $M\text{-}OH \rightarrow M\text{-}O + H^+ + e^-$ Eq. 1.18

3. $H_2O + M\text{-}O \rightarrow M\text{-}O\text{-}OH + H^+ + e^-$ Eq. 1.19

4. $M\text{-}O\text{-}OH \rightarrow M + H^+ + e^- + O_2$ Eq. 1.20

Although the thermodynamic model can predict the activity trends in OER catalysis, it inherently does not account for the very important kinetic effects. This creates an uncertainty in OER mechanisms and emphasizes the essentiality of advanced techniques and studies to unravel the actual mechanism. Further to this ambiguity, OER at electrode surfaces are different in acidic and alkaline mediums. It can be represented by Figure 1.9 in general, based on different proposed mechanisms.[160] M-OH, M-O, and M-OOH are the key intermediates in these reactions,

while the reaction pathways to form oxygen are different. One is the direct combination of two M-O species, and the other involves an M-OOH formation and subsequent decomposition to produce O_2. The bonding interactions and the energies of these intermediates (M-OH, M-O, and M-OOH) are vital in determining the overall electrocatalytic activity of the catalyst and the reaction pathways.

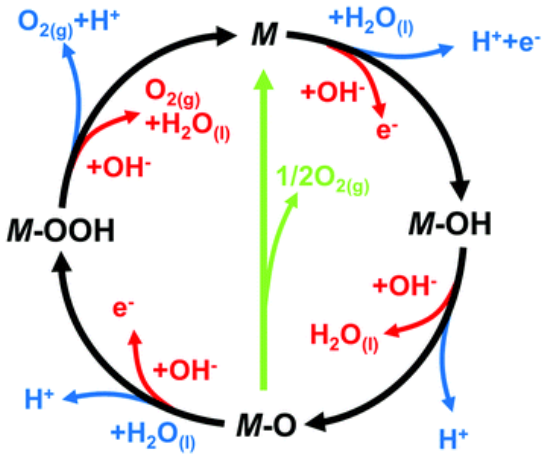

Figure 1.9. The OER mechanism for acid (blue line) and alkaline (red line) conditions. Green line shows a direct reaction route to form O_2 by two adjacent oxo (M–O) intermediates.[160] Adapted with permission from Royal Society of Chemistry.

The overpotential (η) is one of the most important descriptors to assess the kinetics of electrode reactions and the performance of electrocatalysts. The overpotential is calculated as the difference between the experimentally applied potential to drive the reaction (E) and the thermodynamically determined reaction potential at equilibrium (E_{eq}). Following the Nernst equation, the applied potential can be expressed as

$$E = E^0 + \frac{RT}{nF} ln \frac{[Ox]}{[Red]} \quad \text{Eq. 1.21}$$

where E is the applied potential, E^0 is the standard or equilibrium potential of the overall reaction, T is the absolute temperature, R is the universal gas constant, F is Faraday constant, n is the number of electrons that are transferred in the reaction, and [Ox] and [Red] are the concentrations of oxidant and reductant, respectively. In practice, the applied potential always exceeds the potential at equilibrium because of the electrode kinetic barrier of the reaction. The rate of the electron transfer reaction is determined by the applied electrode potential. Therefore, it is a measure of achieving a specific current density. The lower the overpotential at a specific current density, the better electrocatalytic activity it indicates.

The Butler–Volmer equation states the relationship between the current density and overpotential, which can be considered a fundamental equation in understanding electrode kinetics.[158]

$$j = j_0 \left[e^{\frac{(1-\alpha)nF\eta}{RT}} - e^{\frac{-(\alpha nF\eta)}{RT}} \right] \quad \text{Eq. 1.22}$$

where the current density, *j*, depends on the exchange current density, j_0 (current at which $\eta = 0$); overpotential, η; and transfer coefficient, α. The current density, *j*, is a sum of the anodic and cathodic currents. The charge transfer coefficient is a critical parameter in the evaluation of electrode kinetics. It depends on the rate-determining step (RDS), which is the slowest reaction step in the reaction mechanism that determines the kinetic overpotential for a reaction. The charge transfer coefficient is defined by the following equation.

$$\alpha = {}^{n_f}/_{\nu} + n_r\beta \quad \text{Eq. 1.23}$$

where n_f is the number of electrons that are transferred before the RDS, v is one, n_r is the number of transferred electrons in each occurrence of the RDS, and β is electrochemical Brønsted factor with a value of 0.5–1.

1.4.1 The role of an electrocatalyst

In general, a catalyst is a substance that accelerates a chemical reaction by interacting with reactants and a product without itself being consumed or undergoing a permanent change in a reaction. An uncatalyzed reaction can be described by the Arrhenius equation.

$$k = Ae^{\frac{-E_a}{RT}} \qquad \text{Eq. 1.24}$$

where E_a is the activation energy barrier for the reactants to overcome and form products, T is the temperature, R is the gas constant, and A, a constant. The potential energy diagram shows that a catalyzed reaction has a lower activation energy (E_a*) than an uncatalyzed reaction (E_a) by following a different mechanistic pathway because it forms intermediate chemical species with reactants in the reaction (Figure 1.10).

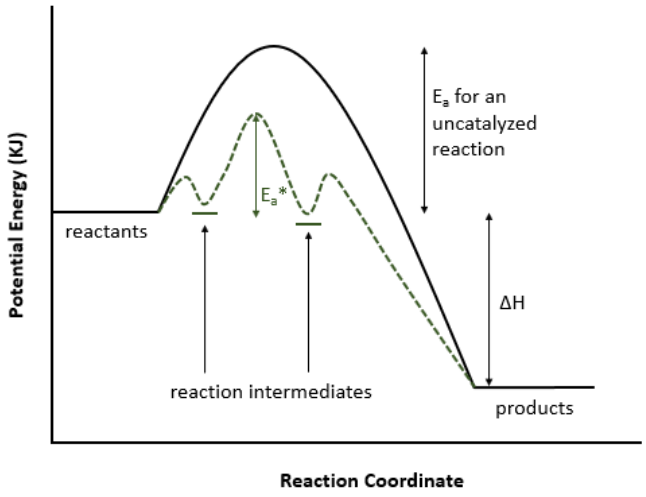

Figure 1.10. Potential energy diagram of a catalyzed and an uncatalyzed reaction

However, the net change in energy between the reactants and the products remains the same. The catalysts drive the reaction faster than in an uncatalyzed reaction because of the lower activation energy at the same conditions. Therefore, suitable electrocatalysts, which can aid in reducing the overpotential and increasing the reaction rate, are essential to improve the kinetics and to minimize the losses in OER. Based on the DFT-predicted pathway, a specific ΔG is associated with every step in the reaction for an ideal catalyst.[161] Water oxidation using an ideal catalyst occurs just above the equilibrium potential of 1.23 V at equal energy steps. Any difference from these equal steps is known as the overpotential. When *U*=0 V versus RHE, a total change in the free energy of 4.92 eV is required for four equal steps. This is the characteristic of a thermodynamically ideal catalyst, which is very different from that of a real catalyst. The most active OER catalyst in acid both theoretically and experimentally is RuO_2.[162] The free energies were calculated for intermediates on RuO_2 for the oxygen evolution at the applied potential, U= 0, 1.23 and 1.60 V, by Rossmeisl et al.(Figure 1.11).[155]

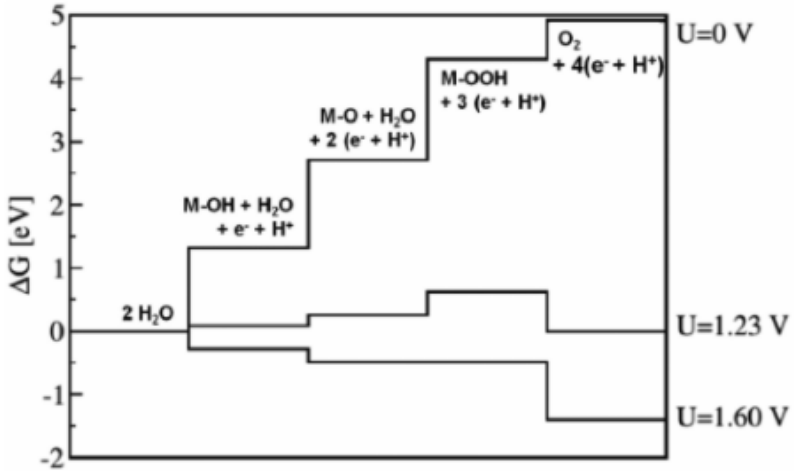

Figure 1.11. The Gibbs free energies of reaction intermediates at different electrode potentials of 0V, 1.23V and 1.60V vs Standard Hydrogen Electrode (SHE) for OER on a (110) RuO_2 surface.[157] Adapted with permission from John Wiley and Sons.

They found that the minimum potential at which all the reaction steps are downhill in energy is only at U= 1.60 V and that an overpotential of 0.37 V is needed for oxygen evolution with RuO_2. According to this, the electrocatalytic activity of the catalysts is mainly determined by the adsorption and desorption of the reaction intermediates to the catalyst surface. The Sabatier principle states that the interaction or the binding energies between reactants and catalysts should neither be too weak nor too strong.[163] If the interaction is too weak, it is difficult for the reactants to bind to the surface of the catalyst, which results in a lack of reaction on the surface. If the interaction is too strong, it is difficult for the product to be desorbed from the surface of the catalyst, which reduces electrocatalytic activity.

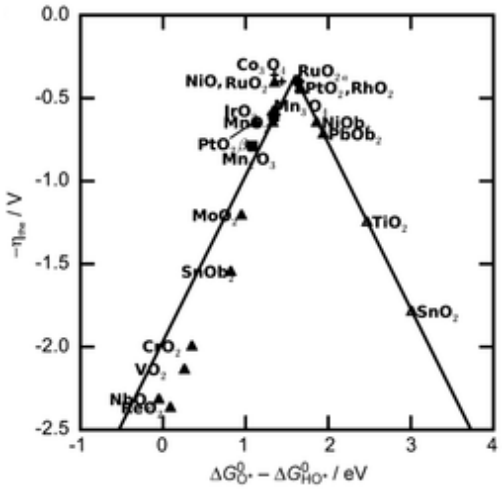

Figure 1.12. Activity trends of metal oxide OER catalysts plotted showing negative values of theoretical overpotential and standard free energy of $\Delta G_{HO^*} - \Delta G_{O^*}$ step.[161] Adapted with permission from John Wiley and Sons.

A volcano plot which is used as a tool for finding suitable catalysts among both heterogenous and homogenous catalysts has an ascending and descending branch and it gives a fair idea on performance of the electrocatalysts.[163,164] Volcano plot confirms the Sabatier principle of an ideal

catalyst by placing thermodynamically optimal catalysts at the top of the volcano plot. The volcano plot for metal oxides showed similar activity for RuO_2 and Co_3O_4 though Co_3O_4 shows higher overpotential than RuO_2 experimentally (Figure 1.12).[161]

1.4.2 The design of OER electrocatalysts

The design and development of efficient electrocatalysts is one of the major concerns in electrochemical water splitting devices. High electrocatalytic activity with good stability and selectivity are the most desired characteristics for any given electrocatalyst. Increasing the number of active sites and their intrinsic activity is the primary strategies to enhance the electrocatalytic activity of a catalyst (Figure 1.13).[165]

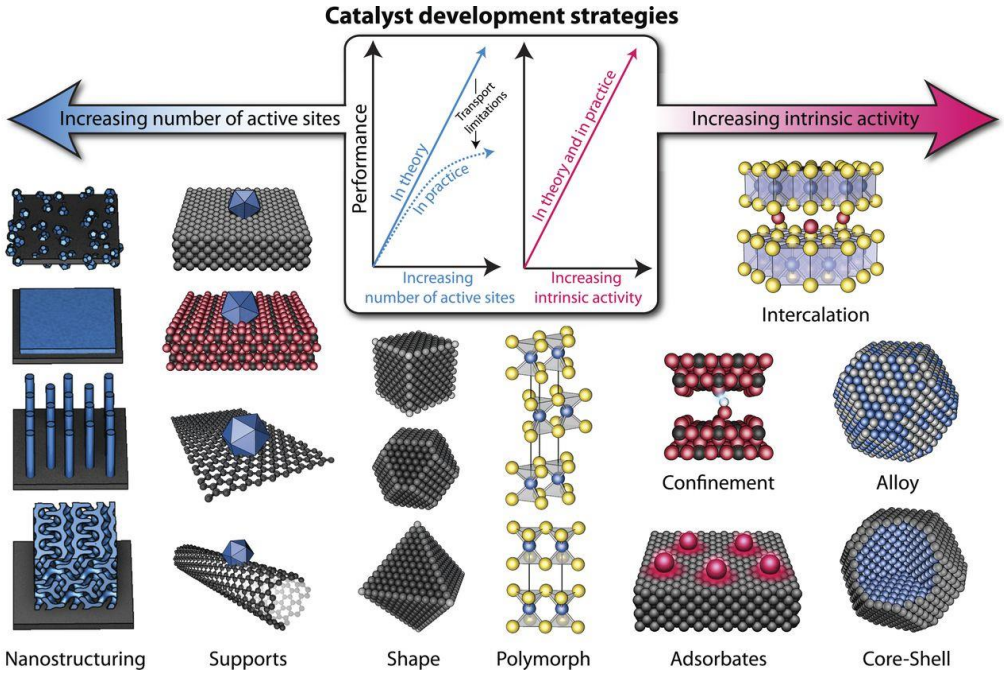

Figure 1.13. A schematic for various catalyst development strategies based on either increasing the active sites or its intrinsic activity.[165] Reprinted with permission from American Association for the Advancement of Science (AAAS).

Increasing the electrochemical surface area or catalyst loading increases the number of active sites on a catalyst. The surface area can be increased by using nanostructured catalysts that have a high surface-to-bulk ratio, and porous substrates such as foam and 3D carbonaceous materials.[166,167] The linear increase of activity with the number of active sites and physical limits along with an increase in catalyst loading on mass and charge transport reduces the extensive use and impact of this approach.[168] However, increasing the intrinsic activity can overcome these physical limitations and even lower the catalyst costs, because this can reduce catalyst loading. Phase, morphology, crystal facet, defect, mixed metals, and strain engineering are investigated to boost the intrinsic activity of the electrocatalysts.[169] Optimizing the binding of the reactants, reactant intermediates, and products to the surface of the catalyst plays a significant role in the electrochemical performance of a catalyst.

Since RuO_2 is a highly active material for OER, Rossmeisl and colleagues predicted that a material that could bind oxygen in a stronger manner than RuO_2 would be able to perform OER at a lower overpotential than with RuO_2.[155] In defect engineering, defects such as O-vacancy on the surface of the catalyst promotes better charge transfer and electrical conductivity, which supports fine-tuning of adsorption species in catalysis. [170,171]Another interesting approach is the forming of mixed metal catalysts. These catalysts provide the freedom to modify the inherent electronic conductivity and other characteristics of the catalyst, and thereby better performance because of synergistic interactions.[172] In strain engineering, depending on whether it is compression or extension, the strain decides how strongly or weakly the reaction species are adsorbed on the surface of the catalyst.[173] The strain also alters the electronic structure by modifying the internal energy.

Apart from these strategies, techniques to enhance the electronic conductivity of the materials need to be considered while designing a catalyst.[174,175] This can increase the charge transfer rate from the surface reaction sites to the substrate electrode, and leads to the mass diffusion within the materials. Although numerous catalysts have been reported in recent years, the linear scaling relationship of the energies between different adsorbed intermediates withhold the performance of the catalyst. There are two main strategies to break the adsorption energy scaling relationship. The first strategy is to use techniques such as the introduction of a second adsorption site, proton donor/acceptor group, and nanoscopic confinement, which helps in selective stabilization of *OOH unaffecting *OH adsorption. the second strategy is to bypass the generation of *OOH by activating lattice oxygen for direct O-O coupling.[176] Further understanding of these mechanisms by combining theoretical and experimental results and using advanced characterization techniques will definitely stimulate the development of highly efficient electrocatalysts for water splitting. Further efforts and investigation of methods to bypass the limitation of the linear scaling relationship by engineering of the catalyst will be a key aspect of designing efficient electrocatalysts in future.

1.4.3 Low-pH OER electrocatalysts

A major limitation of low-pH water electrolyzers is with the anode catalysts; these are problematic in many aspects such as their cost, activity, and durability in operation.[157] Since very few catalysts show stable operation at a low pH under experimental conditions, it is a challenge to find an efficient OER catalyst that is suitable for application in PEM electrolyzers. Currently, the search for water oxidation catalysts that are capable of stable operation at a low pH is an area of intense research. Thus far, only IrO_x- and RuO_x-based materials show reliable performance in

acidic conditions when compared to other catalysts.[177] Some of the best performing OER catalysts in an acidic medium are shown in Table 1.2; most are based on noble metals.

Table 1.2 Comparison of the performance of OER catalysts in acid

Catalyst	Substrate	Electrolyte	Overpotential at 10 mA cm^{-2} / mV	T / °C	Stability / h	Ref.
$IrO_x/SrIrO_3$	$SrTiO_3$	0.5M H_2SO_4	270	23	30	[178]
IrOOH nanosheets	Ti	0.1M $HClO_4$	344	23	7	[179]
$W_{0.57}Ir_{0.43}O_{3-\delta}$	FTO	1M H_2SO_4	370	23	0.55	[180]
RuO_2	FTO	1M H_2SO_4	280	23	4	[181]
RuO_2 nanosheets	Ti	0.1M $HClO_4$	255	23	6	[182]
$CoFePbO_x$	FTO	0.1M H_2SO_4				[183]
$Ni_xMn_{1-x}Sb_{1.6}O_y$	ATO	1M H_2SO_4	672	23	168	[184]
NiFeP	-	0.05M H_2SO_4	540	23	30	[185]
Mn-rich rutile $Mn_xSb_{1-x}O_z$	Pt/Ti/SiO_2/ Si wafer	1M H_2SO_4	580	23	30	[186]
Co_3O_4	FTO	0.5M H_2SO_4	570	23	12	[187]

Despite all the progress that has been made in electrochemical water splitting, there is a critical need for alternative earth-abundant electrocatalysts for low-pH water. In addition to being expensive and scarce in the earth's crust, it is well known that noble metals suffer significant stability issues in an acidic electrolyte, especially RuO_2.[188,189] Although several metal oxides such as perovskites have been reported, these catalysts deactivate in most cases, because they undergo structural transformation during the operation.[178,190,191] This renders the design and development of electrocatalysts for PEM electrolyzers a challenge for further progress in water splitting.

1.4.4 Stability versus activity paradigm

Stability and activity are critical parameters that cannot be compromised upon in catalyst development. There are a few systems that can catalyze the reaction quite well at a low pH; however, all are thermodynamically unstable. The experimentally established overpotential sequence of different metals for OER in acidic solutions is Ru < Ir < Pd < Rh < Pt.[192] The Rutile-type ruthenium oxide (r-RuO_2) is a metal oxide with the highest OER activity in acidic solutions. However, the major drawback is that under high anodic overpotentials of > 1.4 V, it oxidizes to dissolvable RuO_4, and its activity vanishes as predicted by the Pourbaix diagram.[193] IrO_2 possess increased stability up to 2V, although it has a slightly higher overpotential than RuO_2.[194] Iridium-based systems are believed to be the most stable OER catalyst in an acidic medium, which compensates for its lower activity. Iridium is resistant to dissolution in an electrolyte of pH = 0 up to a potential of 0.93 V, according to the Pourbaix diagram.[195] Although it is commonly observed that the activity and the stability of the electrocatalysts are inversely related, the higher activity of hydrated amorphous $Ir^{III/IV}$ oxyhydroxides when compared to crystalline rutile-type IrO_2 questions this notion.[196] It was reported that dissolution increases because IrO_2<RuO_2<Ir <Ru is independent of the electrolyte, and the stability follows a reverse trend.[197] State-of-the-art iridium-based catalysts are discussed in greater detail in the next section.

In electrocatalysts, a clear choice from non-precious elements is transition metals because of their properties: multiple oxidation states, easy interchangeability between the states, and complex formation with reagents.[198] It is reported that the early first-row transition metal oxides are resistant to corrosion in acidic conditions, while the latter ones are not stable and corrode quickly in acidic environments.[199] MnO_x is considered a more abundant and inexpensive

alternative to unstable RuO_2.[200–202] MnO_x has higher intrinsic and functional kinetic stability in acidic electrolytes than other first-row transition metals. However, it dissolves naturally in acidic electrolytes such as other oxides.[203] Its self-healing mechanism and mixing with Ti and Sb are demonstrated to improve the stability of Mn-based catalyst systems.[186,202,204] Co_3O_4 is more electrocatalytically active than MnO_x; however, it corrodes rapidly in acidic conditions.[187]

According to the Pourbaix diagram, Co_3O_4 is stable only over a very narrow range of potentials and pH, while Co species can remain stable at pH < 2 for a bias potential that exceeds 2 V.[203] However, the kinetic stability outside the predicted thermodynamic range can be modified by thermal treatment or incorporation of other anions.[205,206] Although Ni and Fe oxides and their combination demonstrate exceptional stability and catalytic activity in higher pH solutions, these materials shows poor performance in water oxidation in acidic solutions because these metals dissolves at a low pH, which is in agreement with the Pourbaix diagram.[203,207,208] In order to protect these materials from instant dissolution in an acidic environment, strategies such as placing the catalyst in stable metal oxide framework has been reported recently.[209] This analysis shows that the stability of noble-metal-free electrocatalysts is still an unresolved critical issue. More efforts and techniques to prevent the dissolution of these metals, while their activity is maintained are essential to develop cost-effective and competitive electrocatalysts for water oxidation at a low pH.

1.4.5 State-of-the-art Iridium-based catalysts

IrO_x is a state-of-the-art OER catalyst in an acid electrolyte due to its comparatively high catalytic activity and better stability in comparison to RuO_x. Although iridium metal becomes less active when oxidized, as in most cases of other metals, IrO_x is more stable than the iridium

metal.[197] The stability increases with crystallinity of the oxides in iridium-based catalysts and shows a reverse trend in terms of its activity.[210] This is further confirmed by the highest stability number (ratio of amount of oxygen evolved to iridium dissolved in the solution) that is obtained for crystalline IrO_2.[211] Thermally prepared rutile IrO_2 demonstrates the highest stability with lowest iridium dissolution rates, because the dense crystalline film prevents the accessibility of electrolyte to the sub surface iridium and activated oxygen atoms.[211] Despite being predicted as stable by theoretical studies, iridium-based catalysts undergo severe corrosion, although the corrosion is not as severe as other available catalysts.[212,213] Because of the defects and porosity, it is more probable to form molecular O_2 and allow the subsequent dissolution of iridium in hydrous IrO_2. The most active iridium-based material ever reported is $IrO_x/SrIrO_3$, which is followed by ruthenium-based oxides.[178] The formation of IrO_3 or IrO_2 anatase motifs when strontium leaches out results in high catalytic activity, according to DFT calculations.

Although iridium oxide is an appropriate catalyst in PEM electrolyzers, iridium is 10 times less abundant than platinum.[214] Therefore, significant efforts have been made to decrease the amount of iridium in OER catalysts to the minimum without sacrificing their catalytic performances, to make it feasible at a large scale. The general approach to accomplish this is to disperse the iridium oxide on a conducting high surface area support or in a mixture of inert components such as oxides of Ti, Nb, Sb, Sn, Ta, and Si.[215–219] Along with this strategy, tuning the intrinsic activity and the stability of the iridium oxide catalyst is also unavoidable in order to ensure maximum efficiency with a low amount of catalyst. A combined IrO_x/RuO_x system can be a compromise between the excellent catalytic activity of ruthenium oxides and the better stability of iridium oxides because of the interaction of the two elements. A sub monolayer amount of IrO_x at the surface of the RuO_2 reported high current density, while simultaneously reducing Ru

corrosion.[220] Ru–Ir alloys and oxides show enhanced electrochemical activity and thermodynamic stability.[221,222] However, the activity and stability of these mixed oxides depend mostly on the preparation method, since the method decides the surface enrichment and phase formations.

Mixed bimetallic oxides of iridium with earth-abundant transition metals such as nickel along with a low iridium content is also reported; however, the nickel immediately leaches out. Another approach is to replace the bulk of the catalyst with less expensive materials such as tin and nickel along with a low amount of noble metals at the top, because only the outer surface of the catalyst is involved in the reactions, which is similar to the core-shell concept in nanoparticles.[223,224] This not only reduces the noble-metal content, but the underlying bulk material can also positively affect its activity and increase the stability because of the enhanced bond energy between the core-shell materials. Nanostructured materials that have a high index facet on the surface of the catalyst and low loading on high surface area supports were also explored to minimize the amount of active catalyst.[225,226] However, most of these catalysts still have an Ir content of more than 40 %. Further studies and strategies that focus on reducing the noble-metal content without sacrificing the stability of the catalysts is required for maximum utilization of these metals as electrocatalysts for water oxidation.

1.4.6 Design concepts of new OER catalysts for a low pH

Instead of minimizing the noble-metal content in electrocatalysts, recent research in electrochemical water splitting is more focused on finding earth-abundant and less expensive materials as catalysts that are comparable in performance to state-of-the-art catalysts. However, these metal oxide catalysts corrode fast in an acidic environment and the catalytic activity of

these materials remains far inferior to noble-metal catalysts. Nevertheless, it is highly desirable to explore different strategies and techniques to improve the stability of these systems for their potential use in water electrolyzers. Therefore, new design concepts to extend the durability of the catalysts, such as self-healing and the catalyst in a matrix approaches are discussed in this section.

In the self-healing mechanism, the catalyst remains stable through self-healing during the OER process until the degradation of film occurs faster than the repairing of the catalyst, and the in situ-generated oxides catalyze the water oxidation. Similar to the process in nature, in which the structure of the catalyst is continuously repaired to retain its efficiency, if the artificial catalyst can self-repair, this can ultimately pave way for the development of robust electrocatalysts with long lifetimes. This is particularly advantageous if the replacement of the catalyst is not economically viable or practically impossible. MnO_x is intrinsically unstable in water oxidation in an acidic pH regime, but a self-healing mechanism can make it functionally stable.[202] In the case of MnO_x, the reoxidation of manganese ions in the solution makes the catalyst stable. The self-healing process of MnO_2 in the presence of an oxidant is also reported.[227] Self-healing cobalt oxide catalysts were reported for higher pH except under strong acidic conditions.[228]

Another strategy for the stabilization of the catalyst without losing its catalytic activity is the confining of the active catalytic sites of metal oxides within an acid resistant, conductive, and thermodynamically stable metal oxide matrix. The incorporation of catalytically active Ir oxides into the TiO_2 matrix demonstrated enhanced stability without any significant loss in activity.[229] Films of $NiFePbO_x$ and $NiPbO_x$ are reported recently as utilizing the acid stability and conductivity of PbO_x as a framework to stabilize Ni.[209] Another conductive stable matrix

reported is SbO_x, which displayed excellent enhancement in stability with Mn, Ni, and Co oxides in harsh acidic conditions even for long durations.[184,186,230] These reports, in which a stable metal oxide was used as a scaffold for active OER catalysts emphasize that this is a more flexible and rational approach to tune the activity and stability of a catalyst.

Combining the self-healing mechanism to template stabilized electrocatalysts is a promising pathway and strategy for the development of active, stable, robust, and inexpensive OER catalysts for PEM electrolyzers. As an example, Chatti et al. reported an intrinsically stable $CoFePbO_x$ electrocatalyst in a stabilized matrix showing high current densities and reasonable overpotentials for temperatures up to 80 °C in zero pH;[183] however, it is difficult to implement self-healing catalysts in an acidic pH.[231] The increase in the concentration of dissolved metals can, however, reduce the efficiency of the self-healing catalyst. Although it is hard to eliminate the dissolution of catalysts, this strategy is worth exploring for the development of electrocatalysts at a low pH. The decrease in activity, which is observed with this strategy, can certainly be improved by using mixed metal oxides as electrocatalysts.[184] This can lead to the development of the best performing catalysts that have desirable qualities and are suitable for OER in acidic conditions.

Antimony oxide (SbO_x) based catalysts are of a particular interest in this context. The thermodynamic stability of SbO_x under the low pH OER conditions,[232] their reasonable electrical conductivity,[233–235] along with abundance and availability of Sb[236] render these compounds a suitable structural component for acid-stable water oxidation electrocatalysts. Indeed, antimony oxides have been used as stabilizing interlayers and components in robust electrowinning anodes,[237,238] and have recently been also introduced to studies of OER catalysts for acidic water

electrolyzers. In particular, the research teams of Gregorie[239,240] and Lewis[184,241] both reported promising activity and improved stability in operation of antimonates of manganese and nickel. More recent work also described cobalt antimonate OER catalysts.[242] Thus, the stability of transition metal oxides during electrooxidation of water at low pH can be improved *via* combination with the highly promising SbO_x matrix. In the case of Ru, such an approach can also reduce the noble metal loading and thereby the cost of the material. However, the catalysts of this type are currently underexplored and have only recently gained an increased attention.

1.5 SUMMARY AND OBJECTIVES OF THIS WORK

In the current energy scenario, hydrogen is an irreplaceable fuel due to its unique properties and wide range of industrial applications. However, the global production of hydrogen through sustainable technologies needs to increase for hydrogen to be projected as a carbon-free green fuel. Finding alternatives for noble metal electrocatalysts or reducing their content in the electrocatalysts for water splitting is crucial for large-scale commercialization of PEM electrolyzers. However, both non-noble-metal catalysts and catalysts with a low content of noble metals suffer significant degradation in the performance for OER in an acidic electrolyte. Moreover, the discussion above reveals that non-noble-metal-based electrocatalysts that have been reported thus far are not reliable and stable when compared with the competing activity of state-of-the-art catalysts. Not even a single earth-abundant electrocatalyst has been developed as an anode to date for operation at elevated temperatures in harsh acidic conditions. The design and development of stable, cost-effective, and sustainable electrocatalysts is critical, and it should be the main focus of research in this area when exploring new strategies. Forming thin

noble-metal layers on earth-abundant metal supports by tailoring the noble-metal content for maximum utilization will be the best strategy to develop stable and less expensive electrocatalysts using noble metals. In the case of non-noble metals, a greater number of elements need to be tested to develop mixed metal oxides as catalysts along with employing acid-stable matrix and self-healing mechanism to enhance the stability and durability of the catalysts.

Based on the discussion above and the status of research in hydrogen production specifically related to OER electrocatalysts, the overall goal of this thesis is to develop acid stable water oxidation catalysts for PEM electrolyzers. This study aims to develop robust non-noble-metal-based electrocatalysts for long-term operation at a low pH at ambient conditions and elevated temperatures as an alternative lasting solution for the use of expensive noble-metal catalysts in PEM electrolyzers. This work aims to explore a catalyst in matrix approach by using SbO_x combined with the self-healing mechanism of catalysts. In addition, another focus is the investigation of the behavior of various potential metal oxides in water oxidation in extreme acidic conditions, which can serve as a guide for catalyst development. This work also aims to find strategies to improve the electrocatalytic performance of acid-stable anodes through engineering.

The specific objectives of this work are to

- develop robust monometallic OER catalysts using an acid-stable antimony oxide matrix for long-term durable operation in an acidic environment at ambient and elevated temperature;

- investigate the effects of mixing different metals within an antimonate acid stable matrix on the electrocatalytic activity and durability in operation during water electrooxidation at low pH;
- demonstrate surface and substrate engineering of the antimonate-based OER electrocatalysts with different metal oxides as an effective strategy to enhance the activity and stability in operation.

1.6 REFERENCES

(1) Foundation, U. N. Sustainable Energy for All (SE4ALL). **2011**.

(2) SE4ALL Global Tracking Framework.

(3) ONU. *World Urbanization Prospects*; 2018; Vol. 12. https://doi.org/10.4054/demres.2005.12.9.

(4) BP Statistical Review of World Energy. **2019**, No. 68.

(5) BP. Statistical Review of World Energy. **2020**, 66.

(6) Ritchie, H. Renewable Energy.

(7) https://ourworldindata.org/grapher/energy-consumption-by-source-and-region.

(8) IPCC. *Climate Change 2014: Mitigation of Climate Change. Contribution of Working Group III to the Fifth Assessment Report of the Intergovernmental Panel on Climate Change*; 2014. https://doi.org/10.1017/CBO9781107415416.

(9) International Energy Agency. Global Energy & CO_2 Status Report. **2019**.

(10) UNEP. *Emissions Gap Report 2019*; 2019.

(11) IEA (2020), Global Energy Review 2020, IEA, Paris Https://Www.Iea.Org/Reports/Global-Energy-Review-2020. https://doi.org/10.1787/a60abbf2-en.

(12) World Energy Council. COVID-19 Crisis Scenarios. **2020**, No. June 2020.

(13) REN21. *Renewables 2020 Global Status Report*; 2020.

(14) *Renewable Power Generation Costs in 2018*; 2019.

(15) Renewable Energy in Cities. *Int. Renew. Energy Agency* **2016**.

(16) Agency, I. E. Renewables: Analysis and Forecast to 2024. **2019**.

(17) Association, W. N. Renewable Energy and Electricity.

(18) World Energy Council (WEC); Paul Scherrer Institute. World Energy Scenarios 2019. *WEC Publ.* **2019**, 12–16.

(19) Yan, Z.; Hitt, J. L.; Turner, J. A.; Mallouk, T. E. Renewable Electricity Storage Using Electrolysis. *Proc. Natl. Acad. Sci. U. S. A.* **2020**, *117* (23), 12558–12563. https://doi.org/10.1073/pnas.1821686116.

(20) Agency, I. E. The Future of Hydrogen: Seizing Today's Opportunities. *G20, Japan* **2019**. https://doi.org/10.1016/S1464-2859(12)70027-5.

(21) Https://www.iea.org/fuels-and-technologies/hydrogen. Hydrogen.

(22) Agency, I. R. E. *Hydrogen : A Renewable Energy Perspective*; 2019.

(23) Liguori, S.; Kian, K.; Buggy, N.; Anzelmo, B. H.; Wilcox, J. Opportunities and Challenges of Low-Carbon Hydrogen via Metallic Membranes. *Progress in Energy and Combustion Science*. 2020. https://doi.org/10.1016/j.pecs.2020.100851.

(24) Hydrogen Council. Path to Hydrogen Competitiveness: A Cost Perspective. **2020**, No. January, 88.

(25) Climate Finance Leadership Initiative. Financing the Low-Carbon Future. **2019**.

(26) Owusu, P. A.; Asumadu-Sarkodie, S. A Review of Renewable Energy Sources, Sustainability Issues and Climate Change Mitigation. *Cogent Eng.* **2016**, *3* (1), 1–14. https://doi.org/10.1080/23311916.2016.1167990.

(27) World Energy Council. Hydrogen an Enabler of the Grand Transition. **2018**.

(28) Karimi Alavijeh, M.; Yaghmaei, S.; Mardanpour, M. M. Assessment of Global Potential of Biohydrogen Production from Agricultural Residues and Its Application in Nitrogen Fertilizer Production. *Bioenergy Res.* **2020**, *13* (2), 463–476. https://doi.org/10.1007/s12155-019-10046-1.

(29) *Hydrogen Supply Chain: Design, Deployment and Operation*; Azzaro-Pantel, C., Ed.; Academic Press, 2018.

(30) Quarton, C. J.; Tlili, O.; Welder, L.; Mansilla, C.; Blanco, H.; Heinrichs, H.; Leaver, J.; Samsatli, N. J.; Lucchese, P.; Robinius, M.; Samsatli, S. The Curious Case of the Conflicting Roles of Hydrogen in Global Energy Scenarios. *Sustain. Energy Fuels* **2019**, *4* (1), 80–95. https://doi.org/10.1039/c9se00833k.

(31) https://hydrogeneurope.eu/hydrogen-industry.

(32) Cigal, J.-C. Expanding Use of Hydrogen in the Electronics Industry. *Spec. Gas Rep.* **2016**, 26.

(33) Bilik, J.; Pustejovska, P.; Brozova, S.; Jursova, S. Efficiency of Hydrogen Utilization in Reduction Processes in Ferrous Metallurgy. *Scientia Iranica*. 2013, pp 337–342. https://doi.org/10.1016/j.scient.2012.12.028.

(34) M. Marquez, X. T. Hydrogen in Refining. *Linde Gr.* **2016**.

(35) Frontier Economics, W. E. C.; Germany. *International Aspects of a Power-to-X Roadmap*; 2018.

(36) Garagounis, I.; Vourros, A.; Stoukides, D.; Dasopoulos, D.; Stoukides, M. Electrochemical Synthesis of Ammonia: Recent Efforts and Future Outlook. *Membranes (Basel).* **2019**, *9* (9), 1–17. https://doi.org/10.3390/membranes9090112.

(37) Modak, J. M. Haber Process for Ammonia Synthesis. *Resonance* **2011**, *16* (12), 1159–1167. https://doi.org/10.1007/s12045-011-0130-0.

(38) Gunduz, S.; Deka, D. J.; Ozkan, U. S. A Review of the Current Trends in High-Temperature Electrocatalytic Ammonia Production Using Solid Electrolytes. *Journal of Catalysis*. 2020, pp 207–216. https://doi.org/10.1016/j.jcat.2020.04.025.

(39) Wang, L.; Xia, M.; Wang, H.; Huang, K.; Qian, C.; Maravelias, C. T.; Ozin, G. A. Greening Ammonia toward the Solar Ammonia Refinery. *Joule* **2018**, *2* (6), 1055–1074. https://doi.org/10.1016/j.joule.2018.04.017.

(40) Pfromm, P. H. Towards Sustainable Agriculture: Fossil-Free Ammonia. *J. Renew. Sustain. Energy* **2017**, *9* (3). https://doi.org/10.1063/1.4985090.

(41) Bird, F.; Clarke, A.; Davies, P.; Surkovic, E. *Ammonia : Fuel and Energy Store*; 2020.

(42) ASHRAE. Ammonia as a Refrigerant. *ASHRAE* **2017**.

(43) Smith, C.; Hill, A. K.; Torrente-Murciano, L. Current and Future Role of Haber-Bosch Ammonia in a Carbon-Free Energy Landscape. *Energy Environ. Sci.* **2020**, *13* (2), 331–344. https://doi.org/10.1039/c9ee02873k.

(44) Wang, J.; Chen, S.; Li, Z.; Li, G.; Liu, X. Recent Advances in Electrochemical Synthesis of Ammonia through Nitrogen Reduction under Ambient Conditions. *ChemElectroChem* **2020**, *7* (5), 1067–1079. https://doi.org/10.1002/celc.201901967.

(45) MacFarlane, D. R.; Cherepanov, P. V.; Choi, J.; Suryanto, B. H. R.; Hodgetts, R. Y.; Bakker, J. M.; Ferrero Vallana, F. M.; Simonov, A. N. A Roadmap to the Ammonia Economy. *Joule* **2020**, *4* (6), 1186–1205. https://doi.org/10.1016/j.joule.2020.04.004.

(46) Wang, W.; Herreros, J. M.; Tsolakis, A.; York, A. P. E. Ammonia as Hydrogen Carrier for Transportation; Investigation of the Ammonia Exhaust Gas Fuel Reforming. *International Journal of Hydrogen Energy*. **2013**, pp 9907–9917. https://doi.org/10.1016/j.ijhydene.2013.05.144.

(47) Klerke, A.; Christensen, C. H.; Nørskov, J. K.; Vegge, T. Ammonia for Hydrogen Storage: Challenges and Opportunities. *J. Mater. Chem.* **2008**, *18* (20), 2304–2310. https://doi.org/10.1039/b720020j.

(48) J.A., K. *Petroleum and Its Products*; Riegel's Handbook of Industrial Chemistry, **2003**.

(49) Zohuri, B. *Small Modular Reactors as Renewable Energy Sources*; Springer, **2018**.

(50) Kar, S.; Goeppert, A.; Prakash, G. K. S. Catalytic Homogeneous Hydrogenation of CO to Methanol via Formamide. *J. Am. Chem. Soc.* **2019**, *141* (32), 12518–12521. https://doi.org/10.1021/jacs.9b06586.

(51) Verhelst, S.; Turner, J. W.; Sileghem, L.; Vancoillie, J. Methanol as a Fuel for Internal Combustion Engines. *Prog. Energy Combust. Sci.* **2019**, *70*, 43–88. https://doi.org/10.1016/j.pecs.2018.10.001.

(52) Araya, S. S.; Liso, V.; Cui, X.; Li, N.; Zhu, J.; Sahlin, S. L.; Jensen, S. H.; Nielsen, M. P.; Kær, S. K. A Review of the Methanol Economy: The Fuel Cell Route. *Energies* **2020**, *13* (3). https://doi.org/10.3390/en13030596.

(53) B.J. Van Gerpen, B. Shanks, R. Pruszko, D. Clements, G. K. Biodiesel Production Technology. *Natl. Renew. Energy Lab.* **2004**. https://doi.org/10.1002/9783527809080.cataz01943.

(54) Johnston, R. J.; Blakemore, R. The Role of Oil and Gas Companies in the Energy Transition. *Atl. Counc.* **2020**.

(55) German oil refinery to build 30 MW hydrogen electrolysis plant.

(56) Crawford, G. A.; Benzimra, S. Advances in Water Electrolyzers and Their Potential Use in Ammonia Production and Other Applications. *Int. J. Hydrogen Energy* **1986**, *11*, 691–701.

(57) Vogl, V.; Åhman, M.; Nilsson, L. J. Assessment of Hydrogen Direct Reduction for Fossil-Free Steelmaking. *Journal of Cleaner Production*. 2018, pp 736–745. https://doi.org/10.1016/j.jclepro.2018.08.279.

(58) Bos, M. J.; Kersten, S. R. A.; Brilman, D. W. F. Wind Power to Methanol: Renewable Methanol Production Using Electricity, Electrolysis of Water and CO_2 Air Capture. *Applied Energy*. 2020. https://doi.org/10.1016/j.apenergy.2020.114672.

(59) Institute, K. E. T. Hydrogen Applications and Business Models. *Kearney Energy Transit. Inst.* **2020**.

(60) Council, H. Hydrogen Scaling Up. *J. Child Psychol. Psychiatry Allied Discip.* **2017**, *50* (10), 1218–1226. https://doi.org/10.1111/j.1469-7610.2009.02115.x.

(61) Staffell, I.; Scamman, D.; Velazquez Abad, A.; Balcombe, P.; Dodds, P. E.; Ekins, P.; Shah, N.; Ward, K. R. The Role of Hydrogen and Fuel Cells in the Global Energy System. *Energy Environ. Sci.* **2019**, *12* (2), 463–491. https://doi.org/10.1039/c8ee01157e.

(62) Hydrogen and Fuel Cell Technologies for Heating: A Review. *Int. J. Hydrogen Energy* **2015**, *40*, 2065–2083.

(63) Ausfelder, F.; Beilmann, C.; Bertau, M.; Bräuninger, S.; Heinzel, A.; Hoer, R.; Koch, W.;

Mahlendorf, F.; Metzelthin, A.; Peuckert, M.; Plass, L.; Räuchle, K.; Reuter, M.; Schaub, G.; Schiebahn, S.; Schwab, E.; Schüth, F.; Stolten, D.; Teßmer, G.; Wagemann, K.; Ziegahn, K.-F. Energy Storage as Part of a Secure Energy Supply. *ChemBioEng Rev.* **2017**, *4* (3), 144–210. https://doi.org/10.1002/cben.201700004.

(64) IRENA. *Renewable-Powered Future : Solutions To Integrate*; 2019.

(65) Agency, I. E. Building the Hydrogen Economy : Enabling Infrastructure Development Part II : Sharing the European Vision. **2007**.

(66) Andrews, J.; Shabani, B. Where Does Hydrogen Fit in a Sustainable Energy Economy? *Procedia Eng.* **2012**, *49*, 15–25. https://doi.org/10.1016/j.proeng.2012.10.107.

(67) Council, H. How Hydrogen Empowers the Energy Transition. **2017**, No. January, 28.

(68) Rooney, Joshua Burke, M. *Fuelling the Future*; 2018.

(69) Bruckner T., I.A. Bashmakov, Y. Mulugetta, H. Chum, A. de la Vega Navarro, J. Edmonds, A. Faaij, B. Fungtammasan, A. G.; E. Hertwich, D. Honnery, D. Infield, M. Kainuma, S. Khennas, S. Kim, H.B. Nimir, K. Riahi, N. Strachan, R. Wiser, and X. Z. Energy Systems. *Clim. Chang. 2014 Mitig. Clim. Chang. Contrib. Work. Gr. III to Fifth Assess. Rep. Intergov. Panel Clim. Chang.* **2014**, *Cambridge*. https://doi.org/10.2307/j.ctt1hfr0s3.40.

(70) Quarton, C. J.; Samsatli, S. Power-to-Gas for Injection into the Gas Grid: What Can We Learn from Real-Life Projects, Economic Assessments and Systems Modelling? *Renewable and Sustainable Energy Reviews*. 2018, pp 302–316. https://doi.org/10.1016/j.rser.2018.09.007.

(71) Melaina, M.; Antonia, O.; Penev, M. Blending Hydrogen into Natural Gas Pipeline Networks: A Review of Key Issues. *Natl. Renew. Energy Lab.* **2013**. https://doi.org/10.2172/1068610.

(72) Melaina, M. W.; Penev, M.; Zuboy, J. Hydrogen Blending in Natural Gas Pipelines. *Handb. Clean Energy Syst.* **2015**, 1–13. https://doi.org/10.1002/9781118991978.hces205.

(73) GPA Engineering. Hydrogen in the Gas Distribution Networks. **2019**. https://doi.org/GPA Document No: 19184-REP-001.

(74) Committee on Climate Change (CCC). Hydrogen in a Low-Carbon Economy. **2018**.

(75) Nazir, H.; Muthuswamy, N.; Louis, C.; Chavan, S.; Shi, X.; Kauranen, P.; Kallio, T.; Maia, G. Is the H_2 Economy Realizable in the Foreseeable Future? Part III: H_2 Usage Technologies, Applications, and Challenges and Opportunities. *Int. J. Hydrogen Energy* **2020**.

(76) Arasto, A.; Hannula, I.; Lehtonen, J.; Vainikka, P. Carbon Capture and Utilization:The Role of Carbon Capture and Utilisation in Transitioning to a Low-Carbon Future.

(77) Commission, E. Carbon Capture, Utilisation and Storage. *SETIS* **2016**. https://doi.org/10.1039/9781788010115-00198.

(78) World Energy Council. Innovation Insights Brief: New Hydrogen Economy - Hope or Hype? **2019**, 42.

(79) The Oxford Institute for Energy Studies. Power-to-Gas: Linking Electricity and Gas in a Decarbonising World? *Oxford Energy Insight* **2018**, *39* (December 2017).

(80) Eveloy, V.; Gebreegziabher, T. A Review of Projected Power-to-Gas Deployment Scenarios. *Energies* **2018**, *11* (7). https://doi.org/10.3390/en11071824.

(81) Sikarwar, V. S.; Zhao, M.; Clough, P.; Yao, J.; Zhong, X.; Memon, M. Z.; Shah, N.; Anthony, E. J.; Fennell, P. S. An Overview of Advances in Biomass Gasification. *Energy Environ. Sci.* **2016**, *9* (10), 2939–2977. https://doi.org/10.1039/c6ee00935b.

(82) Kodama, T.; Gokon, N. Thermochemical Cycles for High-Temperature Solar Hydrogen Production. *Chem. Rev.* **2007**, *107* (10), 4048–4077. https://doi.org/10.1021/cr050188a.

(83) Ros, C.; Andreu, T.; Morante, J. R. Photoelectrochemical Water Splitting: A Road from Stable Metal Oxides to Protected Thin Film Solar Cells. *J. Mater. Chem. A* **2020**, *8* (21), 10625–10669. https://doi.org/10.1039/d0ta02755c.

(84) Yan, Y.; Xia, B. Y.; Zhao, B.; Wang, X. A Review on Noble-Metal-Free Bifunctional Heterogeneous Catalysts for Overall Electrochemical Water Splitting. *J. Mater. Chem. A* **2016**, *4* (45), 17587–17603. https://doi.org/10.1039/C6TA08075H.

(85) M. Andrew Crews, B. G. S. *Hydrogen Production and Supply: Meeting Refiners' Growing Needs*; **2006**; Vol. 1.

(86) Franchi, G.; Capocelli, M.; De Falco, M.; Piemonte, V.; Barba, D. Hydrogen Production via Steam Reforming: A Critical Analysis of MR and RMM Technologies. *Membranes (Basel).* **2020**, *10* (1). https://doi.org/10.3390/membranes10010010.

(87) Renssen, S. van. The Hydrogen Solution? *Nat. Clim. Chang.* **2020**, *10* (September), 799–801.

(88) Chen, L.; Qi, Z.; Zhang, S.; Su, J.; Somorjai, G. A. Catalytic Hydrogen Production from Methane: A Review on Recent Progress and Prospect. *Catalysts* **2020**, *10* (8), 1–18. https://doi.org/10.3390/catal10080858.

(89) Hrabovsky, M.; Hlina, M.; Kopecky, V.; Maslani, A.; Krenek, P.; Serov, A.; Hurba, O. Steam Plasma Methane Reforming for Hydrogen Production. *Plasma Chem. Plasma Process.* **2018**, *38* (4), 743–758. https://doi.org/10.1007/s11090-018-9891-5.

(90) Fakeeha, A. H.; Arafat, Y.; Ibrahim, A. A.; Shaikh, H.; Atia, H.; Abasaeed, A. E.; Armbruster, U.; Al-Fatesh, A. S. Highly Selective Syngas/H_2 Production via Partial Oxidation of CH_4 Using (Ni, Co and Ni-Co)/ZrO_2 -Al_2O_3 Catalysts: Influence of Calcination Temperature. *Processes* **2019**, *7* (3), 1–15. https://doi.org/10.3390/pr7030141.

(91) Lutz, A. E.; Bradshaw, R. W.; Bromberg, L.; Rabinovich, A. Thermodynamic Analysis of Hydrogen Production by Partial Oxidation Reforming. *International Journal of Hydrogen Energy*. 2004, pp 809–816. https://doi.org/10.1016/j.ijhydene.2003.09.015.

(92) Higman, C.; Tam, S. Advances in Coal Gasification, Hydrogenation, and Gas Treating for the Production of Chemicals and Fuels. *Chem. Rev.* **2014**, *114* (3), 1673–1708. https://doi.org/10.1021/cr400202m.

(93) Goss, R. M. BP Statistical Review of World Energy. **2019**, *68*.

(94) Budinis, S.; Krevor, S.; Dowell, N. Mac; Brandon, N.; Hawkes, A. An Assessment of CCS Costs, Barriers and Potential. *Energy Strategy Reviews*. 2018, pp 61–81. https://doi.org/10.1016/j.esr.2018.08.003.

(95) Edward H Owens , Samuel Chapman, P. A. The Impact of Carbon Capture and Storage on Coal Resource Depletion. *Energy Environ.* **2010**, *21* (8), 925–936.

(96) Takata, T.; Jiang, J.; Sakata, Y.; Nakabayashi, M.; Shibata, N.; Nandal, V.; Seki, K.; Hisatomi, T.; Domen, K. Photocatalytic Water Splitting with a Quantum Efficiency of Almost Unity. *Nature* **2020**, *581* (7809), 411–414. https://doi.org/10.1038/s41586-020-2278-9.

(97) Wang, Z.; Li, C.; Domen, K. Recent Developments in Heterogeneous Photocatalysts for Solar-Driven Overall Water Splitting. *Chem. Soc. Rev.* **2019**, *48* (7), 2109–2125. https://doi.org/10.1039/c8cs00542g.

(98) Yamada, T.; Domen, K. Development of Sunlight Driven Water Splitting Devices towards Future Artificial Photosynthetic Industry. *ChemEngineering* **2018**, *2* (3), 1–18. https://doi.org/10.3390/chemengineering2030036.

(99) Tee, S. Y.; Win, K. Y.; Teo, W. S.; Koh, L. D.; Liu, S.; Teng, C. P.; Han, M. Y. Recent Progress in Energy-Driven Water Splitting. *Adv. Sci.* **2017**, *4* (5). https://doi.org/10.1002/advs.201600337.

(100) Hsieh, C.-W. C.; Felby, C. Biofuels for the Marine Shipping Sector. *IEA Bioenergy* **2017**.

(101) Lee, S. Y.; Sankaran, R.; Chew, K. W.; Tan, C. H.; Krishnamoorthy, R.; Chu, D.-T.; Show, P.-L. Waste to Bioenergy: A Review on the Recent Conversion Technologies. *BMC Energy* **2019**, *1* (1), 1–22. https://doi.org/10.1186/s42500-019-0004-7.

(102) Dou, B.; Zhang, H.; Song, Y.; Zhao, L.; Jiang, B.; He, M.; Ruan, C.; Chen, H.; Xu, Y. Hydrogen Production from the Thermochemical Conversion of Biomass: Issues and Challenges. *Sustain. Energy Fuels* **2019**, *3* (2), 314–342. https://doi.org/10.1039/c8se00535d.

(103) Balat, H.; Kirtay, E. Hydrogen from Biomass - Present Scenario and Future Prospects. *Int. J. Hydrogen Energy* **2010**, *35* (14), 7416–7426. https://doi.org/10.1016/j.ijhydene.2010.04.137.

(104) Carpenter, D.; Westover, T. L.; Czernik, S.; Jablonski, W. Biomass Feedstocks for Renewable Fuel Production: A Review of the Impacts of Feedstock and Pretreatment on the Yield and Product Distribution of Fast Pyrolysis Bio-Oils and Vapors. *Green Chem.* **2014**, *16* (2), 384–406. https://doi.org/10.1039/c3gc41631c.

(105) Rao, C. N. R.; Lingampalli, S. R.; Dey, S.; Roy, A. Solar Photochemical and

Thermochemical Splitting of Water. *Philos. Trans. R. Soc. A Math. Phys. Eng. Sci.* **2016**, *374* (2061). https://doi.org/10.1098/rsta.2015.0088.

(106) Muhich, C. L.; Ehrhart, B. D.; Witte, V. A.; Miller, S. L.; Coker, E. N.; Musgrave, C. B.; Weimer, A. W. Predicting the Solar Thermochemical Water Splitting Ability and Reaction Mechanism of Metal Oxides: A Case Study of the Hercynite Family of Water Splitting Cycles. *Energy Environ. Sci.* **2015**, *8* (12), 3687–3699. https://doi.org/10.1039/c5ee01979f.

(107) Safari, F.; Dincer, I. A Review and Comparative Evaluation of Thermochemical Water Splitting Cycles for Hydrogen Production. *Energy Conversion and Management*. 2020. https://doi.org/10.1016/j.enconman.2019.112182.

(108) Dehghani, S.; Sayyaadi, H.; Pourali, O. Equilibrium Conversion and Reaction Analysis in Sulfur-Iodine Thermochemical Hydrogen Production Cycle. *Can. J. Chem. Eng.* **2015**, *93* (4), 708–726. https://doi.org/10.1002/cjce.22164.

(109) Corgnale, C.; Ma, Z.; Shimpalee, S. Modeling of a Direct Solar Receiver Reactor for Decomposition of Sulfuric Acid in Thermochemical Hydrogen Production Cycles. *International Journal of Hydrogen Energy*. 2019, pp 27237–27247. https://doi.org/10.1016/j.ijhydene.2019.08.231.

(110) Rao, C. N. R.; Dey, S. Solar Thermochemical Splitting of Water to Generate Hydrogen. *Proc. Natl. Acad. Sci. U. S. A.* **2017**, *114* (51), 13385–13393. https://doi.org/10.1073/pnas.1700104114.

(111) Safari, F.; Dincer, I. A Study on the Fe–Cl Thermochemical Water Splitting Cycle for Hydrogen Production. *International Journal of Hydrogen Energy*. 2020, pp 18867–18875. https://doi.org/10.1016/j.ijhydene.2020.04.208.

(112) Naterer, G. F.; Gabriel, K.; Wang, Z. L.; Daggupati, V. N.; Gravelsins, R. Thermochemical Hydrogen Production with a Copper-Chlorine Cycle. I: Oxygen Release from Copper Oxychloride Decomposition. *International Journal of Hydrogen Energy*. 2008, pp 5439–5450. https://doi.org/10.1016/j.ijhydene.2008.05.035.

(113) Onuki, K.; Kubo, S.; Terada, A.; Sakaba, N.; Hino, R. Thermochemical Water-Splitting Cycle Using Iodine and Sulfur. *Energy Environ. Sci.* **2009**, *2* (5), 491–497. https://doi.org/10.1039/b821113m.

(114) Zhang, Y.; Peng, P.; Ying, Z.; Zhu, Q.; Zhou, J.; Wang, Z.; Liu, J.; Cen, K. Experimental Investigation on Multiphase Bunsen Reaction in the Thermochemical Sulfur-Iodine Cycle. *Ind. Eng. Chem. Res.* **2014**, *53* (8), 3021–3028. https://doi.org/10.1021/ie4038856.

(115) Morozov, A. Comparative Analysis of Hydrogen Production Methods with Nuclear Reactors. *IYNC* **2008**, No. 237, 20–26.

(116) Tomar, S.; Pareek, A.; Kondamudi, K.; Upadhyayula, S. Evaluation of Materials of Construction for the Sulfuric Acid Decomposition Section in the Sulfur–Iodine (S–I) Cycle for Hydrogen Production: Some Preliminary Studies on Selected Materials. *J. Chem. Sci.* **2019**, *131* (9), 1–8. https://doi.org/10.1007/s12039-019-1672-z.

(117) Choi, J. Y.; Kim, Y. S.; Sah, I.; No, H. C.; Jang, C. Corrosion Resistances of Alloys in High Temperature Hydrogen Iodide Gas Environment for Sulfur-Iodine Thermochemical Cycle. *International Journal of Hydrogen Energy*. 2014, pp 14557–14564. https://doi.org/10.1016/j.ijhydene.2014.07.082.

(118) B.Wong, R.T.Buckingham, L.C.Brown, B.E.Russ, G.E.Besenbruch, A.Kaiparambil, R.Santhanakrishnan, A. R. Construction Materials Development in Sulfur Iodine Thermochemical Water Splitting Process for Hydrogen Production. *Int. J. Hydrogen Energy* **2007**, *32* (4), 497–504.

(119) Lattin, W. C.; Utgikar, V. P. Global Warming Potential of the Sulfur-Iodine Process Using Life Cycle Assessment Methodology. *International Journal of Hydrogen Energy*. 2009, pp 737–744. https://doi.org/10.1016/j.ijhydene.2008.10.059.

(120) Romero, M.; Steinfeld, A. Concentrating Solar Thermal Power and Thermochemical Fuels. *Energy Environ. Sci.* **2012**, *5* (11), 9234–9245. https://doi.org/10.1039/c2ee21275g.

(121) Coelho, B.; Oliveira, A. C.; Mendes, A. Concentrated Solar Power for Renewable Electricity and Hydrogen Production from Water — a Review. *Energy Environ. Sci.* **2010**, *3*, 1398–1405. https://doi.org/10.1039/b922607a.

(122) Trasatti, S. Water Electrolysis: Who First? *J. Electroanal. Chem.* **1999**, *476* (1), 90–91. https://doi.org/10.1016/S0022-0728(99)00364-2.

(123) Howard, A. S. The Future of Nuclear Energy in the U.S. *Glob. Warm. Energy Policy* **2001**, 213–217. https://doi.org/10.1007/978-1-4615-1323-0_17.

(124) Sartbaeva, A.; Kuznetsov, V. L.; Wells, S. A.; Edwards, P. P. Hydrogen Nexus in a Sustainable Energy Future. *Energy Environ. Sci.* **2008**, *1* (1), 79–85. https://doi.org/10.1039/b810104n.

(125) S. Shiva Kumar, V. H. Hydrogen Production by PEM Water Electrolysis – A Review. *Mater. Sci. Energy Technol.* **2019**, *2* (3), 442–454.

(126) Antar, Y. N. and A. *Hydrogen Generation by Water Electrolysis, Advances In Hydrogen Generation Technologies, Murat Eyvaz, IntechOpen*; 2018.

(127) Richards, J. W. The Electrolysis of Water. *J. Franklin Inst.* **1999**, *160* (5), 92–93. https://doi.org/10.1016/s0016-0032(05)90261-5.

(128) Browne, M. P.; Sofer, Z.; Pumera, M. Layered and Two Dimensional Metal Oxides for Electrochemical Energy Conversion. *Energy Environ. Sci.* **2019**, *12* (1), 41–58. https://doi.org/10.1039/c8ee02495b.

(129) Faulkner, A. J. B. and L. R. Electrochemical Methods: Fundamentals and Applications. *Wiley, New York* **1980**.

(130) Rashid, M. M.; Mesfer, M. K. Al; Naseem, H.; Danish, M. Hydrogen Production by Water Electrolysis: A Review of Alkaline Water Electrolysis, PEM Water Electrolysis and High Temperature Water Electrolysis. *Int. J. Eng. Adv. Technol.* **2015**, No. 3, 2249–8958.

(131) Kim, J. S.; Kim, B.; Kim, H.; Kang, K. Recent Progress on Multimetal Oxide Catalysts for the Oxygen Evolution Reaction. *Adv. Energy Mater.* **2018**, *8* (11), 1–26. https://doi.org/10.1002/aenm.201702774.

(132) Walter, M. G.; Warren, E. L.; McKone, J. R.; Boettcher, S. W.; Mi, Q.; Santori, E. A.; Lewis, N. S. Solar Water Splitting Cells. *Chem. Rev.* **2010**, *110* (11), 6446–6473. https://doi.org/10.1021/cr1002326.

(133) Myland, K. O. J. Fundamentals of Electrochemical Science. *San Diego, USA Acad. Press. Inc* **1993**.

(134) Harrison, K. W.; Remick R.; Martin, G. D.; Hoskin, A. Hydrogen Production: Fundamentals and Case Study Summaries. *Hydrog. fuel cells* **2010**, No. January, 207–226.

(135) Khan, M. A.; Zhao, H.; Zou, W.; Chen, Z.; Cao, W.; Fang, J.; Xu, J.; Zhang, L.; Zhang, J. *Recent Progresses in Electrocatalysts for Water Electrolysis*; 2018; Vol. 1. https://doi.org/10.1007/s41918-018-0014-z.

(136) Scott, K. Chapter 1: Introduction to Electrolysis, Electrolysers and Hydrogen Production. *RSC Energy Environ. Ser.* **2020**, *2020-Janua* (25), 1–27. https://doi.org/10.1039/9781788016049-00001.

(137) Brauns, J.; Turek, T. Alkaline Water Electrolysis Powered by Renewable Energy: A Review. *Processes* **2020**, *8* (2). https://doi.org/10.3390/pr8020248.

(138) Xiang, C.; Papadantonakis, K. M.; Lewis, N. S. Principles and Implementations of Electrolysis Systems for Water Splitting. *Mater. Horizons* **2016**, *3* (3), 169–173. https://doi.org/10.1039/c6mh00016a.

(139) Schalenbach, M.; Tjarks, G.; Carmo, M.; Lueke, W.; Mueller, M.; Stolten, D. Acidic or Alkaline? Towards a New Perspective on the Efficiency of Water Electrolysis. *J. Electrochem. Soc.* **2016**, *163* (11), F3197–F3208. https://doi.org/10.1149/2.0271611jes.

(140) Aricò, A. S.; Siracusano, S.; Briguglio, N.; Baglio, V.; Di Blasi, A.; Antonucci, V. Polymer Electrolyte Membrane Water Electrolysis: Status of Technologies and Potential Applications in Combination with Renewable Power Sources. *J. Appl. Electrochem.* **2013**, *43* (2), 107–118. https://doi.org/10.1007/s10800-012-0490-5.

(141) Leng, Y.; Chen, G.; Mendoza, A. J.; Tighe, T. B.; Hickner, M. A.; Wang, C. Y. Solid-State Water Electrolysis with an Alkaline Membrane. *J. Am. Chem. Soc.* **2012**, *134* (22), 9054–9057. https://doi.org/10.1021/ja302439z.

(142) Holladay, J. D.; Hu, J.; King, D. L.; Wang, Y. An Overview of Hydrogen Production Technologies. *Catalysis Today*. 2009, pp 244–260. https://doi.org/10.1016/j.cattod.2008.08.039.

(143) Miller, H. A.; Bouzek, K.; Hnat, J.; Loos, S.; Bernäcker, C. I.; Weißgärber, T.; Röntzsch, L.; Meier-Haack, J. Green Hydrogen from Anion Exchange Membrane Water Electrolysis: A Review of Recent Developments in Critical Materials and Operating Conditions. *Sustain. Energy Fuels* **2020**, *4* (5), 2114–2133.

https://doi.org/10.1039/c9se01240k.

(144) Vincent, I.; Bessarabov, D. Low Cost Hydrogen Production by Anion Exchange Membrane Electrolysis: A Review. *Renewable and Sustainable Energy Reviews*. 2018, pp 1690–1704. https://doi.org/10.1016/j.rser.2017.05.258.

(145) Ursua, A.; Sanchis, P.; Gandia, L. M. Hydrogen Production from Water Electrolysis : Current Status and Future Trends. *Proc. IEEE* **2012**, *100* (2), 410–426.

(146) Antar, Y. N. and A. Hydrogen Generation by Water Electrolysis, Advances In Hydrogen Generation Technologies, Murat Eyvaz, IntechOpen. *2018*.

(147) Wulf, C.; Zapp, P.; Schreiber, A. Review of Power-to-X Demonstration Projects in Europe. *Front. Energy Res.* **2020**, *8* (September), 1–12. https://doi.org/10.3389/fenrg.2020.00191.

(148) Mayyas, A.; Ruth, M.; Pivovar, B.; Bender, G.; Wipke, K.; Mayyas, A.; Ruth, M.; Pivovar, B.; Bender, G.; Wipke, K. Manufacturing Cost Analysis for Proton Exchange Membrane Water Electrolyzers Manufacturing Cost Analysis for Proton Exchange Membrane Water Electrolyzers. *Natl. Renew. Energy Lab.* **2019**, No. August, 65.

(149) Bernt, M.; Hartig-Weiß, A.; Tovini, M. F.; El-Sayed, H. A.; Schramm, C.; Schröter, J.; Gebauer, C.; Gasteiger, H. A. Current Challenges in Catalyst Development for PEM Water Electrolyzers. *Chemie-Ingenieur-Technik* **2020**, *92* (1–2), 31–39. https://doi.org/10.1002/cite.201900101.

(150) Zeng, K.; Zhang, D. Recent Progress in Alkaline Water Electrolysis for Hydrogen Production and Applications. *Progress in Energy and Combustion Science*. **2010**, pp 307–326. https://doi.org/10.1016/j.pecs.2009.11.002.

(151) Wang, W.; Yang, Y.; Huan, D.; Wang, L.; Shi, N.; Xie, Y.; Xia, C.; Peng, R.; Lu, Y. An Excellent OER Electrocatalyst of Cubic $SrCoO_{3-\delta}$ Prepared by a Simple F-Doping Strategy. *J. Mater. Chem. A* **2019**, *7* (20), 12538–12546. https://doi.org/10.1039/c9ta03099a.

(152) Song, F.; Bai, L.; Moysiadou, A.; Lee, S.; Hu, C.; Liardet, L.; Hu, X. Transition Metal Oxides as Electrocatalysts for the Oxygen Evolution Reaction in Alkaline Solutions: An Application-Inspired Renaissance. *J. Am. Chem. Soc.* **2018**, *140* (25), 7748–7759. https://doi.org/10.1021/jacs.8b04546.

(153) B. E. Conway, M. S. Electrochemical Reaction Orders: Application to the Hydrogen and Oxygen Evolution Reactions. *Electrochim. Acta* **1964**, *9*, 1599.

(154) Over, H. Surface Chemistry of Ruthenium Dioxide in Heterogeneous Catalysis and Electrocatalysis : From Fundamental to Applied Research. *Chem. Rev.* **2012**, *112* (6), 3356–3426.

(155) Rossmeisl, J.; Qu, Z. W.; Zhu, H.; Kroes, G. J.; Nørskov, J. K. Electrolysis of Water on Oxide Surfaces. *Journal of Electroanalytical Chemistry*. **2007**, pp 83–89. https://doi.org/10.1016/j.jelechem.2006.11.008.

(156) Bockris, J. O. M. Kinetics of Activation Controlled Consecutive Electrochemical Reactions: Anodic Evolution of Oxygen. *J. Chem. Phys.* **1956**, *24* (4), 817–827. https://doi.org/10.1063/1.1742616.

(157) Reier, T.; Nong, H. N.; Teschner, D.; Schlögl, R.; Strasser, P. Electrocatalytic Oxygen Evolution Reaction in Acidic Environments – Reaction Mechanisms and Catalysts. *Adv. Energy Mater.* **2017**, *7* (1). https://doi.org/10.1002/aenm.201601275.

(158) Shinagawa, T.; Garcia-Esparza, A. T.; Takanabe, K. Insight on Tafel Slopes from a Microkinetic Analysis of Aqueous Electrocatalysis for Energy Conversion. *Sci. Rep.* **2015**, *5* (May), 1–21. https://doi.org/10.1038/srep13801.

(159) Anantharaj, S.; Ede, S. R.; Karthick, K.; Sam Sankar, S.; Sangeetha, K.; Karthik, P. E.; Kundu, S. Precision and Correctness in the Evaluation of Electrocatalytic Water Splitting: Revisiting Activity Parameters with a Critical Assessment. *Energy Environ. Sci.* **2018**, *11* (4), 744–771. https://doi.org/10.1039/c7ee03457a.

(160) Suen, N. T.; Hung, S. F.; Quan, Q.; Zhang, N.; Xu, Y. J.; Chen, H. M. Electrocatalysis for the Oxygen Evolution Reaction: Recent Development and Future Perspectives. *Chem. Soc. Rev.* **2017**, *46* (2), 337–365. https://doi.org/10.1039/c6cs00328a.

(161) Man, I. C.; Su, H. Y.; Calle-Vallejo, F.; Hansen, H. A.; Martínez, J. I.; Inoglu, N. G.; Kitchin, J.; Jaramillo, T. F.; Nørskov, J. K.; Rossmeisl, J. Universality in Oxygen Evolution Electrocatalysis on Oxide Surfaces. *ChemCatChem* **2011**, *3* (7), 1159–1165. https://doi.org/10.1002/cctc.201000397.

(162) Ma, Z.; Zhang, Y.; Liu, S.; Xu, W.; Wu, L.; Hsieh, Y. C.; Liu, P.; Zhu, Y.; Sasaki, K.; Renner, J. N.; Ayers, K. E.; Adzic, R. R.; Wang, J. X. Reaction Mechanism for Oxygen Evolution on RuO_2, IrO_2, and RuO_2@IrO_2 Core-Shell Nanocatalysts. *Journal of Electroanalytical Chemistry*. 2018, pp 296–305. https://doi.org/10.1016/j.jelechem.2017.10.062.

(163) Wodrich, M. D.; Busch, M.; Corminboeuf, C. Accessing and Predicting the Kinetic Profiles of Homogeneous Catalysts from Volcano Plots. *Chem. Sci.* **2016**, *7* (9), 5723–5735. https://doi.org/10.1039/c6sc01660j.

(164) Busch, M.; Wodrich, M. D.; Corminboeuf, C. Linear Scaling Relationships and Volcano Plots in Homogeneous Catalysis-Revisiting the Suzuki Reaction. *Chem. Sci.* **2015**, *6* (12), 6754–6761. https://doi.org/10.1039/c5sc02910d.

(165) She, Z. W.; Kibsgaard, J.; Dickens, C. F.; Chorkendorff, I.; Nørskov, J. K.; Jaramillo, T. F. Combining Theory and Experiment in Electrocatalysis: Insights into Materials Design. *Science (80-.).* **2017**, *355* (6321). https://doi.org/10.1126/science.aad4998.

(166) Qi, J.; Zhang, W.; Cao, R. Porous Materials as Highly Efficient Electrocatalysts for the Oxygen Evolution Reaction. *ChemCatChem* **2018**, *10* (6), 1206–1220. https://doi.org/10.1002/cctc.201701637.

(167) Lai, J.; Nsabimana, A.; Luque, R.; Xu, G. 3D Porous Carbonaceous Electrodes for Electrocatalytic Applications. *Joule*. **2018**, pp 76–93.

https://doi.org/10.1016/j.joule.2017.10.005.

(168) Lopata, J.; Kang, Z.; Young, J.; Bender, G.; Weidner, J. W.; Shimpalee, S. Effects of the Transport/Catalyst Layer Interface and Catalyst Loading on Mass and Charge Transport Phenomena in Polymer Electrolyte Membrane Water Electrolysis Devices. *J. Electrochem. Soc.* **2020**, *167* (6), 064507. https://doi.org/10.1149/1945-7111/ab7f87.

(169) Huang, Z. F.; Wang, J.; Peng, Y.; Jung, C. Y.; Fisher, A.; Wang, X. Design of Efficient Bifunctional Oxygen Reduction/Evolution Electrocatalyst: Recent Advances and Perspectives. *Adv. Energy Mater.* **2017**, *7* (23), 1–21. https://doi.org/10.1002/aenm.201700544.

(170) He, J.; Zou, Y.; Wang, S. Defect Engineering on Electrocatalysts for Gas-Evolving Reactions. *Dalt. Trans.* **2019**, *48* (1), 15–20. https://doi.org/10.1039/C8DT04026E.

(171) Huang, G.; Xiao, Z.; Chen, R.; Wang, S. Defect Engineering of Cobalt-Based Materials for Electrocatalytic Water Splitting. *ACS Sustain. Chem. Eng.* **2018**, *6* (12), 15954–15969. https://doi.org/10.1021/acssuschemeng.8b04397.

(172) Gu, X. K.; Camayang, J. C. A.; Samira, S.; Nikolla, E. Oxygen Evolution Electrocatalysis Using Mixed Metal Oxides under Acidic Conditions: Challenges and Opportunities. *Journal of Catalysis*. **2020**, pp 130–140. https://doi.org/10.1016/j.jcat.2020.05.008.

(173) Kropp, T.; Mavrikakis, M. Effect of Strain on the Reactivity of Graphene Films. *J. Catal.* **2020**, *390*, 67–71. https://doi.org/10.1016/j.jcat.2020.07.030.

(174) Chen, P.; Xu, K.; Fang, Z.; Tong, Y.; Wu, J.; Lu, X.; Peng, X.; Ding, H.; Wu, C.; Xie, Y. Metallic Co_4N Porous Nanowire Arrays Activated by Surface Oxidation as Electrocatalysts for the Oxygen Evolution Reaction. *Angew. Chemie - Int. Ed.* **2015**, *54* (49), 14710–14714. https://doi.org/10.1002/anie.201506480.

(175) Wan, S.; Qi, J.; Zhang, W.; Wang, W.; Zhang, S.; Liu, K.; Zheng, H.; Sun, J.; Wang, S.; Cao, R. Hierarchical Co(OH)F Superstructure Built by Low-Dimensional Substructures for Electrocatalytic Water Oxidation. *Adv. Mater.* **2017**, *29* (28), 1–10. https://doi.org/10.1002/adma.201700286.

(176) Huang, Z. F.; Song, J.; Dou, S.; Li, X.; Wang, J.; Wang, X. Strategies to Break the Scaling Relation toward Enhanced Oxygen Electrocatalysis. *Matter* **2019**, *1* (6), 1494–1518. https://doi.org/10.1016/j.matt.2019.09.011.

(177) McCrory, C. C. L.; Jung, S.; Ferrer, I. M.; Chatman, S. M.; Peters, J. C.; Jaramillo, T. F. Benchmarking Hydrogen Evolving Reaction and Oxygen Evolving Reaction Electrocatalysts for Solar Water Splitting Devices. *J. Am. Chem. Soc.* **2015**, *137* (13), 4347–4357. https://doi.org/10.1021/ja510442p.

(178) Seitz, L. C.; Dickens, C. F.; Nishio, K.; Hikita, Y.; Montoya, J.; Doyle, A.; Kirk, C.; Vojvodic, A.; Hwang, H. Y.; Norskov, J. K.; Jaramillo, T. F. A Highly Active and Stable $IrO_x/SrIrO_3$ Catalyst for the Oxygen Evolution Reaction. *Science (80-.).* **2016**, *353* (6303).

(179) Weber, D.; Schoop, L. M.; Wurmbrand, D.; Laha, S.; Podjaski, F.; Duppel, V.; Müller, K.; Starke, U.; Lotsch, B. V. IrOOH Nanosheets as Acid Stable Electrocatalysts for the Oxygen Evolution Reaction. *J. Mater. Chem. A* **2018**, *6* (43), 21558–21566. https://doi.org/10.1039/C8TA07950A.

(180) Kumari, S.; Ajayi, B. P.; Kumar, B.; Jasinski, J. B.; Sunkara, M. K.; Spurgeon, J. M. A Low-Noble-Metal $W_{1-X}Ir_xO_{3-\delta}$ Water Oxidation Electrocatalyst for Acidic Media via Rapid Plasma Synthesis. *Energy Environ. Sci.* **2017**, *10* (11), 2432–2440. https://doi.org/10.1039/c7ee02626a.

(181) Salvatore, D. A.; Peña, B.; Dettelbach, K. E.; Berlinguette, C. P. Photodeposited Ruthenium Dioxide Films for Oxygen Evolution Reaction Electrocatalysis. *J. Mater. Chem. A* **2017**, *5* (4), 1575–1580. https://doi.org/10.1039/c6ta09094j.

(182) Laha, S.; Lee, Y.; Podjaski, F.; Weber, D.; Duppel, V.; Schoop, L. M.; Pielnhofer, F.; Scheurer, C.; Müller, K.; Starke, U.; Reuter, K.; Lotsch, B. V. Ruthenium Oxide Nanosheets for Enhanced Oxygen Evolution Catalysis in Acidic Medium. *Adv. Energy Mater.* **2019**, *9* (15), 1–8. https://doi.org/10.1002/aenm.201803795.

(183) Chatti, M.; Gardiner, J. L.; Fournier, M.; Johannessen, B.; Williams, T.; Gengenbach, T. R.; Pai, N.; Nguyen, C.; Macfarlane, D. R.; Hocking, R. K.; Simonov, A. N. Intrinsically Stable in Situ Generated Electrocatalyst for Long-Term Oxidation of Acidic Water at up to 80 °C. *Nat. Catal.* **2019**, *2* (May), 457–465.

(184) Moreno-Hernandez, I. A.; Macfarland, C. A.; Read, C. G.; Papadantonakis, K. M.; Brunschwig, B. S.; Lewis, N. S. Crystalline Nickel Manganese Antimonate as a Stable Water-Oxidation Catalyst in Aqueous 1.0 M H_2SO_4. *Energy Environ. Sci.* **2017**, *10* (10), 2103–2108. https://doi.org/10.1039/c7ee01486d.

(185) Hu, F.; Zhu, S.; Chen, S.; Li, Y.; Ma, L.; Wu, T.; Zhang, Y.; Wang, C.; Liu, C.; Yang, X.; Song, L.; Yang, X.; Xiong, Y. Amorphous Metallic NiFeP: A Conductive Bulk Material Achieving High Activity for Oxygen Evolution Reaction in Both Alkaline and Acidic Media. *Adv. Mater.* **2017**, *29* (32), 1–9. https://doi.org/10.1002/adma.201606570.

(186) Zhou, L.; Shinde, A.; Montoya, J. H.; Singh, A.; Gul, S.; Yano, J.; Ye, Y.; Crumlin, E. J.; Richter, M. H.; Cooper, J. K.; Stein, H. S.; Haber, J. A.; Persson, K. A.; Gregoire, J. M. Rutile Alloys in the Mn-Sb-O System Stabilize Mn^{3+} to Enable Oxygen Evolution in Strong Acid. *ACS Catal.* **2018**, *8* (12), 10938–10948. https://doi.org/10.1021/acscatal.8b02689.

(187) Mondschein, J. S.; Callejas, J. F.; Read, C. G.; Chen, J. Y. C.; Holder, C. F.; Badding, C. K.; Schaak, R. E. Crystalline Cobalt Oxide Films for Sustained Electrocatalytic Oxygen Evolution under Strongly Acidic Conditions. *Chem. Mater.* **2017**, *29* (3), 950–957. https://doi.org/10.1021/acs.chemmater.6b02879.

(188) Lee, Y.; Suntivich, J.; May, K. J.; Perry, E. E.; Shao-Horn, Y. Synthesis and Activities of Rutile IrO_2 and RuO_2 Nanoparticles for Oxygen Evolution in Acid and Alkaline Solutions. *J. Phys. Chem. Lett.* **2012**, *3* (3), 399–404. https://doi.org/10.1021/jz2016507.

(189) Cherevko, S.; Zeradjanin, A. R.; Topalov, A. A.; Kulyk, N.; Katsounaros, I.; Mayrhofer, K. J. J. Dissolution of Noble Metals during Oxygen Evolution in Acidic Media. *ChemCatChem* **2014**, *6* (8), 2219–2223. https://doi.org/10.1002/cctc.201402194.

(190) Song, H. J.; Yoon, H.; Ju, B.; Kim, D. Highly Efficient Perovskite-Based Electrocatalysts for Water Oxidation in Acidic Environments : A Mini Review. *Adv. Energy Mater.* **2020**, *2002428*, 1–13. https://doi.org/10.1002/aenm.202002428.

(191) Yang, L.; Yu, G.; Ai, X.; Yan, W.; Duan, H.; Chen, W.; Li, X.; Wang, T.; Zhang, C.; Huang, X.; Chen, J. S.; Zou, X. Efficient Oxygen Evolution Electrocatalysis in Acid by a Perovskite with Face-Sharing IrO_6 Octahedral Dimers. *Nat. Commun.* **2018**, *9* (1), 1–9. https://doi.org/10.1038/s41467-018-07678-w.

(192) Miles, M. H.; Thomason, M. A. Periodic Variations of Overvoltages for Water Electrolysis in Acid Solutions from Cyclic Voltammetric Studies. *J. Electrochem. Soc.* **1976**, *123* (10), 1459–1461. https://doi.org/10.1149/1.2132619.

(193) Hodnik, N.; Jovanovič, P.; Pavlišič, A.; Jozinović, B.; Zorko, M.; Bele, M.; Šelih, V. S.; Šala, M.; Hočevar, S.; Gaberšček, M. New Insights into Corrosion of Ruthenium and Ruthenium Oxide Nanoparticles in Acidic Media. *J. Phys. Chem. C* **2015**, *119* (18), 10140–10147. https://doi.org/10.1021/acs.jpcc.5b01832.

(194) Martelli, G. N.; Ornelas, R.; Faita, G. Deactivation Mechanisms of Oxygen Evolving Anodes at High Current Densities. *Electrochim. Acta* **1994**, *39* (11–12), 1551–1558. https://doi.org/10.1016/0013-4686(94)85134-4.

(195) Pourbaix, M. J. N.; Van Muylder, J.; de Zoubov, N.; PROTECTION, C. Electrochemical Properties of the Platinum Metals. *Platin. Met. Rev.* **1959**, *3* (2), 47–53.

(196) Pfeifer, V.; Jones, T. E.; Wrabetz, S.; Massué, C.; Velasco Vélez, J. J.; Arrigo, R.; Scherzer, M.; Piccinin, S.; Hävecker, M.; Knop-Gericke, A.; Schlögl, R. Reactive Oxygen Species in Iridium-Based OER Catalysts. *Chem. Sci.* **2016**, *7* (11), 6791–6795. https://doi.org/10.1039/c6sc01860b.

(197) Cherevko, S.; Geiger, S.; Kasian, O.; Kulyk, N.; Grote, J. P.; Savan, A.; Shrestha, B. R.; Merzlikin, S.; Breitbach, B.; Ludwig, A.; Mayrhofer, K. J. J. Oxygen and Hydrogen Evolution Reactions on Ru, RuO_2, Ir, and IrO_2 Thin Film Electrodes in Acidic and Alkaline Electrolytes: A Comparative Study on Activity and Stability. *Catalysis Today*. 2016, pp 170–180. https://doi.org/10.1016/j.cattod.2015.08.014.

(198) Ishaque, M.; Shah, A.; Iftikhar, F. J.; Akbar, M. Development of Transition Metal Based Electrolyzer for Efficient Oxygen Evolution Reaction. *J. Renew. Sustain. Energy* **2020**, *12* (2). https://doi.org/10.1063/1.5123234.

(199) Huynh, M.; Ozel, T.; Liu, C.; Lau, E. C.; Nocera, D. G. Design of Template-Stabilized Active and Earth-Abundant Oxygen Evolution Catalysts in Acid. *Chem. Sci.* **2017**, *8* (7), 4779–4794. https://doi.org/10.1039/c7sc01239j.

(200) Singh, K.; Campos, J. G.; Dinic, F.; Hao, Z.; Yuan, T.; Voznyy, O. Manganese MOF Enables Efficient Oxygen Evolution in Acid. *ACS Mater. Lett.* **2020**, *2*, 798–800.

https://doi.org/10.1021/acsmaterialslett.0c00123.Details.

(201) Hayashi, T.; Bonnet-Mercier, N.; Yamaguchi, A.; Suetsugu, K.; Nakamura, R. Electrochemical Characterization of Manganese Oxides as a Water Oxidation Catalyst in Proton Exchange Membrane Electrolysers. *R. Soc. Open Sci.* **2019**, *6* (5). https://doi.org/10.1098/rsos.190122.

(202) Huynh, M.; Bediako, D. K.; Nocera, D. G. A Functionally Stable Manganese Oxide Oxygen Evolution Catalyst in Acid. *J. Am. Chem. Soc.* **2014**, *136*, 6002−6010. https://doi.org/10.1021/ja413147e.

(203) Bloor, L. G.; Molina, P. I.; Symes, M. D.; Cronin, L. Low PH Electrolytic Water Splitting Using Earth-Abundant Metastable Catalysts That Self-Assemble in Situ. *J. Am. Chem. Soc.* **2014**, *136* (8), 3304–3311. https://doi.org/10.1021/ja5003197.

(204) Frydendal, R.; Paoli, E. A.; Chorkendorff, I.; Rossmeisl, J.; Stephens, I. E. L. Toward an Active and Stable Catalyst for Oxygen Evolution in Acidic Media: Ti-Stabilized MnO_2. *Adv. Energy Mater.* **2015**, *5* (22). https://doi.org/10.1002/aenm.201500991.

(205) Minguzzi, A.; Fan, F. R. F.; Vertova, A.; Rondinini, S.; Bard, A. J. Dynamic Potential-PH Diagrams Application to Electrocatalysts for Water Oxidation. *Chem. Sci.* **2012**, *3* (1), 217–229. https://doi.org/10.1039/c1sc00516b.

(206) Gerken, J. B.; McAlpin, J. G.; Chen, J. Y. C.; Rigsby, M. L.; Casey, W. H.; Britt, R. D.; Stahl, S. S. Electrochemical Water Oxidation with Cobalt-Based Electrocatalysts from PH 0-14: The Thermodynamic Basis for Catalyst Structure, Stability, and Activity. *J. Am. Chem. Soc.* **2011**, *133* (36), 14431–14442. https://doi.org/10.1021/ja205647m.

(207) Kwong, W. L.; Lee, C. C.; Shchukarev, A.; Björn, E.; Messinger, J. High-Performance Iron (III) Oxide Electrocatalyst for Water Oxidation in Strongly Acidic Media. *J. Catal.* **2018**, *365*, 29–35. https://doi.org/10.1016/j.jcat.2018.06.018.

(208) Vij, V.; Sultan, S.; Harzandi, A. M.; Meena, A.; Tiwari, J. N.; Lee, W. G.; Yoon, T.; Kim, K. S. Nickel-Based Electrocatalysts for Energy-Related Applications: Oxygen Reduction, Oxygen Evolution, and Hydrogen Evolution Reactions. *ACS Catal.* **2017**, *7* (10), 7196–7225. https://doi.org/10.1021/acscatal.7b01800.

(209) Li, N.; Keane, T. P.; Veroneau, S. S.; Hadt, R. G.; Hayes, D.; Chen, L. X.; Nocera, D. G. Template-Stabilized Oxidic Nickel Oxygen Evolution Catalysts. *Proc. Natl. Acad. Sci. U. S. A.* **2020**, *117* (28), 16187–16192. https://doi.org/10.1073/pnas.2001529117.

(210) Jovanovič, P.; Hodnik, N.; Ruiz-Zepeda, F.; Arčon, I.; Jozinović, B.; Zorko, M.; Bele, M.; Šala, M.; Šelih, V. S.; Hočevar, S.; Gaberščček, M. Electrochemical Dissolution of Iridium and Iridium Oxide Particles in Acidic Media: Transmission Electron Microscopy, Electrochemical Flow Cell Coupled to Inductively Coupled Plasma Mass Spectrometry, and X-Ray Absorption Spectroscopy Study. *J. Am. Chem. Soc.* **2017**, *139* (36), 12837–12846. https://doi.org/10.1021/jacs.7b08071.

(211) Fu, W. T.; Diaz-morales, O.; Li, Z.; Oellers, T.; Fruchter, L. The Stability Number as a Metric for Electrocatalyst Stability Benchmarking. *Nat. Catal.* **2018**, *1* (July), 1–8.

(212) Kasian, O.; Geiger, S.; Li, T.; Grote, J. P.; Schweinar, K.; Zhang, S.; Scheu, C.; Raabe, D.; Cherevko, S.; Gault, B.; Mayrhofer, K. J. J. Degradation of Iridium Oxides via Oxygen Evolution from the Lattice: Correlating Atomic Scale Structure with Reaction Mechanisms. *Energy Environ. Sci.* **2019**, *12* (12), 3548–3555. https://doi.org/10.1039/c9ee01872g.

(213) Schweinar, K.; Gault, B.; Mouton, I.; Kasian, O. Lattice Oxygen Exchange in Rutile IrO_2 during the Oxygen Evolution Reaction. *J. Phys. Chem. Lett.* **2020**, *11* (13), 5008–5014. https://doi.org/10.1021/acs.jpclett.0c01258.

(214) Carmo, M.; Fritz, D. L.; Mergel, J.; Stolten, D. A Comprehensive Review on PEM Water Electrolysis. *International Journal of Hydrogen Energy*. 2013, pp 4901–4934. https://doi.org/10.1016/j.ijhydene.2013.01.151.

(215) Oh, H. S.; Nong, H. N.; Strasser, P. Preparation of Mesoporous Sb-, F-, and in-Doped SnO_2 Bulk Powder with High Surface Area for Use as Catalyst Supports in Electrolytic Cells. *Adv. Funct. Mater.* **2015**, *25* (7), 1074–1081. https://doi.org/10.1002/adfm.201401919.

(216) Comninellis, C.; Vercesi, G. P. Characterization of DSA®-Type Oxygen Evolving Electrodes: Choice of a Coating. *J. Appl. Electrochem.* **1991**, *21* (4), 335–345. https://doi.org/10.1007/BF01020219.

(217) Ailton J.Terezo, Juan Bisquert, Ernesto C.Pereira, G.-B. Separation of Transport, Charge Storage and Reaction Processes of Porous Electrocatalytic IrO_2 and IrO_2/Nb_2O_5 Electrodes. *J. Electroanal. Chem.* **2001**, *508* (1–2), 59–69.

(218) Guohua Chen, Xueming Chen, and P. L. Y. Electrochemical Behavior of Novel Ti/IrO_x-Sb_2O_5-SnO_2 Anodes. *J. Phys. Chem. B* **2002**, *106* (17), 4364–4369. https://doi.org/10.7868/s0044453715030218.

(219) Zhang, J. J.; Hu, J. M.; Zhang, J. Q.; Cao, C. N. IrO_2-SiO_2 Binary Oxide Films: Geometric or Kinetic Interpretation of the Improved Electrocatalytic Activity for the Oxygen Evolution Reaction. *International Journal of Hydrogen Energy*. 2011, pp 5218–5226. https://doi.org/10.1016/j.ijhydene.2011.01.131.

(220) Escudero-Escribano, M.; Pedersen, A. F.; Paoli, E. A.; Frydendal, R.; Friebel, D.; Malacrida, P.; Rossmeisl, J.; Stephens, I. E. L.; Chorkendorff, I. Importance of Surface IrO_x in Stabilizing RuO_2 for Oxygen Evolution. *J. Phys. Chem. B* **2018**, *122* (2), 947–955. https://doi.org/10.1021/acs.jpcb.7b07047.

(221) Thomas Audichon, Eric Mayousse, Sophie Morisset, Claudia Morais, Clement Comminges, Teko W. Napporn, K. B. Electroactivity of RuO_2-IrO_2 Mixed Nanocatalysts towards the OER in a Water Eletrolyzer. *Int. J. Hydrogen Energy* **2014**, *39* (30), 16785–16796.

(222) Owe, L. E.; Tsypkin, M.; Wallwork, K. S.; Haverkamp, R. G.; Sunde, S. Iridium-Ruthenium Single Phase Mixed Oxides for Oxygen Evolution: Composition Dependence of Electrocatalytic Activity. *Electrochimica Acta*. 2012, pp 158–164.

https://doi.org/10.1016/j.electacta.2012.03.041.

(223) Ledendecker, M.; Geiger, S.; Hengge, K.; Lim, J.; Cherevko, S.; Mingers, A. M.; Göhl, D.; Fortunato, G. V.; Jalalpoor, D.; Schüth, F.; Scheu, C.; Mayrhofer, K. J. J. Towards Maximized Utilization of Iridium for the Acidic Oxygen Evolution Reaction. *Nano Res.* **2019**, *12* (9), 2275–2280. https://doi.org/10.1007/s12274-019-2383-y.

(224) Nong, H. N.; Oh, H. S.; Reier, T.; Willinger, E.; Willinger, M. G.; Petkov, V.; Teschner, D.; Strasser, P. Oxide-Supported $IrNiO_x$ Core-Shell Particles as Efficient, Cost-Effective, and Stable Catalysts for Electrochemical Water Splitting. *Angew. Chemie - Int. Ed.* **2015**, *54* (10), 2975–2979. https://doi.org/10.1002/anie.201411072.

(225) Oh, H. S.; Nong, H. N.; Reier, T.; Gliech, M.; Strasser, P. Oxide-Supported Ir Nanodendrites with High Activity and Durability for the Oxygen Evolution Reaction in Acid PEM Water Electrolyzers. *Chem. Sci.* **2015**, *6* (6), 3321–3328. https://doi.org/10.1039/c5sc00518c.

(226) Zhao, C.; Yu, H.; Li, Y.; Li, X.; Ding, L.; Fan, L. Electrochemical Controlled Synthesis and Characterization of Well-Aligned IrO_2 Nanotube Arrays with Enhanced Electrocatalytic Activity toward Oxygen Evolution Reaction. *Journal of Electroanalytical Chemistry*. 2013, pp 269–274. https://doi.org/10.1016/j.jelechem.2012.08.032.

(227) Najafpour, M. M.; Kompany-Zareh, M.; Zahraei, A.; Jafarian Sedigh, D.; Jaccard, H.; Khoshkam, M.; Britt, R. D.; Casey, W. H. Mechanism, Decomposition Pathway and New Evidence for Self-Healing of Manganese Oxides as Efficient Water Oxidizing Catalysts: New Insights. *J. Chem. Soc. Dalt. Trans.* **2013**, *42* (40), 14603–14611. https://doi.org/10.1039/c3dt51406d.

(228) Mohammadi, M. R.; Loos, S.; Chernev, P.; Pasquini, C.; Zaharieva, I.; González-Flores, D.; Kubella, P.; Klingan, K.; Smith, R. D. L.; Dau, H. Exploring the Limits of Self-Repair in Cobalt Oxide Films for Electrocatalytic Water Oxidation. *ACS Catal.* **2020**, *10* (14), 7990–7999. https://doi.org/10.1021/acscatal.0c01944.

(229) Zhao, L.; Cao, Q.; Wang, A.; Duan, J.; Zhou, W.; Sang, Y.; Liu, H. Iron Oxide Embedded Titania Nanowires – An Active and Stable Electrocatalyst for Oxygen Evolution in Acidic Media. *Nano Energy*. 2018, pp 118–126. https://doi.org/10.1016/j.nanoen.2017.12.029.

(230) Evans, T. A.; Choi, K. S. Electrochemical Synthesis and Investigation of Stoichiometric, Phase - Pure $CoSb_2O_6$ and $MnSb_2O_6$ Electrodes for the Oxygen Evolution Reaction in Acidic Media. *ACS Appl. Energy Mater.* **2020**, *3* (6), 5563–5571. https://doi.org/10.1021/acsaem.0c00526.

(231) Costentin, C.; Nocera, D. G. Self-Healing Catalysis in Water. *Proc. Natl. Acad. Sci. U. S. A.* **2017**, *114* (51), 13380–13384. https://doi.org/10.1073/pnas.1711836114.

(232) Brookins, D. G. Geochemical Behavior of Antimony, Arsenic, Cadmium and Thallium: EhpH Diagrams for 25°C, 1-Bar Pressure. *Chem. Geol.* **1986**, *54* (3–4), 271–278. https://doi.org/10.1016/0009-2541(86)90141-5.

(233) Allen, J. P.; Carey, J. J.; Walsh, A.; Scanlon, D. O.; Watson, G. W. Electronic Structures

of Antimony Oxides. *J. Phys. Chem. C* **2013**, *117* (28), 14759–14769. https://doi.org/10.1021/jp4026249.

(234) Ouni, B.; Haj Lakhdar, M.; Boughalmi, R.; Larbi, T.; Boukhachem, A.; Madani, A.; Boubaker, K.; Amlouk, M. Investigation of Electrical and Dielectric Properties of Antimony Oxide (Sb_2O_4) Semiconductor Thin Films for TCO and Optoelectronic Applications. *J. Non. Cryst. Solids* **2013**, *367* (1), 1–7. https://doi.org/10.1016/j.jnoncrysol.2013.02.006.

(235) He, J.; Wei, Y.; Zhai, T.; Li, H. Antimony-Based Materials as Promising Anodes for Rechargeable Lithium-Ion and Sodium-Ion Batteries. *Mater. Chem. Front.* **2018**, *2* (3), 437–455. https://doi.org/10.1039/c7qm00480j.

(236) Vesborg, P. C. K.; Jaramillo, T. F. Addressing the Terawatt Challenge: Scalability in the Supply of Chemical Elements for Renewable Energy. *RSC Adv.* **2012**, *2* (21), 7933–7947. https://doi.org/10.1039/c2ra20839c.

(237) Chen, B.; Wang, S.; Liu, J.; Huang, H.; Dong, C.; He, Y.; Yan, W.; Guo, Z.; Xu, R.; Yang, H. Corrosion Resistance Mechanism of a Novel Porous Ti/Sn-Sb-RuO_x/β-PbO_2 Anode for Zinc Electrowinning. *Corros. Sci.* **2018**, *144* (August), 136–144. https://doi.org/10.1016/j.corsci.2018.08.049.

(238) Liu, J.; Wang, T.; Chen, B. Effect of Molar Ratio of Ruthenium and Antimony on Corrosion Mechanism of Ti/Sn-Sb-RuO_x Electrode for Zinc Electrowinning . *J. Electrochem. Soc.* **2019**, *166* (15), D798–D803. https://doi.org/10.1149/2.0511915jes.

(239) Zhou, L.; Shinde, A.; Montoya, J. H.; Singh, A.; Gul, S.; Yano, J.; Ye, Y.; Crumlin, E. J.; Richter, M. H.; Cooper, J. K.; Stein, H. S.; Haber, J. A.; Persson, K. A.; Gregoire, J. M. Rutile Alloys in the Mn-Sb-O System Stabilize Mn3+ to Enable Oxygen Evolution in Strong Acid. *ACS Catal.* **2018**, *8* (12), 10938–10948. https://doi.org/10.1021/acscatal.8b02689.

(240) Shinde, A.; Jones, R. J. R.; Guevarra, D.; Mitrovic, S.; Becerra-Stasiewicz, N.; Haber, J. A.; Jin, J.; Gregoire, J. M. High-Throughput Screening for Acid-Stable Oxygen Evolution Electrocatalysts in the (Mn–Co–Ta–Sb)O_x Composition Space. *Electrocatalysis* **2015**, *6* (2), 229–236. https://doi.org/10.1007/s12678-014-0237-7.

(241) Moreno-Hernandez, I. A.; Brunschwig, B. S.; Lewis, N. S. Crystalline Nickel, Cobalt, and Manganese Antimonates as Electrocatalysts for the Chlorine Evolution Reaction. *Energy Environ. Sci.* **2019**, *12* (4), 1241–1248. https://doi.org/10.1039/c8ee03676d.

(242) Evans, T. A.; Choi, K. S. Electrochemical Synthesis and Investigation of Stoichiometric, Phase - Pure $CoSb_2O_6$ and $MnSb_2O_6$ Electrodes for the Oxygen Evolution Reaction in Acidic Media. *ACS Appl. Energy Mater.* **2020**. https://doi.org/10.1021/acsaem.0c00526.

Chapter 2

Experimental Methods

This chapter describes procedures for the synthesis of electrocatalysts studied, materials and chemicals, preparation of electrodes, various physical and chemical characterization techniques, and computational methods used in the present PhD research project.

2.1 MATERIALS AND CHEMICALS

Glass covered with a layer of fluorine-doped tin(IV) oxide (FTO) with a sheet resistivity of 7 $\Omega\,sq^{-1}$ was purchased from *GreatCell Solar*. Manganese(II) chloride (beads, 98%), antimony(III) chloride (ACS, ≥99.0%), cobalt(II) chloride (purum, anhydrous, ≥98.0%), chromium (II) chloride (95%), lead (II) chloride (98%), ruthenium(III) chloride hydrate (ReagentPlus), iron(III) nitrate nonahydrate (≥99.95%), nickel(II) nitrate hexahydrate (99.999%), N,N-dimethylformamide (DMF; anhydrous, 99.8%) and dimethylsulfoxide (DMSO; ACS, ≥99.9%) were purchased from *Sigma-Aldrich*. Sulfuric acid (ACS reagent, 95.0-98.0%, Fe: ≤0.2 ppm, heavy metals (as Pb): ≤1 ppm) was sourced from *Merck*. Platinum plate was purchased from *Sinsil International*. Water used for all experimental procedures had a measured resistivity of 18.2 MΩ cm at ambient temperature (24 ± 2 °C) as achieved through the purification using either *Elix Millipore* or *Sartorious Arium Comfort I Ultrapure Water* systems.

2.2 WORKING ELECTRODE PREPARATION

FTO substrates were cut into pieces (approximately 1 cm × 3 cm) and cleaned by ultrasonication with 2% Helmanex surfactant solution, water, acetone and isopropanol for 15 min in every solvent and dried in an oven at 80 °C in air. The electroactive geometric area of FTO substrates (0.5 cm × 0.5 cm) was defined using *Kapton* polyimide tape. Catalyst precursor solutions were prepared by dissolving 0.1 mmol of the required salt(s) in either 2 ml of pure DMF (for nickel- and iron-containing materials) or 2 ml of DMF + DMSO (1:1 vol.) mixture (for all other materials investigated herein) at 50 °C. Without allowing the precursor solution to cool down, 5 µl thereof were slowly drop-cast onto FTO substrate pre-heated at 50 °C while increasing the substrate temperature to 100 °C over *ca* 2-3 min. The most reliable and stable performance of the $[Ru+Sb]O_y$ samples was achieved when the catalyst was prepared from the solution with a greenish tinge as against solution with a yellow hue; to obtain the solution with a greenish tinge, the as taken precursor solution was sonicated gently for 10 minutes under ambient conditions. For individual oxides, the loading of either metal or antimony on the electrode surface was approximately 1 µmol cm^{-2}; for mixed systems, the loadings were either 0.5 µmol cm^{-2} metal + 1 µmol cm^{-2} Sb ($[M_1+Sb_2]O_y$), or 1 µmol cm^{-2} metal + 1 µmol cm^{-2} Sb ($[M+Sb]O_y$), or 1 µmol cm^{-2} metal + 0.5 µmol cm^{-2} Sb ($[M_2+Sb_1]O_y$). Further, the *Kapton* tape was removed and the modified electrodes were placed in a muffle furnace filled with air, the temperature was ramped at the rate of 4° min^{-1} up to either 500 or 600 °C, kept at this temperature for 6 h, and then allowed to cool down to ambient temperature naturally inside the furnace. Afterwards, the *Kapton* tape mask was applied again.

2.3 ELECTROCHEMICAL EXPERIMENTS

Measurements were carried out in a two compartment Pyrex glass cell with a P4 ceramic frit using either a *Biologic VMP* or an *Metrohm Autolab PGSTAT204* electrochemical workstation operated in a three-electrode mode. The volume of the electrolyte solution in each compartment was maintained constant at *ca* 10 ml; during the long-term experiments water was periodically added to compensate for the unavoidable evaporation. Working electrodes were prepared as explained above and used for electrochemical tests within 12 h after the preparation. Platinum sheet (1.0 cm × 1.5 cm × 0.02 cm) was used as an auxiliary electrode; Ag|AgCl|1 M KCl (*CH Instruments, Inc.*) was used as a reference electrode, which was always positioned at the distance of few mm away from the center of the electroactive area of the working electrode. The potential of the Ag|AgCl|1 M KCl reference electrode was measured *vs.* a home-made reversible hydrogen electrode (RHE; platinized platinum wire immersed in the working electrolyte solution saturated with H_2 and with 1 atm H_2 above[1]) at required temperature. As a supporting electrolyte, 0.5 M H_2SO_4 was used; pH of the electrolyte solutions measured using a *Thermo Fischer* pH-meter at ambient temperature was 0.3. During all chronopotentiometric and chronoamperometric tests, the electrolyte solution was intensively agitated using a Teflon-lined magnetic bar stirrer. Experiments at elevated temperatures were performed by immersing the cell into a silicone oil bath, which temperature was adjusted to achieve the required value in the working electrolyte solution; the latter was continuously monitored using a conventional thermometer.

Electrochemical impedance spectra were recorded at the beginning and the end of every experiment at a potential where no significant faradaic processes occur to determine the uncompensated resistance (R_u) and to confirm that it did not change during tests. Where

specifically mentioned, the reported potentials were post-corrected for the ohmic drop by subtracting the IR_u product from the experimental values. A typical testing procedure involved the following measurements: (i) cyclic voltammetry at 0.02 V s^{-1} until quasi-stabilization (typically, 3 cycles), (ii) galvanostatic electrooxidation at 10 mA cm^{-2} for a required period of time, (iii) potentiostatic electrooxidation at 2.03 and 1.93 V *vs.* RHE for 0.5 h at each potential, and (iv) another set of cyclic voltammetric characterization at 0.02 V s^{-1} until quasi-stabilization. Data presented as average ± one standard deviation are based on tests of at least three independently synthesized samples.

2.4 CHARACTERIZATIONS

2.4.1 Scanning electron microscopy (SEM) and energy dispersive X-ray spectroscopy (EDS)

The SEM and EDS analysis of materials was undertaken using a *FEG-SEM Zeiss/ Ultra 55* scanning electron microscopes equipped with a *Bruker QUANTAX* X-ray detector. Samples for the analysis were cut into pieces of *ca* 0.5 cm × 1 cm, attached to SEM stubs using a double-sided carbon sticky tape and sputter coated with nanoparticulate gold (for 10 s at a discharge power of 4 W); electrical contact was provided using a silver paste. SEM imaging was done at 5 kV and a probe current of 1 nA.

2.4.2 Inductive coupled plasma optical emission spectrometry (ICP-OES)

The ICP-OES analysis was performed using a *Spectro Arcos ICP* spectrometer. For calibration, multi-element *Merck* standard solutions diluted to 25 ppm with aqueous 2 wt.% HNO_3 were

used, which was also a carrier solution. Samples for analysis were withdrawn from the electrochemical cell and diluted with 2 wt.% HNO_3.

2.4.3 Transmission electron microscope (TEM) and scanning transmission electron microscope with EDS elemental mapping (STEM-EDS)

The TEM and STEM-EDS studies were carried out using a *Thermo Instruments / FEI Tecnai* G^2 *TF20 Super-Twin* fitted with a *Bruker X-Flash* SDD windowless X-Ray detector and *Bruker Esprit 2.0* software. STEM images were recorded using *Gatan* bright field and *Fischione Instruments* high angle annular dark-field (HAADF) detectors. TEM images and selected area electron diffraction patterns were recorded with *Gatan* CCD detectors. Samples were prepared by ultrasonically dispersing the catalyst material into *n*-butanol and depositing a droplet of the suspension onto a holey-carbon coated copper grid. The microscope was operated at 200 kV and STEM-EDS mapping utilized an electron probe of approximately 1.5-2.0 nm, determining the X-ray elemental mapping image resolution. Thin regions of the sample were selected for elemental mapping in order to obtain as much spatial resolution as possible.

2.4.4 X-ray diffraction (XRD)

The XRD studies were performed on a *PANanalytical Empyrean* X-ray diffractometer equipped with a *PIXcel1D* detector using Cu K_α radiation (λ= 1.54 Å) generated at 45 kV and 45 mA at room temperature with a step size of 0.026° with 1 s per step. Samples for the XRD analysis were prepared following the procedures used for the working electrode fabrication but with the total material loading increased to *ca* 8 μmol cm^{-2} and with a total sample area of 4 cm^2

deposited onto pure glass (to avoid interference with the FTO reflections). Unfortunately, direct analysis of the actual electrodes used in the experiments produced no meaningful diffraction patterns with the instrument available herein. This also prevented the direct analysis of the electrodes after tests.

2.4.5 X-ray photoelectron spectroscopy (XPS)

The XPS analysis of manganese- and cobalt-based materials was performed using an *AXIS Supra, Kratos Analytical* instrument with a monochromatic Al K_α source (75 W). The analysis chamber was maintained at a pressure of not more than 2.0×10^{-9} mbar. Take-off angle was 90°. FTO electrodes (*ca* 1 cm × 1 cm) modified with the catalysts were mounted onto a 2.36-inch diameter platen and immobilized using a duct tape in the way that there was no electrical contact between the sample and the instrument ground; the samples were charge neutralized before the analysis. Collected spectral data were energy corrected by adjusting the maximum of the C-C peak in C 1s spectra to 284.8 eV. For high resolution scans, pass energy was 20 eV and a resolution was 0.5 eV; for survey scans, a pass energy was 160 eV and a resolution was 2 eV.

Ruthenium-based catalysts were analyzed using a *Nexsa Surface Analysis System, ThermoFisher Scientific* instrument with a monochromatic Al K_α source (1486.6 eV). X-ray spot size was set to 400 μm. The analysis chamber was maintained at a pressure of 1.0×10^{-8} or less. Due to the overlap of the Ru 3d and C 1s spectra and resulting ambiguity in the position of the C-C peak, these samples were mounted in the way providing a direct electrical contact between the catalyst film and the instrument ground using a copper tape. No post-correction to the measured binding energies was applied. Survey scans were recorded at a pass energy of 200 eV and a step size of 1

eV, while high resolution data were obtained at a pass energy of 50 eV and a step size of 0.1 eV. At least two different spots on each sample were probed to ensure the consistency of the results.

Fitting of the Sb 3d + O 1s spectra was undertaken in the following steps: (i) background fitting, (ii) fitting of the Sb $3d_{3/2}$ component that does not overlap with the O 1s peak, (iii) setting the integrated intensity and binding energy of Sb $3d_{5/2}$ peak by using Sb $3d_{3/2}$ fitted component as a guide and taking into account the following constrains: $3d_{3/2}$ to $3d_{5/2}$ integral ratio of 2:3, $3d_{3/2}$ - $3d_{5/2}$ doublet spin-orbit splitting of 9.4 eV,[2,3] and as close as possible full widths at half of maxima for both components; (iv) attributing the remainder of intensity overlapped with the Sb $3d_{5/2}$ peak to the required number of oxygen peaks. Detailed fitting of the Ru 3d + C 1s spectra were undertaken for the simplest case where no significant contribution from Ru^{4+} was detected. The procedure was similar to that described above for the Sb 3d + O 1s data but using Ru $3d_{5/2}$ peak in step (ii) and Ru $3d_{3/2}$ + C 1s signals in step (iii). Approximate estimation of the ruthenium integral in the samples containing significant amount of Ru^{4+} was undertaken by fitting the Ru $3d_{3/2}$ component only and assuming that the intensity of the prominent peak with the maximum in the 284.8-285.0 eV range is dominated by the C-C C 1s signal.

2.4.6 X-ray absorption spectroscopy (XAS)

The hard XAS spectra were collected on the multipole wiggler XAS beamline (12-ID) operating with an electron beam energy of 3.0 GeV and a beam current of 200 mA (maintained in top up mode), at the Australian Synchrotron. Manganese and cobalt K-edge data was collected in mode 1 using a Si (111) monochromator and focusing optics, ruthenium and antimony K-edge data was collected in mode 3 using a Si (311) monochromator. *OKEN* ionization chambers filled with

He (Mn) or N_2 (all other elements) were used to measure the incident radiation and transmission data of both the sample and a metallic reference foil (where the sample was sufficiently transparent) to ensure consistent energy calibration.

All samples were presented to the beam as thin films deposited on FTO glass electrodes, with the exception of the standard materials Sb_2O_5, RuO_2, Co_3O_4, CoOOH, MnO_2, Mn_2O_3 and MnO which were prepared as pressed powders using standard methods.[4] All data were collected on samples frozen in a 10 K liquid helium cryostat using a solid state 100-element Ge detector in transmission mode.

Raw data obtained from the beamline were converted using Sakura,[5] processed using Athena[6] (normalization, background subtraction, energy calibration), PySpline[7] (Fourier transform), and Artemis[6] (data fitting). The edge energy (the first inflection point of the main absorption peak) of the collected spectra were calibrated to the first inflection points of the foils; the values used were those reported by Bearden and Burr:[8,9] 6539 eV (Mn), 7709 eV (Co), 22117.2 eV (Ru) and 30491.2 eV (Sb). The *E0* values were set at 6555 eV (Mn), 7725 eV (Co), 22135 (Ru), and 30510 eV (Sb).

The soft X-ray absorption experiments were carried out at beamline U49-2 PGM-1 utilizing the experimental end station LiXEdrom of the BESSY II synchrotron facility in Berlin, Germany. The samples were arranged in the experimental chamber on a copper block attached to an x-y-z-manipulator to allow for sample positioning and the samples were contacted by a conductive Cu-tape. The measurements were performed in TEY mode, i.e. measuring the electron drain current caused by X-ray induced photoelectrons. Spectra were collected by scanning the incident X-rays across an energy range of 700 to 735 eV and 770 to 810 eV covering the $L_{2,3}$-edges of Fe and Co

as well as across an energy range of 520 to 560 covering the O K-edge, each scan with a step with of 0.1 eV. The energy resolution DE of the incident beam was better than 100meV. At each energy-step the drain current of the sample was collected using a Keithley Amperometer. In addition, the drain current of the refocusing mirror was collected for normalization of the Fe and Co spectra. In order to take into account, the oxygen contamination on the beamline optics, the oxygen spectra were normalized to the mirror current measured with identical beamline settings.

The beamline settings were chosen in a way to reduce the flux as far as possible leading to a maximum sample current of a few pA. This flux reduction was done to ensure that no X-ray induced changes occur in the spectra. To ensure that no damage occurred, all spectra were collected at least 3 times, two times on an identical spot and a third time on a new spot. To further check for possible damage also spectra at ca. 10 times higher flux were collected. In contrast to the spectra taken at low flux, these spectra showed evidence of flux induced sample damage, manifesting itself in a change of spectral features for subsequent scans. Crucially all low flux spectra presented herein were reproducible and showed no evidence of damage.

2.5 COMPUTATIONAL METHODS

The spin-polarized first principles calculations were carried out using projector augmented wave method[10] based on DFT[11,12] as implemented in *Vienna Ab initio Simulation Package* (VASP).[13,14] The exchange-correlation term was treated using gradient-corrected Perdew–Burke–Ernzerhof functional (PBE).[15] The cohesive energy, electronic structure, and magnetic properties of bulk and surfaces of transition metal-based materials were described using PBE augmented with an on-site Hubbard *U* term (PBE+*U*) on the d-electrons of Co and Ru ions.[16] Recent study on

Co_3O_4[17] proposed the use of U = 5.9 eV, which is a weighted average of the U values for Co(II) (4.4 eV) and Co(III) (6.7 eV). This choice of U produces a local electronic structure that is in a fair agreement with the experimental results and was therefore employed in the present study. For Ru, U = 1.3 eV was employed. An 8×8×8 gamma centred *k*-mesh was used for the Brillouin-zone (BZ) sampling of bulk Co_3O_4 and RuO_2, while sampling for $CoSb_2O_6$ was carried out using an 8×8×4 *k*-mesh. For surface calculations, a rectangular slab was chosen, for which a 2×4×1 *k*-mesh was used for the BZ integration. Plane-wave basis set with an energy cut off 520 eV was chosen for both bulk and surface calculations. The threshold criteria for self-consistent field convergence (total energy) were set to 10^{-7} and 10^{-5} eV for bulk and surface calculations, respectively, with Hellmann−Feynman force converging up to 0.05 eV $Å^{-1}$ during geometry optimizations.

The electrochemical stability of electrocatalysts can be correlated with the dissolution of metal ions of oxides and described by the potentials at which the surface dissolution becomes favorable, *viz.* dissolution potentials (E_d).[18] Herein, we calculated the difference in the dissolution potentials (ΔE_d) of Ru in the antimony-doped RuO_2 (Sb:RuO_2) with respect to that in pure RuO_2 as[19]

$$\Delta E_d = -\frac{\mu_{Sb:RuO_2} - \mu_{RuO_2}}{ne} \quad \text{Eq. 2.1}$$

where $\mu_{Sb:RuO_2}$ and μ_{RuO_2} are the chemical potentials of metal atoms in Sb:RuO_2 and RuO_2, respectively (μ are the energy differences of the systems with and without metal vacancy), e = 1.602 × 10^{-19} C is the electron charge, while n is the number of electrons transferred during the electrooxidation reaction leading to the dissolution. Corrosion of ruthenium (IV) in RuO_2 is initiated by its oxidation to $Ru^{VIII}O_4$,[20]and therefore n = 4 in this case. Positive values of ΔE_d

would indicate that the dissolution of metal ions in Sb:RuO_2 should occur at more positive electrode potential than in RuO_2, *viz.* increased stability towards electrocorrosion of the antimony-doped metal oxide.

The oxygen grand potential for the Ru-Sb-O system was calculated using the following expression:

$$\phi(T, P, N_{\mathrm{Ru}}, N_{\mathrm{Sb}}, \mu_{\mathrm{O}}) = G(T, P, N_{\mathrm{Ru}}, N_{\mathrm{Sb}}, \mu_{\mathrm{O}}) - \mu_{\mathrm{O}} N_{\mathrm{O}} \qquad \text{Eq. 2.2}$$

where, G is the Gibbs free energy of the system, T, P, N_i and μ_{O} are temperature, pressure, number of atoms of constituent element i in the system and the oxygen chemical potential, respectively.

Gibbs free energy is defined as $G = E + PV - TS$, where E is the total intrinsic energy, V is the volume and S is entropy. Since the compounds involved in the analysis herein are solids, we assume $\Delta(PV) \approx 0$, and neglect this term in calculations. The entropy term ($-TS$) can be also considered negligible since another entropy contribution that is a part of μ_{O} is significantly higher.

Upon normalization through the introduction of the atomic fractions of the constituent elements, *i.e.* by using $x_i = \frac{N_i}{N_{\mathrm{Ru}} + N_{\mathrm{Sb}}}$ instead of N_i, the final expression for the grand potential becomes:

$$\phi_{\mathrm{norm}}(T, P, x_{\mathrm{Ru}}, x_{\mathrm{Sb}}, \mu_{\mathrm{O}}) = \frac{\phi}{N_{\mathrm{Ru}} + N_{\mathrm{Sb}}} = \frac{E - \mu_{\mathrm{O}} N_{\mathrm{O}}}{N_{\mathrm{Ru}} + N_{\mathrm{Sb}}} \qquad \text{Eq. 2.3}$$

μ_{O} was simulated at the temperature and oxygen partial pressure as those used during the synthesis of the Ru-Sb mixed oxide samples according to the procedures described in the literature.[21]

2.6 REFERENCES

(1) Chatti, M.; Gardiner, J. L.; Fournier, M.; Johannessen, B.; Williams, T.; Gengenbach, T. R.; Pai, N.; Nguyen, C.; Macfarlane, D. R.; Hocking, R. K.; Simonov, A. N. Intrinsically Stable in Situ Generated Electrocatalyst for Long-Term Oxidation of Acidic Water at up to 80 °C. *Nat. Catal.* **2019**, *2* (May), 457–465. https://doi.org/10.1038/s41929-019-0277-8.

(2) C. D. Wanger, W. M. Riggs, L. E. Davis, J. F. M. and G. E. M. Handbook of X-ray Photoelectron Spectroscopy. *Perkin-Elmer Corp.* **1979**.

(3) Matthew, J. Surface Analysis by Auger and X-Ray Photoelectron Spectroscopy. D. Briggs and J. T. Grant (Eds). IMPublications, Chichester, UK and SurfaceSpectra, Manchester, UK, 2003. 900 Pp., ISBN 1-901019-04-7, 900 Pp. *Surf. Interface Anal.* **2004**, *36* (13), 1647–1647. https://doi.org/10.1002/sia.2005.

(4) King, H. J.; Bonke, S. A.; Chang, S. L. Y.; Spiccia, L.; Johannessen, B.; Hocking, R. K. Engineering Disorder into Heterogenite-Like Cobalt Oxides by Phosphate Doping: Implications for the Design of Water-Oxidation Catalysts. *ChemCatChem* **2017**, *9* (3), 511–521. https://doi.org/10.1002/cctc.201600983.

(5) Kappen, P.; Ruben, G. Sakura. *Aust. Synchrotron* **2013**.

(6) Ravel, B.; Newville, M. ATHENA, ARTEMIS, HEPHAESTUS: Data Analysis for X-Ray Absorption Spectroscopy Using IFEFFIT. *J. Synchrotron Radiat.* **2005**, *12* (4), 537–541. https://doi.org/10.1107/S0909049505012719.

(7) Tenderholt, A.; Hedman, B.; Hodgson, K. O. PySpline: A Modern, Cross-Platform Program for the Processing of Raw Averaged XAS Edge and EXAFS Data. *AIP Conf. Proc.* **2007**, *882* (February 2007), 105–107. https://doi.org/10.1063/1.2644442.

(8) J. A. Bearden, A. F. B. Reevaluation of X-Ray Atomicenergy Levels. *Rev. Mod. Phys.* **1967**, *39* (1).

(9) Reference X-Ray Spectra of Metal Foils. *Exafs Mater.*

(10) Joubert, D. From Ultrasoft Pseudopotentials to the Projector Augmented-Wave Method. *Phys. Rev. B - Condens. Matter Mater. Phys.* **1999**, *59* (3), 1758–1775. https://doi.org/10.1103/PhysRevB.59.1758.

(11) W. Kohn, L. S. Self-Consistent Equations Including Exchange and Correlation Effects. *Phys. Rev. A* **1965**, *140* (1133).

(12) R.G. Parr, W. Y. Density-functional Theory of Atoms and Molecules. *Oxford Univ. Press. New York, Oxford* **1989**. https://doi.org/10.1046/j.1035-6851.2001.00246.x-i3.

(13) Kresse, G.; Furthmüller, J. Efficient Iterative Schemes for Ab Initio Total-Energy Calculations Using a Plane-Wave Basis Set. *Phys. Rev. B - Condens. Matter Mater. Phys.*

1996, *54* (16), 11169–11186. https://doi.org/10.1103/PhysRevB.54.11169.

(14) Kresse, G.; Furthmüller, J. Efficiency of Ab-Initio Total Energy Calculations for Metals and Semiconductors Using a Plane-Wave Basis Set. *Computational Materials Science*. 1996, pp 15–50. https://doi.org/10.1016/0927-0256(96)00008-0.

(15) Perdew, J. P.; Burke, K.; Ernzerhof, M. Generalized Gradient Approximation Made Simple. *Phys. Rev. Lett.* **1996**, *77* (18), 3865–3868. https://doi.org/10.1103/PhysRevLett.77.3865.

(16) Dudarev, S.; Botton, G. Electron-Energy-Loss Spectra and the Structural Stability of Nickel Oxide: An LSDA+U Study. *Phys. Rev. B - Condens. Matter Mater. Phys.* **1998**, *57* (3), 1505–1509. https://doi.org/10.1103/PhysRevB.57.1505.

(17) Chen, J.; Selloni, A. Electronic States and Magnetic Structure at the Co_3O_4 (110) Surface: A First-Principles Study. *Phys. Rev. B - Condens. Matter Mater. Phys.* **2012**, *85* (8), 1–9. https://doi.org/10.1103/PhysRevB.85.085306.

(18) Greeley, J.; Nørskov, J. K. Electrochemical Dissolution of Surface Alloys in Acids: Thermodynamic Trends from First-Principles Calculations. *Electrochim. Acta* **2007**, *52* (19), 5829–5836. https://doi.org/10.1016/j.electacta.2007.02.082.

(19) He, X.; Mo, Y. Accelerated Materials Design of $Na_{0.5}Bi_{0.5}TiO_3$ Oxygen Ionic Conductors Based on First Principles Calculations. *Phys. Chem. Chem. Phys.* **2015**, *17* (27), 18035–18044. https://doi.org/10.1039/c5cp02181b.

(20) Gajic-Krstajic, L. M. T. L. T. N. V. K. Spectrophotometric Study of the Anodic Corrosion of Ti-RuO_2 Electrode in Acid Sulfate Solution. *Corros. Sci.* **2004**, *46*, 65–74.

(21) Xiao, B. B.; Jiang, X. B.; Jiang, Q. Density Functional Theory Study of Oxygen Reduction Reaction on Pt/Pd3Al(111) Alloy Electrocatalyst. *Phys. Chem. Chem. Phys.* **2016**, *18* (21), 14234–14243. https://doi.org/10.1039/c6cp01066k.

Chapter 3

Mixed Metal-Antimony Oxides: High-Durability Catalysts for Low pH Water Oxidation at Ambient and Elevated Temperatures

3.1 INTRODUCTION

Water electrolysers based on a proton-exchange membrane (PEM) electrolyte are currently seen as the preferred technology for the production of *green* hydrogen from renewables.[1-2] Double digit megawatt PEM plants are already available and even larger installations are planned.[3] Recent breakthroughs in the design of bipolar plates and cathode catalysts for the PEM electrolysers now throw a spotlight on the membrane and anode electrocatalysts as the components requiring further significant cost-efficiency improvements.[4] Catalysts for the oxygen evolution reaction (OER) are particularly problematic in essentially all key aspects – price, availability, activity and stability. While iridium oxides provide perhaps the best combination of the activity and stability among known monometallic catalysts,[1] there is not enough of this exceptionally rare metal currently available to us to bring the PEM water electrolysis to the TW scale.[5] Moreover, both theoretical and extensive experimental studies reveal the unavoidable degradation of iridium-based OER catalysts even under ambient conditions,[6–10] and especially in

industrially relevant high-temperature tests,[11] which is among the reasons for the comparatively high loadings of Ir in the anodes of PEM electrolyzers.

Alternative OER catalysts based on more abundant and cheaper elements exist, in particular lead(IV)-based oxides developed through many decades of research on the anodes for metal electrowinning,[12] though their specific activity is significantly lower than that of iridium-based systems and the stability is often even worse.[13] Among other non-noble metal options, the most obvious candidates are oxides of manganese, cobalt, nickel and iron, which have been widely investigated as OER catalysts for the alkaline and near neutral conditions.[1,14,23,15–22] Notably, monometallic oxides of Mn and Co have also been examined for applications in acidic environment, and in contrast to Ni and Fe which immediately dissolve,[24,25] relatively stable performance for at least several hours was demonstrated.[26,27] However, eventual degradation and essentially complete loss of activity is still unavoidable. A noble alternative to iridium is also well-known – ruthenium oxides are reported to be at least as active OER catalysts.[28,29] While the amount of Ru in the Earth's crust is only slightly higher than that of Ir[30] and it continues to rise in price, ruthenium is still more than five-fold cheaper,[31] is easier to refine and is produced on an order of magnitude higher scale as compared to iridium.[32] However, rapid degradation of RuO_2 anodes is again a major issue.[29,33,34]

Overall, it is highly unlikely that any monometallic oxide can provide an optimal combination of characteristics required to be a high-performance OER catalyst. In contrast, new materials with improved activity and/or stability emerge from the exploration of multielement oxide systems that sometimes combine the properties of individual compounds or exhibit distinct properties of their own. In the context of the design of electrocatalysts for the OER at low pH, successful

approaches often emerge from combining a highly catalytically active oxide with the one that is significantly more stable under operating conditions to enable improved long-term operation with decreased losses in specific activity.[35,36] This strategy has been broadly adopted for many years in the research on the electrowinning anode catalysts using PbO_2 as a "matrix" that stabilizes oxides of cobalt, manganese, silver and other metals.[12,18,37–39] The same approach is now also applied in the design of anode catalysts for PEM water electrolysers.[28-30] Improved electrochemical activity and durability during the OER in acidic solutions has been reported when catalytically active metals have been combined with the oxides of Ta^{IV},[14,19] Sn^{IV},[19,20,40] Ti^{IV},[21] Pb^{IV},[15] Y^{III},[22] Cr^{IV},[23] and also Sb^{V}.[16,17] Out of these, SbO_x generate deep interest because of its characteristics suitable as a stable structural matrix for low pH water oxidation catalysts which are discussed in the first chapter and the recent studies reported in the literature.[16,17,41–43]

In the search for highly active, and genuinely stable catalysts under practical operating conditions, the core aim of this chapter is the systematic investigation of the electrocatalytic activity and stability of mixed metal-antimony oxides towards the oxidation of acidic water. Specific emphasis is made on the stability, which is rarely assessed rigorously in the current literature, *viz.* the experiments are commonly limited to several hours and ambient temperature conditions only. Moreover, even such mild conditions cause continuous degradation of many catalysts, which sometimes remains underestimated when the stability data are recorded and presented in the galvanostatic mode. Herein, the initial tests were also undertaken under ambient conditions to identify the most promising catalysts, which were further investigated at elevated temperatures to assess and demonstrate the genuine suitability of antimony-metal oxides for operation under the conditions relevant to the PEM electrolyzers. Electrochemical, physical, and structural characteristics of the catalysts before and after exhaustive electrocatalytic tests are

compared and discussed, and new insights into the stability of antimonates derived through the density functional theory (DFT) calculations are presented.

3.2 RESULTS AND DISCUSSION

All materials in this work were synthesized *via* annealing of precursor salts deposited from their solutions in dimethylformamide and/or dimethylsulphoxide onto nominally flat glass supports covered with a thin conductive layer of fluorine-doped tin (IV) oxide (FTO). While sputtering and similar advanced techniques provide a better control over the morphology and composition, our choice over the much simpler drop-casting/annealing fabrication protocol was motivated by the ease of the future optimization of this approach for the creation of high-surface area catalysts of applied significance. All electrochemical tests were undertaken in 0.5 M H_2SO_4 with measured pH of 0.3 (at ambient temperature). All galvanostatic data are presented below after manual post-correction for ohmic losses using the uncompensated (R_u) values measured by the electrochemical impedance spectroscopy. However, the correction was generally not applied to cyclic voltammograms, where currents cannot be always confidently attributed to the stationary catalytic OER process only.

3.2.1 Characterization and electrocatalytic activity of individual oxides

Notwithstanding the individual metal oxides (MO_x) considered herein, *viz.* RuO_x, CoO_x, MnO_x, NiO_x and FeO_x, as well as SbO_x, were not expected to provide sufficient activity and/or stability during the OER at low pH to be of independent interest, the electrocatalytic properties of these materials were briefly examined to understand relevant differences in the key performance

parameters that are likely to affect those of the corresponding metal-antimony oxides. X-ray diffraction (XRD) and scanning electron microscopic (SEM) analysis of the prepared MO_x and SbO_x indicate that the materials were dominated by single oxide phases RuO_2, Co_3O_4, Mn_2O_3, NiO, Fe_2O_3, and Sb_2O_4 (Figure 3.S1) of variable morphology (Figure 3.S2).

Under voltammetric conditions, all as-prepared monometallic oxides exhibited measurable catalytic activity towards water electrooxidation in contrast to SbO_x, which produced negligible oxidation currents up to 2.2 V *vs.* reversible hydrogen electrode (RHE) (Figures 3.1a and 3.S3). Notwithstanding its reasonable initial activity, RuO_x was highly unstable in 0.5 M H_2SO_4 (Figures 3.S3e and 3.S4a), consistent with previous reports.[23] Upon initial loss of activity during the first hour of tests at a current density of 10 mA cm^{-2} (hereinafter, all currents are normalized to the geometric surface area of the electrodes), RuO_x was further able to sustain this rate of the OER at an IR_u-corrected potential (E_{IR}) of *ca* 2.0 V *vs.* RHE for more than 23 h (Figure 3.S4a), although subsequent short-term potentiostatic tests revealed that the performance was still slowly degrading (Figure 3.S4c). Degradation of RuO_x might be interpreted in terms of the formation of soluble hyperruthenic acid,[44,45] while the remaining catalytic activity might be attributed to the oxides of ruthenium in higher oxidation states that remain quasi-stable on the electrode surface yet are not highly catalytically active for the OER under the employed conditions.[46]

Among the examined non-noble metal oxides, CoO_x exhibited the best initial electrocatalytic activity enabling the rate of the OER of 10 mA cm^{-2} at an IR_u-corrected overpotential (η_{IR}) of only *ca* 0.53 V (Figures 3.1a and 3.S4a), which is comparable to the results reported by Schaak and colleagues ($\eta_{IR} \approx 0.58$ V).[27] Cobalt oxide synthesized herein sustained its initial activity for *ca* 5 h (*cf.* 12 h in Ref.[27]) before visually complete dissolution and dramatic deterioration of the

activity occurred, as expected from the Pourbaix diagram.[47] Nevertheless, the quasi-stabilized performance was still better than that of blank FTO suggesting that a very small amount of catalytic CoO_x still remained on the surface (Figure 3.S4a), probably, operating through a self-healing mechanism.[15] However, the CoO_x remaining on the electrode could not be detected by cyclic voltammetry (Figure 3.S5a), either reflecting their low amount or instability at not very positive potentials.[15,48] FeO_x exhibited qualitatively similar behavior to that of CoO_x, although the initial activity was worse, and the final performance was close to that of unmodified FTO; NiO_x suffered essentially immediate dissolution (Figure 3.S3c and 3.S4b).

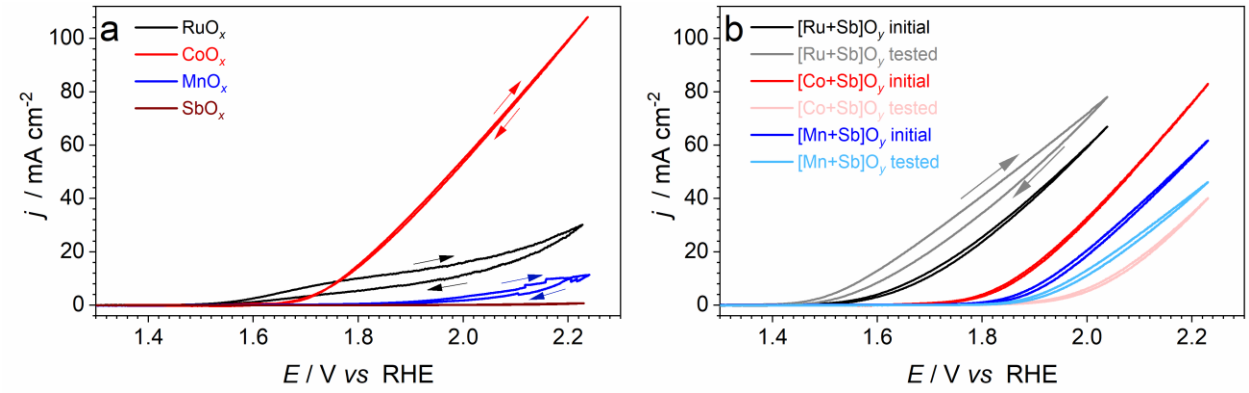

Figure 3.1. Cyclic voltammetry (scan rate, v = 0.020 V s^{-1}) recorded using stirred 0.5 M H_2SO_4 electrolyte solution and FTO electrodes modified with as-prepared (a) individual and (b) mixed metal-antimony oxides based on: ruthenium (*black*), cobalt (*red*), and manganese (*blue*). Data for SbO_x are shown in panel (a) as *brown* curve. In panel (b), *grey*, *pink* and *light blue* curves show data for the same $[Ru+Sb]O_y$, $[Co+Sb]O_y$, and $[Mn+Sb]O_y$ catalysts, respectively, after 24 h galvanostatic (10 mA cm^{-2}) and 1 h potentiostatic (2.03 and 1.93 V *vs.* RHE for 0.5 h at each potential) tests. Currents are normalized to the geometric surface area of the electrodes; potential values were not corrected for the iR_u drop. Third voltammetric scans are shown. Arrows show the direction of the voltammetric sweeps; in panel (b), arrows are provided for the *grey* trace only since the rest exhibited qualitatively the same behavior.

Manganese and antimony oxides demonstrated low activity towards the OER, but their performance was stable and even slightly improved during tests under ambient conditions on a 24 h timescale (Figure 3.S4a and 3.S4b). This was accompanied by essentially complete loss of the voltammetric signals associated with the Mn redox transformations, again pointing to a possibility for the catalytically active MnO_x being formed on the electrode surface at positive potentials only (Figure 3.S5b). In the SbO_x case, a notable enhancement of the featureless pseudocapacitive currents, most likely reflecting the roughening of the material surface resulting in the minor activity improvement, was observed (Figure 3.S5f). The quasi-stabilized overpotential required to maintain the OER rate of 10 mA cm^{-2} with SbO_x- and MnO_x-functionalized electrodes was *ca* 1.15 and 0.84, respectively (Figure 3.S4).

3.2.2 Electrocatalytic activity under ambient conditions

Further studies focused on mixed metal-antimony oxides; these are referred to by a general formula $[M+Sb]O_y$ which reflects the variable and not accurately known composition of the material under the operating conditions. In what follows, the presented metal-antimony oxide catalysts were synthesized with a 1:1 molar precursor ratio, and the initial loading of both elements of 1 μmol cm^{-2}, unless stated otherwise, but the actual composition during the OER is different due to the unavoidable corrosion in acidic solutions. The degree of this corrosion for the selected key materials was quantified (Figure 3.2 and Table 3.S1) and is discussed later in this chapter. Initial loading of the catalysts did not affect the areal electrocatalytic activity of the electrodes to a significant extent (exemplified for $[Mn+Sb]O_y$ and $[Ru+Sb]O_y$ in Figure 3.S6),

indicating that the catalytically active surface area does not increase with the amount of material deposited. This suggests a close to flat morphology of the catalyst layers.

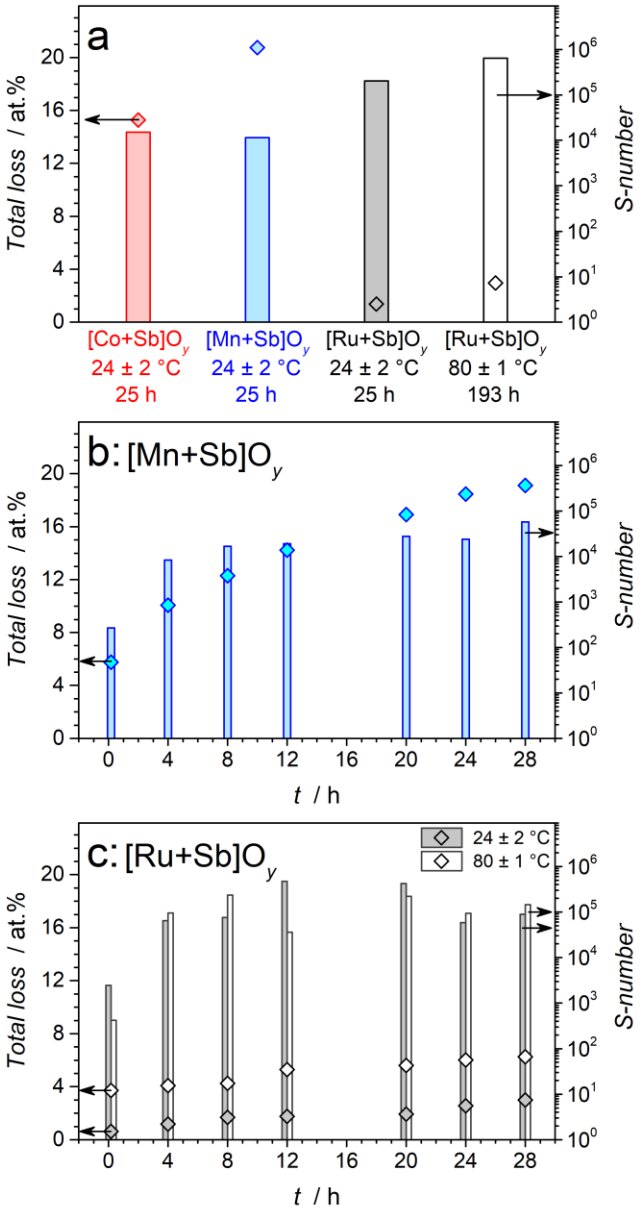

Figure 3.2. Loss of metals from catalysts (*diamonds*) during the OER in stirred 0.5 M H_2SO_4 and corresponding S-numbers (*bars*) under different conditions. (a) Tests of [Co+Sb]O_y (*red*), [Mn+Sb]O_y (*blue*) and [Ru+Sb]O_y (*black*) at 24 ± 2 °C over 25 h (24 h at 10 mA cm^{-2}; 0.5 h at 2.03 V *vs.* RHE; 0.5 h at 1.93 V *vs.* RHE) and 80 ± 1 °C for 193 h (192 h at 10 mA cm^{-2}; 0.5 h at 2.03 V *vs.* RHE; 0.5 h at 1.93 V *vs.* RHE) with the

ICP-OES analysis undertaken upon completion of the measurements only. (b-c) Galvanostatic (10 mA cm^{-2}) tests of $[Mn+Sb]O_y$ and $[Ru+Sb]O_y$ at (b-c) 23 ± 2 and (c) 80 ± 1 °C with periodic withdrawal of samples for the ICP-OES analysis (5 mL) and addition of pure 0.5 M H_2SO_4 to keep the total electrolyte solution volume constant at 20 mL; S-numbers are calculated for periods between sampling.

First, we exclude Ni- and Fe-based systems from detailed analysis, as these materials rapidly degraded under the OER conditions (Figure 3.S7 and 3.S8). Attempts to improve their performance through variations in the metal : antimony ratios and annealing temperature were not successful. The effect of the latter parameter was also briefly considered for the much better performing Co-, Mn- and Ru-Sb oxide catalysts. The best results were always obtained at 600 °C (Figure 3.S9), which is the highest value we could use due to thermal instability of FTO.[49,50] Hence, all results discussed here in this chapter were obtained with the catalysts synthesized at 600 °C better stability of the catalysts at 600°C is a result of the more crystalline nature of the catalysts compared to a lower annealing temperature.

Voltammetric assessment of the initial OER catalytic activity of CoO_x and $[Co+Sb]O_y$ revealed lower performance of the latter (Figure 3.3), which is likely associated with the reduced amount of the active cobalt oxide surface species, as also measured by cyclic voltammetry (*cf.* Figures 3.S5a and 3.S10a). Subsequently recorded chronopotentiograms reveal the significant initial degradation of the cobalt-antimony-modified electrode, though more importantly $[Co+Sb]O_y$ catalysts do not completely lose their activity and sustain a current density of 10 mA cm^{-2} at a reasonable overpotential (Figure 3.3a). The duration of the initial drop increased with an increase in the Co : Sb ratio used for the synthesis, while the best stabilized activity was demonstrated by the catalysts prepared with equimolar amounts of Co and Sb (Figure 3.S11). Specifically,

chronopotentiograms recorded with the latter type of [Co+Sb]O_y at 10 mA cm^{-2} stabilized at a well-reproducible IR_u-corrected overpotential of 0.769 ± 0.010 V (Figures 3.3a and 3.S12). Subsequent potentiostatic tests at 2.03 and 1.93 V *vs.* RHE also did not reveal further significant losses in the catalytic activity (Figure 3.3b). A plausible explanation of the rapid initial loss of the performance is provided in the following section, while at this stage we conclude that [Co+Sb]O_y exhibits a reasonable short-term stability during the OER at low pH and ambient temperature, yet its catalytic activity is not high.

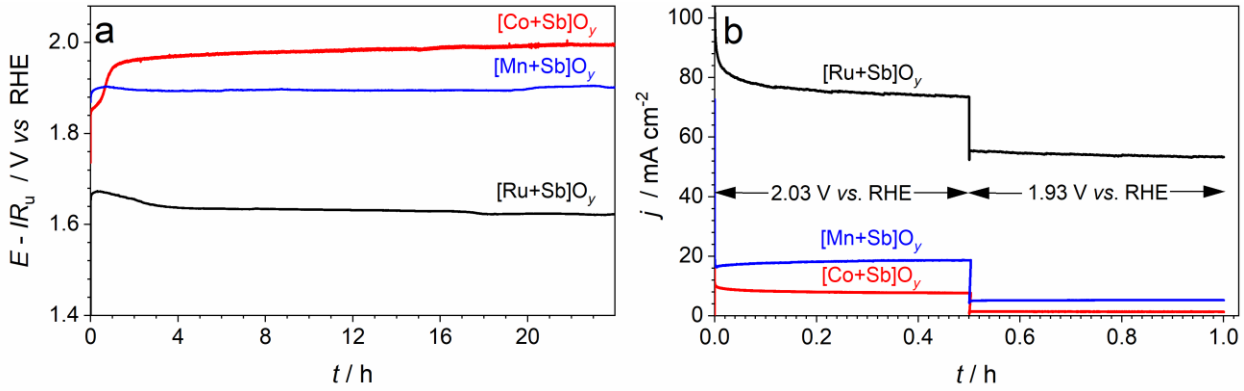

Figure 3.3. (a) IR_u-corrected chronopotentiograms (current density 10 mA cm$^{-2}_{geom.}$) and (b) subsequently recorded chronoamperograms (at a non-IR_u-corrected potentials of 2.03 and 1.93 V *vs.* RHE) for FTO electrodes modified with [Co+Sb]O_y (*red*), [Mn+Sb]O_y (*blue*) and [Ru+Sb]O_y (*black*) in contact with stirred 0.5 M H_2SO_4 at 24 ± 2 °C.

In contrast to the cobalt-based materials, combination of Mn with Sb produced a very significant improvement in the OER catalytic activity with respect to monometallic MnO_x (Figure 3.1). The [M+Sb]O_y catalysts were also able to maintain the initial performance during 24 h galvanostatic tests (Figure 3.3a). Variations in the Mn to Sb precursor ratio revealed that the manganese-rich materials (synthesized with Mn : Sb = 2 : 1) suffer slow deterioration in performance (Figure

3.S13), which was also recently reported for manganese antimonate with a similar starting composition and under comparable conditions by Gregoire and co-workers.[43] Contrasting this behavior, the activity of the [M+Sb]O_y catalysts synthesized herein with 1 : 1 and 1 : 2 ratio was highly stable. Between these two types of materials, the Sb-rich one was found to be less active, exhibiting η_{IR} for 10 mA cm^{-2} of *ca* 0.70 V. The best-performing [Mn+Sb]O_y electrocatalysts with the initial equimolar Mn : Sb ratio stably maintain the OER current density of 10 mA cm^{-2} for at least 24 hours under ambient conditions at a highly reproducible overpotential of 0.677 ± 0.008 V (Figures 3.3a and 3.S14).

The combination of ruthenium with the antimonate matrix produced catalysts that exhibit a stable cyclic voltammetric response typical of a robust and highly active OER catalyst up to 2.03 V *vs.* RHE, in contrast to unstable RuO_x (Figures 3.1, 3.S3e and 3.S7e). Moreover, galvanostatic tests at 10 mA cm^{-2} improved the performance of the [Ru+Sb]O_y materials by *ca* 0.04 V over the initial *ca* 10-12 h of experiments, eventuating in a reproducible stabilized IR_u-corrected overpotential of η_{IR} = 0.39 ± 0.03 V (Figures 3.3a and 3.S15).

Overall, this analysis of the initial catalytic performance and 25 h stability at ambient temperature of the metal-antimony oxides revealed a synergistic effect of the combination of a catalytically active metal and acid-stable Sb for the [Mn_n+Sb_m]O_y system, where a significant improvement in the activity was achieved. The key advantage of combining Co and Ru with the SbO_x matrix is in the substantial improvements in the stability, which is a highly favorable outcome given that the instability of the OER anode catalysts is among the most technologically pressing problems of the PEM water electrolysers.[51,52]

3.2.3 Characterization of the mixed metal-oxide catalysts

To enable deeper understanding of the observed trends in the electrocatalytic performance of the investigated metal-antimony oxides, physical characterization of the key materials was undertaken using the state-of-the-art techniques.

3.2.3.1 Corrosion during operation.

SEM images of the catalysts were taken to visualize their morphology and changes thereof after the water electrooxidation tests (Figure 3.S16). As-prepared catalysts were essentially flat coatings with no notable features, with the exception of [Mn+Sb]O_y which contained grains of a few hundred nanometres in size forming a layer with occasional voids of similar dimensions (Figure 3.S16a). Galvanostatic tests at ambient temperature for 24 h caused partial erosion of the catalyst layers resulting in pitting of the surface for [Co+Sb]O_y (Figure 3.S16d), [Ru+Sb]O_y (Figure 3.S16f), and [Fe+Sb]O_y (Figure 3.S16j), further development of cracks between the grains for [Mn+Sb]O_y (Figure 3.S16b), and substantial roughening of the [Ni+Sb]O_y surface due to the loss of material (Figure 3.S16h).

The level of corrosion during the OER was quantified for the key catalysts examined, *viz.* [Mn+Sb]O_y, [Co+Sb]O_y and [Ru+Sb]O_y. Complete dissolution of the materials for analysis was not possible even with the use of oxidizing acids (conc. H_2SO_4, HNO_3, aqua regia) under boiling conditions, as well as under extreme electro oxidative conditions (e.g. 0.5 A cm^{-2} constant current or *ca* 5 V *vs.* RHE). Therefore, the ICP-OES analysis focused on the electrolyte solutions only, while the changes in the catalyst surface compositions were estimated by X-ray photoelectron spectroscopy (XPS). One should keep in mind that there is a significant level of

uncertainty in the compositions derived from XPS, especially for [Ru+Sb]O_y where quantitative analysis was complicated by overlapping C 1s and Ru 3d spectra (*vide infra*).

After 24 h galvanostatic followed by 1 h potentiostatic tests at ambient temperature, the levels of corrosion of metals and antimony from [Co+Sb]O_y and [Mn+Sb]O_y into the electrolyte solutions were comparable (Figure 3.2), notwithstanding a very distinct electrocatalytic behaviour (Figure 3.3a). XPS showed that quasi-stabilized concentrations of the metals at the surface of [Co+Sb]O_y and [Mn+Sb]O_y were also similar (Table 3.1). At the same time, voltammetric analysis, which provides the only reliable means of probing the catalytically active species on the electrode surface, shows that tested [Mn+Sb]O_y catalysts still exhibit detectable peaks associated with Mn redox transformations (Figure 3.S10b), while tested [Co+Sb]O_y materials present a featureless response (Figure 3.S10a). These observations might reflect the differences in the quasi-stabilized concentrations of the catalytically active metals in the top-most layers of the Co-Sb and Mn-Sb oxide systems. While the [Co+Sb]O_y surface loses a very significant part of its cobalt, [Mn+Sb]O_y is likely to maintain a higher amount of manganese available for the OER catalysis. In another test of [Mn+Sb]O_y at 10 mA cm^{-2} over 28 h, samples of the electrolyte solutions for the analysis of dissolved metal and antimony were periodically withdrawn and replaced with fresh 0.5 M H_2SO_4 to maintain the total volume of the electrolyte solution unchanged (Figure 3.2b). The results indicate that the most significant corrosion occurred during the initial 4-8 h of operation, followed by a slower and progressively decreasing rate of the metal loss. This is best seen from the comparisons of corresponding S-numbers, *viz.* the amount of O_2 evolved per the amount of the catalytically active metal dissolved, which increase throughout the test (Figure 3.2b and Table 3.S1).

The lowest level of metal corrosion was observed for [Ru+Sb]O_y where the amount of lost ruthenium was not more than 1 at.% at ambient temperature, but the amount of antimony released into the electrolyte solution was significant (Figure 3.2). Changes in the pre-catalytic features in the cyclic voltammetry were inconclusive, but an increase in the currents in the whole range examined was observed (Figure 3.S10e). Critically, long-term tests of [Ru+Sb]O_y at elevated temperature of 80 °C (*vide infra*) caused only slightly higher level of corrosion (Figure 3.2), while XPS consistently demonstrated that the surface Ru : Sb atomic ratio significantly increased up to *ca* 1 : 1 (Table 3.1). Thus, [Ru+Sb]O_y suffers a favorable corrosion of antimony that improves the electrocatalytic activity of the material towards the OER (Figures 3.1b and 3.3a) through an enrichment of the surface layer in catalytically active ruthenium.

When considered together, the observed levels of corrosion (Table 3.1 and Figure 3.2) and stable electrocatalytic performance of the manganese-, cobalt- and ruthenium-antimony oxides (except for the initial drop in the [Co+Sb]O_y performance) (Figure 3.3) suggest that a quasi-equilibrium between the solid oxides and dissolved forms of Mn/Co/Ru and Sb is rapidly established in the system. Such an equilibrium between dissolution/redeposition of metal oxides is likely to sustain the observed stable electrocatalytic operation. This is circumstantially confirmed by slightly higher loss of ruthenium during the [Ru+Sb]O_y tests with continuous sampling at 23 ± 2 and 80 ± 1 °C (Figure 3.2c), as compared to the experiments where the final electrolyte solution was analyzed (Figure 3.2a). Indeed, periodic removal of dissolved ruthenium might induce additional corrosion of the solid catalyst to reinstall a quasi-stabilized concentration of Ru species in the electrolyte solution. Thus, the examined OER catalysts might operate in a self-healing mode,[15,53–56] with the Sb oxide matrix acting to facilitate the redeposition and suppress the dissolution of the active component.

Table 3.1. Relative surface concentrations of metals for catalysts[a] before and after OER tests in stirred 0.5 M H_2SO_4 as determined by XPS.

Catalyst	As prepared	Tested at	
		24 ± 2 °C [b]	80 °C [c]
[Mn+Sb]O_y	23 ± 1	12 ± 2	n.a.
[Co+Sb]O_y	34 ± 2	9 ± 4	n.a.
[Ru+Sb]O_y	9 ± 5	n.a.	44 ± 5

[a] at.% with respect to total metal + antimony amount quantified by XPS; data are presented as a mean ± one standard deviation for several measurements. [b] 10 mA cm^{-2} for 24 h and 2.03 and 1.93 V *vs.* RHE for 0.5 h at each potential. [c] 10 mA cm^{-2} for 10 h.

3.2.3.2 Structural features.

The structural features and the oxidation states of metals and antimony in the key [Co+Sb]O_y, [Mn+Sb]O_y and [Ru+Sb]O_y samples were probed by XAS (Figure 3.4), XPS (Figures 3.S17-3.S19) and XRD (Figure 3.5). The ruthenium-antimony system was additionally investigated by TEM (Figure 3.6).

High-resolution Sb 3d + O 1s spectra exhibited two signals, *viz.* a well-resolved Sb $3d_{3/2}$ peak and a superposition of Sb $3d_{5/2}$ with the O1 s spectrum (Figure 3.S17). Fitting of these data and comparisons to the literature[57,58] confirmed that antimony adopts a dominant oxidation state 5+ in all catalysts after the OER tests, as well as in most of the untreated samples. The Sb K-edge XANES recorded for Mn-, Co- and Ru-Sb mixed oxides reproduced well the data reported elsewhere for manganese antimonates,[43] and have similar energy position to Sb_2O_5, consistent with the antimony having a 5+ oxidation state (Figure 3.4a and 3.S20). A slight shift to higher energy was noted in the Sb K-edge data for the catalysts after the OER tests (Figures 3.S20).

Sb K-edge EXAFS of the investigated metal-antimony oxides are similar to each other and to Sb_2O_5 in that none of the datasets exhibit any notable second coordination sphere peaks in the Fourier Transform (FT) of EXAFS beyond the first coordination sphere apparent distances (*R*') of 2 Å (Figures 3.4a and 3.S21). This would be consistent with antimony being present as a part of a highly disordered phase or might be the consequence of how the distances in the structure cancel each other out as exemplified by fitting for Sb_2O_5 (Figure 3.S21 and Table 3.S2).

The shape and position of the Mn $2p_{5/2}$ peaks for fresh $[Mn+Sb]O_y$ (Figure 3.S18a) are similar to those reported for the oxide/oxyhydroxide Mn^{3+} compounds,[59] and show only a slight shift towards higher binding energies after catalytic tests. Comparisons of the Mn K-edge XANES data obtained for $[Mn+Sb]O_y$ to the data for the MnO, Mn_2O_3 and MnO_2 standards suggest that the oxidation state of the metal in the bulk of the as-prepared material is between 2+ and 3+, while Mn^{3+} becomes a dominant component after the electrocatalytic tests (Figures 3.4b and 3.S22). The Co K-edge XANES of as-prepared $[Co+Sb]O_y$ is consistent with a cobalt oxidation state between 2+ and 3+, or a material like Co_3O_4 where both Co^{2+} and Co^{3+} are present in the lattice structure (Figure 3.4c). The Co K pre-edge intensity decreases after the OER test, which would be consistent with the loss of the Co_3O_4 phase with a tetrahedral Co^{2+} site (Figure 3.S23a-b). A change in the profile of the XANES can be also indicative of the loss of a phase (Figure 3.4c). Although the Co 2p XP spectra of $[Co+Sb]O_y$ have a low signal-to-noise ratio (Figure 3.S18b), the major Co oxidation state on the surface can be also ascribed to 3+ based on the comparisons to the tabulated spectra.[59] Thus, both XPS and XANES indicate that the dominating oxidation states of manganese and cobalt in as-prepared metal- antimony mixed oxides are between 2+ and 3+.

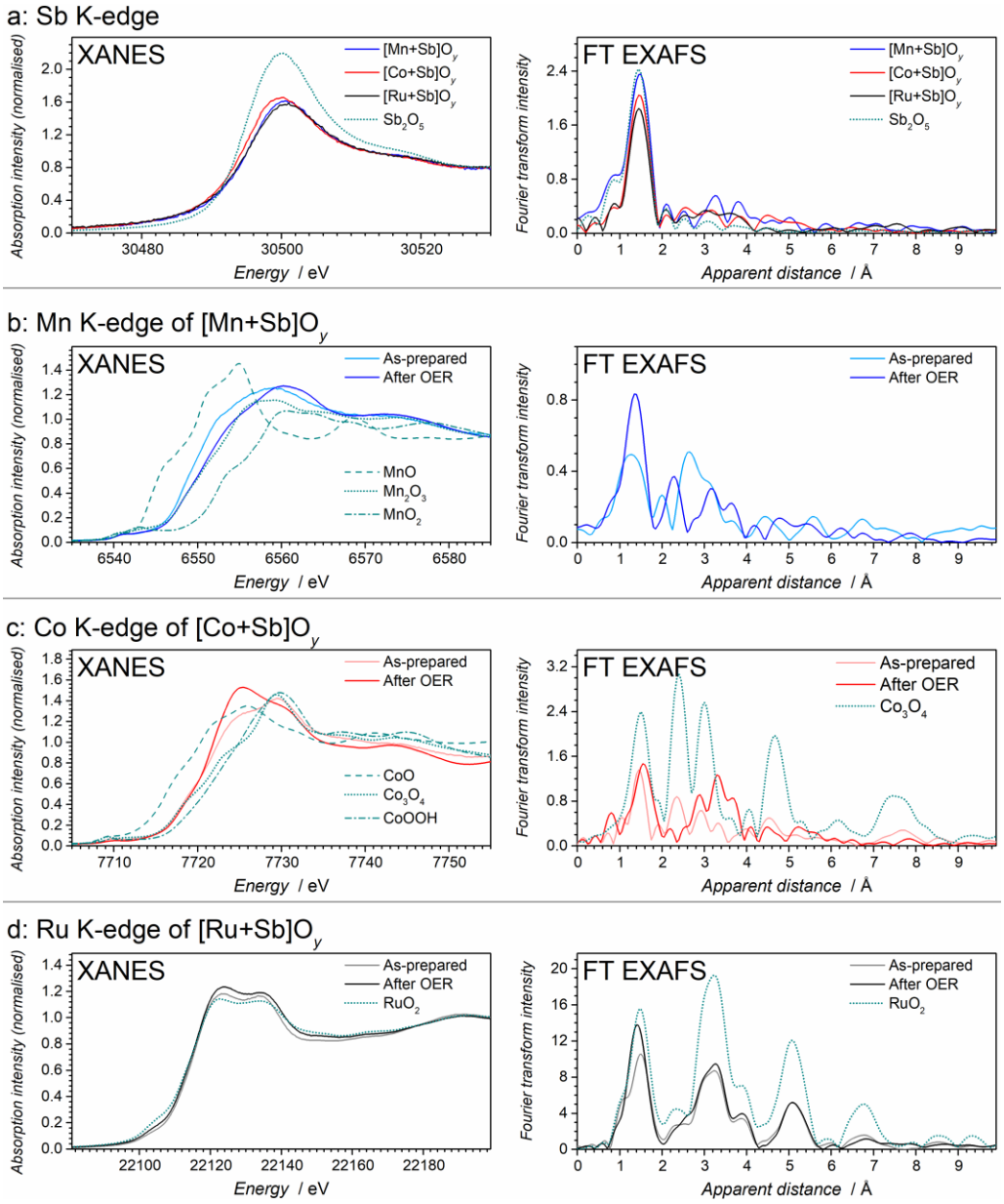

Figure 3.. XAS data at (a) Sb, (b) Mn, (c) Co and (d) Ru K-edges obtained for [Mn+Sb]O_y (*blue*), [Co+Sb]O_y (*red*) and [Ru+Sb]O_y (black) before (pale solid traces) and after (vivid solid traces) electrocatalytic tests in 0.5 M H_2SO_4 compared to the defined reference materials (shown as dashed/dotted teal traces). (e-h) Fourier Transform of EXAFS at (e) Sb, (f) Mn, (g) Co and (h) Ru K-edges. [Mn+Sb]O_y and [Co+Sb]O_y were tested for 24 h at 10 mA cm^{-2} and then for 1 h at 2.03 and 1.93 V vs. RHE at ambient temperature; [Ru+Sb]O_y was tested for 12 h at 10 mA cm^{-2} at 80 °C.

Although Mn and Co at the catalytic surfaces most likely adopt higher oxidation states during the OER, those cannot be detected by *ex situ* analysis due to their very high oxidative reactivity and immediate conversion into states that are thermodynamically favorable under ambient environment.[60–62] X-ray diffractograms of [Co+Sb]O_y and [Mn+Sb]O_y exhibited a set of peaks typical of a tetragonal trirutile phase with major 110, 013 and 123 reflections at *ca* 27, 35 and 53°, respectively (Figure 3.5a-b). Qualitatively similar XRD patterns were obtained for the mixed nickel-antimony and iron-antimony samples (Figure 3.S24). These data agree with the recent studies,[17,42,43,63] and it formally suggest that the metal-antimony phase in the investigated materials is structurally similar to $CoSb_2O_6$ (ICSD-108964), where 2+ is expected to be the dominant oxidation state of the metal.

However, both [Co+Sb]O_y and [Mn+Sb]O_y materials also contained individual metal oxides with 3+ oxidation states, *viz.* Co_3O_4, Mo_2O_3 and Mo_3O_4, which contribute to XANES and XPS. It is also worth noting that the mean crystallite sizes for the individual metal oxides phases detected by XRD were notably higher than those for the antimonate phase (Figure 3.5a-b), suggesting that the former are present as larger agglomerates as compared to the latter.

Well-defined FT EXAFS beyond the first coordination sphere were observed up to $R' = 5$ at the metal K-edges for both [Co+Sb]O_y and [Mn+Sb]O_y (Figure 3.4b-c), which is consistent with the metal site(s) being ordered. This indicates that the metals do not simply dope the dominant Sb location in the antimony oxide lattice, in contrast to what was observed previously for the conceptually similar Co-Fe-Pb oxide OER catalyst,[15] and more complicated structural scenarios apply. To describe the metal-antimony phases in [Co+Sb]O_y and [Mn+Sb]O_y, EXAFS simulations based on the crystal structure of $MnSb_2O_6$[64] and that of $CoSb_2O_6$[65] were undertaken.

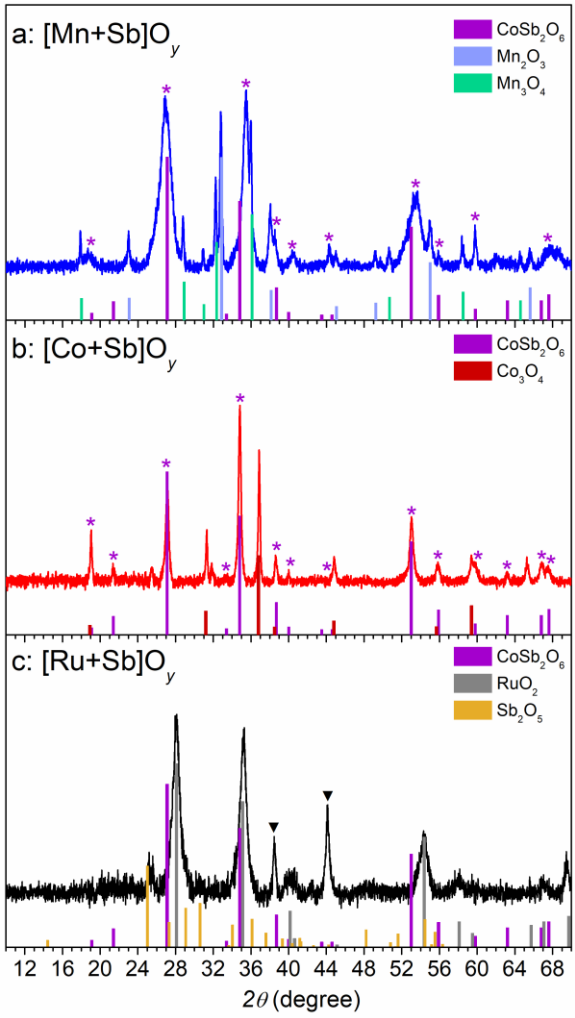

Figure 3.5. X-ray diffractograms of as-synthesized (a) $[Mn+Sb]O_y$, (b) $[Co+Sb]O_y$ and (c) $[Ru+Sb]O_y$. Vertical lines show tabulated positions and relative intensities for (a-c) $CoSb_2O_6$ ICSD-108964, (a) Mn_2O_3 ICDD-00-041-1442 and Mn_3O_4 ICDD-01-075-1560, (b), Co_3O_4 ICSD-36256, (c) RuO_2 ICSD-731469 and Sb_2O_5 PDF-01-071-0256. Mean crystallite sizes calculated using Scherrer equation were: (a) $d_{XRD}(MnSb_2O_6) \approx 7$ nm, $d_{XRD}(Mn_2O_3) \approx 35$ nm, $d_{XRD}(Mn_3O_4) \approx 41$ nm; (b) $d_{XRD}(CoSb_2O_6) \approx 24$ nm; $d_{XRD}(Co_3O_4) \approx 43$ nm; (c) $d_{XRD}(RuO_2) \approx 10$ nm. Asterisks indicate diffraction peaks attributed to the antimonate phase. Triangles indicate peaks which assignment is not straightforward.

As expected from XRD (Figure 3.5a), $MnSb_2O_6$ alone could not reliably describe the Mn K-edge EXAFS for as-prepared [Mn+Sb]O_y (Table 3.S3). This can be explained by the presence of a manganese oxide compound, most likely Mn_2O_3, which produces a peak at *ca* 2.5-2.6 Å in FT EXAFS of as-prepared [Mn+Sb]O_y (Figures 3.4b and 3.S22f). If the material were composed of Mn_2O_3 imbedded in a Mn-Sb mixed oxide, a substantial dampening of the EXAFS, and therefore of the Fourier transform of the EXAFS, due to a combination of disorder and self-absorption by the matrix would be expected. After the OER, the intensity of the FT EXAFS signal at *ca* 2.5-2.6 Å and Mn_2O_3 features in EXAFS are suppressed (Figures 3.4b and 3.S22c), which indicates loss of Mn_2O_3, consistent with the observed corrosion of manganese (Figure 3.2).

Given that this loss does not induce a notable degradation in the electrocatalytic activity (Figure 3.3b), we conclude that monometallic Mn oxides do not make a significant contribution to the OER performance of [Mn+Sb]O_y. However, the XAS data for the tested sample still cannot be described by a pure $MnSb_2O_6$ phase (Table 3.S3), suggesting that the material maintains some amount of Mn oxide(s) along with the antimonate phase after being operated as an OER catalyst.

XAS data recorded at the Co K-edge for [Co+Sb]O_y confirmed the XRD observations of the presence of Co_3O_4 in the as-prepared material, which vanished after the OER tests as best seen in the FT EXAFS (Figure 3.4g and 3.S23c,e). The XAS data of the tested cobalt-antimony oxide catalyst are well fit with the simulations based on the $CoSb_2O_6$ structure[65] (Figure 3.S23c,f and Table 3.S4). On this basis, we interpret the initial rapid drop in the performance of [Co+Sb]O_y (Figure 3.3b) by the dissolution of the catalytically more active Co_3O_4 phase from the material surface, while the quasi-stabilized performance achieved after *ca* 20 h is ascribed to the true catalytic activity of cobalt antimonate.

The most challenging to interpret set of physical characterization data among examined systems was obtained for the top-performing [Ru+Sb]O_y OER catalysts. Analysis of the Ru 3d XP spectra are complicated by a direct overlap with C 1s signals (Figure 3.S18c), but reasonable assignments were still possible. The surface state of ruthenium in as-prepared [Ru+Sb]O_y can be ascribed to Ru^{3+},[66] which in some cases could be well resolved through fitting (Figure 3.S19c), intermixed with Ru^{4+}. Operation of the catalyst induced oxidation of a significant portion of the surface metal to Ru^{4+} (Figure 3.S18c).[66] In turn, Ru K-edge XANES recorded for fresh and tested [Ru+Sb]O_y were in a perfect agreement with the Ru^{4+} oxidation state, closely resembling the spectra of the RuO_2 reference (Figure 3.4d).

Interpretation of the XRD data for [Ru+Sb]O_y was not straightforward as the diffraction pattern of rutile RuO_2 is similar to that of the anticipated trirutile antimonate phase. Nevertheless, the major set of broad diffraction peaks at 28, 35, 40, 54 and 69.5° matches well the positions and relative intensities of the tabulated pattern of ruthenium (IV) oxide (*grey bars* in Figure 3.5c). This interpretation suggests that the Sb component(s) give rise to a set of broad low-intensity signals at *ca* 25, 30.5 and 48° that can be attributed to a highly disordered Sb_2O_5, along with two narrower peaks at *ca* 38.5 and 44° (marked with triangles Figure 3.5c). One might suggest that these two reflections can be attributed to an antimonate phase which other diffraction peaks are presumably merged with the major signals of RuO_2. However, as will become evident from the analysis of the XAS data below, the presence of the antimonate phase in the actual catalyst material, prepared as a much thinner layer than the XRD sample (see Chapter 2), is highly unlikely. At this point, we cannot unambiguously assign the diffraction peaks at *ca* 38.5 and 44°. Notwithstanding this uncertainty, we conclude that the dominating metal-based phase in

[Ru+Sb]O_y is ruthenium(IV) oxide, which contrasts the Co- and Mn-Sb systems where a clear XRD evidence for the formation of the antimonates was obtained (Figure 3.5).

Detailed and highly resolved Ru K-edge EXAFS up to *R*' = 8 Å were collected for [Ru+Sb]O_y, both as-deposited and after catalytic tests (Figures 3.4d and 3.S25). Fitting of these data with simulations based on a $RuSb_2O_6$-type lattice where metal was doped into the site between the two SbO_3 layers did not produce any satisfactory level of agreement (Figure 3.S25 and Table 3.S5). Clearly resolved FT EXAFS peaks at high *R*' of 3.1, 3.9, 5.1, 6.8 Å are present in the Ru-Sb catalyst before and after the OER tests; these are associated with groups of Ru-Ru distances at 5.0, 6.8 and 7.2 Å, and cannot be explained by the $RuSb_2O_6$ phase. In fact, the EXAFS and XANES of [Ru+Sb]O_y are almost perfectly consistent with the RuO_2 structure, although with a slightly increased level of disorder (Figures 3.4d and 3.S25, Table 3.S5), which partially corroborates the XRD data (Figure 3.5c).

Taken together, the XAS and XRD data suggest that the ruthenium structure in [Ru+Sb]O_y is very close to that of the RuO_2 lattice, which opens a question on the origin of the significantly improved electrocatalytic performance of the mixed oxide system as opposed to RuO_2 (Figure 3.1). To shed light on this, detailed transmission electron microscopic investigations with elemental mapping was undertaken.

At low to moderate magnification, STEM-EDS analysis of [Ru+Sb]O_y showed ruthenium and antimony to be intimately mixed, both before and after the OER tests (Figures 3.6a-b and 3.S26). Conventional TEM imaging demonstrated that the catalyst represents a very fine assembly of nanocrystals, typically less than 10 nm in size, embedded into another material that appears significantly more structurally disordered (Figures 3.6c-d and 3.S27). Higher magnification

images revealed clear lattice fringes of *ca* 3 Å for the crystalline nanoparticles, which can be attributed to RuO_2 with a relatively high degree of crystalline order (Figure 3.6c-d).

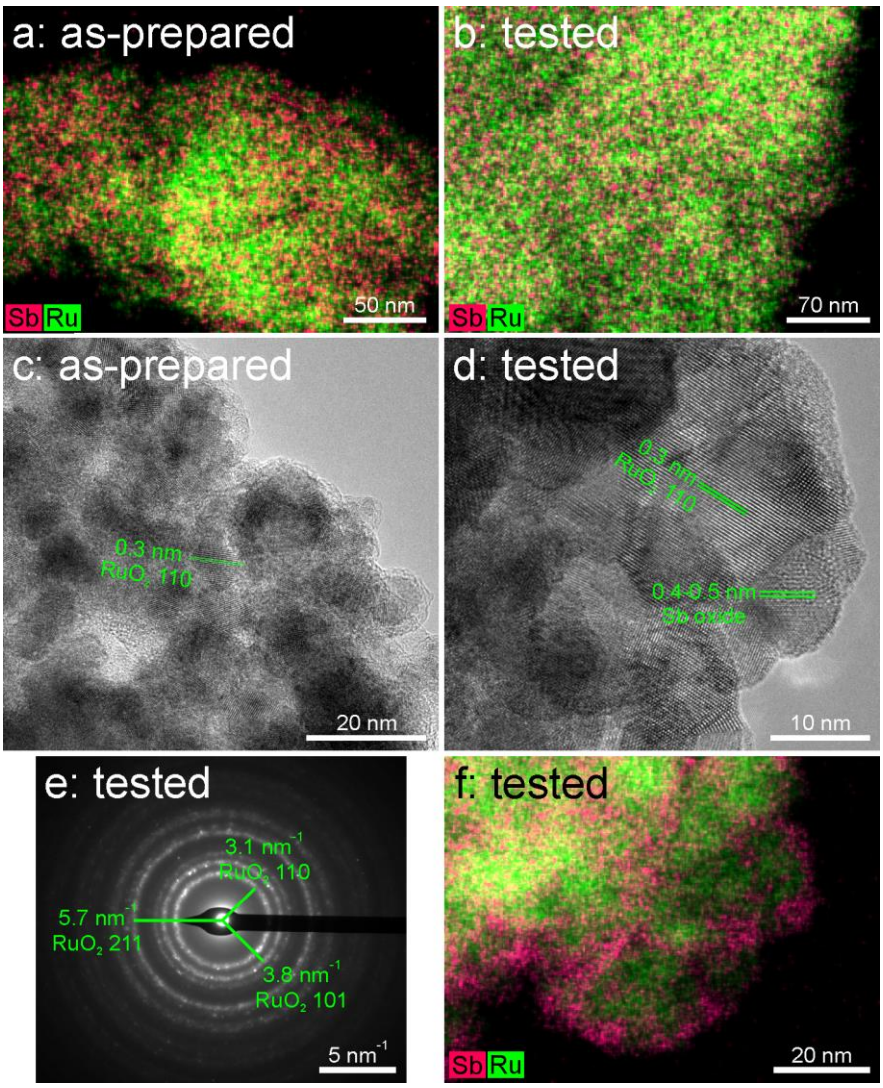

Figure 3.6. TEM and STEM-EDS characterization of $[Ru+Sb]O_y$ before and after OER tests at 10 mA cm^{-2} for 24 h at 80 °C: (a-b) medium magnification STEM-EDS mapping of the (a) as-prepared and (b) tested catalyst; (c-d) TEM micrographs of the (c) as-prepared and (d) tested catalyst; (e) selected area electron diffraction taken from a region containing large amounts of both Ru and Sb for the tested catalyst. (f) STEM-EDS mapping analysis of the extended area of the tested catalyst around the region shown in panel d.

This is also illustrated in the selected area electron diffraction pattern, which can be indexed as essentially pure RuO_2 (Figure 3.6e) notwithstanding it was recorded from a large fragment containing both ruthenium and antimony. The material closely neighboring RuO_2 nanocrystals exhibited larger lattice fringes of *ca* 4-5 Å (Figure 3.6d), which cannot be ascribed to ruthenium oxide and therefore are attributed to antimony oxides. STEM-EDS mapping of this area confirmed the partial segregation of ruthenium and antimony at the nanoscale (Figure 3.6f), although we note that the two elements were still found to be mixed very finely, even when analyzed at up to 1.3M× magnification (Figures 3.6f and 3.S28).

Other antimony rich areas were devoid of clear lattice fringes (Figure 3.6c-d), and although this does not definitely rule out crystallinity, it tends to support a hypothesis that Sb oxides in $[Ru+Sb]O_y$ exhibit a very high level of disorder and perhaps are majorly amorphous rather than nanocrystalline. We also note that the Sb phase appears to coat the edges and interstices of the RuO_2 nanocrystals in the catalysts after the OER test (Figure 3.6f), suggesting that antimony has been lost from a previously predominating antimony-based coating of ruthenium oxide particles rather than a simple aggregation of two phases. This supports the corrosion data discussed above (Figure 3.2).

Overall, the physical characterization data reveal several fundamental differences in the investigated catalysts. As-prepared $[Mn+Sb]O_y$ and $[Co+Sb]O_y$ contain a mixture of individual metal oxides, which majorly dissolve during the OER tests, with a metal antimonate oxide phase. While the latter is most likely $CoSb_2O_6$ in $[Co+Sb]O_y$, the structure of the manganese-antimony oxide in $[Mn+Sb]O_y$ exhibits clear distinctions from the published features of the antimonate phase and a significant level of disorder. At the same time, no evidence for the formation of a

ruthenium antimonate in the [Ru+Sb]O_y samples was obtained using the characterization techniques employed herein. Instead, these catalysts were found to contain highly dispersed RuO_2 crystallites embedded into and decorated with disordered antimony oxides. One might hypothesize that an interaction and intermixing between ruthenium and antimony oxides might still occur, but at the topmost surface layers of RuO_2, especially at the abundant intergrain boundaries visualized by TEM (Figure 3.6c-d), rather than in the bulk phase. To assess this possibility and further assist in establishing a plausible explanation of the improved electrocatalytic performance of [Ru+Sb]O_y, theoretical analysis of the metal-antimonate systems was undertaken.

3.2.4 Theoretical insights into the improved stability of the Co-Sb and Ru-Sb oxides

Experimental evidence on the stabilization against corrosion of the oxides of transition metals like Co, Mn, Ni and Ru, through their combination with the oxides that are thermodynamically stable under the OER conditions exists,[17,18,21,67,68] including the new results reported in the present work. However, there is a lack of the understanding behind this stabilizing effect, which we aimed to address through the theoretical analysis of two systems of interest herein – Co-Sb and Ru-Sb mixed oxides. Extending the analysis to the Mn-Sb combination could not be realized due to well-documented complex ground state magnetic structure of Mn_2O_3, which exhibits noncollinear magnetic ordering and introduces significant uncertainties to the modelling of the electronic structure.[69,70]

Assessment of the electrochemical and structural stability was undertaken through the computation of cohesive energies of the materials of interest and also differences in the

dissolution potentials (ΔE_d)[71,72] for the Ru-Sb system. Both approaches have been validated through comparisons of the theoretical predictions and experimental electrochemical stability data for a range of systems, in particular metal oxides.[73–75] For the Co-Sb combination, the simulated compositional phase diagram (Figure 3.7a) indicates a broad chemical potentials space that favors the formation of $CoSb_2O_6$ (structure shown in Figure 3.S29), as opposed to a range of individual oxides. As elaborated above, experimental data suggest that this phase dominates the investigated [Co+Sb]O_y catalyst under the OER conditions and was therefore used for further theoretical analysis. As a point of reference in the calculations, Co_3O_4 – the dominating phase of the CoO_x control samples – was considered. Cohesive energies for Co_3O_4 and $CoSb_2O_6$ were simulated as -12.8 eV and -15.4 eV per formula unit, respectively, which indicates improved overall structural and electrochemical stability[76] of the antimonate as compared to the monometallic oxide. The improvement in cohesive energies is likely to be partially associated with the higher bond energy for Sb-O (434 kJ mol^{-1}) as compared to Co-O (397 kJ mol^{-1}),[77] although one might note that this difference does not appear sufficient to explain the calculated cohesive energies. Therefore, we hypothesized if the presence of Sb in the structure might strengthen the Co-O bond through changes in the electronic structure.

The above supposition was assessed through the analysis of the atom/orbital projected partial density of states (PDOS), calculated bond lengths and Bader charges. The PDOS for Co_3O_4 demonstrates a reasonable hybridization of the oxygen p-orbitals with d-orbitals of cobalt in tetrahedral sites but not in octahedral ones; this is in contrast to $CoSb_2O_6$ where only one type of cobalt sites is present and is strongly hybridized with O 2p (Figure 3.S30a-b). It is also noted that the latter interact much stronger with Co 3d orbitals rather than with Sb 5p. Since the electro corrosion of materials is an interfacial phenomenon, the above findings were also corroborated

by the analysis of the characteristic catalyst surfaces – (110) oriented facet for $CoSb_2O_6$ and (110)-A terminated surface for Co_3O_4[78–80] (Figure 3.S29c-d). Comparisons of the PDOS of bulk and (110) surfaces suggest that the slab geometry produces surface states just above the valence band due to the undercoordinated Co^{3+}, Co^{2+} and O^{2-} ions, which renders these surfaces metallic. Similar to the bulk, 2p orbitals of the surface oxygen in $CoSb_2O_6$ interact stronger with Co 3d as compared to Sb 5p orbitals. Enhanced O-p – Co-d orbital interaction in $CoSb_2O_6$ is additionally verified by the calculated PDOS of sub d-orbitals of Co^{2+} in Co_3O_4 and $CoSb_2O_6$ (Figure 3.S31).

The features of the PDOS discussed above can be expected to make the overall cohesive energy of $CoSb_2O_6$ more negative than that of Co_3O_4 and hence enhance the driving force required for the electro corrosion of cobalt. Furthermore, the simulated Co-O and Sb-O bond lengths in $CoSb_2O_6$ were lower and higher than the corresponding expected values based on the combined ionic radii, respectively (2.08 Å calculated *vs.* 2.105 Å expected for high spin Co-O; 2.02 Å calculated *vs.* 1.98 Å expected for Sb-O). This internal compressive strain of the Co-O bonds can be associated with the higher electronegativity of antimony as compared to cobalt. Additionally, calculated Bader charges on Co^{2+} in Co_3O_4 and $CoSb_2O_6$ were +1.31*e* and +1.36*e*, respectively, which further supports the stronger Co-O bond in the antimonate as compared to the individual metal oxide.

Next, the ruthenium-antimony system was analyzed following a similar approach. As discussed above, unambiguous identification of the structure of the investigated $[Ru+Sb]O_y$ was significantly more challenging than for the Co-Sb oxides, and in fact no robust experimental evidence for the formation of a stabile ruthenium-antimony oxide phase was obtained. In line with the experimental observations (Figures 3.4d, 3.5c and 3.S25, Table 3.S5), total energies

calculated by DFT simulations indicated that hypothesized $RuSb_2O_6$ phase is unstable with respect to the individual oxides RuO_2, Sb_2O_3, Sb_2O_5, SbO_2 (Table 3.S6). This prompted us to undertake a simulation of a grand potential phase diagram of the Ru-Sb system (Figure 3.7b), which enables prediction of the most thermodynamically stable compositions that can be formed under relevant synthesis conditions,[81] *i.e.* at T = 600°C and 0.2 atm O_2 partial pressure in the present work. Oxygen grand potentials were calculated for various $[Ru_n+Sb_m]O_y$ structures and compositions as a function of the metal atomic fraction, $x_{Ru} = n/(n + m)$.

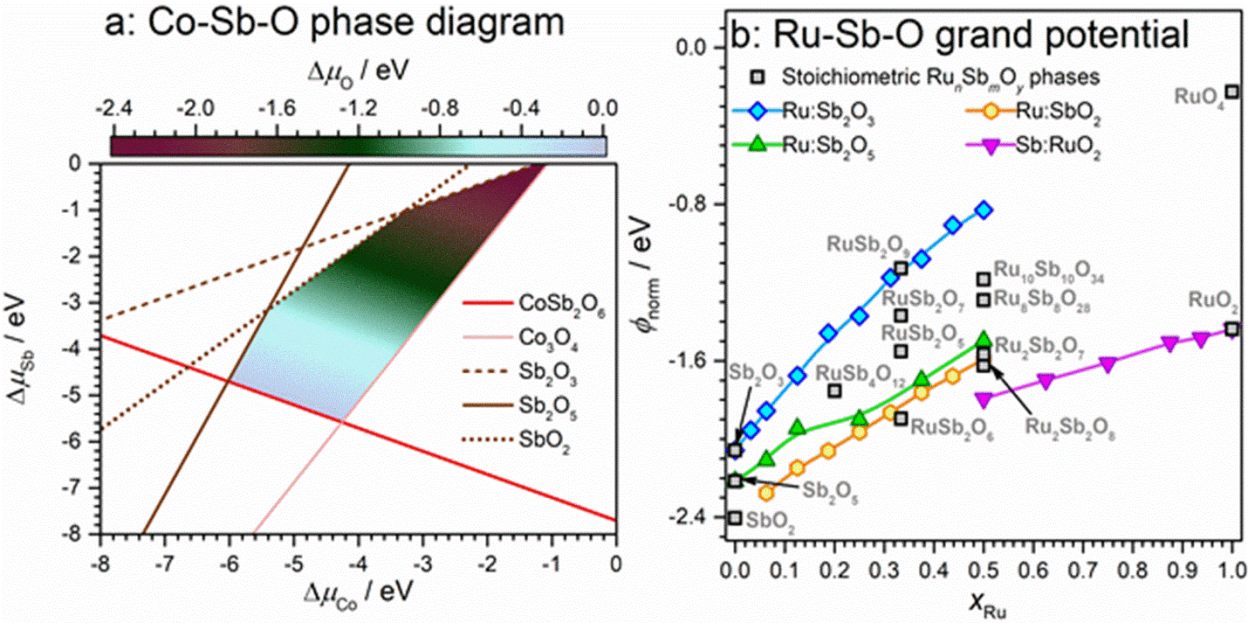

Figure 3.7. (a) Simulated compositional phase diagram of $CoSb_2O_6$ against individual oxides. Shaded area corresponds to the stable region of $CoSb_2O_6$, where the color scale shows the allowed chemical potentials for oxygen; colored lines and the corresponding spaces opposite to the shaded region present the stable regions of the identified individual oxides. (b) Normalized oxygen grand potential (ϕ_{norm}) *vs*. ruthenium atomic fraction, $x_{Ru} = n/(n + m)$, calculated for $[Ru_n+Sb_m]O_y$ at T = 600 °C and 0.21 atm O_2 partial pressure. Sb:RuO_2 – Sb-doped RuO_2; Ru:SbO_2, Ru:Sb_2O_3 and Ru:Sb_2O_5 –

Ru-doped antimony oxides. Calculated data are shown as symbols; lines are guides to an eye.

In addition to a broad range of stoichiometric compounds, substitutional doping of Sb into RuO_2 (Sb:RuO_2) and Ru in antimony oxides was considered. Among these different possibilities, the lowest ϕ_{norm} at $x_{Ru} = 0.5$, *i.e.* the highest stability under the conditions employed during the synthesis of [Ru+Sb]O_y, was calculated for the ruthenium(IV) oxide doped with antimony. In fact, Sb:RuO_2 are theoretically predicted to be more stable than the parent metal oxide within the x_{Ru} range examined (Figure 3.7b). At the same time, the experimental XAS data provide a compelling evidence for the dominant state of ruthenium in [Ru+Sb]O_y being very similar to that in RuO_2 (*vide supra*). On this basis, further analysis focused on RuO_2 at low levels of Sb doping.

Differences in the electronic properties of the RuO_2 reference and Sb:RuO_2 were investigated based on the computations with a 2×2×2 supercell of tetragonal 6-atom RuO_2 unit cell containing 16 Ru and 32 O atoms. First, through the examination of the calculated spin polarized total density of states, we note that Sb substitution into RuO_2 maintains its metallic character and even further improves the electrical conductivity as concluded from the shift of the conduction band (Figure 3.S32), which is a positive finding from the perspective of the electrocatalytic activity. Further, and most importantly, improved stability of Ru^{4+} within the Sb:RuO_2 materials was confirmed by the positive difference in the dissolution potential[46,82] ΔE_d = 0.08 V and by the negative increase in the cohesive energies when compared to undoped RuO_2. Specifically, the cohesive energy changes from -3.28 (RuO_2) to -3.51 ($Sb_{0.0625}$:$Ru_{0.9375}O_2$) and -3.62 eV per unit formula ($Ru_{0.813}Sb_{0.187}O_2$). This favorable change is again explained by the enhanced strength of the Ru-O bond, which is indicated by the stronger overlap of O 2p and Ru 3d orbitals in the

PDOS (Figure 3.S33) as well as by the higher Bader charge on ruthenium in $Sb_{0.0625}:Ru_{0.9375}O_2$ (+1.76e) as compared to RuO_2 (+1.70e). Enhanced charge donation from ruthenium to neighboring oxygen atoms is also supported by the differences in the partial density of states of Ru 4d sub-orbitals (Figure 3.S34).

In summary, the computational analysis suggests that the improvement in the stability of Ru and Co oxides upon combination with antimony oxide is majorly stemming from the electronic effects of Sb that strengthen the metal-oxygen bonds. Aggregating the experimental and computational data for the Ru-Sb system suggests that, although the well-defined phase of the ruthenium antimonate is unlikely to be formed, minor doping of ruthenium(IV) oxide with antimony is possible. Taking into account the experimental XRD, XAS and TEM data that indicate the formation of only slightly distorted RuO_2 phase (Figures 3.4d, 3.5c and 3.6) and the very significant level of corrosion of antimony but not of ruthenium during the OER tests of $[Ru+Sb]O_y$ (Table 3.1 and Figure 3.2), we hypothesize that antimony doping might be majorly confined to the surface layer of the RuO_2 crystallites. The formation of this protective layer is likely to be sufficient to provide the enhanced stability of the material against the electro corrosion highlighted above (Figure 3.3) and as even more strongly emphasized through the durability tests at elevated temperature that are discussed below.

3.2.5 Longer-term operation at elevated temperature

A final set of tests was undertaken to assess the ability of the two most promising metal-antimony oxide OER catalysts investigated herein, *viz.* $[Mn+Sb]O_y$ and $[Ru+Sb]O_y$, to operate for extended periods of time and at elevated temperatures. Although the FTO substrate is

unstable at 60 °C and low pH at positive potentials,[15] a dense coating of its surface with antimony-based catalysts was found to provide a sufficiently stable protective layer. However, we note that special care should be taken to ensure complete coverage of the whole FTO area exposed to the electrolyte solution with a catalyst layer and a protective adhesive tape (see Figure 3.S35 exemplifying an experiment where the protection was not properly provided). Voltammetric analysis confirmed the expected positive effect of increasing the operating temperature on the kinetics of the OER catalyzed by both manganese- and ruthenium-based materials (Figure 3.8a-b). The apparent activation energy of the OER at an *IR*-corrected overpotential of 0.6 V approximated from the backward potentiodynamic scans for $[Mn+Sb]O_y$ is *ca* 20 ± 10 kJ mol^{-1} (Figure 3.S36). This is notably lower than values reported for other OER catalysts operating at low pH,[83,84] and probably reflects the increasing instability of this material at elevated temperatures as discussed below.

While no significant deterioration of the $[Mn+Sb]O_y$ performance was observed in the voltammetric regime (Figure 3.S37a), short-term 24 h galvanostatic tests revealed that this catalyst suffers detectable losses in activity when operated at 60 °C (Figure 3.S37b-c). During these experiments, the overpotential required to maintain the OER rate of 10 mA cm^{-2} increased almost linearly, meaning an exponential decrease in the activity of the catalyst, at an average rate of *ca* 0.001-0.002 V h^{-1}. When longer-term testing was undertaken at 80 °C, degradation at essentially the same rate was observed over the initial *ca* 100 h of measurements (Figure 3.8b). Afterwards, an abrupt loss of the performance, reflected by an increase of the potential to *ca* 2.1 V *vs.* RHE occurred, which was then maintained for at least another 24 h. The latter observation suggests that the change in the OER activity observed in these experiments is unlikely to be associated with the degradation of the FTO support, which would result in a complete loss of any

ability of the electrode to sustain water electrooxidation due to the disruption of the electrical contact. On the basis of the data obtained herein (Figures 3.3b and 3.8b; Figure 3.S37b) and reported previously,[17] we conclude that manganese antimonate is a promising non-noble-metal-based water oxidation catalyst capable of a reasonably stable operation in acidic electrolyte solutions, but it is unlikely to be suitable for applications at 60 °C and higher temperatures.

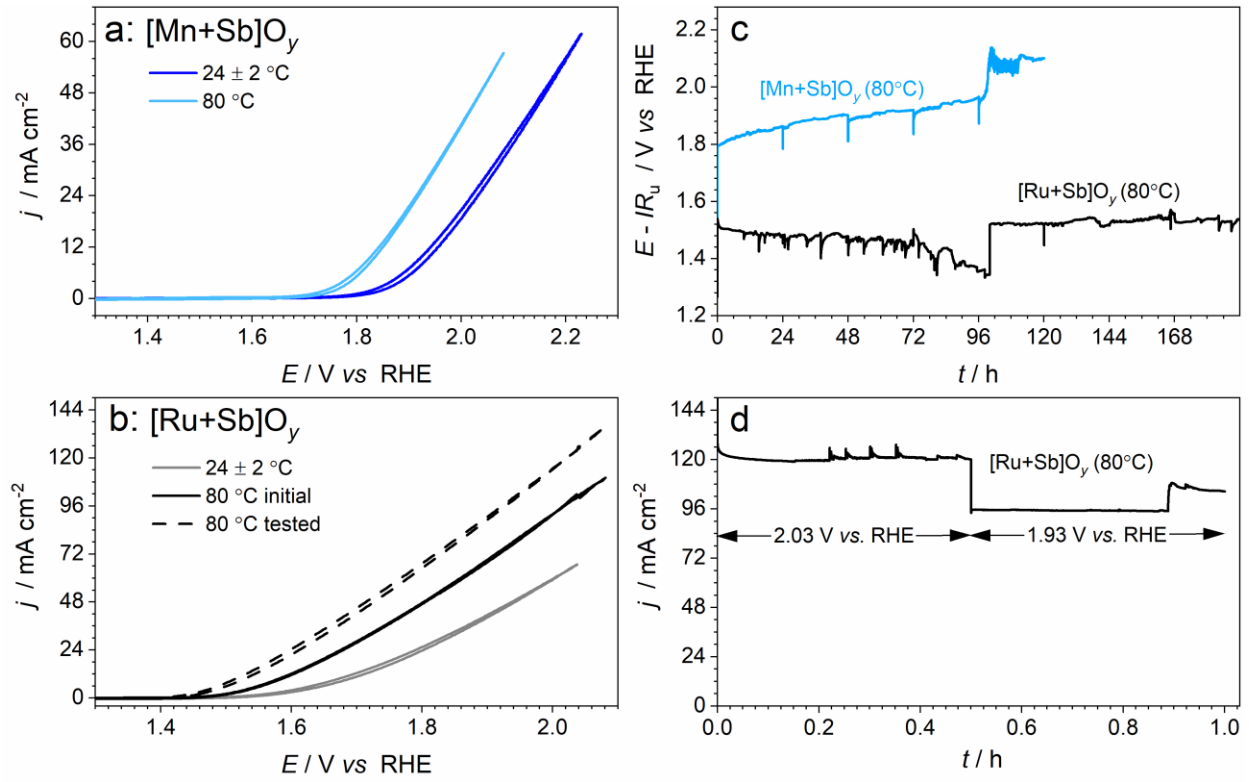

Figure 3.8. Effect of temperature on the catalytic activity and long-term stability of FTO-supported (a, b) [Mn+Sb]O_y and (b-d) [Ru+Sb]O_y in stirred 0.5 M H_2SO_4. (a, b) Cyclic voltammetry (scan rate 0.02 V s^{-1}; data are not *IR*-corrected) at 24 ± 2 (a – *blue*; b - *grey*), and 80 °C (a – *light blue*; b - *black*); in panel (b), data recorded before and after 193 h of operation at 80 °C (see panels (c) and (d)) are shown as *solid* and *dashed* curves, respectively. (c) *IR*-corrected chronopotentiograms (current density of 10 mA $cm^{-2}_{geom.}$) for [Mn+Sb]O_y (*light blue*) and [Ru+Sb]O_y (*black*) at 80 °C. (d) Chronoamperogram recorded at 2.03 (0.5 h) and 1.93 V *vs.* RHE (0.5 h) for [Ru+Sb]O_y after test in panel (c).

The behavior of [Ru+Sb]O_y at 80 °C was remarkably different to that of the manganese-antimony oxide (Figures 3.8c and 3.S38). First, the ruthenium-based catalyst demonstrated a robust operation for 192 h of chronopotentiometry at 10 mA cm^{-2} and additional 1 h of chronoamperometry at 2.03 and 1.93 V *vs.* RHE (Figure 3.8c-d). Apart from the self-healing Co-Fe-Pb system,[15] we are not aware of any other recently reported OER electrocatalyst capable of similarly stable operation under such comparably harsh conditions. Second, comparisons of the cyclic voltammetric data recorded before and after long-term tests reveal a notable improvement in the performance of the catalyst. This positive change was also observed in short-term ambient temperature tests (Figure 3.3b) and is likely to be associated with a significant increase of the amount of ruthenium on the surface due to the loss of the catalytically inactive SbO_x (Table 3.1). The stabilized catalytic activity for the OER of an essentially flat [Ru+SbO_y] electrode at 80 °C and pH 0.3 corresponds to the reaction rate of 10 mA $cm^{-2}_{geom.}$ at an *IR*-corrected overpotential of 0.31-0.33 V (1.51-1.53 V *vs.* RHE).

3.3 CONCLUSIONS

The combination of transition metal and antimony oxides in a pursuit of the creation of robust and active catalysts for the electrooxidation of water under acidic conditions was found to produce very different outcomes depending on the chemical nature of the metal employed. While nickel and iron did not yield efficient catalytic systems, mixing Sb with cobalt, manganese and ruthenium resulted in materials with quite distinct structural features, but all demonstrating one very significant and critically important advantage with respect to the individual metal oxides – significantly improved operational stability. The origin of this positive effect can now be

explained by the antimony-induced increase in the metal-oxygen bond strength, which substantially suppresses the electro oxidative dissolution, as revealed through the computational studies. The theoretical treatment implemented herein might be considered for future high-throughput screening studies for the identification of robust electrocatalysts for the OER.

Another set of key findings of the present work stems from the exhaustive durability tests of the materials at different temperatures. While demonstration of apparently stable operation of the oxygen evolution reaction catalysts at low pH and ambient temperature on a short timescale does not present a very significant research challenge anymore, longer term operation at elevated temperatures of practical interest is still hard to achieve. Herein, the instability of the promising manganese-antimony oxide catalysts at 60-80 °C was revealed to indicate that this system needs to be further improved if it is intended to be designed for operation in PEM water electrolysers. Contrasting this behavior, mixed ruthenium-antimony oxides were found to exhibit high stability in operation at 80 °C for at least one week, accompanied by very little loss of the catalytically active metal into the solution. The lack of any recent reports on a similar performance during the electrooxidation of acidic water under comparably harsh conditions allows us to consider this result as outstanding and highly promising in the context of the development of the anode catalysts for PEM water electrolyzers.

Finally, the aggregate of results presented herein suggests that there might be two different mechanisms for stabilizing electrocatalytically active species like cobalt, manganese, or ruthenium oxides *via* the combination with an acid-stable "matrix" during water oxidation. The first is the formation of metal-matrix compounds either through doping[15] or *via* transformation into new phases like antimonates. The second, less obvious and highlighted in detail herein for

the ruthenium-antimony oxide system, is based on the intimate mixing of the discrete phases at the nanoscale. This mechanism might form a basis for a new promising strategy towards the design of electrocatalytic systems that exhibit outstanding stability while maintaining the high activity of the individual metal oxide.

3.4 SUPPLEMENTARY INFORMATION

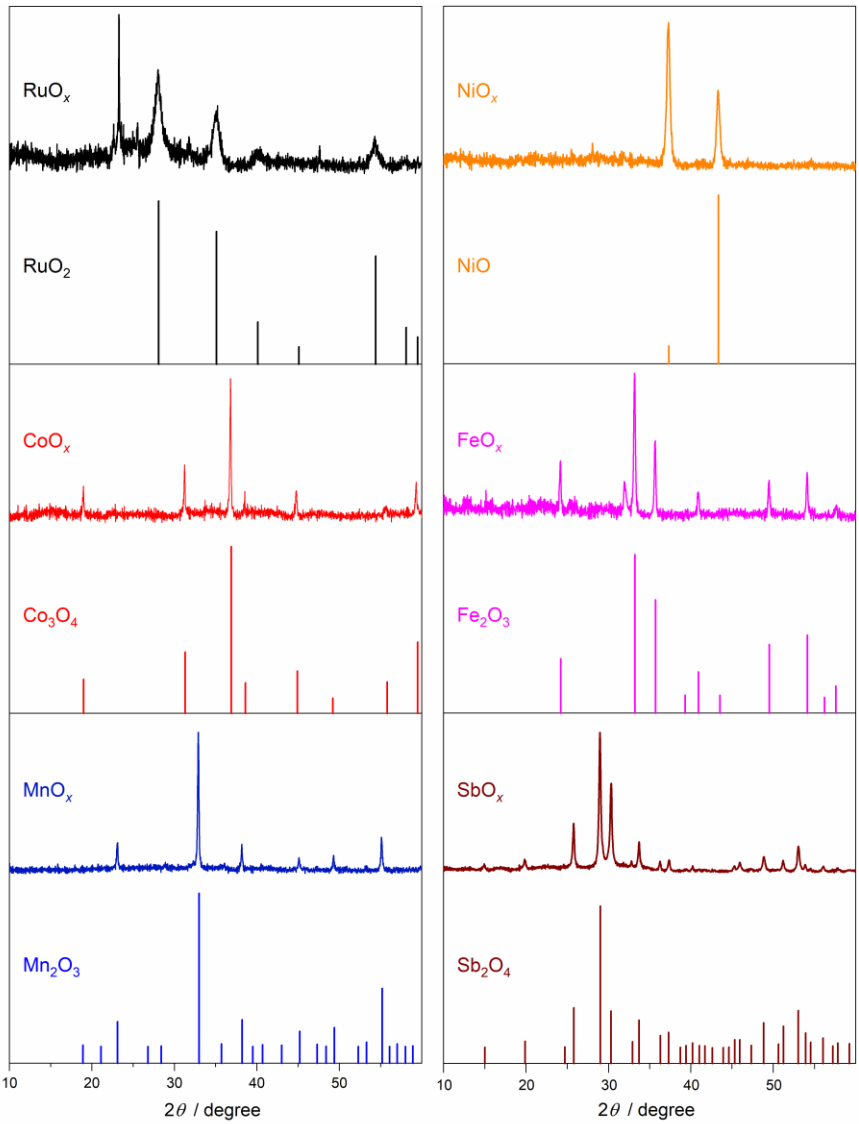

Figure 3.S1. X-ray diffractograms for individual oxides investigated herein along with the tabulated positions and intensities of reflections for RuO_2 (ICSD – 84619), Co_3O_4 (ICSD – 36256), Mn_2O_3 (ICSD – 9090), NiO (ICSD – 28910), Fe_2O_3 (ICSD – 40142), and Sb_2O_4 (ICSD – 153154). Mean crystallite sizes calculated using the Scherrer equation were *ca* 18 nm for RuO_2, *ca* 48 nm for Co_3O_4, *ca* 45 nm for Mn_2O_3, *ca* 16 nm for NiO, *ca* 34 nm for Fe_2O_3, and *ca* 30 nm for Sb_2O_4.

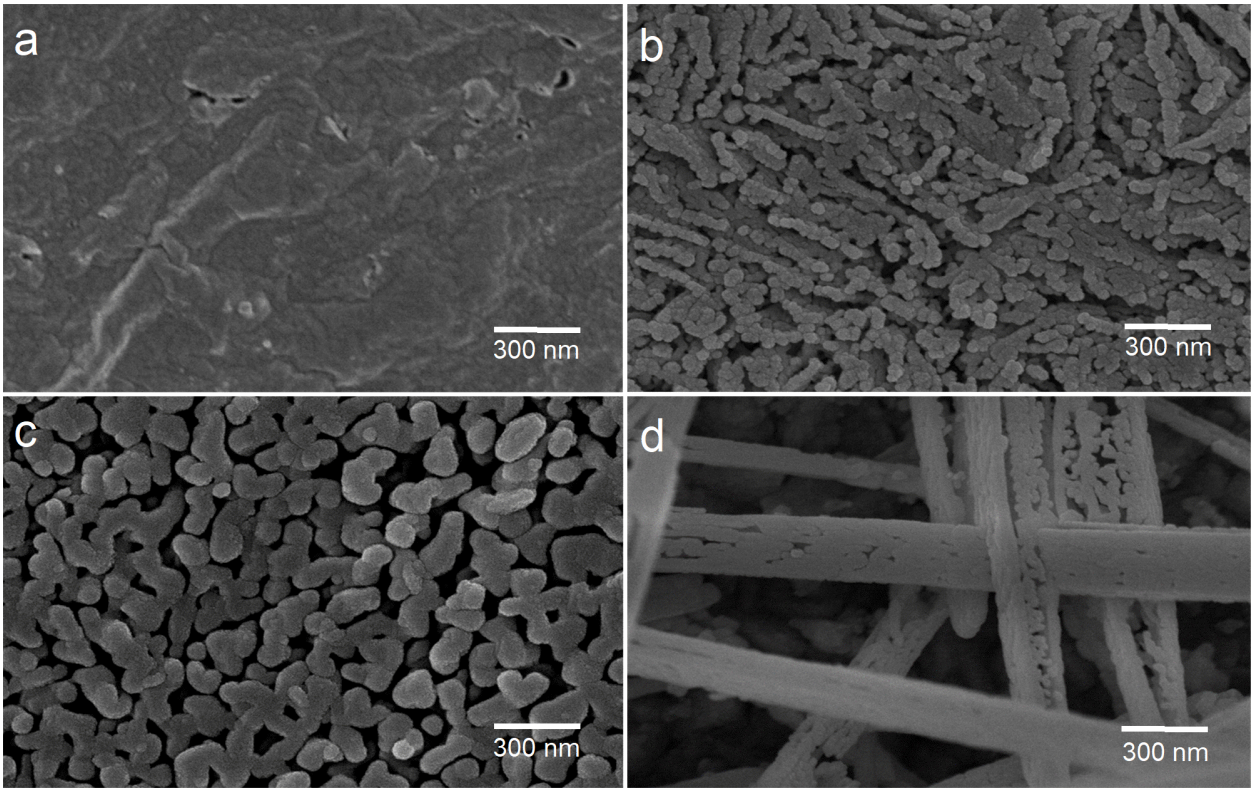

Figure 3.S2. Scanning electron micrographs of (a) RuO_x, (b) CoO_x, (c) MnO_x and (d) SbO_x.

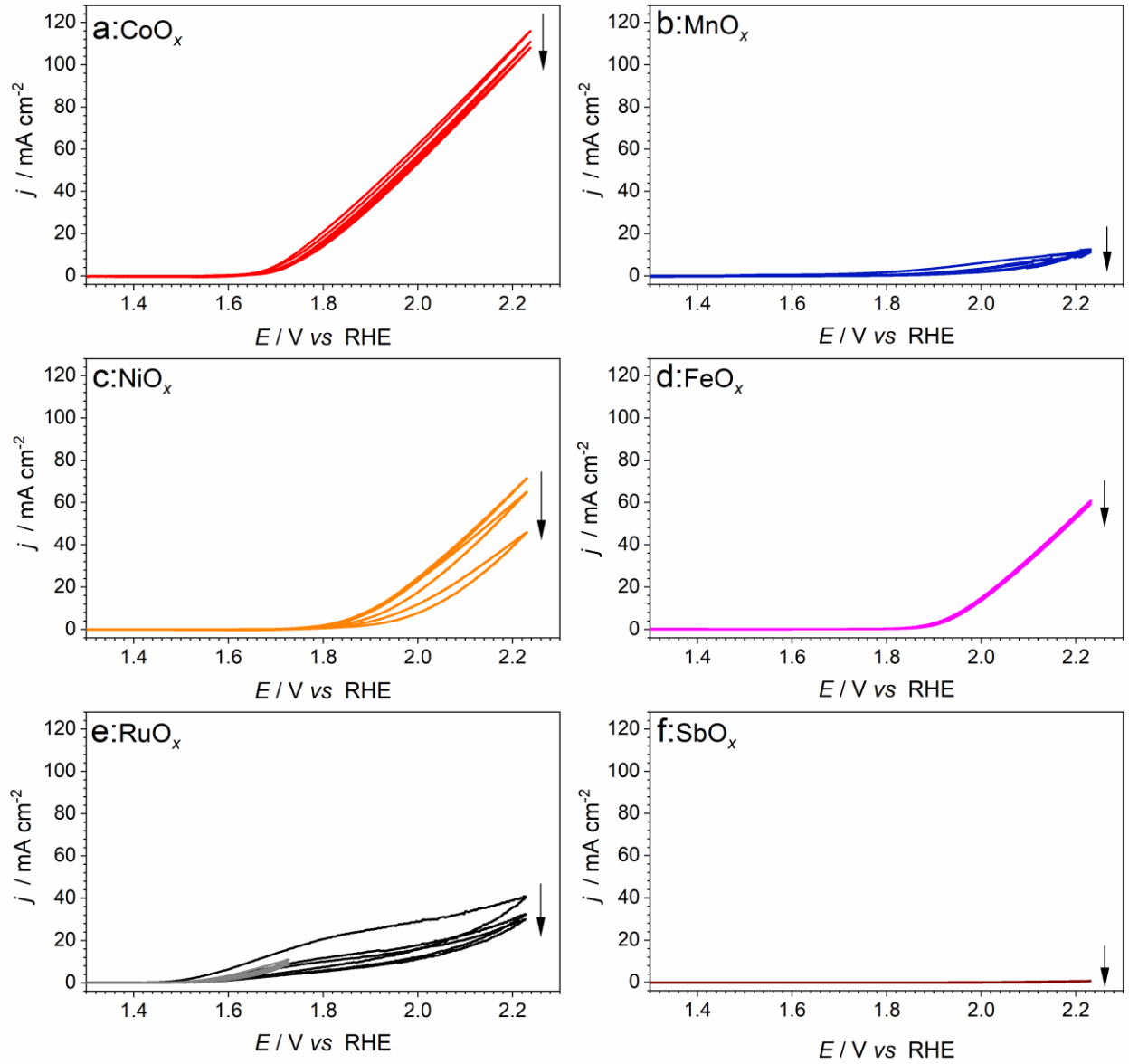

Figure 3.S3. Cyclic voltammetry (scan rate, v = 0.020 V s^{-1}) recorded at ambient temperature using 0.5 M H_2SO_4 electrolyte solution and FTO electrodes modified with as-prepared metal oxides: (a) CoO_x, (b) MnO_x, (c) NiO_x, (d) FeO_x, (e) RuO_x, and (f) SbO_x. For RuO_x, voltammograms recorded up to 1.73 (*grey*) and 2.23 V *vs.* RHE (*black*) are shown. Currents are normalized to the geometric surface area. Arrows demonstrate the evolution of the voltammetric response with cycling.

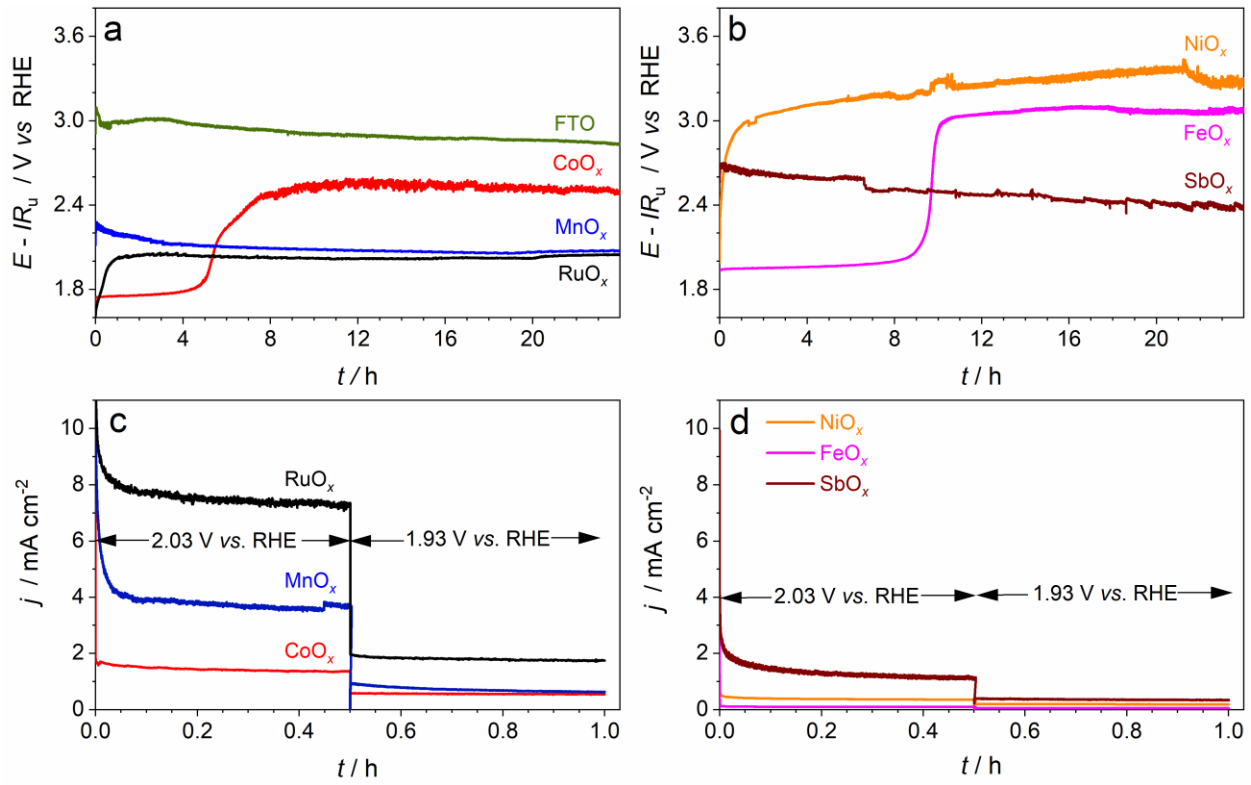

Figure 3.S4. (a-b) Chronopotentiograms at 10 mA $cm^{-2}_{geom.}$ corrected for ohmic losses, and (c-d) chronoamperograms at non-corrected potentials of 2.03 and 1.93 V *vs.* RHE recorded for FTO electrodes functionalized with RuO_x (*black*), CoO_x (*red*), MnO_x (*blue*), NiO_x (*orange*), FeO_x (*magenta*), SbO_x (*brown*) and bare FTO (*olive green*) in contact with 0.5 M H_2SO_4 at 24 ± 2 °C. Data in panels (c) and (d) were obtained immediately after measurements shown in panels (a) and (b), respectively. Currents are normalized to the geometric surface area.

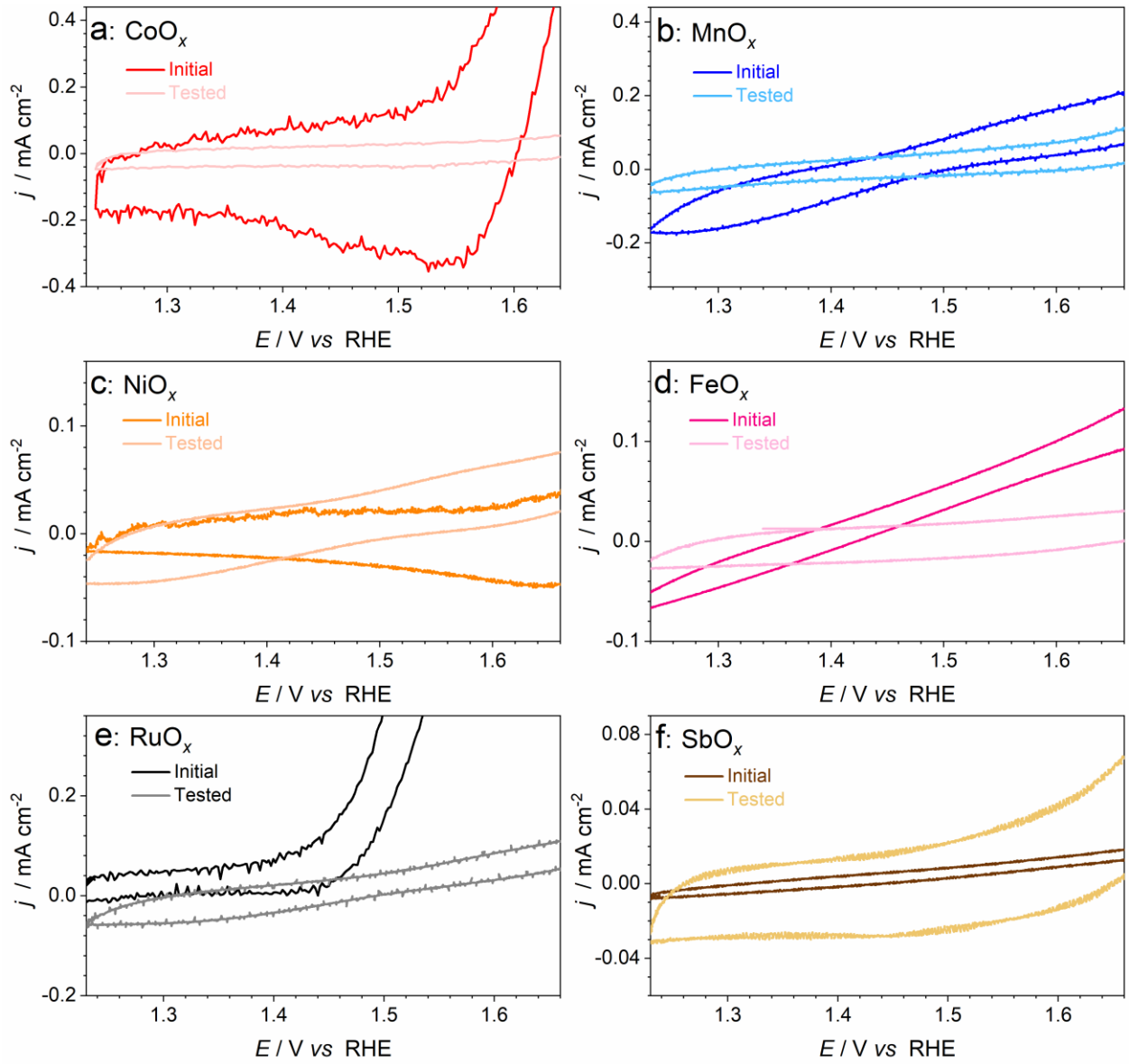

Figure 3.S5. Comparison of the pre-catalytic regions of the quasi-stabilized cyclic voltammograms (scan rate, v = 0.020 V s^{-1}) of (a) CoO_x, (b) MnO_x, (c) NiO_x, (d) FeO_x (e) RuO_x and (f) SbO_x in 0.5 M H_2SO_4 at ambient temperature before (pale traces) and after (vivid traces) 25 h durability tests (24 h at 10 mA cm^{-2}; 0.5 h at 2.03 V *vs.* RHE; 0.5 h at 1.93 V *vs.* RHE) under the same conditions. Currents are normalized to the geometric surface area of the electrode; potentials were not corrected for the iR_u-drop.

Table 3.S1. Relative loss of antimony from catalysts (at.%) during the OER in stirred 0.5 M H2SO4 as determined by ICP-OES.

Catalyst	Samples	Time of analysis	24 ± 2 °C	Time of analysis	80 °C
			Sb		Sb
[Mn+Sb]O_y	1	25	17		Not analyzed
	2	0.16	3.5		
		4	12.0		
		8	14.6		
		12	17.1		
		20	21.0		
		24	23.0		
		28	24.4		
[Co+Sb]O_y	1	25	26		
[Ru+Sb]O_y	1	25	37	193	47
	2	0.16	4.9	0.16	12.1
		4	9.4	4	34
		8	11.5	8	37.5
		12	14.0	12	38
		20	18.1	20	36.0
		24	19.7	24	36.1
		28	20.6	28	36.4

Calculation is based on the amount of Sb deposited onto electrodes (1 μmol cm^{-2} each) and the amounts measured in solutions after the OER tests.

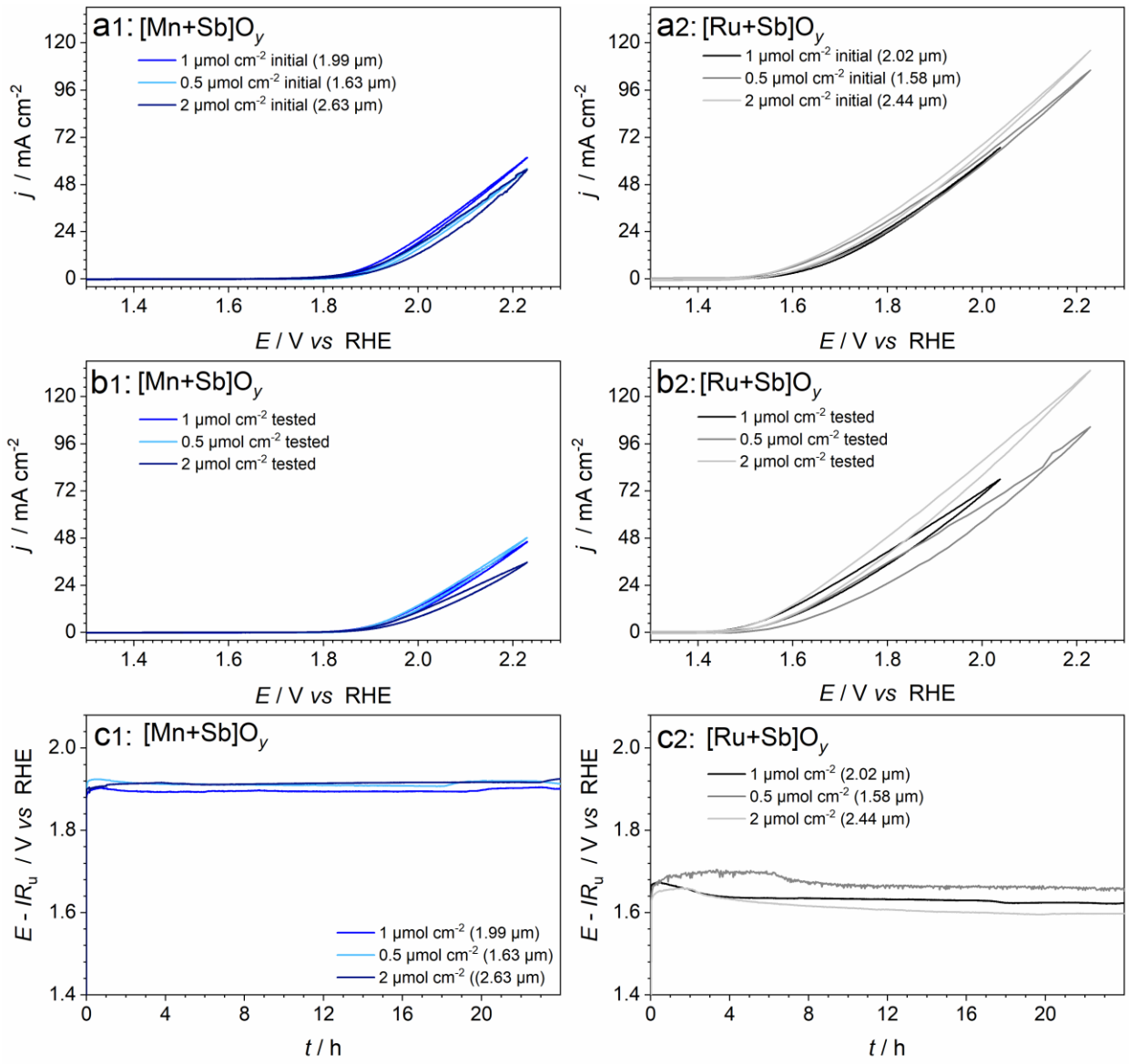

Figure 3.S6. Electrocatalytic performance of the FTO electrodes modified with (1) [Mn+Sb]O_y and (2) [Ru+Sb]O_y at different loadings for the OER in stirred 0.5 M H_2SO_4 at 24 ± 2 °C: (a) initial and (b) final cyclic voltammetry (v = 0.020 V s^{-1}; no IR_u-correction applied); (c) IR_u-corrected chronopotentiograms (10 mA cm^{-2}) recorded between voltammetric measurements shown in panels (a) and (b). The initial amount of metals and antimony deposited (only one value is shown since the initial M : Sb ratio was 1 : 1) along with thickness of the catalyst layers (in brackets) are shown in the figure legend. Apparent increase in the final (but not initial) activity of

[Ru+Sb]O_y with loading likely reflects slight roughening of the electrode surface during operation due to the loss of antimony oxide. However, the differences between electrode with different loading are not significant and are incomparably lower than differences in the catalyst loading.

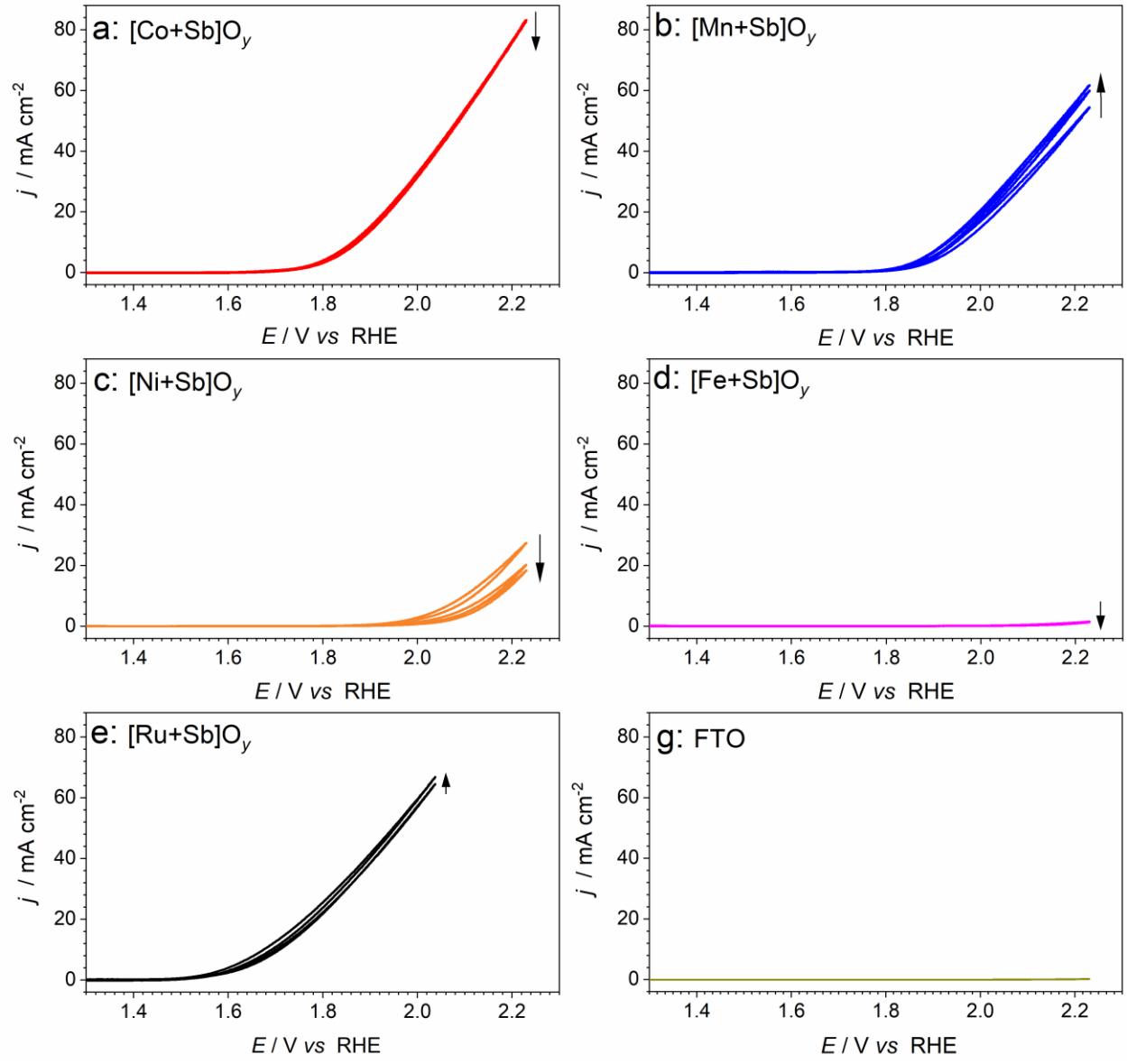

Figure 3.S7. Evolution of cyclic voltammograms (scan rate, v = 0.020 V s^{-1}; three consecutive cycles shown) of (a) [Co+Sb]O_y, (b) [Mn+Sb]O_y, (c) [Ni+Sb]O_y, (d)

[Fe+Sb]O_y, (e) [Ru+Sb]O_y and (f) bare FTO in 0.5 M H_2SO_4 at ambient temperature. Arrows show the evolution of the current density with cycling, while insets show magnified plots of the pre-catalytic regions. Currents are normalized to the geometric surface area of the electrode; potential values were not corrected for the IR_u-drop.

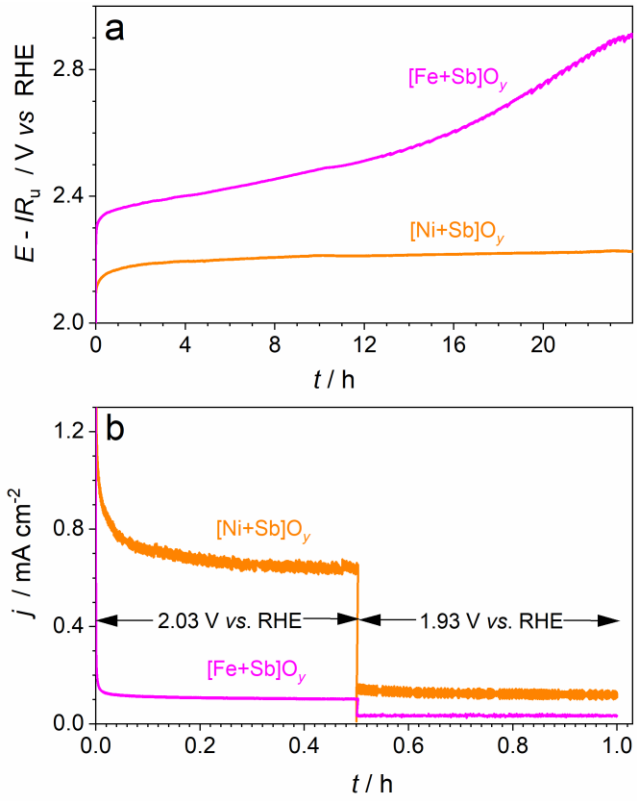

Figure 3.S8. (a) Chronopotentiograms (current density 10 mA $cm^{-2}_{geom.}$) corrected for ohmic losses, and (b) chronoamperograms at non–IR_u corrected potentials of 2.03 and 1.93 V *vs.* RHE recorded for FTO electrodes modified with [Ni+Sb]O_y (*orange*) and [Fe+Sb]O_y (*magenta*) in contact with 0.5 M H_2SO_4 at 24 ± 2 °C. Chronoamperograms were recorded immediately after galvanostatic tests shown in panel (a). Currents are normalized to the geometric surface area.

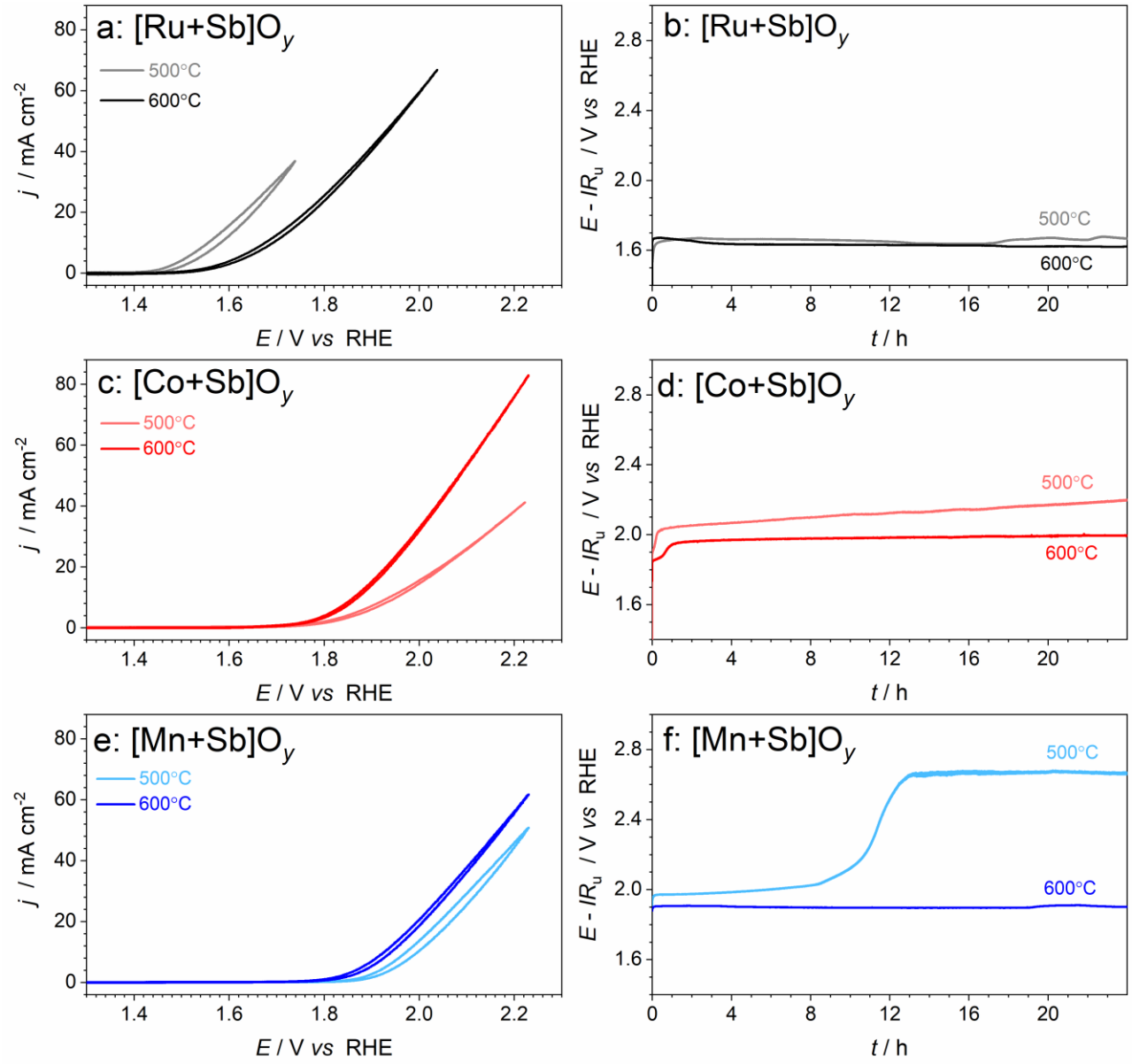

Figure 3.S9. Effect of annealing temperature (500 °C – pale traces; 600 °C – vivid traces) on the electrocatalytic activity of (a-b) [Ru+Sb]O_y, (c-d) [Co+Sb]O_y and (e-f) [Mn+Sb]O_y for the OER in 0.5 M H_2SO_4 at 24 ± 2 °C: (a, c, e) cyclic voltammetry (potentials are not corrected for ohmic losses), and (b, d, f) IR_u-corrected chronopotentiograms (current density 10 mA cm$^{-2}_{geom.}$).

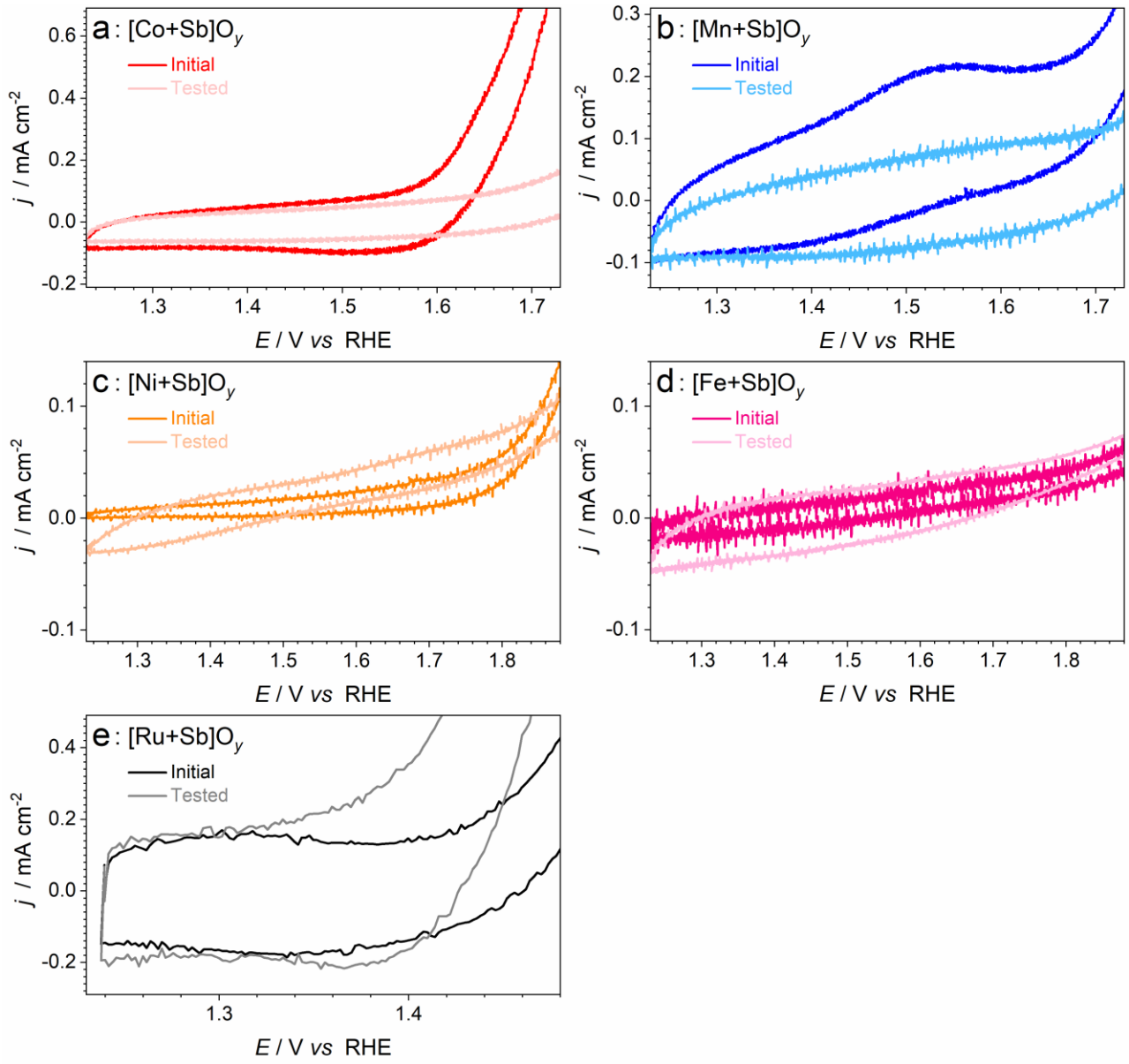

Figure 3.S10. Comparison of the pre-catalytic regions of the quasi-stabilized cyclic voltammograms (scan rate, v = 0.020 V s^{-1}) of (a) [Co+Sb]O$_y$, (b) [Mn+Sb]O$_y$, (c) [Ni+Sb]O$_y$, (d) [Fe+Sb]O$_y$ and (e) [Ru+Sb]O$_y$ in 0.5 M H_2SO_4 at ambient temperature before (pale traces) and after (vivid traces) 25 h durability tests (24 h at 10 mA cm^{-2}; 0.5 h at 2.03 V *vs.* RHE; 0.5 h at 1.93 V *vs.* RHE) under the same conditions. Currents are normalized to the geometric surface area of the electrode; potentials were not corrected for the IR_u-drop.

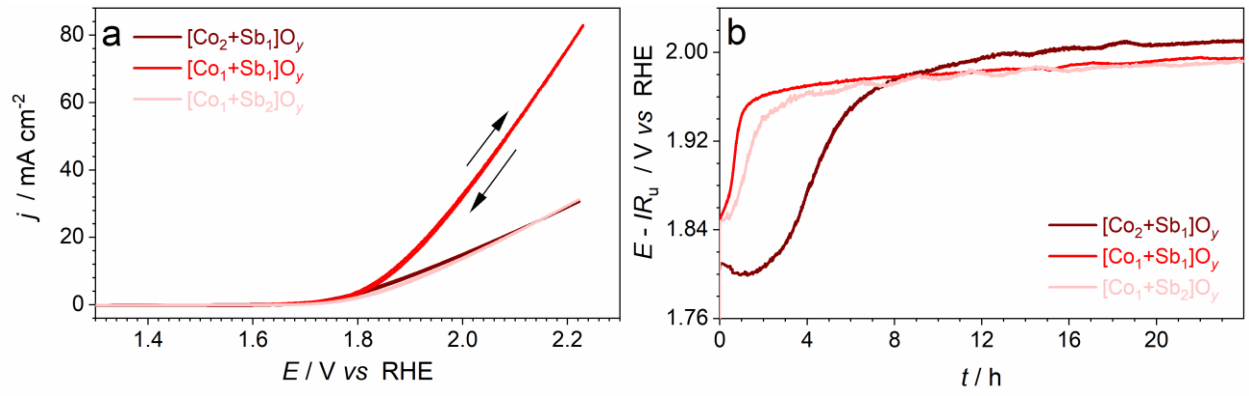

Figure 3.S11. (a) Cyclic voltammetry (potentials are not corrected for the IR_u-drop), and (b) IR_u-corrected chronopotentiograms (current density 10 mA $cm^{-2}_{geom.}$) for FTO electrodes modified with cobalt-antimony oxides synthesized using different molar Co : Sb precursor ratios in contact with 0.5 M H_2SO_4 at 24 ± 2 °C. Currents are normalized to the geometric surface area. In panel (a), arrows exemplify the direction of the forward and backward sweeps.

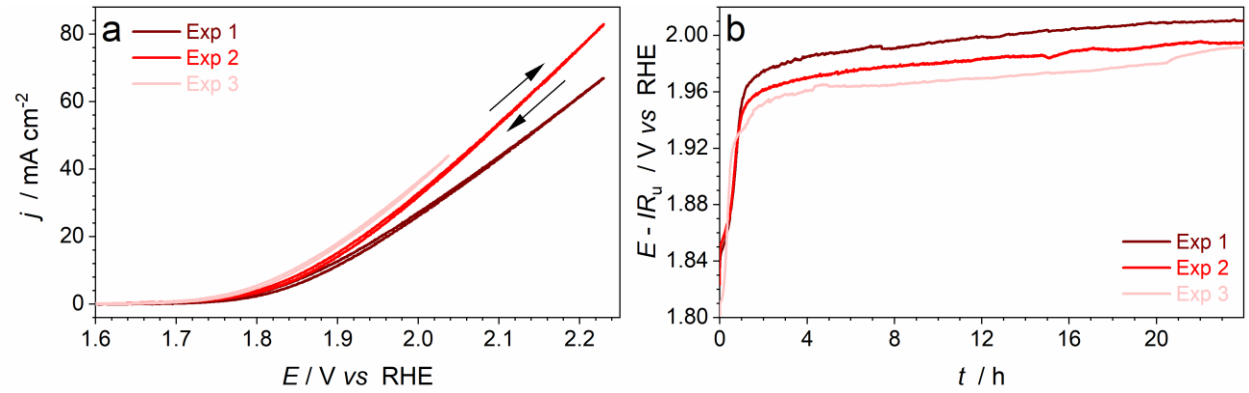

Figure 3.S12. Reproducibility of the electrocatalytic properties of [Co+Sb]O_y (molar Co : Sb precursor ratio 1 : 1) demonstrated for three independent samples tested in 0.5 M H_2SO_4 at 24 ± 2 °C: (a) cyclic voltammetry (potentials are not corrected for ohmic losses), and (b) IR_u-corrected chronopotentiograms (current density 10 mA $cm^{-2}_{geom.}$). Currents are normalized to the geometric surface area. In panel (a), arrows exemplify the direction of the forward and backward sweeps.

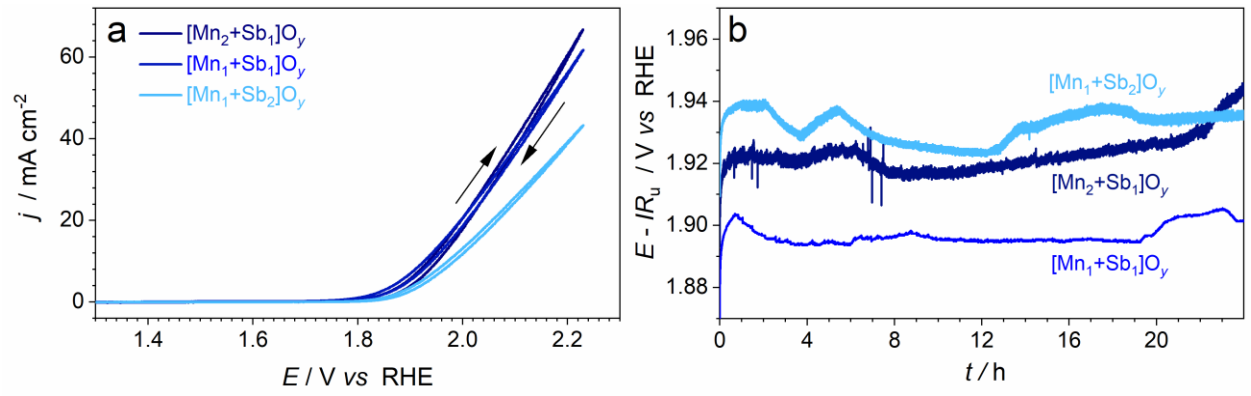

Figure 3.S13. (a) Cyclic voltammetry (potentials are not corrected for the IR_u-drop), and (b) IR_u-corrected chronopotentiograms (current density 10 mA $cm^{-2}_{geom.}$) for FTO electrodes modified with manganese antimony oxides synthesized using different molar Mn:Sb precursor ratios in contact with 0.5 M H_2SO_4 at 24 ± 2 °C. Currents are normalized to the geometric surface area. In panel (a), arrows exemplify the direction of the forward and backward sweeps.

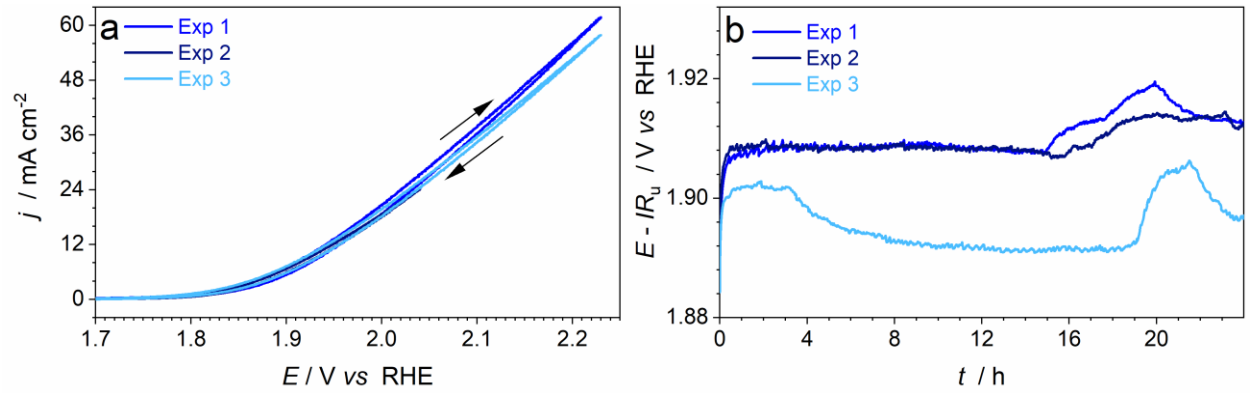

Figure 3.S14. Reproducibility of the electrocatalytic properties of [Mn+Sb]O_y (molar Mn : Sb precursor ratio 1 : 1) demonstrated for three independent samples tested in 0.5 M H_2SO_4 at 24 ± 2 °C: (a) cyclic voltammetry (potentials are not corrected for ohmic losses), and (b) IR_u-corrected chronopotentiograms (current density 10 mA $cm^{-2}_{geom.}$). Currents are normalized to the geometric surface area. In panel (a), arrows exemplify the direction of the forward and backward sweeps.

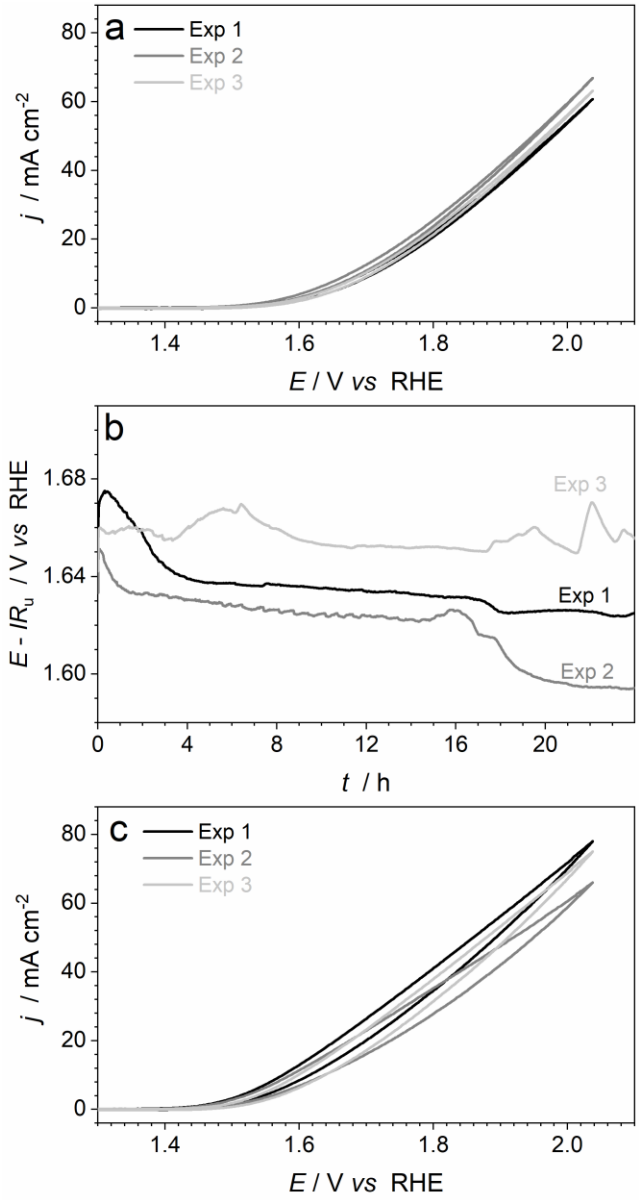

Figure 3.S15. Reproducibility of the electrocatalytic properties of [Ru+Sb]O_y demonstrated for three independent samples tested in 0.5 M H_2SO_4 at 24 ± 2 °C: (a) initial cyclic voltammetry (potentials are not corrected for ohmic losses), (b) IR_u-corrected chronopotentiograms collected at 10 mA $cm^{-2}_{geom.}$, and (c) subsequently recorded cyclic voltammetry (potentials are not IR_u-corrected).

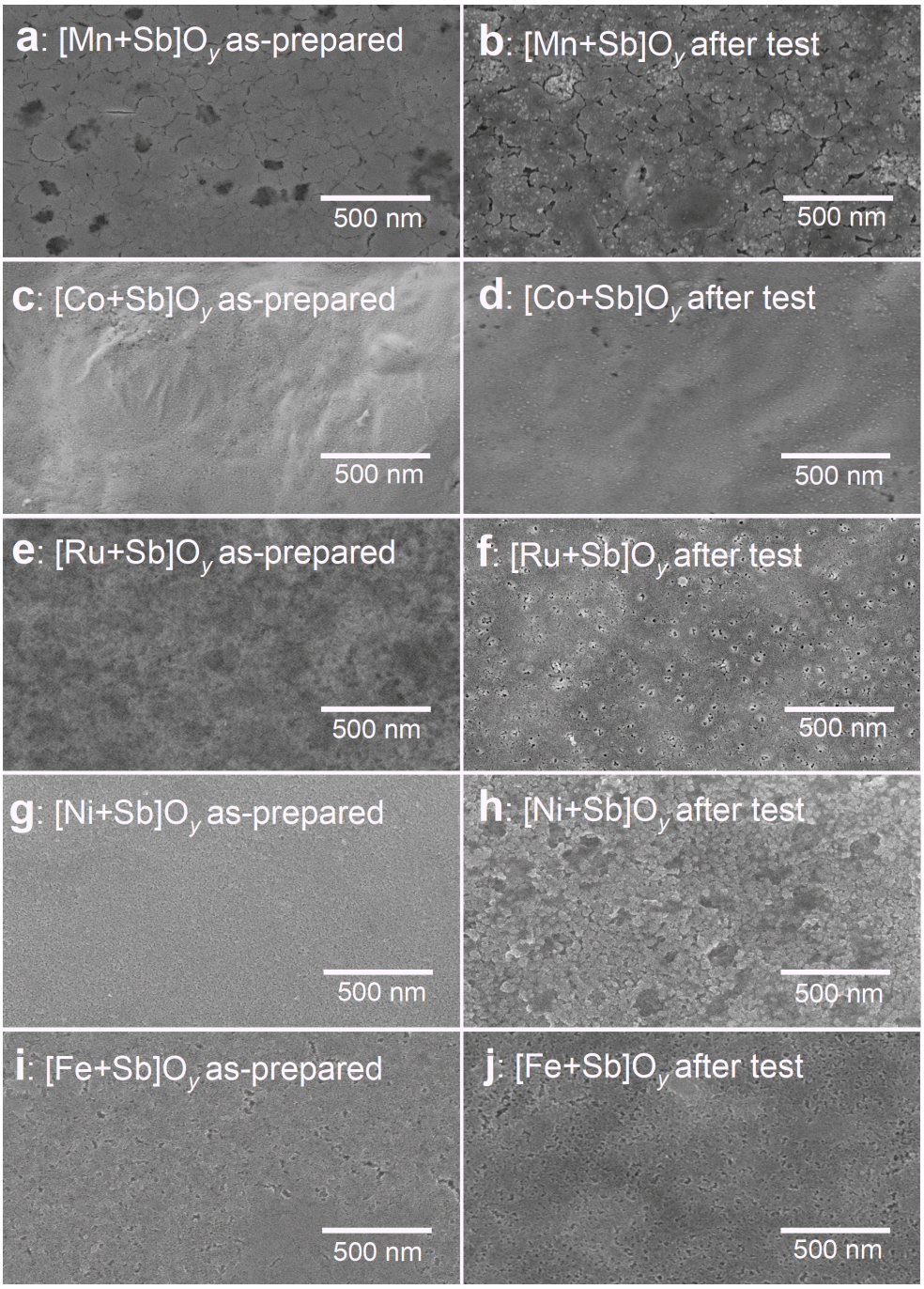

Figure 3.S16. Scanning electron micrographs of (a-b) [Mn+Sb]O_y, (c-d) [Co+Sb]O_y, (e-f) [Ru+Sb]O_y, (g, h) [Ni+Sb]O_y and (i-j) [Fe+Sb]O_y (a, c, e, g, i) before and (b, d, f, h, j) after 24 h galvanostatic (10 mA cm^{-2}) and subsequent 1 h potentiostatic (2.03 and 1.93 V *vs.* RHE for 0.5 h at each potential) operation in stirred 0.5 M H_2SO_4 at ambient temperature.

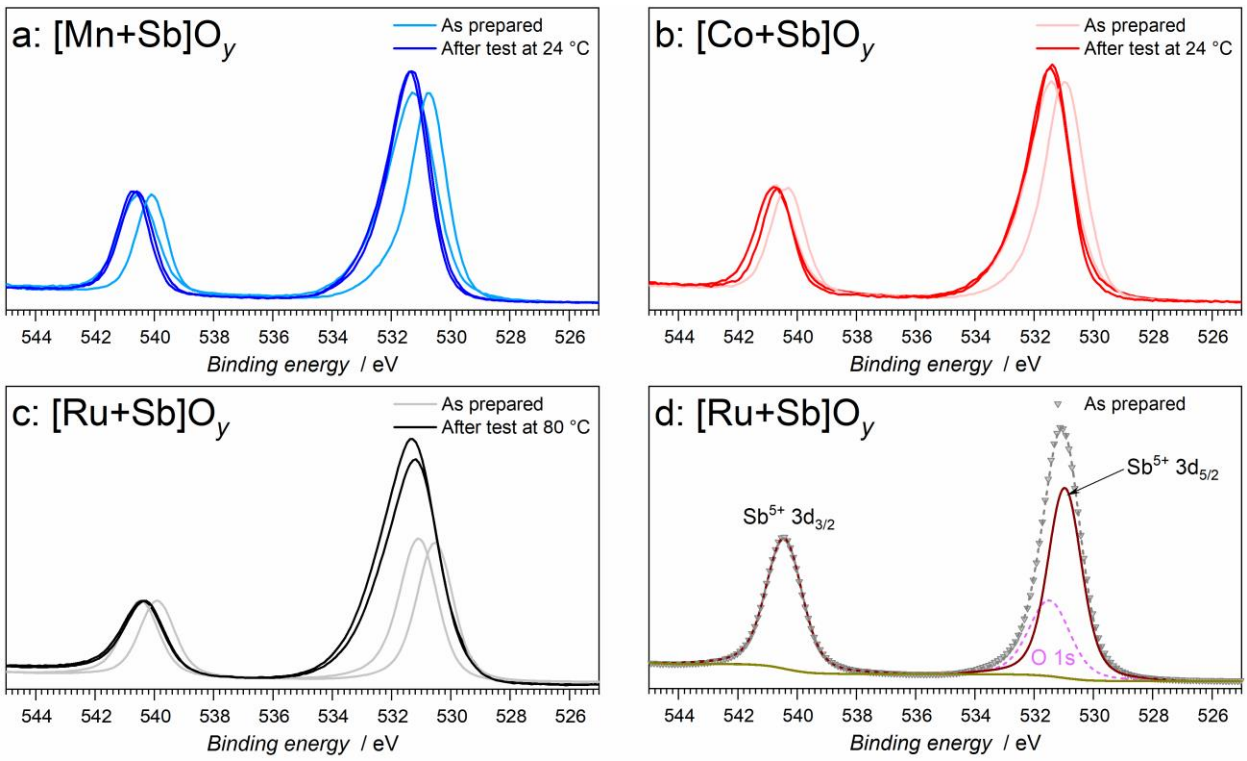

Figure 3.S17. Sb 3d + O 1s spectra for (a) [Mn+Sb]O_y, (b) [Co+Sb]O_y and (c) [Ru+Sb]O_y before (*pale traces*) and after (*vivid traces*) electrocatalytic tests in 0.5 M H_2SO_4. Panel (d) shows an example of fitting of the Sb 3d + O 1s spectrum for as-prepared [Ru+Sb]O_y (*triangles*) exhibiting the Sb^{5+} (*brown*) and O 1s (*light magenta*) signals; background is shown as *dark yellow*, while cumulative fitting curve is *dashed grey*. [Mn+Sb]O_y and [Co+Sb]O_y were tested subsequently for 24 h at 10 mA cm^{-2}, 0.5 h at 2.03 V *vs.* RHE, and 0.5 h at 1.93 V *vs.* RHE at ambient temperature; [Ru+Sb]O_y was tested for 10 h at 10 mA cm^{-2} at 80 °C. Two curves of each color in panels (a-c) exemplify the reproducibility of the spectral patterns.

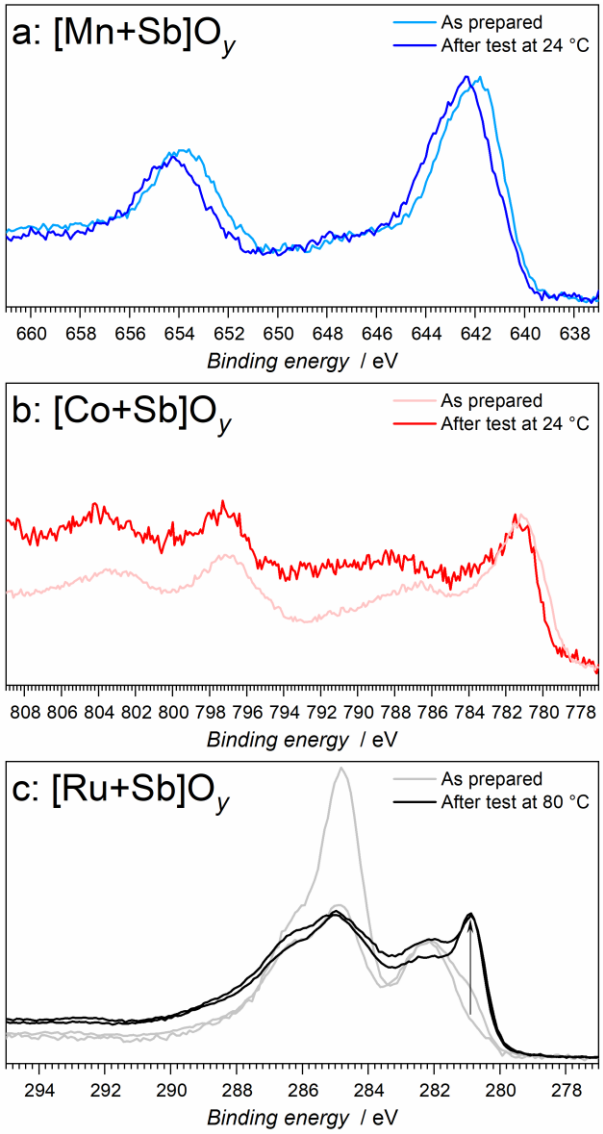

Figure 3.S18. (a) Mn 2p spectra for [Mn+Sb]O_y, (b) Co 2p spectra for [Co+Sb]O_y and (c) Ru 3d + C 1s spectra for [Ru+Sb]O_y before (*pale traces*) and after (*vivid traces*) electrocatalytic tests in 0.5 M H_2SO_4. [Mn+Sb]O_y and [Co+Sb]O_y were tested for 24 h at 10 mA cm^{-2} and then for 1 h at 2.03 and 1.93 V *vs.* RHE at ambient temperature; [Ru+Sb]O_y was tested for 12 h at 10 mA cm^{-2} at 80 °C. In panel (b), two curves of each colour exemplify the reproducibility of the spectral patterns, while arrow highlights the evolution of the Ru $3d_{5/2}$ signal ascribed to Ru^{4+}.

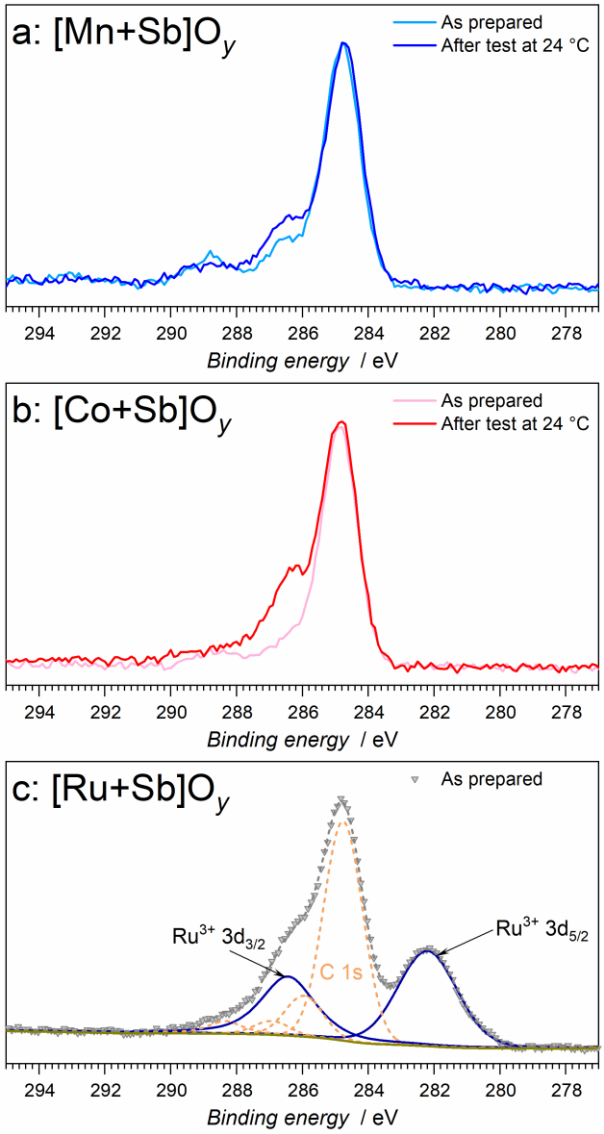

Figure 3.S19. C 1a spectra for (a) [Mn+Sb]O_y, and (b) [Co+Sb]O_y before (pale traces) and after (vivid traces) electrocatalytic tests in 0.5 M H_2SO_4 (24 h at 10 mA cm^{-2}, 0.5 h at 2.03 V *vs.* RHE, and 0.5 h at 1.93 V *vs.* RHE at ambient temperature). Panel (c) exemplifies fitting of the Ru 3d + C 1s spectrum for as-prepared Ru+SbO_y (*triangles*) exhibiting the Ru^{3+} (*dark blue*) and C 1s (*yellow*) signals; background is shown as *dark yellow*, while the cumulative fitting curve is *dashed grey*.

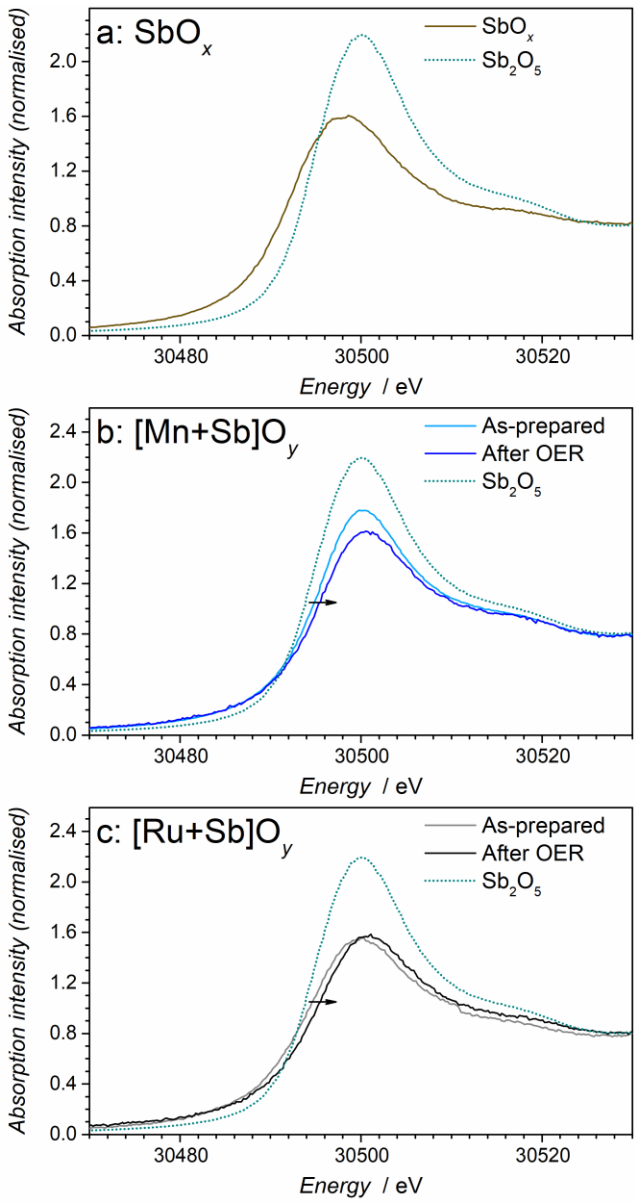

Figure 3.S20. Sb K-edge XANES data for (a) SbO_x (*brown*), (b) $[Mn+Sb]O_y$ before (*light blue*) and after (*blue*) the OER in stirred 0.5 M H_2SO_4 at 24 ± 2 °C at 10 mA cm^{-2} for 24 h and (c) $[Ru+Sb]O_y$ before (*grey*) and after (*black*) the OER in stirred 0.5 M H_2SO_4 for 10 h at 10 mA cm^{-2} at 80 °C. Reference data for Sb_2O_5 (*dotted teal*) are also shown. Arrows show slight positive energy shift induced by testing the catalysts.

Table 3.S2. Crystal structure parameters used for the EXAFS simulations to fit the experimental data for Sb_2O_5 shown in Figure 3.S21.

		Distance / Å		
Atomic Pair	**Number**	**Tabulated [b]**	**Simulation**	**Debye-Waller (s2)**
Sb-O	3	1.91	1.95	0.0000
Sb-O	3	2.10	2.10	0.0036
Sb-Sb	3	3.24	3.24	0.0049
Sb-Sb	2	3.42	3.42	0.0065

[a] Other parameters: *S02* = 1.184, *E0* = 10.73 eV, R-factor=0.02. [b] As reported in Ref.[85]

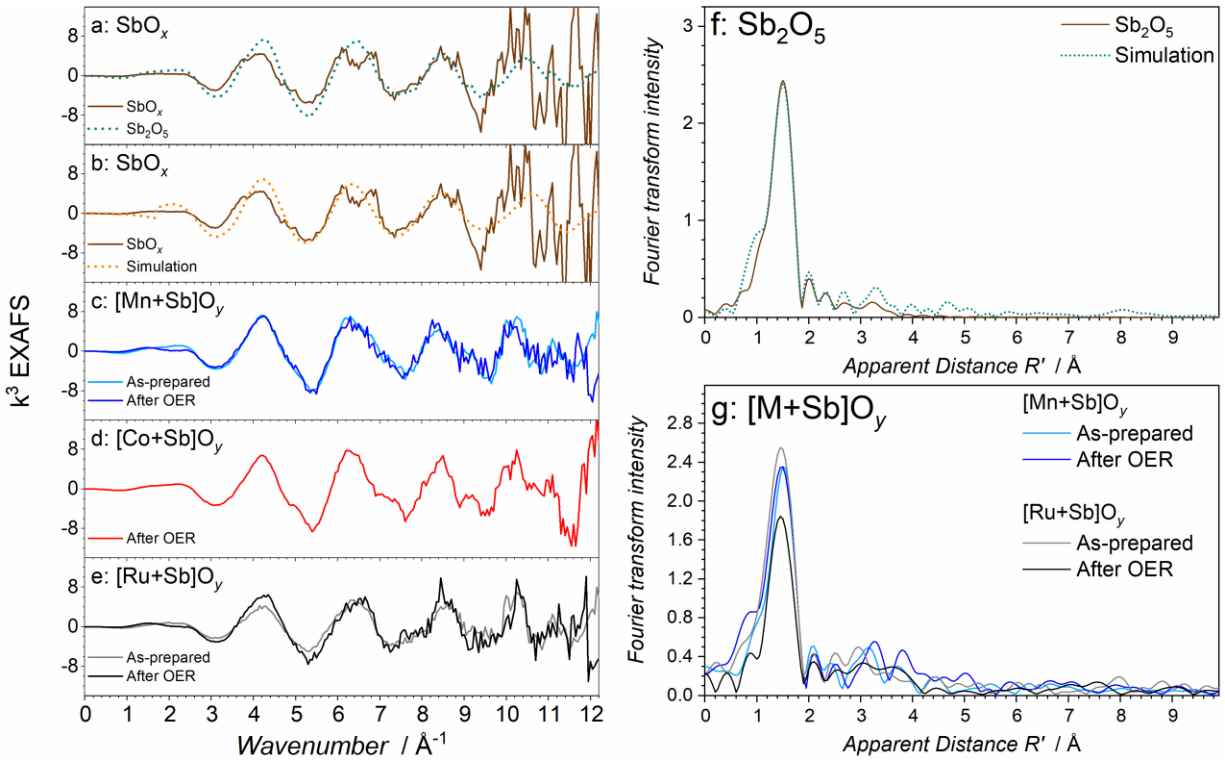

Figure 3.S21. Sb K-edge EXAFS data for (a) SbO_x (*brown*), (b) Sb_2O_5 (*teal*) (c) $[Mn+Sb]O_y$ before (*light blue*) and after (*blue*) the OER, (d) $[Co+Sb]O_y$ after the OER(*red*), and (e) $[Ru+Sb]O_y$ before (*grey*) and after (*black*) the OER. Fourier transform of the Sb K-edge EXAFS is shown for (f) Sb_2O_5 as well as for (g) $[Mn+Sb]O_y$ and $[Ru+Sb]O_y$ before (*pale traces*) and after (*vivid traces*) tests. Panel (a) additionally shows reference data for Sb_2O_5 (*dotted teal*), while panels (b) and (f) feature a simulation (*dotted orange*) based on the parameters in Table 3.S2.

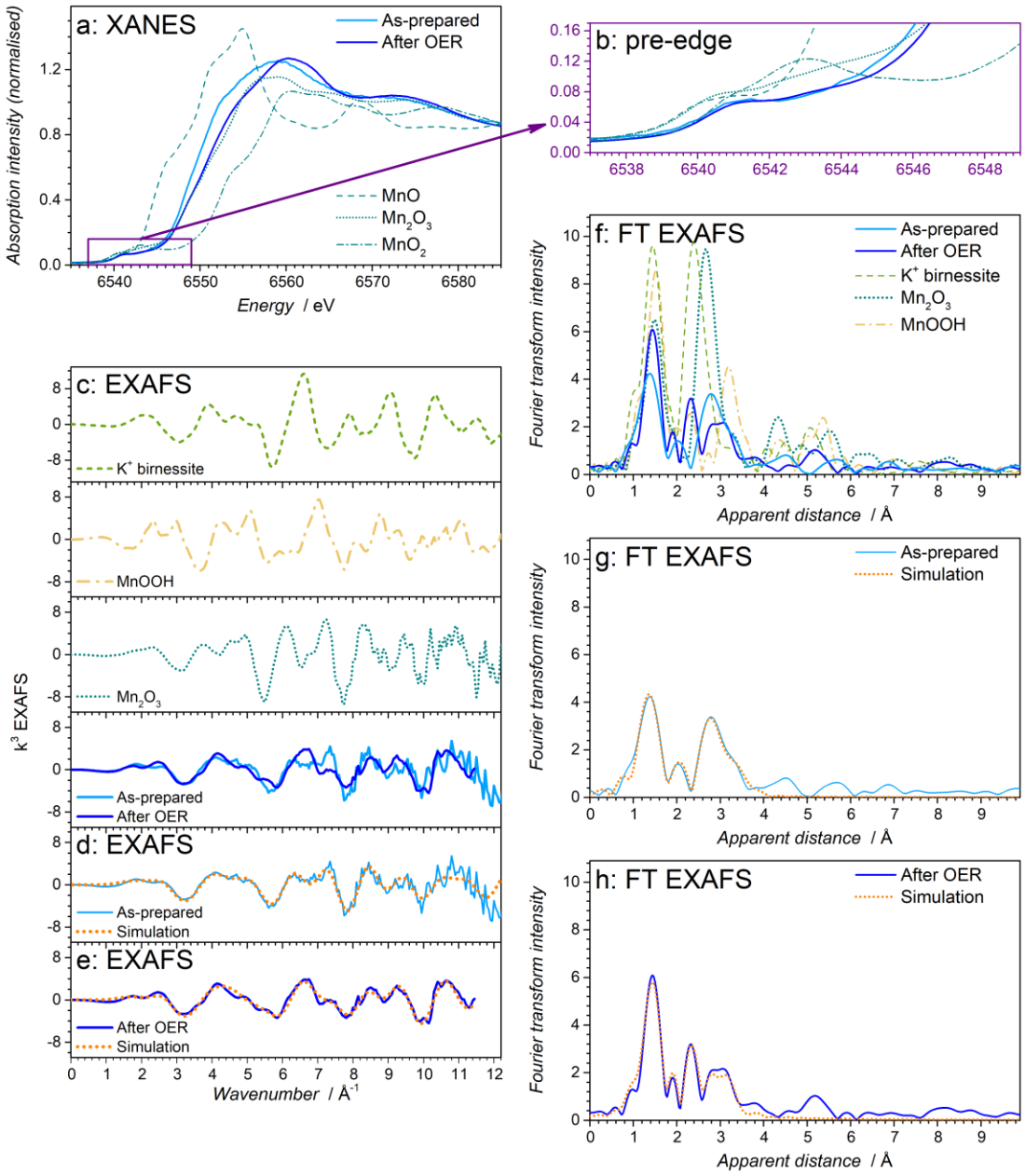

Figure 3.S22. Mn K-edge XAS data for [Mn+Sb]O_y before (light blue) and after (blue) OER test in stirred 0.5 M H_2SO_4 for 24 h at 10 mA cm-2 at 24 ± 2 °C: (a) XANES, (b) XANES pre-edge, (c-e) EXAFS, (f-h) Fourier transform of the EXAFS. Panels (a-c) and (f) show reference data for MnO, Mn_2O_3, MnO_2, MnOOH and K+-birnessite (dashed/dotted traces). Panels (d-e) and (g-h) show simulations (dotted orange) based on the parameters summarized in Table 3.S3.

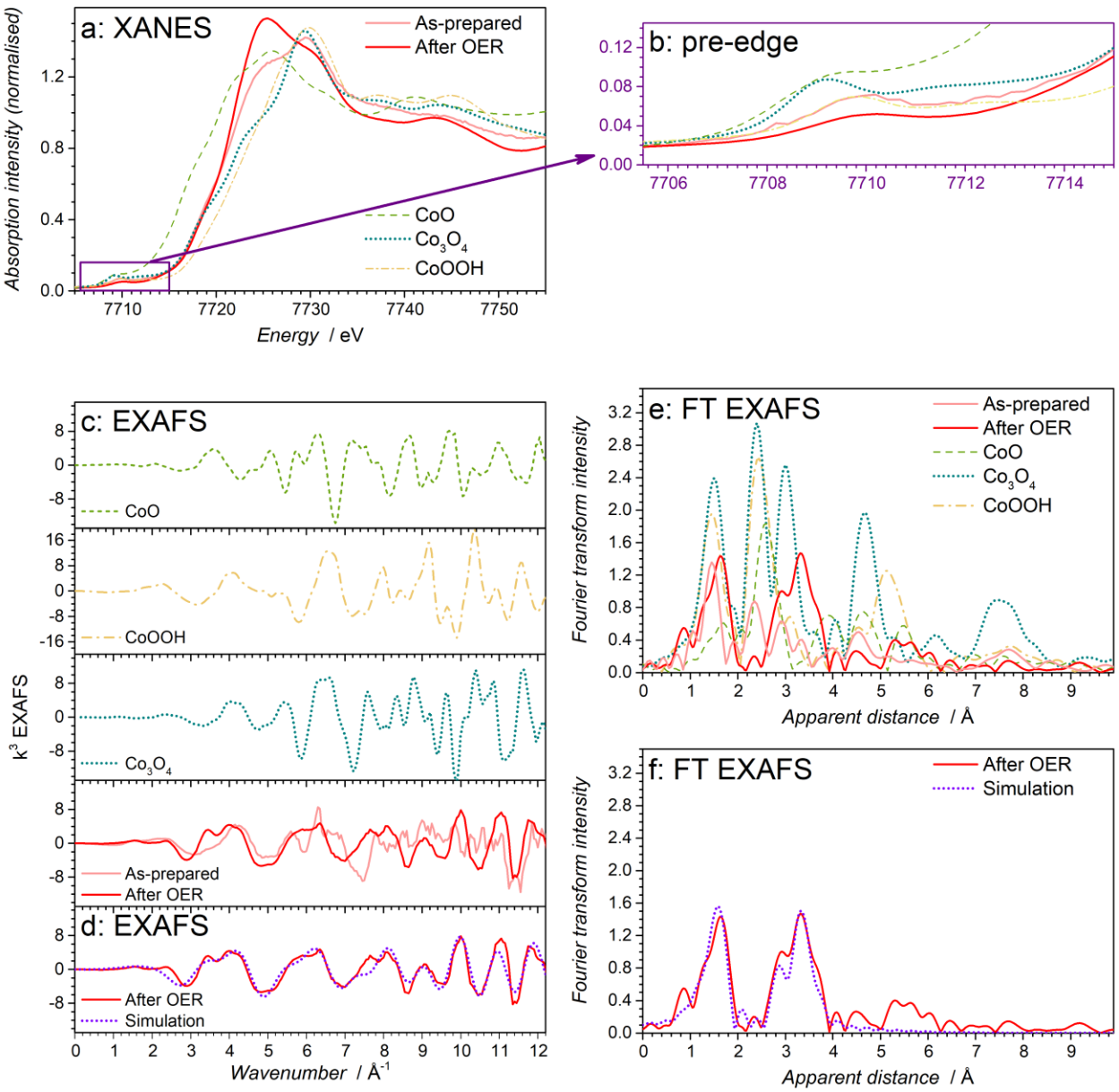

Figure 3.S23. Co K-edge XAS data for [Co+Sb]O_y before (*pink*) and after (*red*) OER test in stirred 0.5 M H_2SO_4 for 24 h at 10 mA cm^{-2} at 24 ± 2 °C: (a) XANES, (b) XANES pre-edge, (c-d) EXAFS, (e-f) Fourier transform of the EXAFS. Panels (a-c) show reference data for CoO, Co_3O_4 and CoOOH (*dashed/dotted traces*). Panels (d) and (f) show simulations (*dotted purple*) based on the parameters summarized in Table 3.S4.

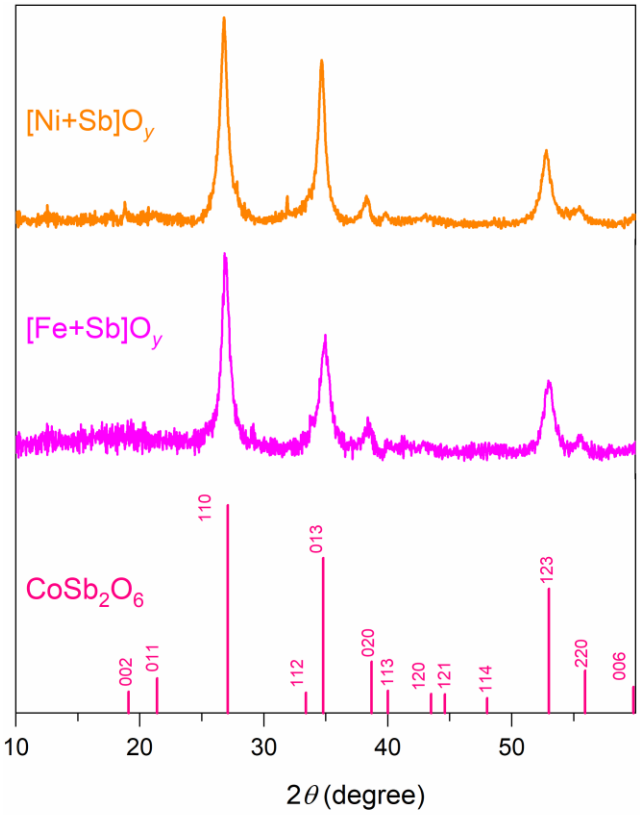

Figure 3.S24. X-ray diffractograms of as-synthesized nickel-antimony (*orange*) and iron-antimony (*magenta*) oxides. Vertical lines show tabulated positions and relative intensities for $CoSb_2O_6$ (ICSD 108964).

Table 3.S3. $MnSb_2O_6$ crystal structure parameters used for the EXAFS simulations to fit the experimental data for $[Mn+Sb]O_y$ shown in Figure 3.S22.

		Distance / Å		
Atomic Pair	**Number**	**Tabulated [a]**	**Simulation**	**Debye-Waller (s2)**
As-prepared [b]				
Mn-O	4	2.124	1.91	0.006
Mn-O	2	2.28	2.18	0.010
Mn-Sb	**2**	**not present [d]**	**2.82**	**0.004**
Mn-Sb	3	3.24	3.23	0.005
Mn-Sb	**3**	**not present [d]**	**3.49**	**0.002**
Mn-Sb	2	3.63	3.61	0.026
After the OER test [c]				
Mn-O	6	2.12	1.88	0.0052
Mn-Sb	**2**	**not present [d]**	**2.6**	**0.0076**
Mn-Sb	3	3.24	3.21	0.0061
Mn-Sb	**2**	**not present [d]**	**3.61**	**0.0009**
Mn-Sb	3	3.67	3.67	0.0029

[b] As reported in Ref.[85b] Other parameters: *S02* = 0.610, *E0* = -2.490 eV, R-factor=0.0059.[c] Other parameters: *S02* = 0.400, *E0* = -6.794 eV, R-factor = 0.067. [d] Additional interactions were needed to explain the experimentally observed intensity patterns.

Table 3.S4. $CoSb_2O_6$ crystal structure parameters[a] used for the EXAFS simulations to fit the experimental data for tested $[Co+Sb]O_y$ shown in Figure 3.S23.

		Distance / Å		
Atomic Pair	**Number**	**Tabulated [b]**	**Simulation**	**Debye-Waller (s2)**
Co-O	6	2.00	2.00	0.0058
Co-Sb	2	3.09	3.09	0.0071
Co-Sb	8	3.63	3.63	0.0060
Co..O..Sb	16	3.83	3.83	0.0026

[b] Other parameters: *S02* = 0.89, *E0* = -6.117 eV, R-factor=0.040. [b] As reported in Ref.[85]

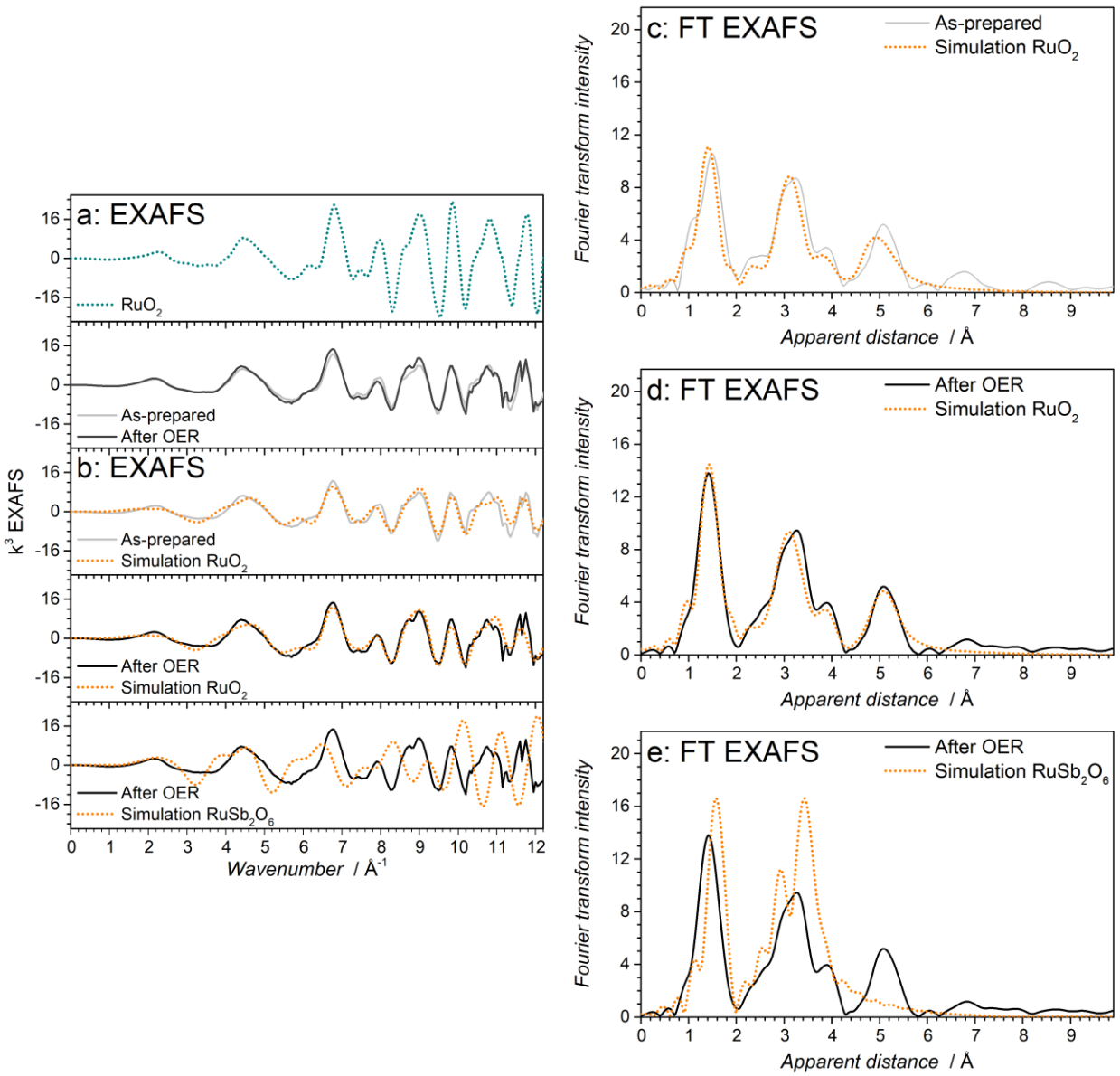

Figure 3.S25. Ru K-edge XAS data for [Ru+Sb]O_y before (*grey*) and after (*black*) OER test in stirred 0.5 M H_2SO_4 for 10 h at 10 mA cm^{-2} at 80 °C: (a-b) EXAFS, (c-e) Fourier transform of the EXAFS. Panel (a) shows reference data for RuO_2 (*dotted teal*). Panels (b-f) show simulations (*dotted orange*) based on RuO_2 and $RuSb_2O_6$ and on the parameters summarized in Table 3.S5.

Table 3.S5. RuO_2 and $MnSb_2O_6$ crystal structure parameters used for the EXAFS simulations to fit the experimental data for $[Ru+Sb]O_y$ shown in Figure 3.S25.

		Distance / Å		
Atomic Pair	**Number**	**Tabulated [a]**	**Simulation**	**Debye-Waller (s2)**
As-prepared [b]				
		RuO_2		
Ru-O	6	1.94	1.94	0.0037
Ru-Ru	2	3.11	3.11	0.0043
Ru-Ru	8	3.53	3.53	0.0049
Ru-Ru	4	4.49	4.45	0.0047
Ru-Ru	8	5.46	5.41	0.0019
Ru..O..Ru	16	5.64	5.64	0.0127
After the OER test [c]				
		RuO_2		
Ru-O	6	1.94	1.94	0.0016
Ru-Ru	2	3.11	3.11	0.0029
Ru-Ru	8	3.53	3.53	0.0043
Ru-Ru	4	4.49	4.46	0.0041
Ru-Ru	8	5.46	5.46	0.0049
Ru..O..Ru	16	5.64	5.62	0.0052
		$RuSb_2O_6$		
Ru-O	6	2.00	2.00	0.002
Ru-Sb	2	3.09	3.09	0.002
Ru-Sb	8	3.63	3.63	0.006
Ru-Sb..O	16	3.83	3.83	0.006

[b] As reported in Ref.[86] for RuO_2; $RuSb_2O_6$ model was developed based on Ref.[87] [b] Other parameters: *S02* = 0.912, *E0* = -10.069 eV, R-factor = 0.070. [c] Other parameters: *S02* = 0.912, *E0* = -9.505, R-factor = 0.14 for RuO_2; *S02* = 0.912, *E0* = 5.72 eV, R-factor = 200 for $RuSb_2O_6$.

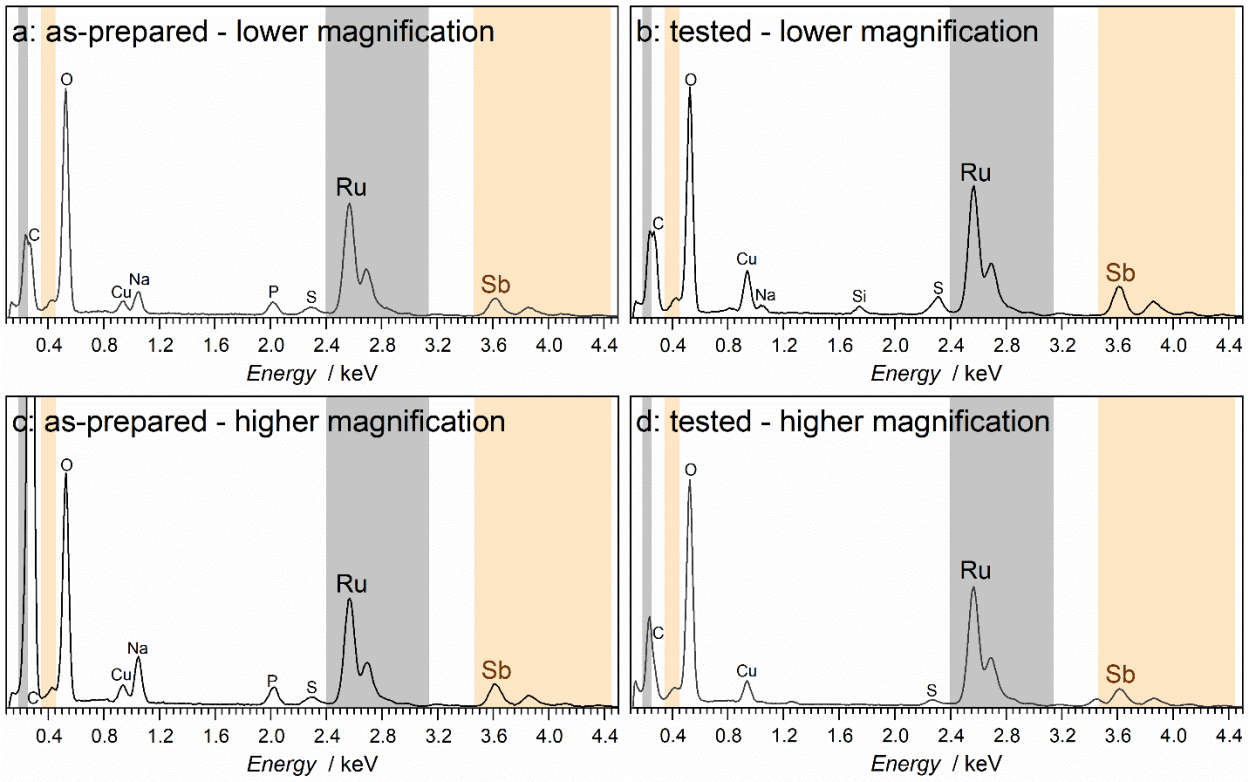

Figure 3.S26. Examples of the energy dispersive X-ray spectra collected during the (a-b) lower and (c-d) higher magnification STEM-EDS mapping for $[Ru+Sb]O_y$. (a, c) before and (b, d) after test at 10 mA cm^{-2} for 24 h at 80 °C. Cu signal is attributed to the TEM grid. Si, Na, P and S signals are associated with the unknown admixtures, which have been most probably introduced during detaching the catalyst material off the FTO-coated glass slides for the TEM sample preparation.

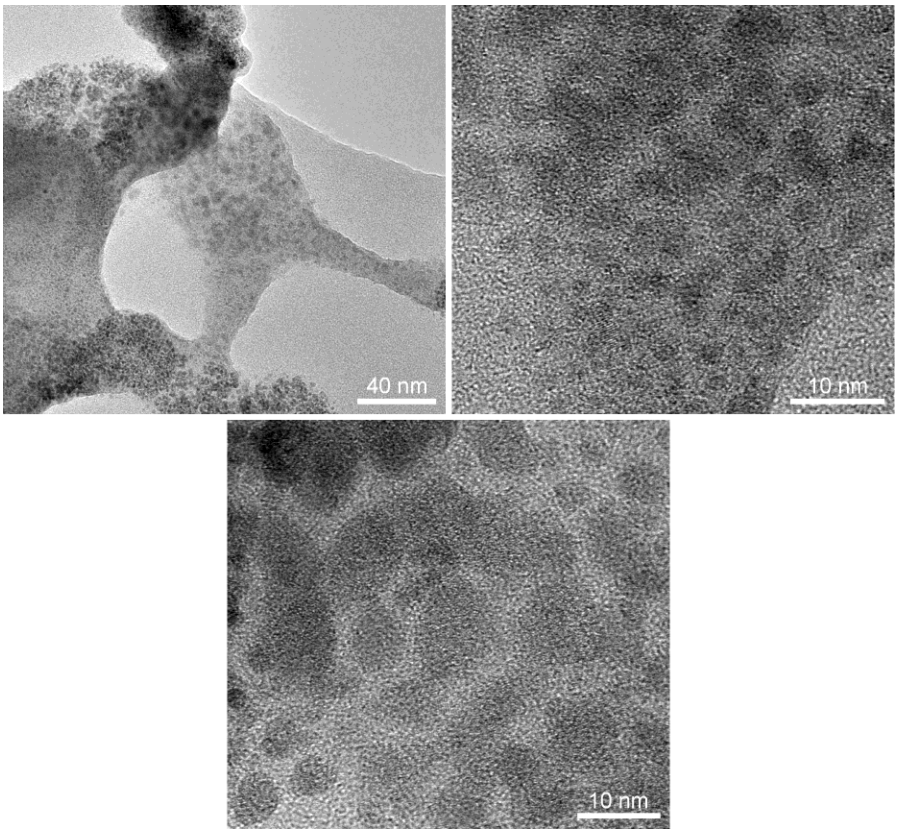

Figure 3.S27. TEM imaging of as-prepared [Ru+Sb]O_y at different magnification.

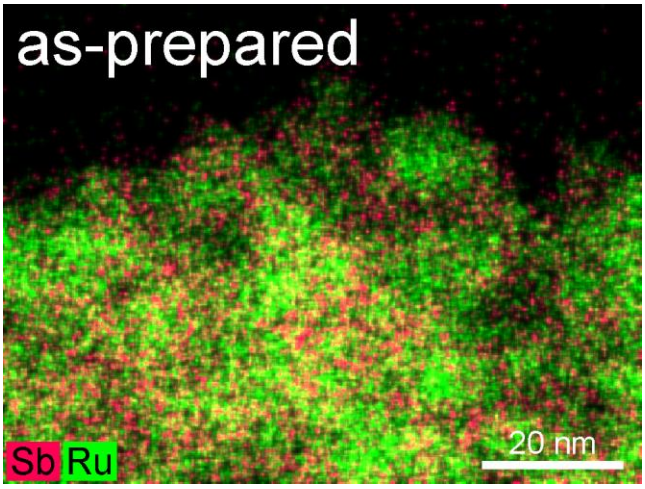

Figure 3.S28. High-magnification STEM-EDS mapping of the as-prepared [Ru+Sb]O_y catalyst.

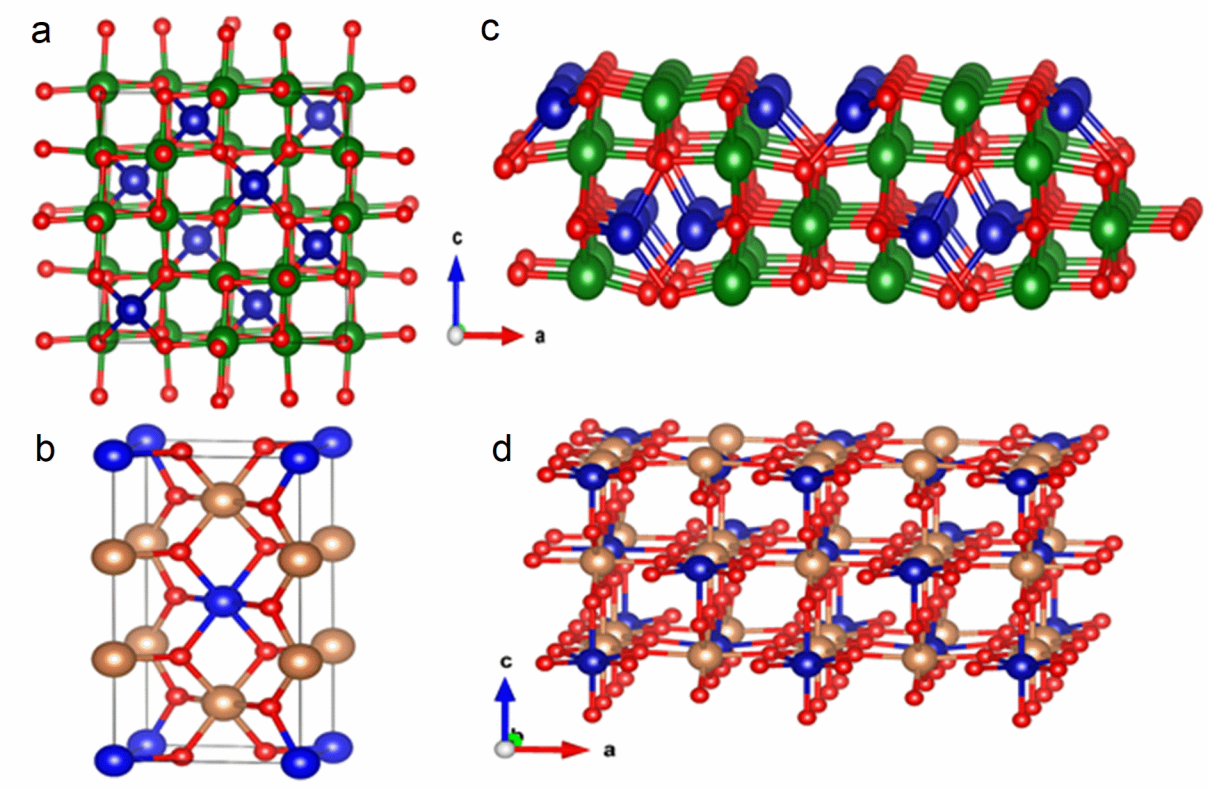

Figure 3.S29. Model crystal structures of (a) Co_3O_4 [$Co^{2+}(Co^{3+})_2O_4$] and (b) $CoSb_2O_6$ [$Co^{2+}(Sb^{5+})_2O_6$], and surface models for (c) (110)-A Co_3O_4 and (d) (110) $CoSb_2O_6$ (*blue*, *green*, *orange* and *red* spheres show Co^{2+}, Co^{3+}, Sb^{5+} and O^{2-}, respectively).

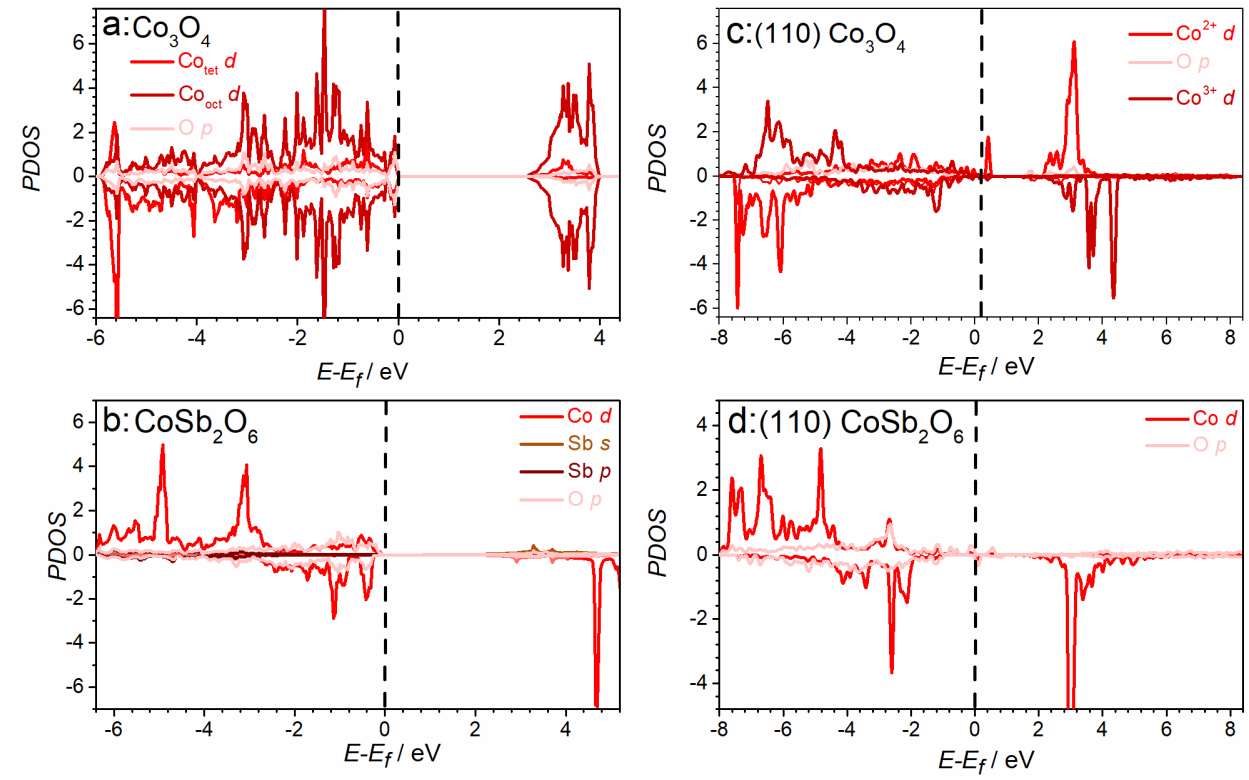

Figure 3.S30. Spin polarized atom/orbital projected partial density of states (PDOS) for bulk (a) Co_3O_4 and (b) $CoSb_2O_6$ and surface (c) (110)-A Co_3O_4 and (d) (110) $CoSb_2O_6$. Fermi levels are set at 0 eV (indicated by vertical dashed lines).

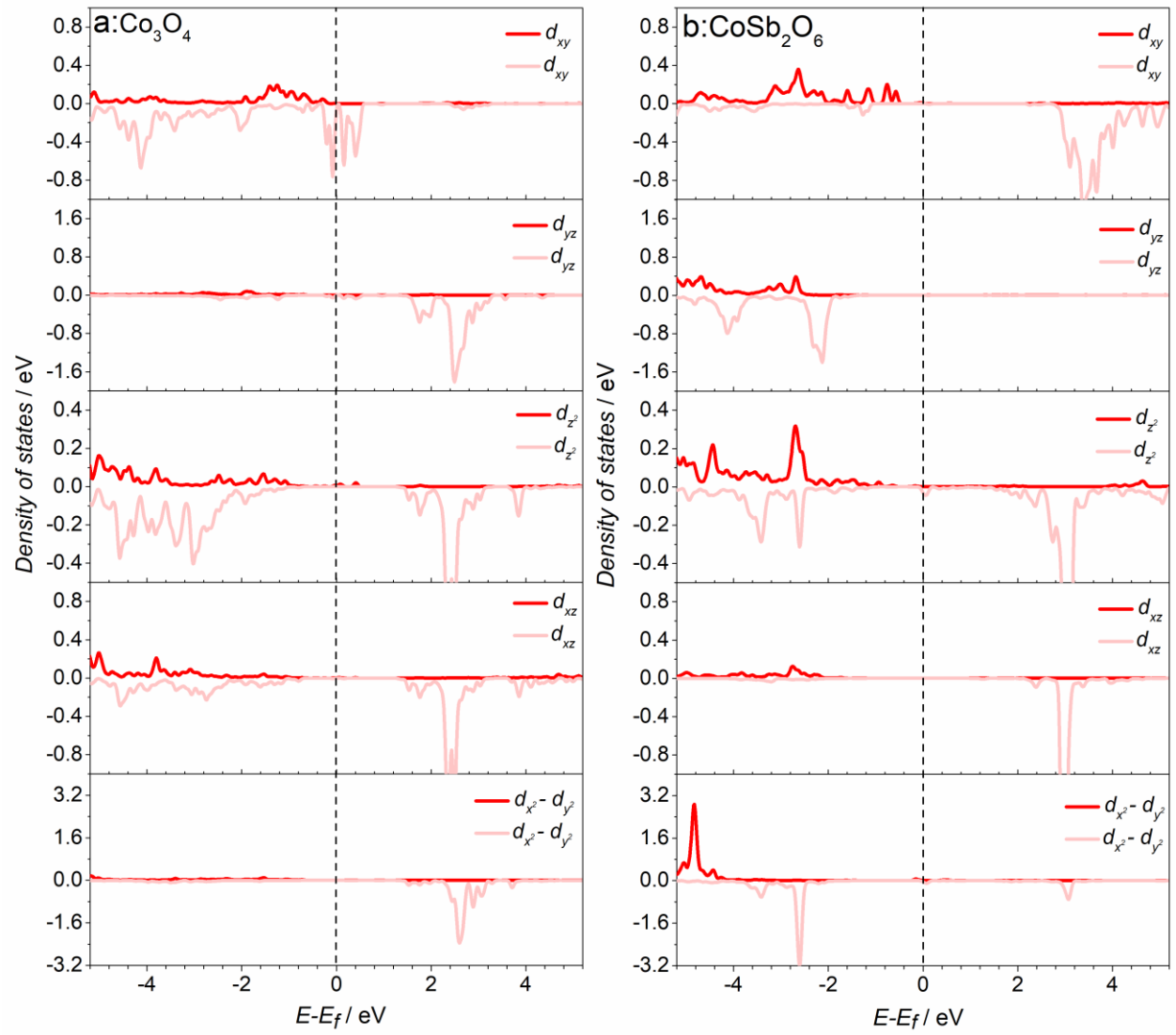

Figure 3.S31. PDOS of Co 3d sub-orbitals d_{xy}, d_{xz}, d_{yz}, d_{z2} and d_{x2-y2} for (a) (110)-A Co_3O_4 and (b) (110) $CoSb_2O_6$ surface models. Fermi levels are set at 0 eV (indicated by vertical lines). The DOS of spin down channel of d_{xy}, d_{yz} and d_{xz} of Co d states has finite value at the Fermi level of Co_3O_4; in $CoSb_2O_6$, the Co d state intensity near and at the Fermi level is substantially diminished. This suggests facilitated charge transfer from Co of $CoSb_2O_6$ to its neighbouring oxygen atoms, which is indicative of the improved bond strength.

Table 3.S6. Enthalpies of formation of the [Ru_n+Sb_m]O_y phases considered for the oxygen grand potential diagram.

Composition	ΔH_f (eV per f.u.)	Composition	ΔH_f (eV per f.u.)
Ru	0	**Ru:SbO_2** [b]	
Sb	0	Ru_2:$Sb_{30}O_{64}$	-136.5754
O	0	Ru_4:$Sb_{28}O_{64}$	-132.4576
Individual oxides		Ru_6:$Sb_{26}O_{64}$	-129.6658
SbO_2	-4.3953	Ru_8:$Sb_{24}O_{64}$	-126.56
Sb_2O_3	-7.1036	Ru_{10}:$Sb_{22}O_{64}$	-123.4152
Sb_2O_5	-9.4111	Ru_{12}:$Sb_{20}O_{64}$	-120.1204
RuO_2	-3.4289	Ru_{14}:$Sb_{18}O_{64}$	-117.4506
RuO_4	-4.2085	Ru_{16}:$Sb_{16}O_{64}$	-114.6668
Stoichiometric phases		**Ru:Sb_2O_3** [b]	
$RuSb_2O_6$	-11.6643	Ru_1:$Sb_{31}O_{48}$	-110.3403
$RuSb_2O_5$	-9.6335	Ru_2:$Sb_{30}O_{48}$	-107.1917
$RuSb_4O_{12}$	-20.7176	Ru_4:$Sb_{28}O_{48}$	-101.44
$Ru_2Sb_2O_9$	-12.346	Ru_6:$Sb_{26}O_{48}$	-94.4664
$Ru_{10}Sb_{10}O_{34}$	-57.539	Ru_8:$Sb_{24}O_{48}$	-91.672
$Ru_8Sb_8O_{28}$	-48.5294	Ru_{10}:$Sb_{22}O_{48}$	-85.4024
$Ru_2Sb_2O_8$	-14.4598	Ru_{12}:$Sb_{20}O_{48}$	-82.3354
$Ru_2Sb_2O_7$	-13.2396	Ru_{14}:$Sb_{18}O_{48}$	-76.8166
$RuSb_2O_7$	-11.0804	Ru_{16}:$Sb_{16}O_{48}$	-74.3198
Sb:RuO_2 [a]		**Ru:Sb_2O_5** [b]	
Sb_1:$Ru_{15}O_{32}$	-55.6121	Ru_1:$Sb_{15}O_{40}$	-73.5697
Sb_2:$Ru_{14}O_{32}$	-55.939	Ru_2:$Sb_{14}O_{40}$	-70.9568
Sb_2:$Ru_{12}O_{32}$	-57.6568	Ru_4:$Sb_{12}O_{40}$	-70.249
Sb_6:$Ru_{10}O_{32}$	-59.0276	Ru_6:$Sb_{10}O_{40}$	-67.0202
Sb_8:Ru_8O_{32}	-60.5614	Ru_8:Sb_8O_{40}	-63.7794

[a] Sb-doped RuO_2; [b] Ru-doped antimony oxides.

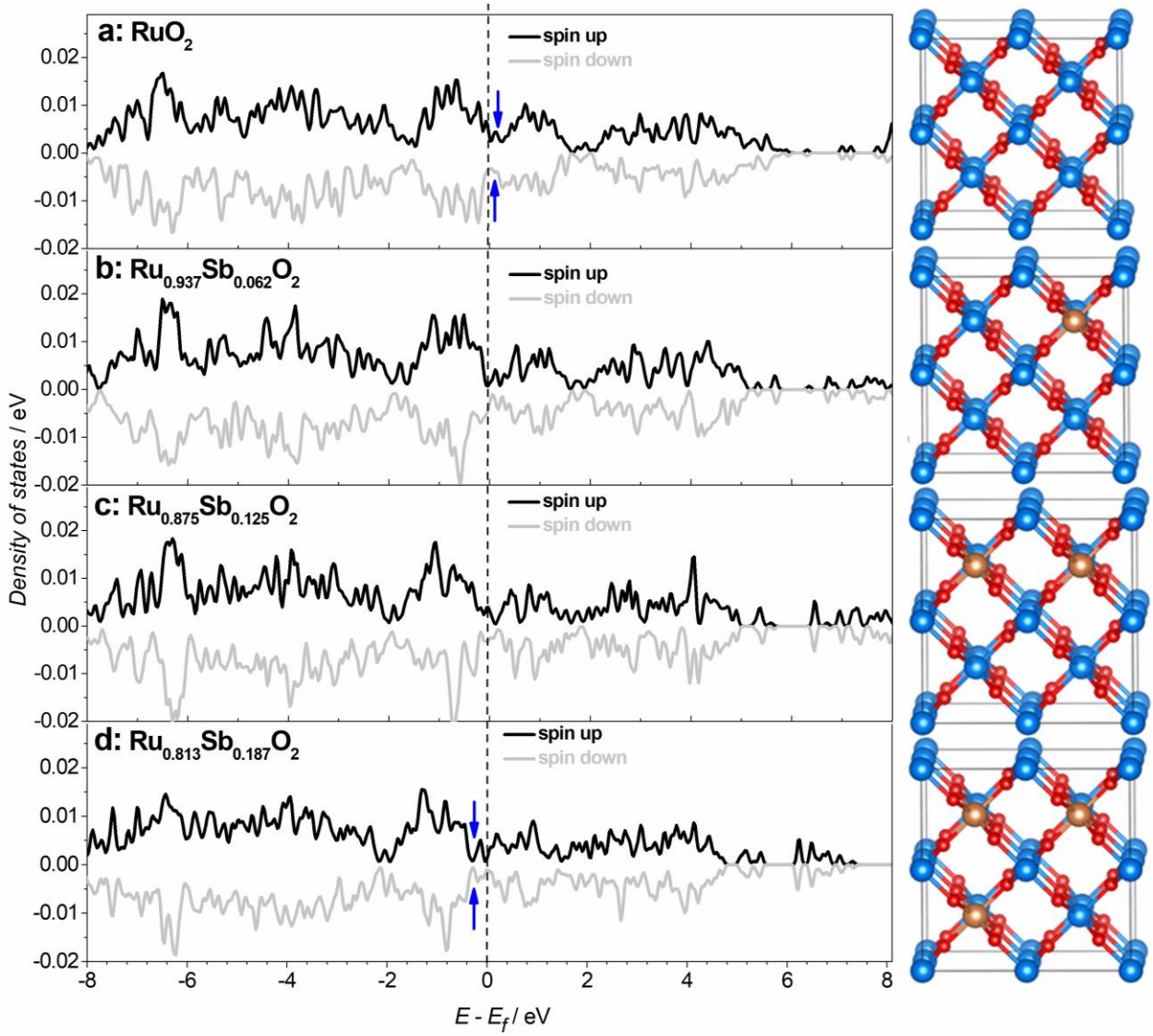

Figure 3.S32. Spin polarized total density of states (TDOS) for (a) RuO_2, (b) $Sb_{0.0625}:Ru_{0.9375}O_2$, (c) $Sb_{0.125}:Ru_{0.875}O_2$, and (d) $Sb_{0.187}:Ru_{0.813}O_2$. Fermi levels are set at 0 eV (indicated by vertical dashed lines). Blue arrows indicate unoccupied states which are filled up and shifted to lower energy. This might be attributed to replacement of Ru^{4+} by higher valency Sb^{5+} atoms as discussed in the main text. Corresponding supercells are shown against the plots on the right (*light blue*, *orange* and *red* spheres show Ru^{2+}, Sb^{5+} and O^{2-}, respectively).

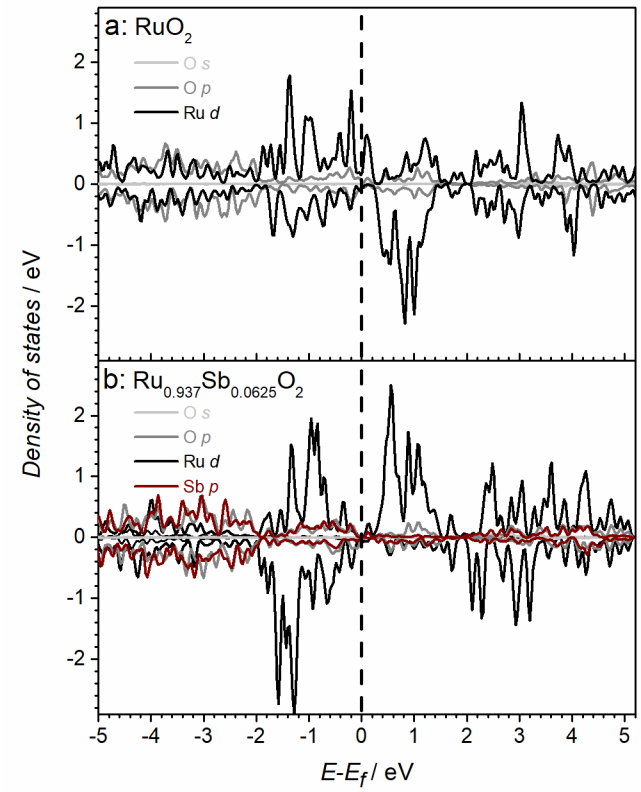

Figure 3.S33. PDOS of (a) RuO_2 and (b) $Sb_{0.0625}$:$Ru_{0.9375}O_2$. Fermi levels are set at 0 eV (indicated by vertical dashed lines). Enhanced overlap of Ru d and O p orbitals near the Fermi level induced by doping with antimony suggests enhanced Ru-O interaction.

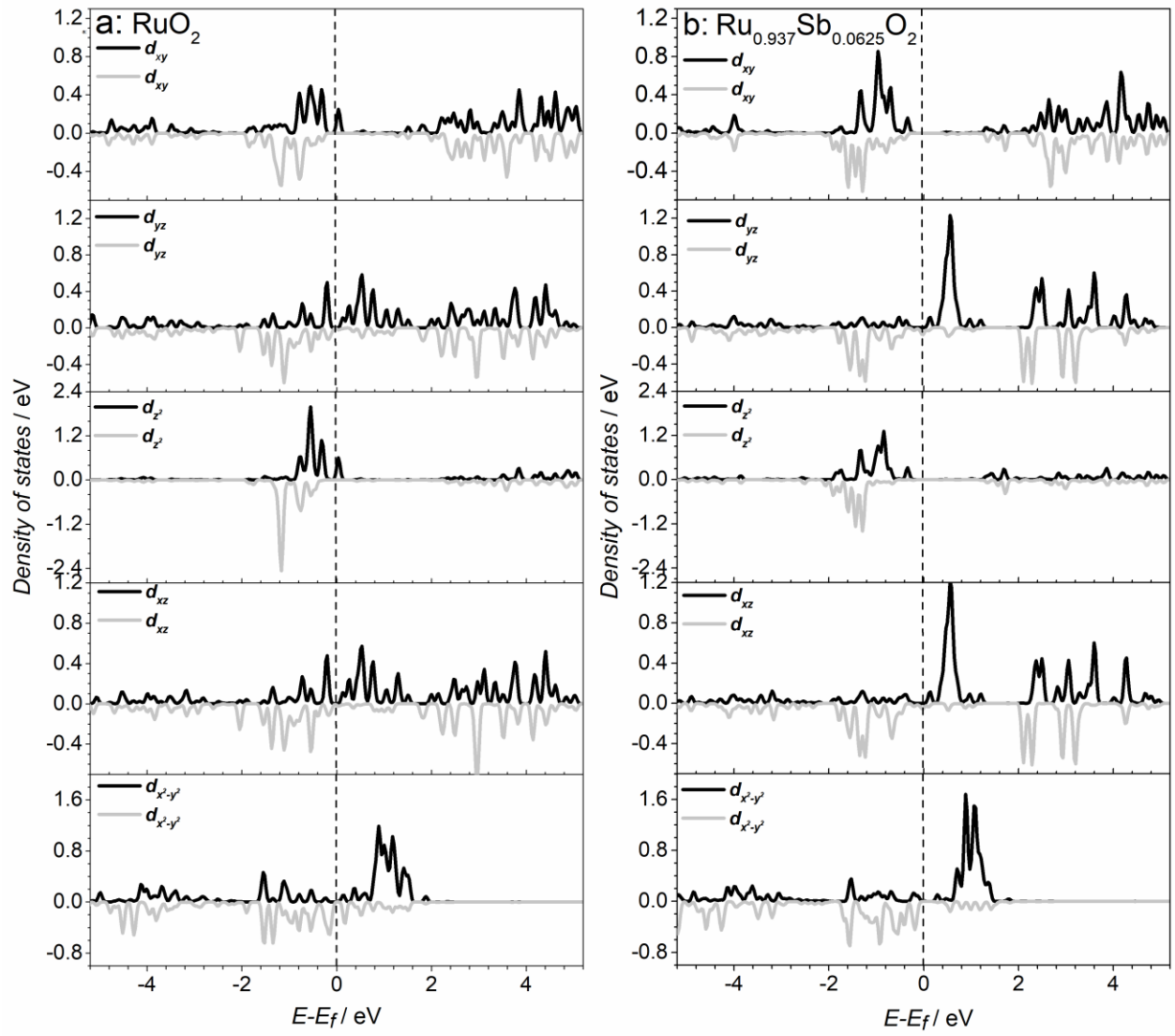

Figure 3.S34. Spin polarized PDOS of Ru 4d sub-orbitals d_{xy}, d_{xz}, d_{yz}, d_{z2} and d_{x2-y2} for (a) RuO_2 and (b) $Sb_{0.0625}$:$Ru_{0.9375}O_2$. Fermi levels are set at 0 eV (indicated by vertical dashed lines). Upon doping of RuO_2 with antimony, states near the Fermi level of d_{yz}, d_{xz} and d_{z2} diminish, which indicates the enhanced electron donation from Ru to O and thus implies stronger Ru-O interaction.

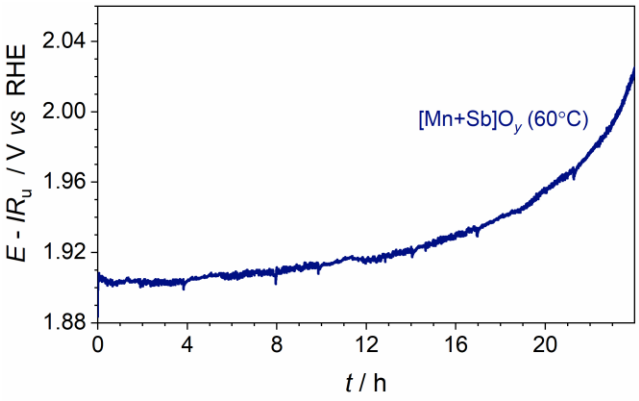

Figure 3.S35. Example of a failed experiment due to inadequate protection of the FTO surface during galvanostatic electrooxidation (current density 10 mA $cm^{-2}_{geom.}$; data are IR_u corrected) of 0.5 M H_2SO_4 at 60 °C using a [Mn+Sb]O_y-modified electrode.

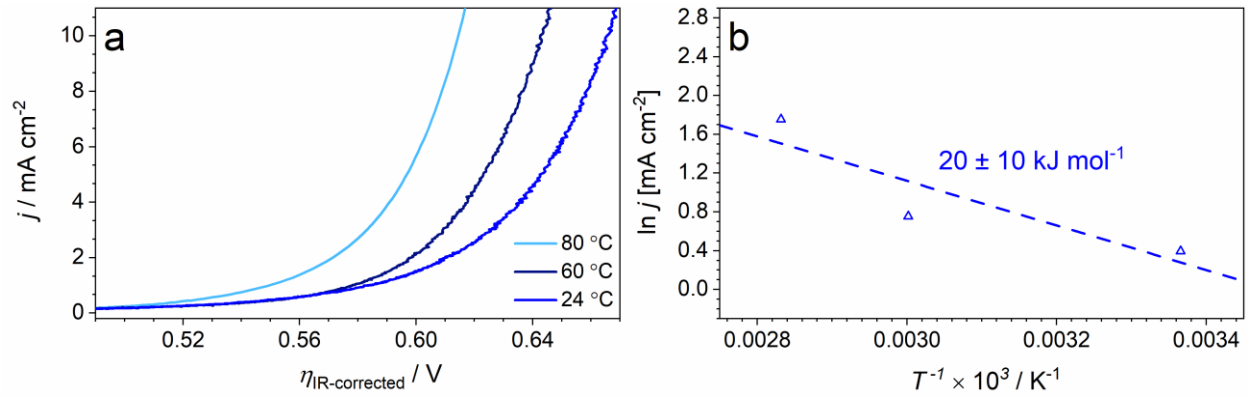

Figure 3.S36. (a) IR_u-corrected backward sweeps of quasi-stabilized cyclic voltammograms for the [Mn+Sb]O_y-catalyzed OER in 0.5 M H_2SO_4 at 24 ± 2 (*blue*), 60 (*dark blue*) and 80 °C (*light blue*). (b) Arrhenius plots constructed based on the data in panel (a) for the OER overpotential of 0.6 V (see figure). Dashed lines show tentative linear approximations, while values show corresponding estimates of the apparent activation energy.

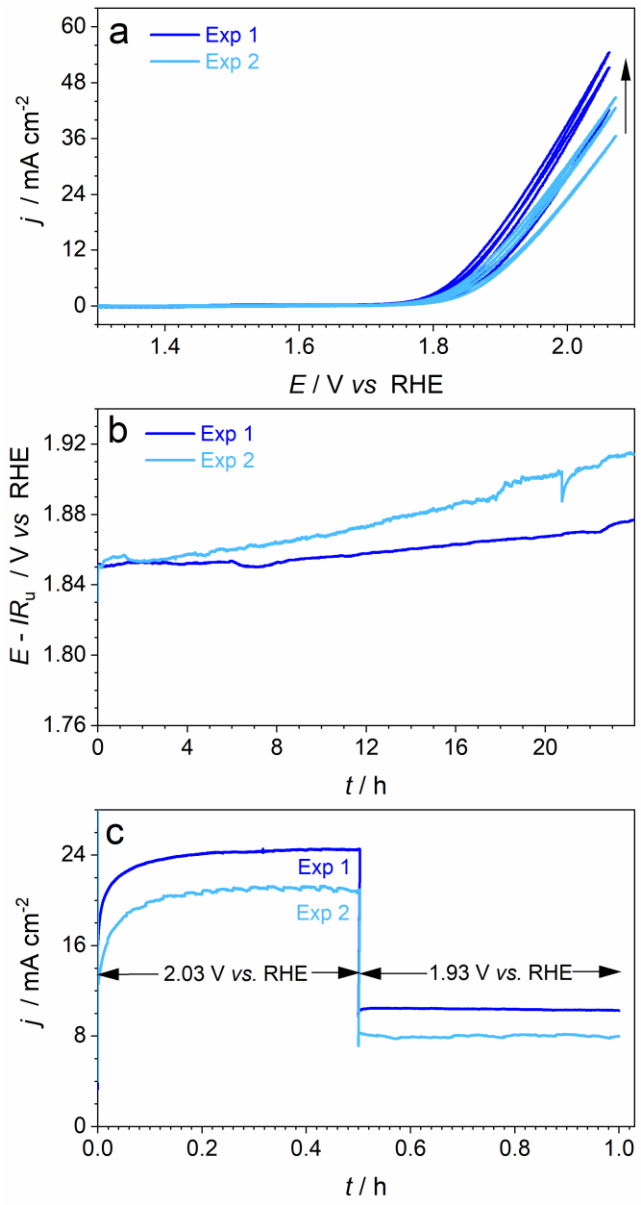

Figure 3.S37. Reproducibility of the OER catalytic activity of [Mn+Sb]O_y in 0.5 M H_2SO_4 at 60 °C: (a) cyclic voltammetry (scan rate 0.020 V s^{-1}; first three cycles shown; potentials are not corrected for ohmic losses), (b) IR_u-corrected chronopotentiograms at 10 mA $cm^{-2}_{geom.}$, and (c) subsequently recorded chronoamperograms at 2.03 and 1.93 V *vs.* RHE. Current is normalized to the geometric surface area of the electrodes. Arrows in panel (a) show the evolution of voltammograms with cycling.

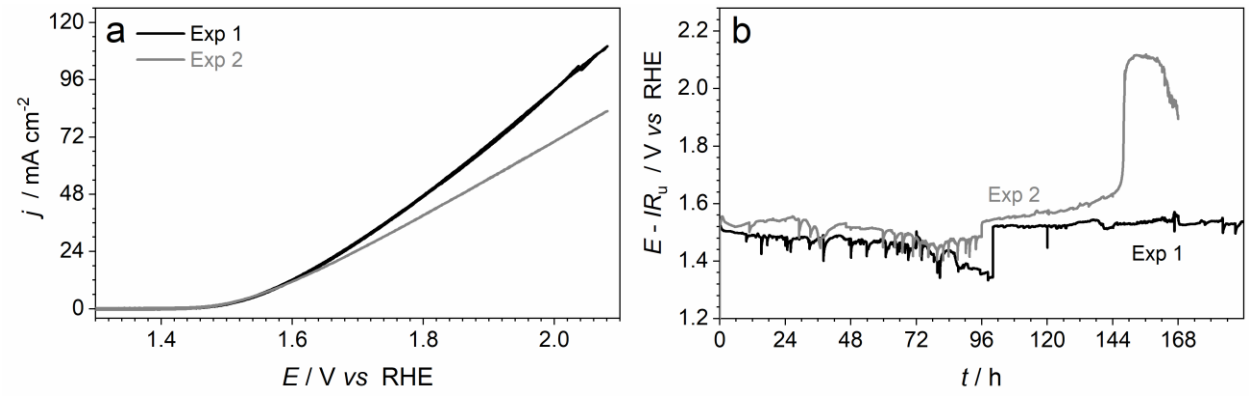

Figure 3. S38. Reproducibility of the long-term performance of [Ru+Sb]O_y in 0.5 M H_2SO_4 at 80 °C: (a) initial cyclic voltammetry (potentials are not IR_u-corrected), (b) chronopotentiograms at 10 mA $cm^{-2}_{geom.}$ (data are corrected for ohmic losses). Current is normalized to the geometric surface area of the electrodes. Experiment 2 failed after *ca* 100 h of operation due to the irrevocable degradation of the reference electrode.

3.5 REFERENCES

(1) Reier, T.; Nong, H. N.; Teschner, D.; Schlögl, R.; Strasser, P. Electrocatalytic Oxygen Evolution Reaction in Acidic Environments – Reaction Mechanisms and Catalysts. *Adv. Energy Mater.* **2017**, *7* (1). https://doi.org/10.1002/aenm.201601275.

(2) MacFarlane, D. R.; Choi, J.; Suryanto, B. H. R.; Jalili, R.; Chatti, M.; Azofra, L. M.; Simonov, A. N. Liquefied Sunshine: Transforming Renewables into Fertilizers and Energy Carriers with Electromaterials. *Adv. Mater.* **2019**, *1904804*, 1–13. https://doi.org/10.1002/adma.201904804.

(3) https://www.hydrogenics.com/2019/02/25/hydrogenics-to-deliver-worlds-largest-hydrogen-electrolysis-plant/.

(4) Ayers, K.; Danilovic, N.; Ouimet, R.; Carmo, M.; Pivovar, B.; Bornstein, M. Perspectives on Low-Temperature Electrolysis and Potential for Renewable Hydrogen at Scale. *Annu. Rev. Chem. Biomol. Eng.* **2019**, *10* (1), 219–239. https://doi.org/10.1146/annurev-chembioeng-060718-030241.

(5) She, Z. W.; Kibsgaard, J.; Dickens, C. F.; Chorkendorff, I.; Nørskov, J. K.; Jaramillo, T. F. Combining Theory and Experiment in Electrocatalysis: Insights into Materials Design. *Science (80-.).* **2017**, *355* (6321). https://doi.org/10.1126/science.aad4998.

(6) Fu, W. T.; Diaz-morales, O.; Li, Z.; Oellers, T.; Fruchter, L. Electrocatalyst Stability Benchmarking. *Nat. Catal.* **2018**, *1* (July), 1–8. https://doi.org/10.1038/s41929-018-0085-

6.

(7) Kasian, O.; Grote, J. P.; Geiger, S.; Cherevko, S.; Mayrhofer, K. J. J. The Common Intermediates of Oxygen Evolution and Dissolution Reactions during Water Electrolysis on Iridium. *Angew. Chemie - Int. Ed.* **2018**, *57* (9), 2488–2491. https://doi.org/10.1002/anie.201709652.

(8) Claudel, F.; Dubau, L.; Berthomé, G.; Sola-Hernandez, L.; Beauger, C.; Piccolo, L.; Maillard, F. Degradation Mechanisms of Oxygen Evolution Reaction Electrocatalysts: A Combined Identical-Location Transmission Electron Microscopy and X-Ray Photoelectron Spectroscopy Study. *ACS Catal.* **2019**, *9* (5), 4688–4698. https://doi.org/10.1021/acscatal.9b00280.

(9) Kasian, O.; Geiger, S.; Li, T.; Grote, J. P.; Schweinar, K.; Zhang, S.; Scheu, C.; Raabe, D.; Cherevko, S.; Gault, B.; Mayrhofer, K. J. J. Degradation of Iridium Oxides via Oxygen Evolution from the Lattice: Correlating Atomic Scale Structure with Reaction Mechanisms. *Energy Environ. Sci.* **2019**, *12* (12), 3548–3555. https://doi.org/10.1039/c9ee01872g.

(10) Saveleva, V. A.; Wang, L.; Kasian, O.; Batuk, M.; Hadermann, J.; Gallet, J. J.; Bournel, F.; Alonso-Vante, N.; Ozouf, G.; Beauger, C.; Mayrhofer, K. J. J.; Cherevko, S.; Gago, A. S.; Friedrich, K. A.; Zafeiratos, S.; Savinova, E. R. Insight into the Mechanisms of High Activity and Stability of Iridium Supported on Antimony-Doped Tin Oxide Aerogel for Anodes of Proton Exchange Membrane Water Electrolyzers. *ACS Catal.* **2020**, *10* (4), 2508–2516. https://doi.org/10.1021/acscatal.9b04449.

(11) Chen, G.; Li, J.; Lv, H.; Wang, S.; Zuo, J.; Zhu, L. Mesoporous $Co_xSn_{(1-x)}O_2$ as an Efficient Oxygen Evolution Catalyst Support for Spe Water Electrolyzer. *R. Soc. Open Sci.* **2019**, *6* (4). https://doi.org/10.6084/m9.figshare.

(12) Li, X.; Pletcher, D.; Walsh, F. C. Electrodeposited Lead Dioxide Coatings. *Chem. Soc. Rev.* **2011**, *40* (7), 3879–3894. https://doi.org/10.1039/c0cs00213e.

(13) Lei, Z.; Wang, T.; Zhao, B.; Cai, W.; Liu, Y.; Jiao, S.; Li, Q.; Cao, R.; Liu, M. Recent Progress in Electrocatalysts for Acidic Water Oxidation. *Adv. Energy Mater.* **2020**, *2000478*, 1–18. https://doi.org/10.1002/aenm.202000478.

(14) Marshall, A. T.; Sunde, S.; Tsypkin, M.; Tunold, R. Performance of a PEM Water Electrolysis Cell Using $Ir_xRu_yTa_zO_2$ Electrocatalysts for the Oxygen Evolution Electrode. *Int. J. Hydrogen Energy* **2007**, *32* (13), 2320–2324. https://doi.org/10.1016/j.ijhydene.2007.02.013.

(15) Chatti, M.; Gardiner, J. L.; Fournier, M.; Johannessen, B.; Williams, T.; Gengenbach, T. R.; Pai, N.; Nguyen, C.; Macfarlane, D. R.; Hocking, R. K.; Simonov, A. N. Intrinsically Stable in Situ Generated Electrocatalyst for Long-Term Oxidation of Acidic Water at up to 80 °C. *Nat. Catal.* **2019**, *2* (May), 457–465. https://doi.org/10.1038/s41929-019-0277-8.

(16) Shinde, A.; Jones, R. J. R.; Guevarra, D.; Mitrovic, S.; Becerra-Stasiewicz, N.; Haber, J. A.; Jin, J.; Gregoire, J. M. High-Throughput Screening for Acid-Stable Oxygen Evolution Electrocatalysts in the $(Mn–Co–Ta–Sb)O_x$ Composition Space. *Electrocatalysis* **2015**, *6*

(2), 229–236. https://doi.org/10.1007/s12678-014-0237-7.

(17) Moreno-Hernandez, I. A.; Macfarland, C. A.; Read, C. G.; Papadantonakis, K. M.; Brunschwig, B. S.; Lewis, N. S. Crystalline Nickel Manganese Antimonate as a Stable Water-Oxidation Catalyst in Aqueous 1.0 M H_2SO_4. *Energy Environ. Sci.* **2017**, *10* (10), 2103–2108. https://doi.org/10.1039/c7ee01486d.

(18) Schmachtel, S.; Murtomäki, L.; Aromaa, J.; Lundström, M.; Forsén, O.; Barker, M. H. Simulation of Electrochemical Processes during Oxygen Evolution on Pb-MnO_2 Composite Electrodes. *Electrochim. Acta* **2017**, *245*, 512–525. https://doi.org/10.1016/j.electacta.2017.04.131.

(19) Tunold, R.; Marshall, A. T.; Rasten, E.; Tsypkin, M.; Owe, L.-E.; Sunde, S. Materials for Electrocatalysis of Oxygen Evolution Process in PEM Water Electrolysis Cells. **2010**, *25* (23), 103–117. https://doi.org/10.1149/1.3328515.

(20) Wu, X.; Scott, K. RuO_2 Supported on Sb-Doped SnO_2 Nanoparticles for Polymer Electrolyte Membrane Water Electrolysers. *Int. J. Hydrogen Energy* **2011**, *36* (10), 5806–5810. https://doi.org/10.1016/j.ijhydene.2010.10.098.

(21) Oakton, E.; Lebedev, D.; Povia, M.; Abbott, D. F.; Fabbri, E.; Fedorov, A.; Nachtegaal, M.; Copéret, C.; Schmidt, T. J. IrO_2-TiO_2: A High-Surface-Area, Active, and Stable Electrocatalyst for the Oxygen Evolution Reaction. *ACS Catal.* **2017**, *7* (4), 2346–2352. https://doi.org/10.1021/acscatal.6b03246.

(22) Kim, J.; Shih, P. C.; Tsao, K. C.; Pan, Y. T.; Yin, X.; Sun, C. J.; Yang, H. High-Performance Pyrochlore-Type Yttrium Ruthenate Electrocatalyst for Oxygen Evolution Reaction in Acidic Media. *J. Am. Chem. Soc.* **2017**, *139* (34), 12076–12083. https://doi.org/10.1021/jacs.7b06808.

(23) Lin, Y.; Tian, Z.; Zhang, L.; Ma, J.; Jiang, Z.; Chen, L.; Deibert, B. J.; Ge, R. Chromium-Ruthenium Oxide Solid Solution Electrocatalyst for Highly Efficient Oxygen Evolution Reaction in Acidic Media. *Nat. Commun.* **2019**, *10* (2019), 162. https://doi.org/10.1038/s41467-018-08144-3.

(24) Trotochaud, L.; Young, S. L.; Ranney, J. K.; Boettcher, S. W. Nickel-Iron Oxyhydroxide Oxygen-Evolution Electrocatalysts: The Role of Intentional and Incidental Iron Incorporation. *J. Am. Chem. Soc.* **2014**, *136* (18), 6744–6753. https://doi.org/10.1021/ja502379c.

(25) Louie, M. W.; Bell, A. T. An Investigation of Thin-Film Ni-Fe Oxide Catalysts for the Electrochemical Evolution of Oxygen. *J. Am. Chem. Soc.* **2013**, *135* (33), 12329–12337. https://doi.org/10.1021/ja405351s.

(26) Vos, J. G.; Wezendonk, T. A.; Jeremiasse, A. W.; Koper, M. T. M. MnO_x/IrO_x as Selective Oxygen Evolution Electrocatalyst in Acidic Chloride Solution. *J. Am. Chem. Soc.* **2018**, *140* (32), 10270–10281. https://doi.org/10.1021/jacs.8b05382.

(27) Mondschein, J. S.; Callejas, J. F.; Read, C. G.; Chen, J. Y. C.; Holder, C. F.; Badding, C. K.; Schaak, R. E. Crystalline Cobalt Oxide Films for Sustained Electrocatalytic Oxygen Evolution under Strongly Acidic Conditions. *Chem. Mater.* **2017**, *29* (3), 950–957.

https://doi.org/10.1021/acs.chemmater.6b02879.

(28) Kibsgaard, J.; Hellstern, T. R.; Choi, S. J.; Reinecke, B. N.; Jaramillo, T. F. Mesoporous Ruthenium/Ruthenium Oxide Thin Films: Active Electrocatalysts for the Oxygen Evolution Reaction. *ChemElectroChem* **2017**, *4* (10), 2480–2485. https://doi.org/10.1002/celc.201700334.

(29) Song, S.; Zhang, H.; Ma, X.; Shao, Z.; Baker, R. T.; Yi, B. Electrochemical Investigation of Electrocatalysts for the Oxygen Evolution Reaction in PEM Water Electrolyzers. *Int. J. Hydrogen Energy* **2008**, *33* (19), 4955–4961. https://doi.org/10.1016/j.ijhydene.2008.06.039.

(30) Bradley S. Van Gosen, Philip L. Verplanck, Robert R. Seal II, K. R. L.; Gambogi, and J. Rare-Earth Elements Chapter O of Critical Mineral Resources of the United States — Economic and Environmental Geology and Prospects for Future Supply Professional Paper 1802 – O U . S . Department of the Interior. **2013**.

(31) Bloxham, L.; Cowley, A.; Han, L.; Shao, E. Pgm Market Report. *JM* **2020**, No. February, 1–48.

(32) Schulte, R. F. Platinum-Group Metals. *USGS* **2018**, No. 703, 124–125.

(33) Cherevko, S.; Geiger, S.; Kasian, O.; Kulyk, N.; Grote, J. P.; Savan, A.; Shrestha, B. R.; Merzlikin, S.; Breitbach, B.; Ludwig, A.; Mayrhofer, K. J. J. Oxygen and Hydrogen Evolution Reactions on Ru, RuO_2, Ir, and IrO_2 Thin Film Electrodes in Acidic and Alkaline Electrolytes: A Comparative Study on Activity and Stability. *Catalysis Today*. 2016, pp 170–180. https://doi.org/10.1016/j.cattod.2015.08.014.

(34) Kasian, O.; Geiger, S.; Stock, P.; Polymeros, G.; Breitbach, B.; Savan, A.; Ludwig, A.; Cherevko, S.; Mayrhofer, K. J. J. On the Origin of the Improved Ruthenium Stability in RuO_2–IrO_2 Mixed Oxides . *J. Electrochem. Soc.* **2016**, *163* (11), F3099–F3104. https://doi.org/10.1149/2.0131611jes.

(35) Zhang, B.; Zheng, X.; Voznyy, O.; Comin, R.; Bajdich, M.; García-Melchor, M.; Han, L.; Xu, J.; Liu, M.; Zheng, L.; De Arquer, F. P. G.; Dinh, C. T.; Fan, F.; Yuan, M.; Yassitepe, E.; Chen, N.; Regier, T.; Liu, P.; Li, Y.; De Luna, P.; Janmohamed, A.; Xin, H. L.; Yang, H.; Vojvodic, A.; Sargent, E. H. Homogeneously Dispersed Multimetal Oxygen-Evolving Catalysts. *Science (80-.).* **2016**, *352* (6283), 333–337. https://doi.org/10.1126/science.aaf1525.

(36) Huynh, M.; Ozel, T.; Liu, C.; Lau, E. C.; Nocera, D. G. Design of Template-Stabilized Active and Earth-Abundant Oxygen Evolution Catalysts in Acid. *Chem. Sci.* **2017**, *8* (7), 4779–4794. https://doi.org/10.1039/c7sc01239j.

(37) Nikoloski, A. N.; Nicol, M. J. Addition of Cobalt to Lead Anodes Used for Oxygen Evolutiona Literature Review. *Miner. Process. Extr. Metall. Rev.* **2010**, *31* (1), 30–57. https://doi.org/10.1080/08827500903404872.

(38) Li, Y.; Jiang, L.; Li, J.; Liu, Y. Novel Phosphorus-Doped Lead Oxide Electrode for Oxygen Evolution Reaction. *RSC Adv.* **2014**, *4* (11), 5339–5342. https://doi.org/10.1039/c3ra45760e.

(39) Velichenko, A. B.; Girenko, D. V.; Nikolenko, N. V.; Amadelli, R.; Baranova, E. A.; Danilov, F. I. Oxygen Evolution on Lead Dioxide Modified with Fluorine and Iron. *Russ. J. Electrochem.* **2000**, *36* (11), 1216–1220. https://doi.org/10.1007/BF02757697.

(40) Wu, X.; Tayal, J.; Basu, S.; Scott, K. Nano-Crystalline $Ru_xSn_{1-X}O_2$ Powder Catalysts for Oxygen Evolution Reaction in Proton Exchange Membrane Water Electrolysers. *Int. J. Hydrogen Energy* **2011**, *36* (22), 14796–14804. https://doi.org/10.1016/j.ijhydene.2011.01.067.

(41) Moreno-Hernandez, I. A.; Brunschwig, B. S.; Lewis, N. S. Crystalline Nickel, Cobalt, and Manganese Antimonates as Electrocatalysts for the Chlorine Evolution Reaction. *Energy Environ. Sci.* **2019**, *12* (4), 1241–1248. https://doi.org/10.1039/c8ee03676d.

(42) Evans, T. A.; Choi, K. S. Electrochemical Synthesis and Investigation of Stoichiometric, Phase - Pure $CoSb_2O_6$ and $MnSb_2O_6$ Electrodes for the Oxygen Evolution Reaction in Acidic Media. *ACS Appl. Energy Mater.* **2020**. https://doi.org/10.1021/acsaem.0c00526.

(43) Zhou, L.; Shinde, A.; Montoya, J. H.; Singh, A.; Gul, S.; Yano, J.; Ye, Y.; Crumlin, E. J.; Richter, M. H.; Cooper, J. K.; Stein, H. S.; Haber, J. A.; Persson, K. A.; Gregoire, J. M. Rutile Alloys in the Mn-Sb-O System Stabilize Mn^{3+} to Enable Oxygen Evolution in Strong Acid. *ACS Catal.* **2018**, *8* (12), 10938–10948. https://doi.org/10.1021/acscatal.8b02689.

(44) Povar, I.; Spinu, O. Ruthenium Redox Equilibria: 3. Pourbaix Diagrams for the Systems Ru-H_2O and Ru-Cl--H_2O. *J. Electrochem. Sci. Eng.* **2016**, *6* (1), 145. https://doi.org/10.5599/jese.229.

(45) Mun, C.; Cantrel, L.; Madic, C. Review of Literature on Ruthenium Behavior in Nuclear Power Plant Severe Accidents. *Nucl. Technol.* **2006**, *156* (3), 332–346. https://doi.org/10.13182/NT156-332.

(46) Kötz, R.; Lewerenz, H. J.; Stucki, S. XPS Studies of Oxygen Evolution on Ru and RuO_2 Anodes. *J. Electrochem. Soc.* **1983**, *130* (4), 825–829. https://doi.org/10.1149/1.2119829.

(47) Gerken, J. B.; McAlpin, J. G.; Chen, J. Y. C.; Rigsby, M. L.; Casey, W. H.; Britt, R. D.; Stahl, S. S. Electrochemical Water Oxidation with Cobalt-Based Electrocatalysts from PH 0-14: The Thermodynamic Basis for Catalyst Structure, Stability, and Activity. *J. Am. Chem. Soc.* **2011**, *133* (36), 14431–14442. https://doi.org/10.1021/ja205647m.

(48) Bloor, L. G.; Molina, P. I.; Symes, M. D.; Cronin, L. Low PH Electrolytic Water Splitting Using Earth-Abundant Metastable Catalysts That Self-Assemble in Situ. *J. Am. Chem. Soc.* **2014**, *136* (8), 3304–3311. https://doi.org/10.1021/ja5003197.

(49) Allegrezza, M.; Canino, M.; Bellettato, M.; Summonte, C. Transparent Conducting Oxides for High Temperature Processing. *Energy Procedia*. 2014, pp 23–31. https://doi.org/10.1016/j.egypro.2013.12.005.

(50) Yang, J. K.; Liang, B.; Zhao, M. J.; Gao, Y.; Zhang, F. C.; Zhao, H. L. Reference of Temperature and Time during Tempering Process for Non-Stoichiometric FTO Films. *Sci. Rep.* **2015**, *5*, 1–6. https://doi.org/10.1038/srep15001.

(51) Miller, H. A.; Bouzek, K.; Hnat, J.; Loos, S.; Bernäcker, C. I.; Weißgärber, T.; Röntzsch,

L.; Meier-Haack, J. Green Hydrogen from Anion Exchange Membrane Water Electrolysis: A Review of Recent Developments in Critical Materials and Operating Conditions. *Sustain. Energy Fuels* **2020**, *4* (5), 2114–2133. https://doi.org/10.1039/c9se01240k.

(52) Spöri, C.; Kwan, J. T. H.; Bonakdarpour, A.; Wilkinson, D. P.; Strasser, P. The Stability Challenges of Oxygen Evolving Catalysts: Towards a Common Fundamental Understanding and Mitigation of Catalyst Degradation. *Angew. Chemie - Int. Ed.* **2017**, *56* (22), 5994–6021. https://doi.org/10.1002/anie.201608601.

(53) Costentin, C.; Nocera, D. G. Self-Healing Catalysis in Water. *Proc. Natl. Acad. Sci. U. S. A.* **2017**, *114* (51), 13380–13384. https://doi.org/10.1073/pnas.1711836114.

(54) Lutterman, D. A.; Surendranath, Y.; Nocera, D. G. A Self-Healing Oxygen-Evolving Catalyst. *JACS Commun.* **2009**, No. 131, 3838–3839.

(55) Huynh, M.; Bediako, D. K.; Nocera, D. G. A Functionally Stable Manganese Oxide Oxygen Evolution Catalyst in Acid. *JACS* **2014**, No. 136, 6002–6010. https://doi.org/10.1021/ja413147e.

(56) Bonke, S. A.; Abel, K. L.; Hoogeveen, D. A.; Chatti, M.; Gengenbach, T.; Fournier, M.; Spiccia, L.; Simonov, A. N. Electrolysis of Natural Waters Contaminated with Transition-Metal Ions: Identification of A Metastable FePb-Based Oxygen-Evolution Catalyst Operating in Weakly Acidic Solutions. *Chempluschem* **2018**, *83* (7), 704–710. https://doi.org/10.1002/cplu.201800020.

(57) C. D. Wanger, W. M. Riggs, L. E. Davis, J. F. M. and G. E. M. Handbook of X-ray Photoelectron Spectroscopy. *Perkin-Elmer Corp.* **1979**.

(58) Matthew, J. Surface Analysis by Auger and X-Ray Photoelectron Spectroscopy. D. Briggs and J. T. Grant (Eds). IMPublications, Chichester, UK and SurfaceSpectra, Manchester, UK, 2003. 900 Pp., ISBN 1-901019-04-7, 900 Pp. *Surf. Interface Anal.* **2004**, *36* (13), 1647–1647. https://doi.org/10.1002/sia.2005.

(59) Biesinger, M. C.; Payne, B. P.; Grosvenor, A. P.; Lau, L. W. M.; Gerson, A. R.; Smart, R. S. C. Resolving Surface Chemical States in XPS Analysis of First Row Transition Metals, Oxides and Hydroxides: Cr, Mn, Fe, Co and Ni. *Appl. Surf. Sci.* **2011**, *257* (7), 2717–2730. https://doi.org/10.1016/j.apsusc.2010.10.051.

(60) Sabri, M.; King, H. J.; Gummow, R. J.; Lu, X.; Zhao, C.; Oelgemöller, M.; Chang, S. L. Y.; Hocking, R. K. Oxidant or Catalyst for Oxidation? A Study of How Structure and Disorder Change the Selectivity for Direct versus Catalytic Oxidation Mediated by Manganese(III,IV) Oxides. *Chem. Mater.* **2018**, *30* (22), 8244–8256. https://doi.org/10.1021/acs.chemmater.8b03661.

(61) Hocking, R. K.; Gummow, R. J.; King, H. J.; Sabri, M.; Kappen, P.; Dwyer, C.; Chang, S. L. Y. Direct Formation of 2D-MnO_x under Conditions of Water Oxidation Catalysis. *ACS Appl. Nano Mater.* **2018**, *1* (4), 1603–1611. https://doi.org/10.1021/acsanm.8b00095.

(62) King, H. J.; Fournier, M.; Bonke, S. A.; Seeman, E.; Chatti, M.; Jumabekov, A. N.; Johannessen, B.; Kappen, P.; Simonov, A. N.; Hocking, R. K. Photon-Induced, Timescale,

and Electrode Effects Critical for the in Situ X-Ray Spectroscopic Analysis of Electrocatalysts: The Water Oxidation Case. *J. Phys. Chem. C* **2019**, *123* (47), 28533–28549. https://doi.org/10.1021/acs.jpcc.9b06944.

(63) Reimers, J. N.; Greedan, J. E.; Stager, C. V.; Kremer, R. Crystal Structure and Magnetism in $CoSb_2O_6$ and $CoTa_2O_6$. *Journal of Solid State Chemistry*. 1989, pp 20–30. https://doi.org/10.1016/0022-4596(89)90049-2.

(64) H.Vincent, X.Turrillas, I. R. A Novel Structural Type of Hexagonal Closest Packing the Ternary Oxide, β-$MnSb_2O_6$. *Mater. Res. Bull.* **1987**, *22* (10), 1369–1379.

(65) Donaldson, J. D.; Kjekshus, A.; Nicholson, D. G.; Rakke, T. Properties of Sb-Compounds with Rutile like Structures. *Acta Chem. Scand. A 29* **1975**, 803–809.

(66) Morgan, D. J. Resolving Ruthenium: XPS Studies of Common Ruthenium Materials. *Surf. Interface Anal.* **2015**, *47* (11), 1072–1079. https://doi.org/10.1002/sia.5852.

(67) Ardizzone, S.; Bianchi, C. L.; Cappelletti, G.; Ionita, M.; Minguzzi, A.; Rondinini, S.; Vertova, A. Composite Ternary SnO_2-IrO_2-Ta_2O_5 Oxide Electrocatalysts. *J. Electroanal. Chem.* **2006**, *589* (1), 160–166. https://doi.org/10.1016/j.jelechem.2006.02.004.

(68) Etzi Coller Pascuzzi, M.; Goryachev, A.; Hofmann, J. P.; Hensen, E. J. M. Mn Promotion of Rutile TiO_2-RuO_2 Anodes for Water Oxidation in Acidic Media. *Applied Catalysis B: Environmental*. 2020. https://doi.org/10.1016/j.apcatb.2019.118225.

(69) Kropáček, V.; Krs, M.; Bucha, V. Magnetic Properties of Natural Mn-Oxides. *Stud. Geophys. Geod.* **1975**, *19* (3), 261–274. https://doi.org/10.1007/BF01614255.

(70) Ganguly, S.; Kabir, M.; Sanyal, B.; Mookerjee, A. Unusual Structure and Magnetism in Manganese Oxide Nanoclusters. *Phys. Rev. B - Condens. Matter Mater. Phys.* **2011**, *83* (2), 2–5. https://doi.org/10.1103/PhysRevB.83.020411.

(71) Ghadge, S. D.; Velikokhatnyi, O. I.; Datta, M. K.; Shanthi, P. M.; Tan, S.; Kumta, P. N. Computational and Experimental Study of Fluorine Doped $(Mn_{1-X}Nb_x)O_2$ Nanorod Electrocatalysts for Acid-Mediated Oxygen Evolution Reaction. *ACS Appl. Energy Mater.* **2020**, *3* (1), 541–557. https://doi.org/10.1021/acsaem.9b01796.

(72) Xiao, B. B.; Jiang, X. B.; Jiang, Q. Density Functional Theory Study of Oxygen Reduction Reaction on Pt/Pd3Al(111) Alloy Electrocatalyst. *Phys. Chem. Chem. Phys.* **2016**, *18* (21), 14234–14243. https://doi.org/10.1039/c6cp01066k.

(73) Russell, A. E. Electrocatalysis: Theory and Experiment at the Interface. *Phys. Chem. Chem. Phys.* **2008**, *10* (25), 3607–3608. https://doi.org/10.1039/b808799g.

(74) Lv, X.; Wei, W.; Wang, H.; Huang, B.; Dai, Y. Multifunctional Electrocatalyst PtM with Low Pt Loading and High Activity towards Hydrogen and Oxygen Electrode Reactions: A Computational Study. *Applied Catalysis B: Environmental*. 2019. https://doi.org/10.1016/j.apcatb.2019.05.045.

(75) Wang, L.; Roudgar, A.; Eikerling, M. Ab Initio Study of Stability and Site-Specific Oxygen Adsorption Energies of Pt Nanoparticles. *J. Phys. Chem. C* **2009**, *113* (42), 17989–17996. https://doi.org/10.1021/jp900965q.

(76) Kadakia, K.; Datta, M. K.; Velikokhatnyi, O. I.; Jampani, P.; Park, S. K.; Saha, P.; Poston, J. A.; Manivannan, A.; Kumta, P. N. Novel (Ir,Sn,Nb)O_2 Anode Electrocatalysts with Reduced Noble Metal Content for PEM Based Water Electrolysis. *International Journal of Hydrogen Energy*. 2012, pp 3001–3013. https://doi.org/10.1016/j.ijhydene.2011.11.055.

(77) Luo, Y. R. Comprehensive Handbook of Chemical Bond Energies. *CRC Press. Boca Rat.* **2007**.

(78) Chen, J.; Selloni, A. Electronic States and Magnetic Structure at the Co_3O_4(110) Surface: A First-Principles Study. *Phys. Rev. B - Condens. Matter Mater. Phys.* **2012**, *85* (8), 1–9. https://doi.org/10.1103/PhysRevB.85.085306.

(79) C.A.F.Vaz, H.-Q.Wang, C.H.Ahn, V.E.Henrich, M.Z.Baykara, T.C.Schwendemann, N.Pilet, B.J.Albers, U.D.Schwarz, L.H.Zhang, Y.Zhu, J.Wang, E. I. A. Interface and Electronic Characterization of Thin Epitaxial Co3O4 Films. *Surf. Sci.* **2009**, *603* (2), 291–297.

(80) Tasker, P. W. The Stability of Ionic Crystal Surfaces. *J. Phys. C Solid State Phys.* **1979**, *12* (22), 4977–4984. https://doi.org/10.1088/0022-3719/12/22/036.

(81) Ong, S. P.; Wang, L.; Kang, B.; Ceder, G. Li - Fe - P - O_2 Phase Diagram from First Principles Calculations. *Chem. Mater.* **2008**, *20* (5), 1798–1807. https://doi.org/10.1021/cm702327g.

(82) Gaudet, J.; Tavares, A. C.; Trasatti, S.; Guay, D. Physicochemical Characterization of Mixed RuO_2-SnO_2 Solid Solutions. *Chem. Mater.* **2005**, *17* (6), 1570–1579. https://doi.org/10.1021/cm048129l.

(83) Eskandrani, A. A.; Ali, S. M.; Al-Otaibi, H. M. Study of the Oxygen Evolution Reaction at Strontium Palladium Perovskite Electrocatalyst in Acidic Medium. *Int. J. Mol. Sci.* **2020**, *21* (11). https://doi.org/10.3390/ijms21113785.

(84) Suermann, M.; Schmidt, T. J.; Büchi, F. N. Comparing the Kinetic Activation Energy of the Oxygen Evolution and Reduction Reactions. *Electrochimica Acta*. 2018, pp 466–471. https://doi.org/10.1016/j.electacta.2018.05.150.

(85) Jansenyl, V. M. Kristallstruktur von Sb2O5. *Angew. Chem.* **1978**, *690* (2), 141–142.

(86) Boman, C.-E.; Danielsen, J.; Haaland, A.; Jerslev, B.; Schäffer, C. E.; Sunde, E.; Sørensen, N. A. Refinement of the Crystal Structure of Ruthenium Dioxide. *Acta Chemica Scandinavica*. 1970, pp 116–122. https://doi.org/10.3891/acta.chem.scand.24-0116.

(87) J.D. Donaldson, A. Kjekshus, D.G. Nicholson, T. R. Properties of Sb-Compounds with Rutile like Structures. *Acta Chem. Scand. A 29* **1975**, 803–809.

Chapter 4

Enhancement of the performance of Manganese Antimonate Electrocatalysts through Modification with Different Metal Oxides for the Acidic Water Oxidation at Ambient and Elevated Temperatures

4.1 INTRODUCTION

The previous chapter has demonstrated a highly durable and active catalytic material composed of nanocrystalline RuO_2 and highly disordered Sb^V oxides capable of operation at 80 °C at pH 0.3 for at least one week with no losses in performance. Combination of antimony with catalytically active cobalt and manganese produces corresponding antimonates which also exhibit improved stability during the OER in 0.5-1.0 M H_2SO_4 electrolyte solutions under ambient conditions,[1–4] which might be associated with the enhancement in the hybridisation of the oxygen p- and metal d-orbitals.[5] However, tests at elevated temperatures cause continuous degradation of Mn-Sb oxide catalysts during water electrooxidation at low pH, while the previously reported cobalt antimonate materials do not seem to exhibit neither sufficiently high catalytic activity nor stability.

This chapter aims to further explore the possibilities for the improvement in the performance of the mixed manganese-antimony oxide OER catalysts through the modification with other metals.

Our initial hypotheses were that the combinations of Mn-Sb oxides with Co[6] or small amounts of Ru[5,7–9] might enhance the catalytic activity, while the introduction of Pb[10–13] or Cr[14] can possibly improve the durability, although we also expected that some of these modifications can promote both key metrics of the catalytic system. Investigated materials were prepared as nominally flat films supported on F-doped SnO_2 electrodes by thermal decomposition of precursor salts (examples of scanning electron micrographs are shown in Figure 4.S1) and tested as water electrooxidation catalysts in 0.5 M H_2SO_4 under ambient conditions as well as at 60 and 80 °C. As a benchmark, a similarly synthesised $[Mn+Sb]O_x$ catalyst described in the previous chapter was used, which electrocatalytic activity and stability during the OER are alike to those of the highly-crystalline manganese antimonate described by others.[2]

4.2 RESULTS

The initial composition of the examined water oxidation electrocatalysts always included 1 μmol cm^{-2} Sb mixed with 1 μmol cm^{-2} of metals. For the major manganese-containing samples, the metal ratios were Mn : M = 0.67 : 0.33 for M = Co, Pb or Cr, Mn : Co : Pb = 0.50 : 0.25 : 0.25 and Mn : Ru = 0.95 : 0.05. During operation, this composition changed due to the corrosion (*vide infra*), which is unavoidable for essentially any known OER catalyst operating at low pH and especially at elevated temperatures.

4.2.1 Physical characterization

According to X-ray diffraction (XRD) analysis, the manganese-cobalt-antimony oxide system preserves the same major phase as in the previously studied $[Mn+Sb]O_x$ and $[Co+Sb]O_x$

materials, *viz.* tetragonal trirutile (Mn or Co)Sb_2O_6 antimonate structure,[5] and also contains a small admixture of Mn_3O_4 but not Co_3O_4 (Figure 4.1a). Contrasting this, intermixing Mn and Pb along with the antimony oxide matrix produces a different intermetallic phase – trigonal pyrochlore-related $(Mn\text{-}Pb)_2Sb_2O_7$ (Figure 4.1b). The observed positions of the major diffraction peaks for $[MnPb+Sb]O_x$ are located between the tabulated ones for $Mn_2Sb_2O_7$ and $Pb_2Sb_2O_7$, probably suggesting that manganese and lead are occupying the same metal sites and are homogenously intermixed within the crystal structure. The same pyrochlore-related phase was found as a dominant component of the control $[Pb+Sb]O_x$ material as well, which however also contained some $PbSb_2O_6$ (Figure 4.S2a). At the same time, the trimetallic Mn+Pb+Co combination was again found to favour the formation of the trirutile phase, yet with altered relative diffraction peak intensities indicative of some changes in the preferential crystallite orientation (Figure 4.1c).

The XRD data for the $[MnRu+Sb]O_x$ catalyst revealed a mixed structural scenario in this case with both $MnSb_2O_6$-type and $Mn_2Sb_2O_7$-type phases present (Figure 4.1d). This observation suggests that the presence of even a very low amount of ruthenium changes the way manganese-antimony oxides crystallise, notwithstanding previously demonstrated lack of the formation of any individual ruthenium antimonate phases under the employed synthesis conditions. Addition of chromium to the manganese-antimony oxide system produces an XRD pattern very closely matching the tabulated data for trirutile antimonate phase along with low-intensity signals from Mn_2O_3 admixture and probably very minor admixture of the $Mn_2Sb_2O_7$-type phase (Figure 4.1e), although the $[Cr+Sb]O_x$ control appeared to majorly contain $CrSbO_4$ (Figure 4.S2b).

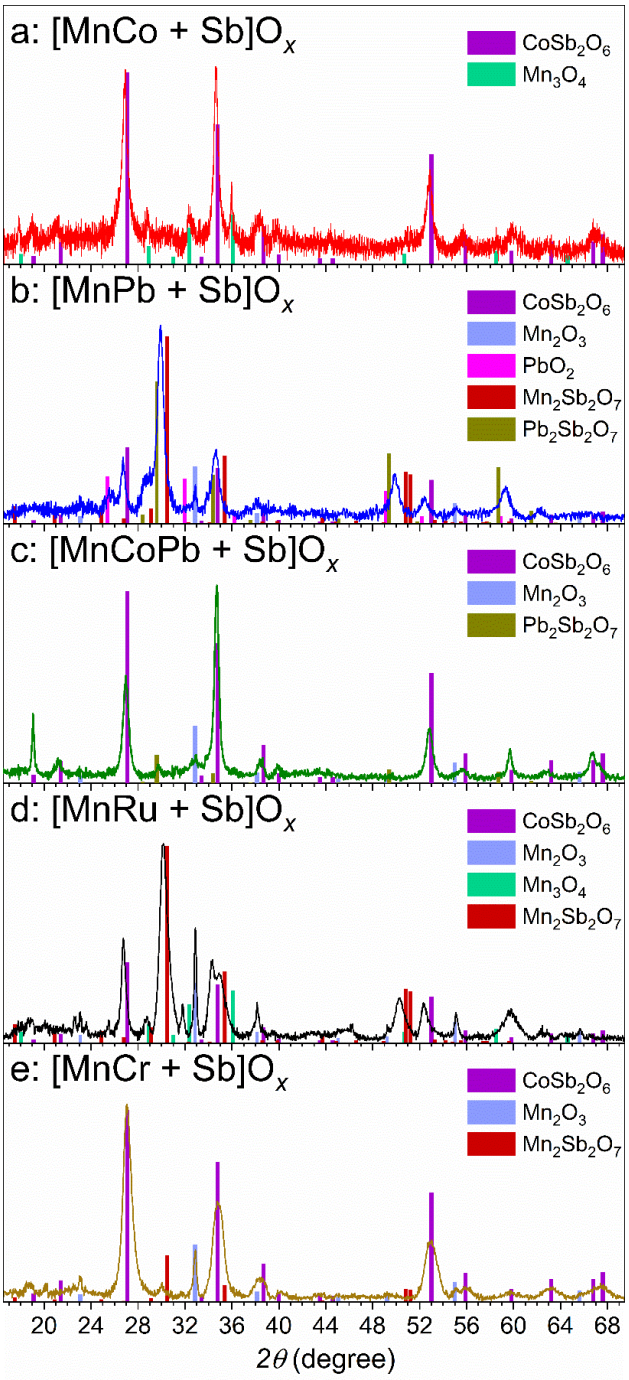

Figure 4.1. X-ray diffraction patterns of (a) [MnCo+Sb]O_x, (b) [MnPb+Sb]O_x, (c) [MnPbCo+Sb]O_x, (d) [MnRu+Sb]O_x, and (e) [MnCr+Sb]O_x. Vertical bars show tabulated positions and relative intensities for (a-e) $CoSb_2O_6$ ICSD-108964, (b-e) Mn_2O_3 ICDD-00-041-1442, (a, d) Mn_3O_4 ICDD-01-075-1560, (b, d-e) $Mn_2Sb_2O_7$ ICSD-1190856, (b) PbO_2 ICSD-23292 and (b-c) $Pb_2Sb_2O_7$ ICSD-24246.

X-ray photoelectron spectroscopic (XPS) analysis of the catalysts before and after (*vide infra*) electrocatalytic tests confirmed that antimony always adopts a ~5+ oxidation state in all multimetal antimony oxide catalysts studied herein (Figure 4.S3a-e), which is consistent with previous reports.[1,5] Major signal in the Mn 2p spectra was also similar for all freshly prepared and tested manganese-metal-antimony materials and consistent with the Mn^{3+} oxide/oxyhydroxide type species (Figure 4.S4a-e), although it is well-known that unambiguous discrimination between the manganese states based on the Mn 2p spectral data is highly ambiguous.[15] Nevertheless, it was noted that introduction of lead, chromium and ruthenium seems to increase the contribution of Mn^{2+} as suggested by the relative increase in the shake-up signal at *ca* 646-647 eV.[15] This effect appears to be most pronounced for the Pb-containing catalysts combinations [MnPb+Sb]O_x and [MnCoPb+Sb]O_x and quite interestingly was found to persist even after the OER tests (Figure 4.S4b-c). Similarly robust were the Co 2p spectra for [MnCo+Sb]O_x and [MnCoPb+Sb]O_x (Figure 4.S5) and Cr 2p data for [MnCr+Sb]O_x (Figure 4.S6). In both cases, the signals can be attributed to metals in their 3+ oxidation states.[15]

The Pb 4f spectra of the [MnPb+Sb]O_x and [MnCoPb +Sb]O_x catalysts as well as of the [Pb+Sb]O_x control exhibited major Pb $4f^{5/2}$ and Pb $4f^{7/2}$ signals at approximately 143.4-143.8 and 138.6-138.9 eV, respectively (Figure 4.S7), which are lower than those expected for individual Pb(IV) and Pb(II) oxides, although the available data do not allow to claim that none of those are actually present on the materials surface both before and after tests. Observed peaks are positioned in the binding energies range typical of inorganic Pb^{2+} salts, like lead titanate,[16] which is in principle consistent with the $Pb_2Sb_2O_7$-type compounds detected by XRD (Figure 4.1a). There were likely at least two components giving rise to signals with slightly different binding energies (within <0.5 eV) contributing to the detected Pb 4f spectra and changing in their ratio to

each other before and after tests (Figure 4.S7); however, we could not establish any conclusive trends associated with these observations.

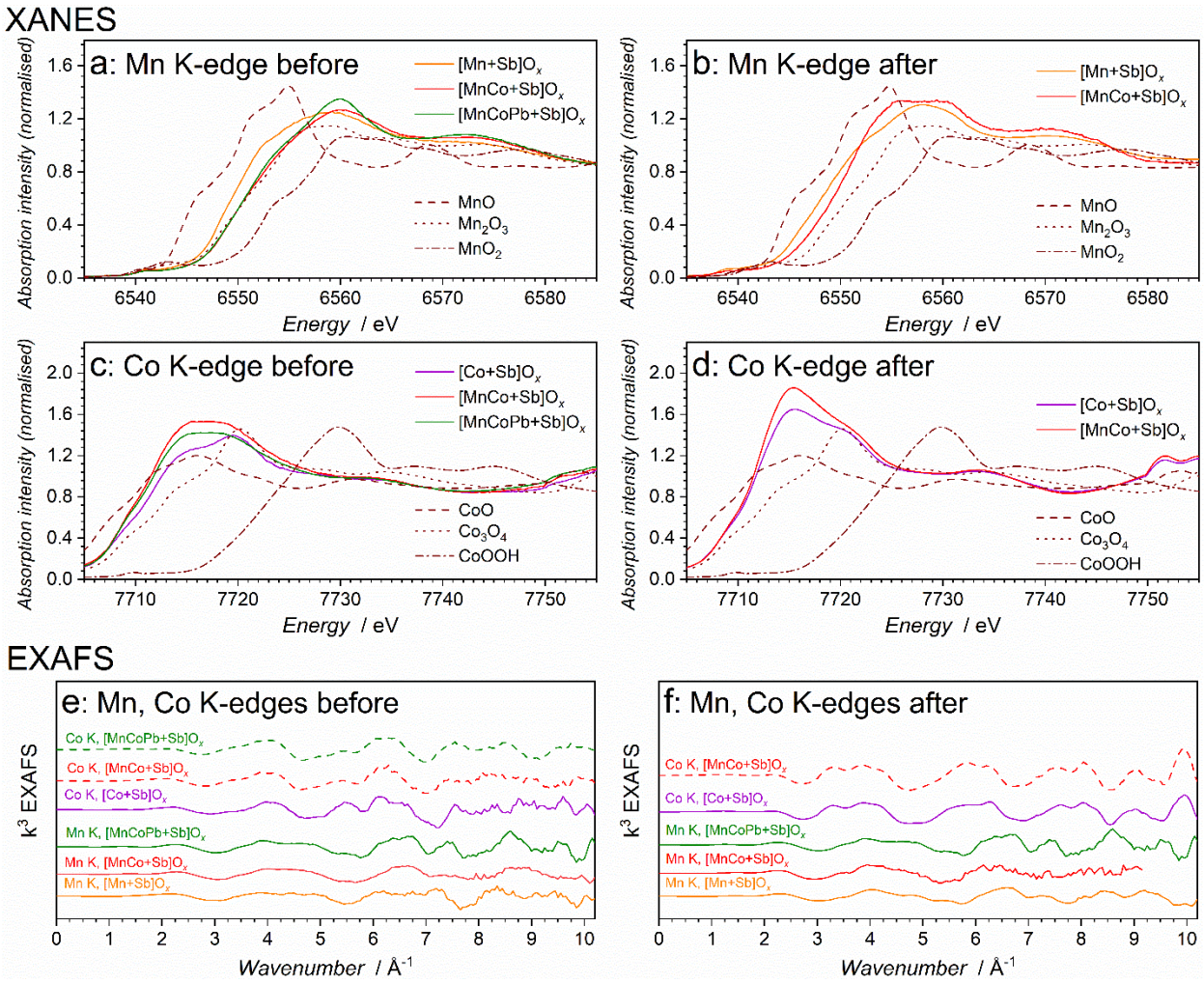

Figure 4.2. (a-d) XANES and (e-f) EXAFS data collected at Mn and Co K-edges for the [MnCo+Sb]O_x (*red*) and [MnCoPb+Sb]O_x (*green*) catalysts before and after OER tests (10 mA cm-2, 24 h, 24 ± 2 °C) compared to that for as-prepared and tested [Mn+Sb]O_x (*orange*) and [Co+Sb]O_x (*purple*) as well as relevant reference materials (see figure).

Finally, the small amounts of ruthenium introduced into the [MnRu+Sb]O_x catalyst could not be detected, which probably indicates their very low concentration on the surface in the as-prepared

sample. However, low-intensity signals that could be tentatively attributed to a combination of Ru^{3+}+Ru^{4+} emerged after the OER tests (Figure 4.S3d).[17]

To gain deeper insights into the structural features of the Co-based multimetallic antimonate catalysts, X-ray absorption spectroscopic (XAS) analysis was undertaken at Mn K, Co K, Pb L and Sb K-edges (Figure 4.2 and 4.3). Comparisons of the X-ray absorption near edge structure (XANES) data indicated that both Co and Mn appear more oxidised, with the dominating 3+ state, in the as-prepared [MnCo+Sb]O_x and [MnCoPb+Sb]O_x samples as opposed to the states found in [Mn+Sb]O_x and [Co+Sb]O_x (Figure 4.2a-b). This is likely due to the higher concentration of the individual metal oxide admixtures found in the monometallic reference materials (see Figure 3.3 in Chapter 3 and Ref.[5]). After the catalytic OER tests, the Mn K-edge XANES data for [MnCo+Sb]O_x and [Mn+Sb]O_x still showed some differences, though not to that significant extent as in the as-prepared materials (Figure 4.2c), which suggests similar states of manganese in the catalytically relevant state. Moreover, extended X-ray absorption fine structure (EXAFS) data show very similar features for these catalyst (Figure 4.2e), which are majorly consistent with the antimonate structure.[5] Even better agreement was observed at the Co K-edge XANES and EXAFS of the tested materials, where the data closely matched each other for [MnCo+Sb]O_x and [Co+Sb]O_x (Figure 4.2d and 4.2f), again attesting to the formation of the mixed metal trirutile antimonate phase, consistent with the XRD data (Figure 4.1a).

The oxidation state and structural features of lead in the as-prepared [MnCoPb+Sb]O_x material are clearly different from the examined Pb^{2+} and Pb^{4+} reference materials (Figure 4.3a and 4.3e), presumably reflecting possible incorporation of the lead into the multimetallic antimonate structure as suggested by XRD (Figure 4.1c). However, significant structural changes in the lead

component of this catalyst were induced by the OER tests (*vide infra*). Specifically, operating this material as a water oxidation catalyst resulted in essentially complete transformation of the lead component into lead(IV) oxide phase, as concluded on the basis of close to perfect match of both XANES and EXAFS data collected for tested [MnCoPb+Sb]O_x and PbO_2 reference (Figure 4.3b and 4.3f).

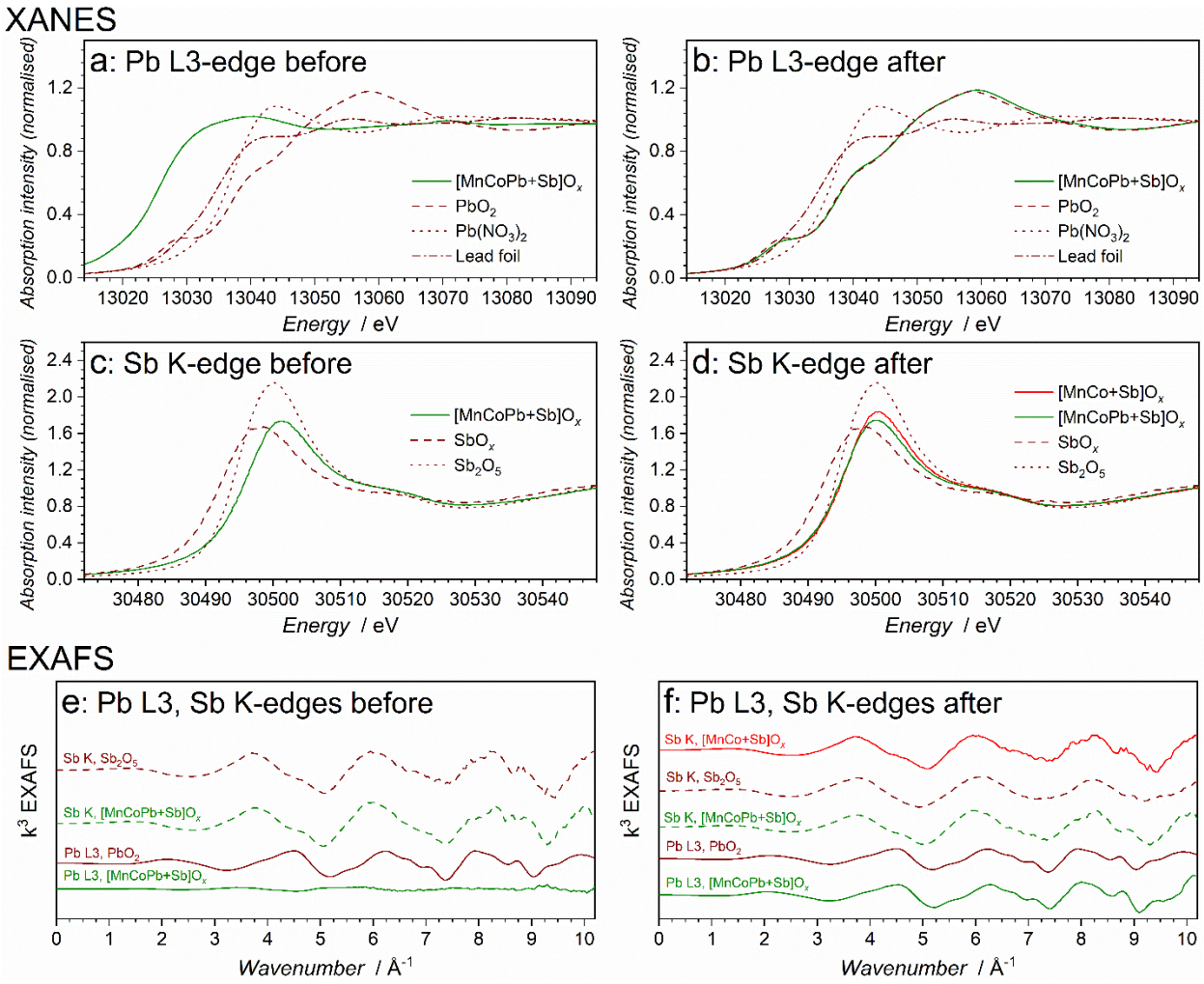

Figure 4.3. (a-d) XANES and (e-f) EXAFS data collected at Pb L and Sb K-edges for the [MnCo+Sb]O_x (*red*) and [MnCoPb+Sb]O_x (*green*) catalysts before and after OER tests (10 mA cm-2, 24 h, 24 ± 2 °C) compared to relevant reference materials (see figure).

In fact, this is consistent with the voltammetric data which exhibited a $Pb^{4+/2+}$ redox process discussed below (*vide infra*) – a fingerprint of the PbO_2-based electrodes.[13,18] Finally, Sb K-edge XAS data were majorly consistent with the antimony being present in the predominant 5+ oxidation state before and after catalytic tests (Figure 4.3c and 4.3d), closely matching the results obtained before for monometallic antimony-oxide based materials (Chapter 3 and Ref.[5]).

The aggregate of the physical characterization data described above attests to the successful integration of cobalt, lead and chromium oxides into the manganese-antimony oxide structure without formation of segregated metal oxide phases except for minor admixtures of Mn_2O_3 or Mn_3O_4, which were also observed in the control $[Mn+Sb]O_x$ catalyst. Another important observation is that major antimonate structure was $MnSb_2O_6$ trirutile for the materials containing cobalt and chromium, but combination of manganese-antimony oxides with Pb and Ru resulted in the formation of a pyrochlore-related $Mn_2Sb_2O_7$-type structures.

4.2.2 Electrocatalytic performance

All multimetallic OER catalysts examined herein reproducibly demonstrated improved activity with respect to the $[Mn+Sb]O_x$ control at ambient temperature (Figure 4.4a-c and Figures 4.S8-4.S12). Initially recorded voltammograms were reasonably stable and did not undergo significant changes with cycling except for the minor improvements in the oxidative currents for some of the catalysts (Figure 4.S13). The best OER activity was achieved for the $[MnRu+Sb]O_x$, which initially contained only 5 at.% Ru (with respect to the total metal loading) and enabled the water electrooxidation at the rate of 10 mA cm^{-2} (hereinafter all currents are normalised to the

geometric surface area of the electrodes) at an *IR*-corrected overpotential of η_{IR} = 0.45 ± 0.03 V at the start of the chronopotentiometric measurements (Figure 4.4b and Figure 4.S8).

Notably, this initial activity is only slightly lower than that of the similarly synthesised [Ru+Sb]O_x catalyst containing intermixed RuO_2 and Sb^V nanocrystallites (η_{IR} = 0.43 ± 0.01 V) described in the previous work. However, in contrast to the ruthenium-antimony system which only improved its activity during the operation, [MnRu+Sb]O_x slowly degraded to η_{IR} of 0.53 ± 0.03 V after 24 h of galvanostatic tests at 10 mA cm^{-2} (Figure 4.4b and Figure 4.S8). Although the chronopotentiometric measurements showed no stabilisation in the performance, the subsequently recorded short-term chronoamperograms were reasonably stable (Figure 4.4c) and voltammograms recorded before and after did not differ significantly both in the OER (Figure 4.S13a) and pre-catalytic regions (Figure 4.S14a). Collectively, these observations indicate that although the degradation is continuous, it is very slow on the examined timescale. The fact that ruthenium was detectable on the catalyst surface only after the OER tests (Figure 4.S3) along with the observed negligible level of the Ru corrosion and significant loss of Mn over the 24 h of operation (Table 4.1) suggest that the latter is the major cause of the observed deterioration of the activity. In other words, manganese-based species on the [MnRu+Sb]O_x appear to make a significant contribution to the electrocatalytic activity of the material, but are less stable than those in the [Mn+Sb]O_x reference which suffers negligible loss in the activity under the same conditions (Figure 4.4b). Among non-noble metal promoters, Cr induced the most significant enhancement in the initial performance (Figure 4.4a), notwithstanding similarly prepared CrO_y and [Cr+Sb]O_x references turned out to be essentially catalytically inactive towards the OER under examined conditions (Figure 4.S15).

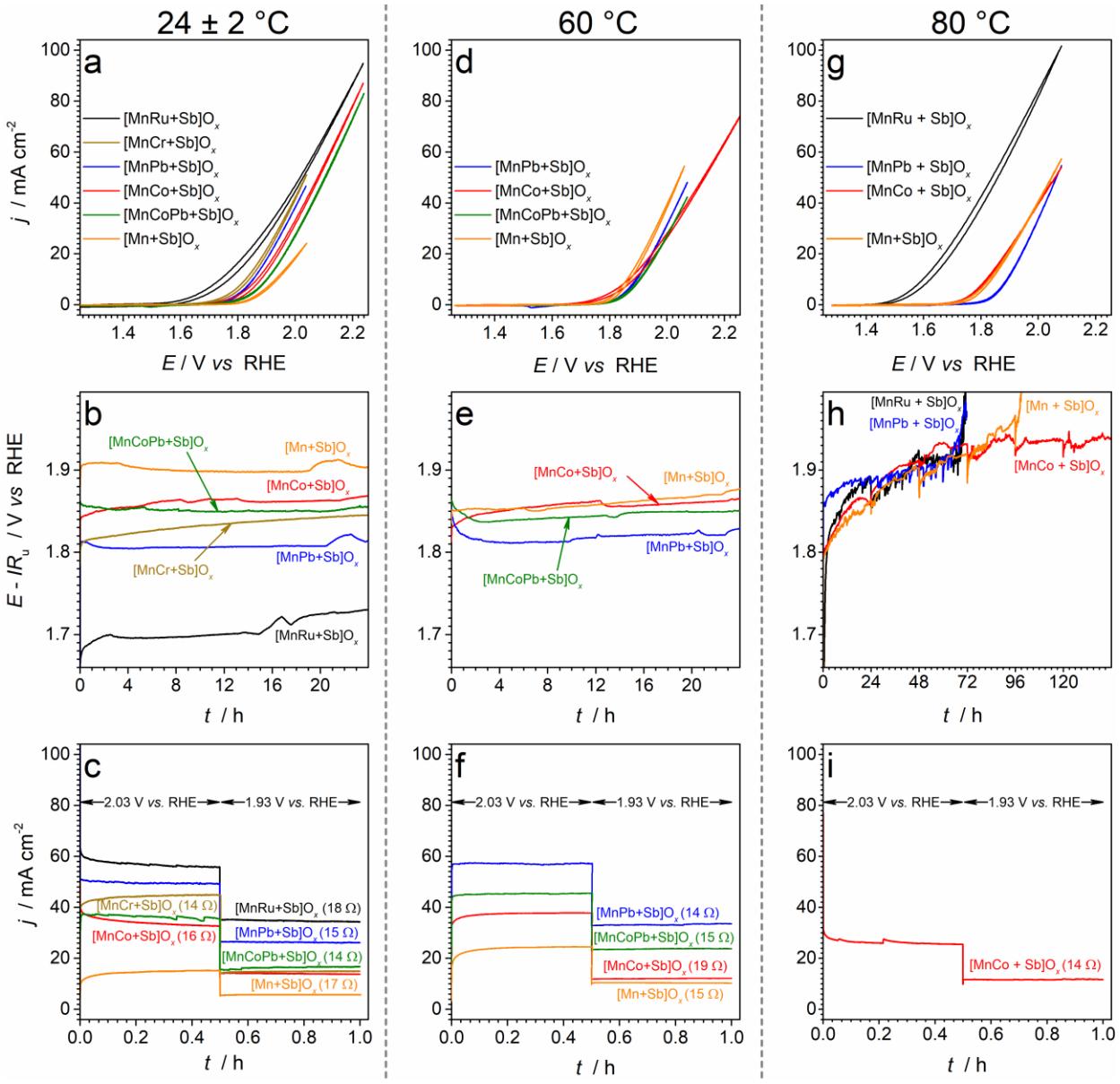

Figure 4.4. Electrocatalytic OER performance of the [MnRu+Sb]O_x (*black*), [MnCr+Sb]O_x (*dark yellow*), [MnPb+Sb]O_x (*blue*), [MnCo+Sb]O_x (*red*), [MnCoPb+Sb]O_x (*green*) and [Mn+Sb]O_x (*orange*) catalysts in stirred 0.5 M H_2SO_4 at (a-c) 24 ± 2, (d-f) 60 and (g-i) 80 °C: (a,d,g) cyclic voltammetry (scan rate 0.020 V s^{-1}; potentials are not IR_u-corrected), (b,e,h) IR_u-corrected chronopotentiograms (current density 10 mA $cm^{-2}_{geom.}$), and (c, f, i) chronoamperograms at potentials of 2.03 and 1.93 V *vs.* RHE. Currents are normalized to the geometric surface area. In panels c, f, and i, corresponding R_u values are provided in the brackets.

Table 4.1. Corrosion of catalysts[a] (at.%) during the OER in 0.5 M H_2SO_4.

Catalyst	24 ± 2 °C [b]			80 °C [c]		
	Mn	M	Sb	Mn	M	Sb
$[MnRu+Sb]O_x$	42	0	38	51	0	67
$[MnCr+Sb]O_x$	25	18	11	Not examined		
$[MnPb+Sb]O_x$	2	14	31	30	72	61
$[MnCo+Sb]O_x$	27	17	16	47	65	51

[a] Calculated based on the amount of metals initially deposited onto electrodes and the amounts of metal and Sb measured in the electrolyte solutions after tests using ICP-OES. [b] Chronopotentiometry at 10 mA cm^{-2} for 24 h and subsequent chronoamperometry at 2.03 and 1.93 V *vs.* RHE for 0.5 h at each potential. [c] Chronopotentiometry at 10 mA cm^{-2} after 72 h for $[MnRu+Sb]O_x$, 72 h for $[MnPb+Sb]O_x$ and 144 h for $[MnCo+Sb]O_x$, and subsequent chronoamperometry at 2.03 and 1.93 V *vs.* RHE for 0.5 h at each potential.

Previously, chromium has been suggested to increase the activity of noble metal and non-noble metal -based water electrooxidation catalysts in both acidic and alkaline medium through altered electronic structures, increase in surface active sites and adsorption energy of surface intermediates which led to enhanced reaction kinetics.[19–22] Although similar effects cannot be excluded for the $[MnCr+Sb]O_x$ system.

We also note that this particular catalyst exhibited the highest manganese-related redox signals in the pre-catalytic range of cyclic voltammograms (Figure 4.S14d) and the highest surface concentration of Mn derived from the XPS data (Table 4.S1) as compared to other catalysts investigated herein. In other words, its higher initial activity might be majorly associated with the increased concentration of the catalytically active Mn on the surface. This is circumstantially corroborated by a significant deterioration of the electrocatalytic performance during the galvanostatic test (Figure 4.4b, Figure 4.S12 and Figure 4.S13d) accompanied by a loss of Mn from $[MnCr+Sb]O_x$ (Table 4.1 and Table 4.S1). Most critically, the catalytic activity of the

manganese-chromium-based catalyst does not stabilise and continues to decline even after 24 h even at room temperature.

Notwithstanding the low pH OER electrocatalytic activity of [Co+Sb]O_x (η_{IR} = 0.769 ± 0.010 at 10 mA cm^{-2}, 24 ± 2 °C) is even lower than that of [Mn+Sb]O_x, the [MnCo+Sb]O_x catalyst combing the two metals demonstrated an improved performance with respect to the monometallic compounds (Figure 4.4a-c). Examination of the voltammetric (Figure 4.S14) and XPS data (Table 4.S1) did not reveal notable increase in the surface concentration of manganese species in this case. These observations suggest a synergistic effect of combining manganese and cobalt in a bimetallic antimonate trirutile-type phase on the water electrooxidation activity, although the magnitude of the enhancement was not very significant. Investigation of the effects of the initial metals ratio on the OER performance indicated that the increase in the cobalt amount beyond Mn : Co = 2 : 1 deteriorates the activity (Figure 4.S16). When operated over 24 h at a constant current density of 10 mA cm^{-2}, [MnCo+Sb]O_x cannot maintain its initial activity and suffers partial corrosion of all elements (Table 4.1) resulting in a decrease in the surface concentrations of the catalytically active species (Table 4.S1). However, in contrast to [MnCr+Sb]O_x, the Mn-Co-based catalyst reproducibly achieved stabilised performance after approximately 12 h of operation at 10 mA cm^{-2} (Figure 4.S9) with an IR_u-corrected overpotential approximately 0.03 V less than that for the manganese-antimony oxide reference.

The key distinction of [MnPb+Sb]O_x from other bimetallic systems analysed herein was the very low level of corrosion of Mn during operation at ambient temperature both in the bulk (Table 4.1) and on the surface (Table 4.S1), highlighting the cumulative stabilising effect of lead and antimony oxides. In fact, this effect applied to both [MnPb+Sb]O_x and [MnCoPb+Sb]O_x,

which maintained the OER rate of 10 mA cm^{-2} at highly stable and reproducible overpotentials during 24 h tests that were lower by *ca* 0.09 V and 0.05 V with respect to $[Mn+Sb]O_x$, respectively (Figure 4.4a-c). Given that both PbO_y and $[Pb+Sb]O_x$ are not highly active OER catalysts under examined conditions (Figure 4.S15) and no enrichment of the catalyst surfaces with Mn was found upon introduction of Pb (Table 4.S1), the enhanced activity can be attributed to the promoting effect of lead on the catalytic activity of the manganese-based active species. In fact, voltammetric characterisation after the OER tests indicated significant increase in the amount of Pb on the electroactive surface (concluded from the enhanced intensity of the typical $Pb^{4+/2+}$ reduction peak at *ca* 1.49 V *vs.* RHE; Figure 4.S14c,e), which further emphasise an important role of lead in stabilising and improving the performance of the Mn-Sb oxide system. As mentioned above, this observation is consistent with the XAS data, which indicate the formation of significant amount of PbO_2 after the OER tests in the $[MnCoPb+Sb]O_x$ catalyst (Figure 4.3). This suggests that lead is present as Pb^{4+} on the active catalyst surface, and probably stabilises the catalytically active species through the formation of the acid stable PbO_2 matrix. Another interesting observation was that the stabilised activity of $[MnPb+Sb]O_x$, dominated by a $(Pb+Mn)_2Sb_2O_7$ pyrochlore-related phase, was slightly better than that of $[MnCoPb+Sb]O_x$, which majorly contained a trirutile antimonate phase (best seen in chronoamperograms in Figure 4.4c).

While improved catalytic activity coupled to reasonable stability achieved at ambient temperature through the modification of $[Mn+Sb]O_x$ with some of the metals is a promising result, the conclusion on the suitability of the new catalysts for the applications in PEM water electrolysers can be only made is they maintain integrity at elevated temperatures. Previous study revealed that $[Mn+Sb]O_x$ continuously degraded at a slow but persistent rate of *ca* 0.002 V h^{-1}

when tested at 60 and 80 °C in 0.5 M H_2SO_4, and it was important to explore if any of the promoters could improve on this behaviour. [MnCr+Sb]O_x was not considered for the detailed studies at elevated temperatures due to the very rapid and complete degradation (Figure 4.S17), consistent with the instability observed even at 24 ± 2 °C (Figure 4.4b).

When tested at 60 °C, a positive effect of temperature on the OER kinetics was not observed for any of the new catalysts even in the initially recorded voltammograms, contrasting the behaviour of the [Mn+Sb]O_x reference which demonstrated an expected enhancement in the water oxidation rate (Figure 4.4d-f and Figure 4.S18-4.S19). In essence, the increase in temperature from 24 ± 2 to 60 °C did not change the potentials recorded at 10 mA cm^{-2} for [MnCo+Sb]O_x, [MnPb+Sb]O_x and [MnPbCo+Sb]O_x. This unfavourable behaviour likely reflects a significant degradation of active sites which occurs immediately upon immersion of the catalysts into the heated electrolyte solution. On a positive side, the most stable [MnPb+Sb]O_x and [MnPbCo+Sb]O_x materials undergo partial self-healing during the initial hours of operation at 60 °C and improve in their performance with time, eventually demonstrating the quasi-stabilised OER activity better than that of [Mn+Sb]O_x (Figure 4.4e and Figure 4.S20). Most likely, this improvement occurs through the redeposition of the dissolved metals and antimony species at positive potentials,[13] but the available concentrations of the catalyst precursors are not sufficient to enable expected high catalytic activity at elevated temperature.

Operation at 80 °C did not allow for any improvements in the initial performance of the noble-metal-free [MnPb+Sb]O_x and [MnCo+Sb]O_x, but the voltammetric characterisation of the most active [MnRu+Sb]O_x catalyst under these conditions did demonstrate the conventional effect of temperature on the OER kinetics (Figure 4.4g). Subsequent galvanostatic tests were undertaken

for the extended periods of time to assess if establishment of an equilibrium between dissolved precursors and solid catalyst species on the electrode surface is possible under such harsh conditions. Previously reported tests of [Mn+Sb]O_x at 80 °C demonstrated that this catalyst starts losing its activity very rapidly after approximately 96 h of slow degradation. Herein, qualitatively similar behaviour was demonstrated by both [MnRu+Sb]O_x and [MnPb+Sb]O_x, although the initial slow deterioration period was even shorter (*ca* 63 h) (Figure 4.4h). This indicates that the kinetics of the catalyst dissolution at this temperature notably outruns the corresponding rates of the competing catalyst self-healing processes through the *in-situ* electrodeposition. Most interestingly, it was found that the [MnCo+Sb]O_x system was the only that could achieve a quasi-stabilised state after approximately 80 h of slow degradation up to potential of 1.92 V *vs.* RHE, which was further maintained relatively stable for at least 64 h (Figure 4.4h). Subsequently recorded chronoamperograms further confirmed the stability of the system (Figure 4.4i). At this point, approximately 50% of the initially deposited Mn, Co and Sb was released into the electrolyte solution (Table 4.1), which turned out to be sufficient to achieve a dissolution/redeposition equilibrium enabling operation of the catalyst in a self-healing mode.

4.3 DISCUSSION

Figure 4.5 provides a summary of the electrocatalytic performance of the multimetallic manganese-based antimonate OER catalysts operating in 0.5 M H_2SO_4 compared to [Mn+Sb]O_x. The key conclusion from these data is that the significant improvements in activity are achieved at 24 ± 2 °C only, while operation at higher temperatures induces notable losses in the catalytically active sites on the surface of multimetal materials.

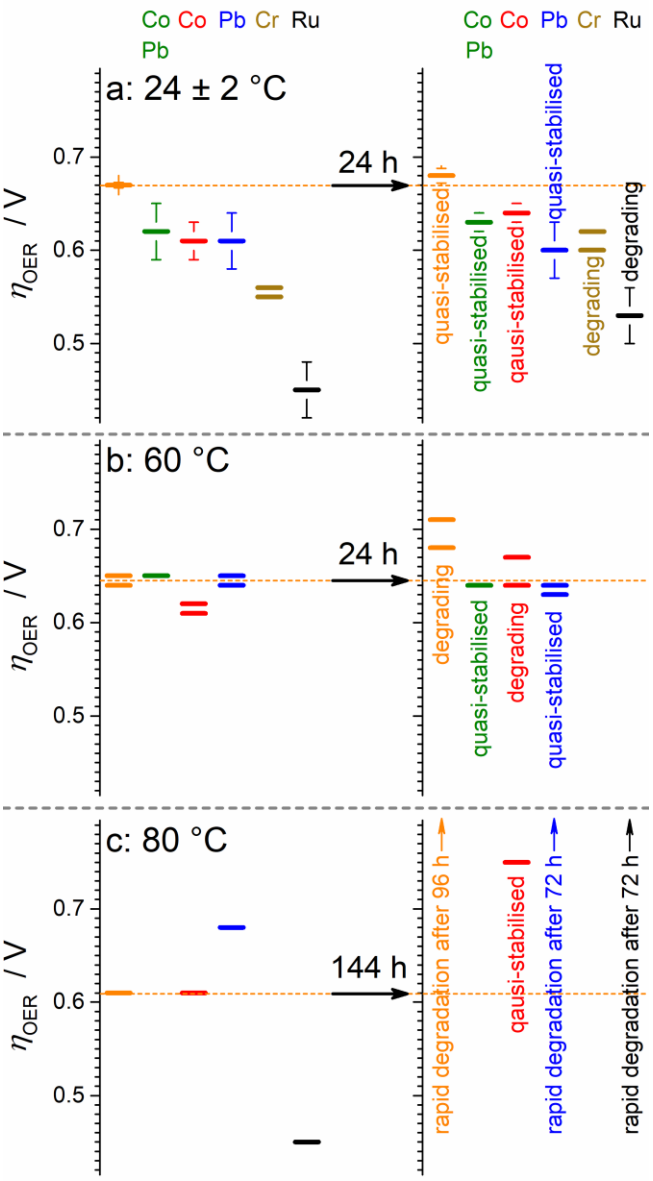

Figure 4.5. Summary of the effects of different promotors on the electrocatalytic activity of the manganese-antimony oxide catalysts for the OER in stirred 0.5 M H_2SO_4 at the beginning (*left*) and the end (*right*) of the tests at (a) ambient temperature, (b) 60 and (c) 80 °C. Data are presented either as mean ± one standard deviation for at least three independent repeats or as individual experimental data points where only one or two independent tests were undertaken. Data are colour coded as follows: $[Mn+Sb]O_x$ – *orange*; $[MnCoPb+Sb]O_x$ – *green*; $[MnCo+Sb]O_x$ – *red*; $[MnPb+Sb]O_x$ – *blue*; $[MnCr+Sb]O_x$ – *dark yellow*; and $[MnCo+Ru]O_x$ – *black*.

Enhanced performance provided by chromium modification is majorly attributed to the increased surface concentration of manganese in [MnCr+Sb]O_x, which also results in the weakest operational stability of this catalysts among examined materials. A more interesting scenario applies in the case of Co and Pb promotors, which produce structurally different materials – (MnCo)Sb_2O_6 and $(MnPb)_2Sb_2O_7$ antimonates. Comparisons of the stabilised catalytic activity of the two at 24 ± 2 °C (Figure 4.5a) suggests that the pyrochlore-related phase is more catalytically active. This hypothesis is circumstantially confirmed by the fact that the stabilised activity of [MnCoPb+Sb]O_x, also dominated by the trirutile-type structure, is similar to that of [MnCo+Sb]O_x but is lower than that of [MnPb+Sb]O_x.

While the [MnRu+Sb]O_x catalyst also contains the $Mn_2Sb_2O_7$-type phase, the presence of ruthenium is likely a more dominant factor determining its higher activity as compared to other catalysts. At the same time, notwithstanding the pyrochlore-related structure might provide advantages in activity, it also appears to be less stable than the trirutile antimonate phase. This is particularly best seen when considering the results at 80 °C, where a potentially more stable lead-containing [MnPb+Sb]O_x system was found to degrade rapidly after initial slow decay in performance, while the [MnCo+Sb]O_x catalyst achieved a quasi-stabilisation (Figure 4.5c). The latter observation highlights that future optimisation are possible through the provision of appropriate self-healing conditions, *i.e.* intentional introduction of the metal precursors to the electrolysed solutions. This should be also possible with the more catalytically active [MnPb+Sb]O_x material as demonstrated by the gradual improvements in its activity at 60 °C upon initial degradation (Figure 4.4e and Figure 4.5b).

4.4 CONCLUSIONS

Overall, the present study demonstrates significant enhancements in the performance of the promising manganese-antimony acidic water oxidation catalysts through the modification with other metals. The most notable improvements are achieved upon introduction of lead and small amounts of ruthenium. The ability of Pb to further stabilise manganese active sites within the antimonate matrix is another important finding. Future work building upon these findings and implementing the strategies to improve the stability discussed above is likely to open a range of opportunities for the design of new, more stable OER catalysts operating at low pH and elevated temperature.

4.5 SUPPLEMENTARY INFORMATION

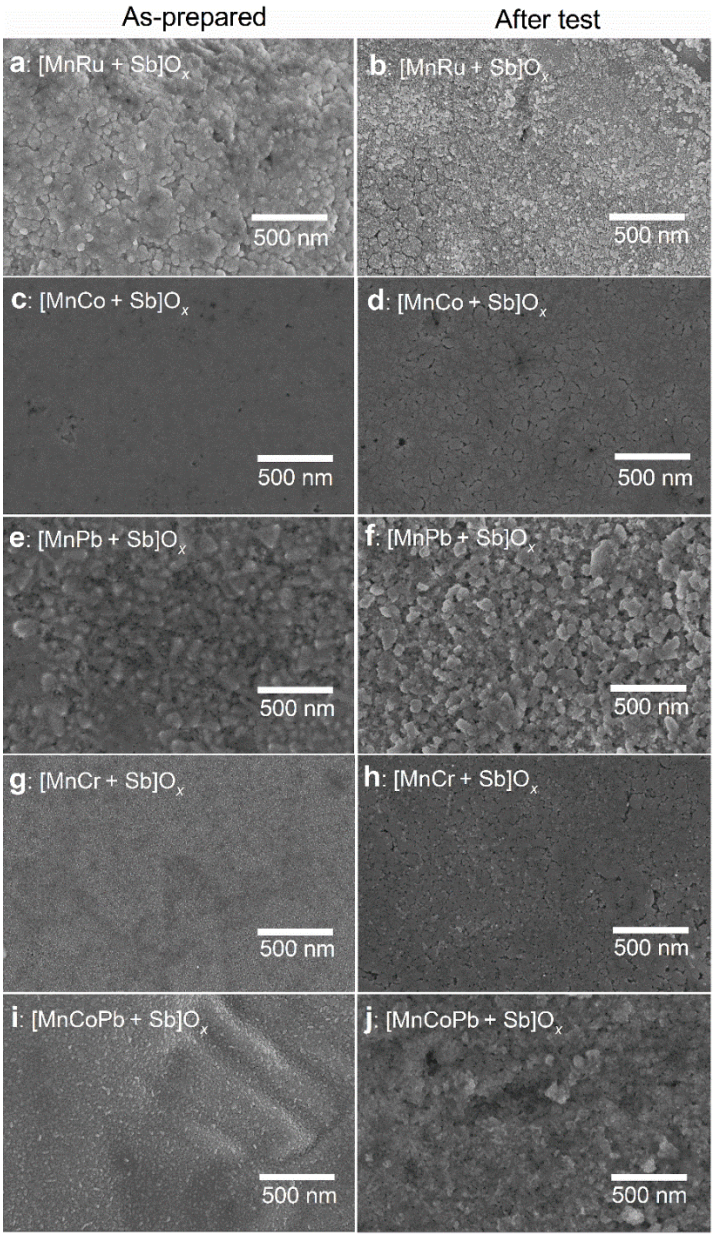

Figure 4.S1. Scanning electron micrographs of the catalysts (a-b) [MnRu + Sb]O_x, (c-d) [MnCo + Sb]O_x, (e-f) [MnPb + Sb]O_x, (g-h) [MnCr + Sb]O_x and (i-j) [MnPbCo + Sb]O_x where (a, c, e, g, i) before and (b, d, f, h, j) after 24 h galvanostatic (at 10 mA $cm^{-2}_{geom.}$) and subsequent 1 h potentiostatic (at 2.03 and 1.93 V *vs.* RHE for 0.5 h at each potential) operation in stirred 0.5 M H_2SO_4 at ambient temperature.

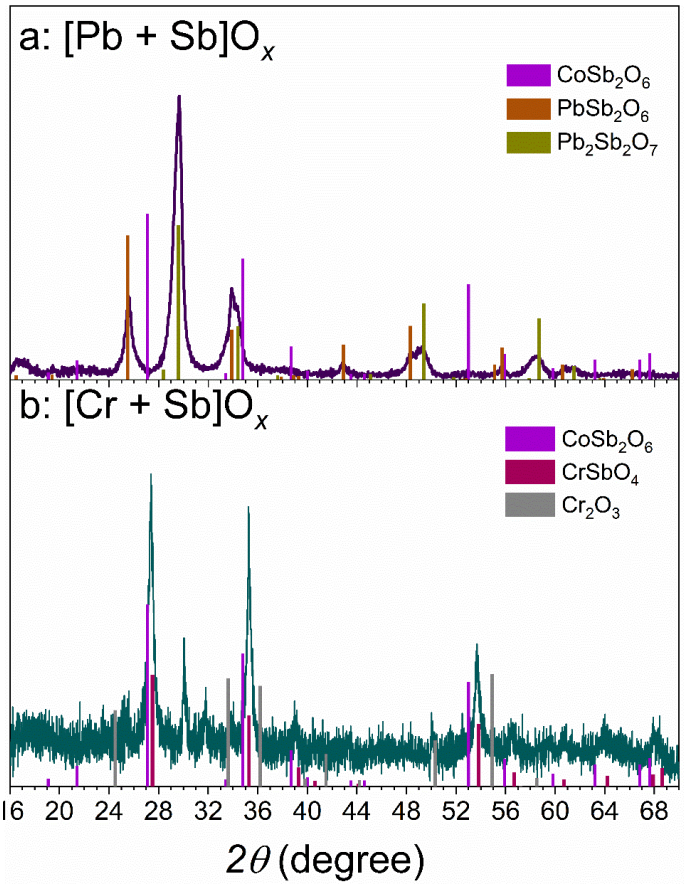

Figure 4.S2. X-ray diffraction patterns of (a) [Pb + Sb]O_x, and (b) [Cr + Sb]O_x. Vertical bars show tabulated positions and relative intensities for (a-b) $CoSb_2O_6$ ICSD-108964, (a) $PbSb_2O_6$ ICSD-81387, (a) $Pb_2Sb_2O_7$ ICSD-24246, (b) $CrSbO_4$ ICSD-108880 and (b) Cr_2O_3 ICSD-167268.

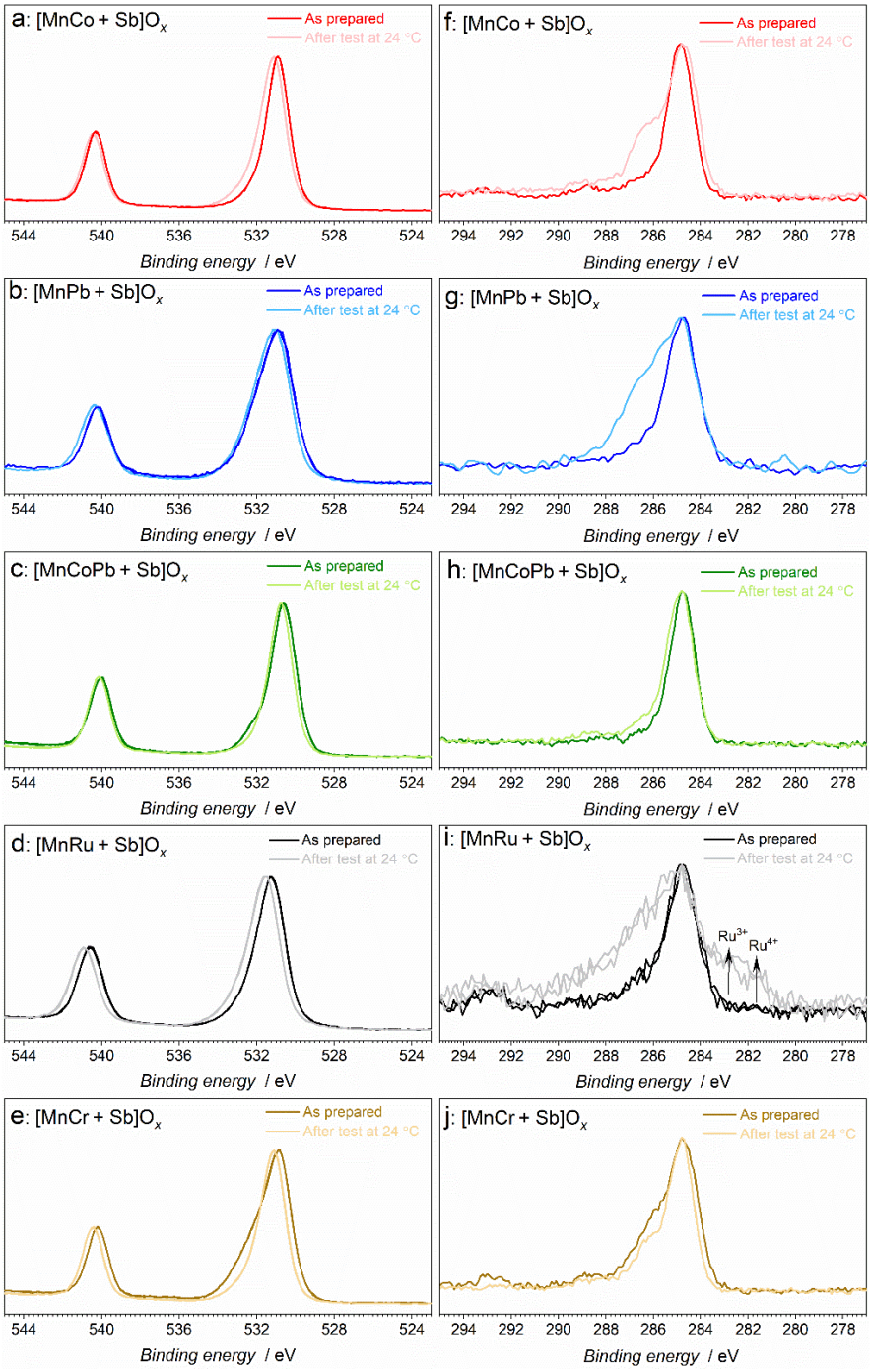

Figure 4.S3. (a-e) Sb 3d + O 1s and (f-j) C 1s (+ Ru 3d) spectra for the catalysts (a, f) [MnCo + Sb]O$_x$, (b, g) [MnPb + Sb]O$_x$, (c, h) [MnCoPb + Sb]O$_x$, (d, i) [MnRu + Sb]O$_x$ and (e, j) [MnCr + Sb]O$_x$ before (vivid traces) and after (pale traces) electrocatalytic OER tests in stirred 0.5 M H_2SO_4. The catalysts were tested subsequently for 24 h at 10 mA cm^{-2}, 0.5 h at 2.03 V *vs.* RHE, and 0.5 h at 1.93 V *vs.* RHE at ambient temperature.

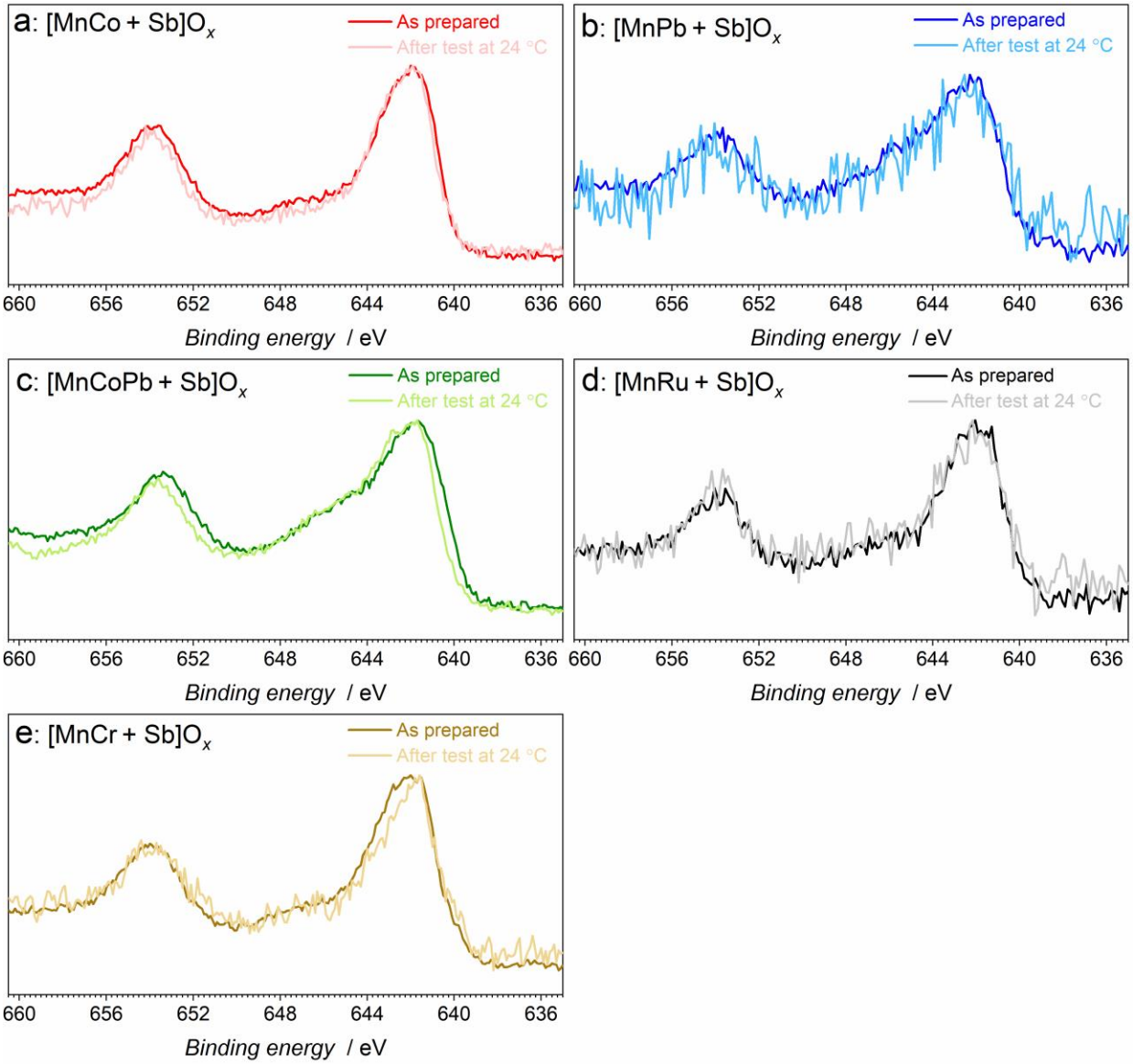

Figure 4.S4. Mn 2p spectra for catalysts (a) [MnCo + Sb]O_x, (b) [MnPb + Sb]O_x, (c) [MnCoPb + Sb]O_x, (d) [MnRu + Sb]O_x and (e) [MnCr + Sb]O_x before (vivid traces) and after (pale traces) electrocatalytic OER tests in stirred 0.5 M H_2SO_4. The catalysts were tested subsequently for 24 h at 10 mA cm^{-2}, 0.5 h at 2.03 V *vs.* RHE, and 0.5 h at 1.93 V *vs.* RHE at ambient temperature.

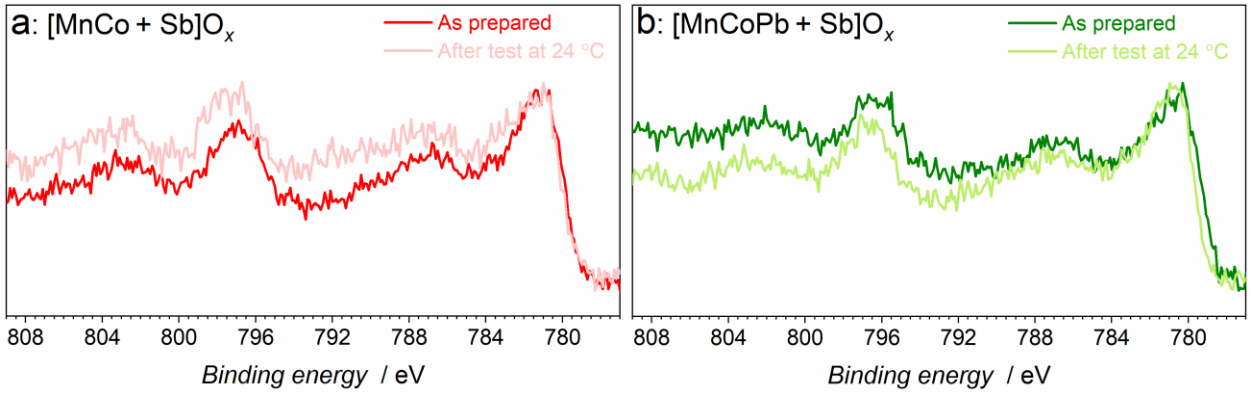

Figure 4.S5. Co 2p spectra for (a) [MnCo + Sb]O_x, and (b) [MnCoPb + Sb]O_x before (vivid traces) and after (pale traces) electrocatalytic OER tests in stirred 0.5 M H_2SO_4. The catalysts were tested subsequently for 24 h at 10 mA cm^{-2}, 0.5 h at 2.03 V *vs.* RHE, and 0.5 h at 1.93 V *vs.* RHE at ambient temperature.

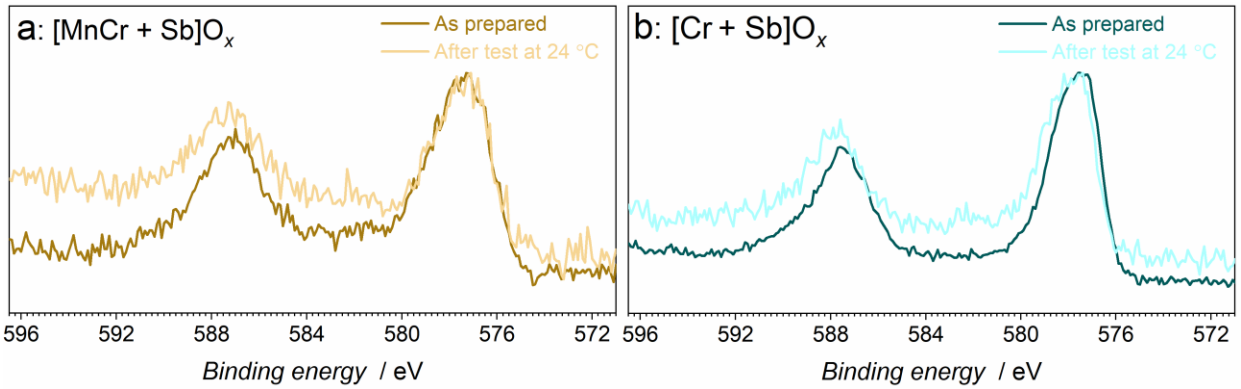

Figure 4.S6. Cr 2p spectra for (a) [MnCr + Sb]O_x, and (b) [Cr + Sb]O_x before (vivid traces) and after (pale traces) electrocatalytic OER tests in stirred 0.5 M H_2SO_4. The catalysts were tested subsequently for 24 h at 10 mA cm^{-2}, 0.5 h at 2.03 V *vs.* RHE, and 0.5 h at 1.93 V *vs.* RHE at ambient temperature.

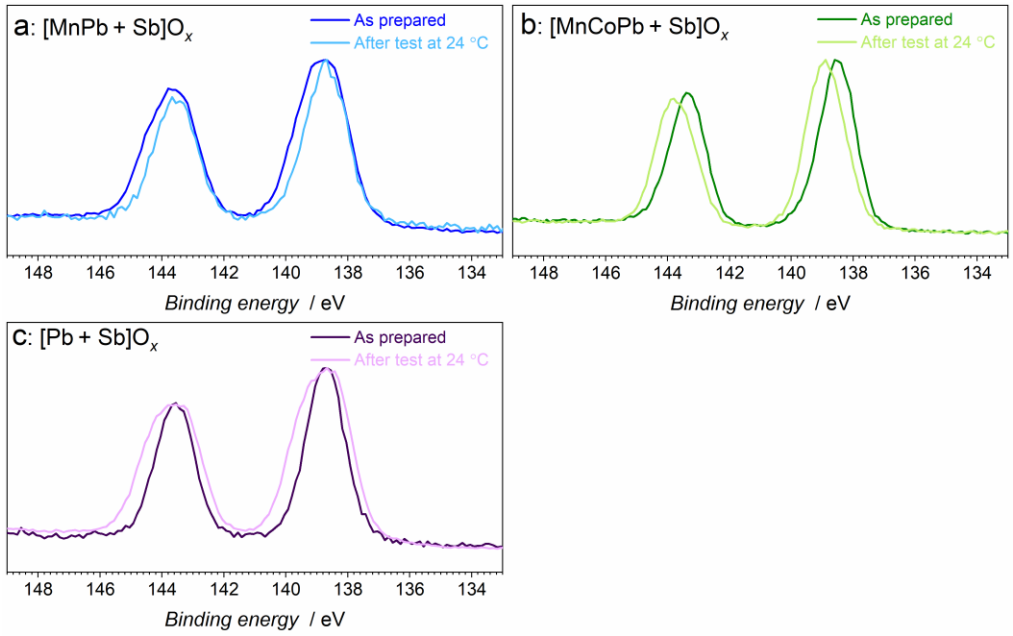

Figure 4.S7. Pb 4f spectra for catalysts (a) [MnPb + Sb]O_x, (b) [MnCoPb + Sb]O_x and (c) [Pb + Sb]O_x before (vivid traces) and after (pale traces) electrocatalytic OER tests in stirred 0.5 M H_2SO_4. The catalysts were tested subsequently for 24 h at 10 mA cm^{-2}, 0.5 h at 2.03 V *vs.* RHE, and 0.5 h at 1.93 V *vs.* RHE at ambient temperature.

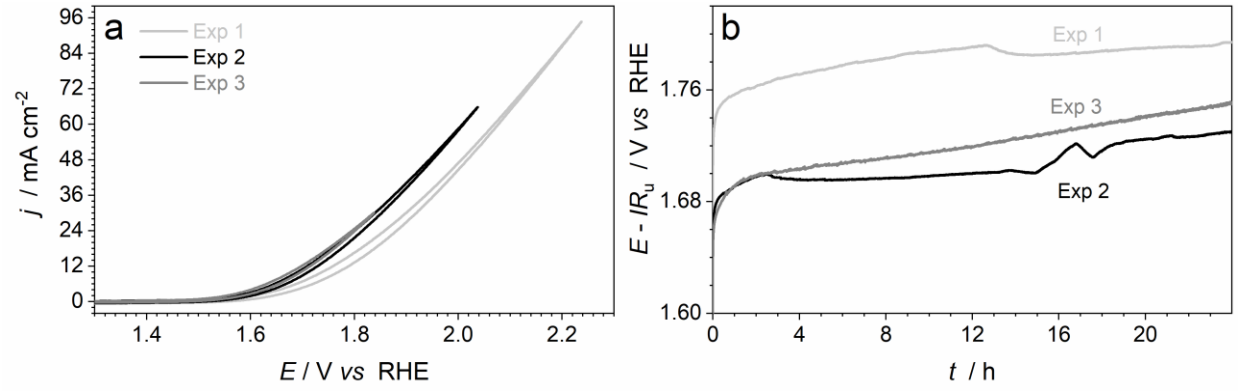

Figure 4.S8. Reproducibility of the electrocatalytic properties of [MnRu+Sb]O_x demonstrated for three independent samples tested in stirred 0.5 M H_2SO_4 at 24 ± 2 °C: (a) initial cyclic voltammetry (scan rate 0.020 V s^{-1}; potentials are not corrected for ohmic losses; currents are normalized to the geometric surface area), and (b) IR_u-corrected chronopotentiograms (current density 10 mA $cm^{-2}_{geom.}$).

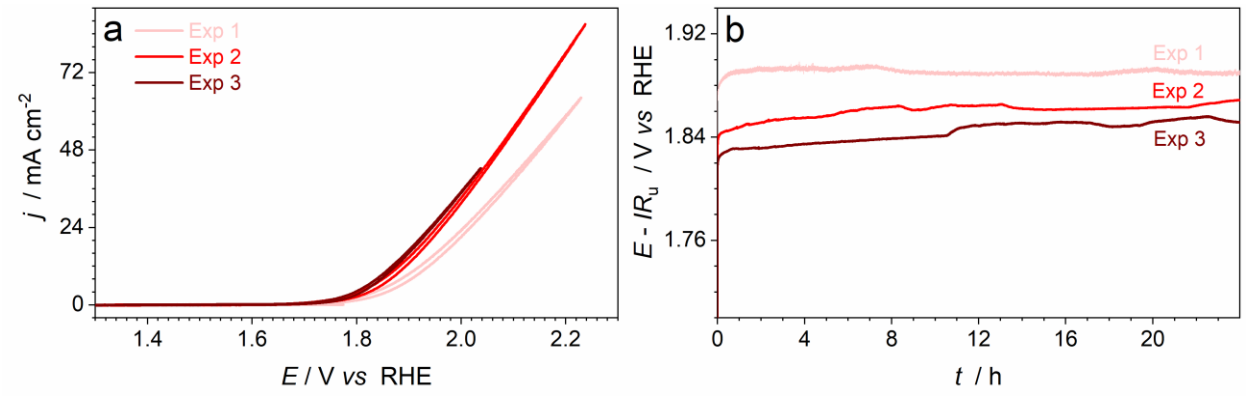

Figure 4.S9. Reproducibility of the electrocatalytic properties of [MnCo+Sb]O_x demonstrated for three independent samples tested in stirred 0.5 M H_2SO_4 at 24 ± 2 °C: (a) initial cyclic voltammetry (scan rate 0.020 V s^{-1}; potentials are not corrected for ohmic losses; currents are normalized to the geometric surface area), and (b) IR_u-corrected chronopotentiograms (current density 10 mA $cm^{-2}_{geom.}$).

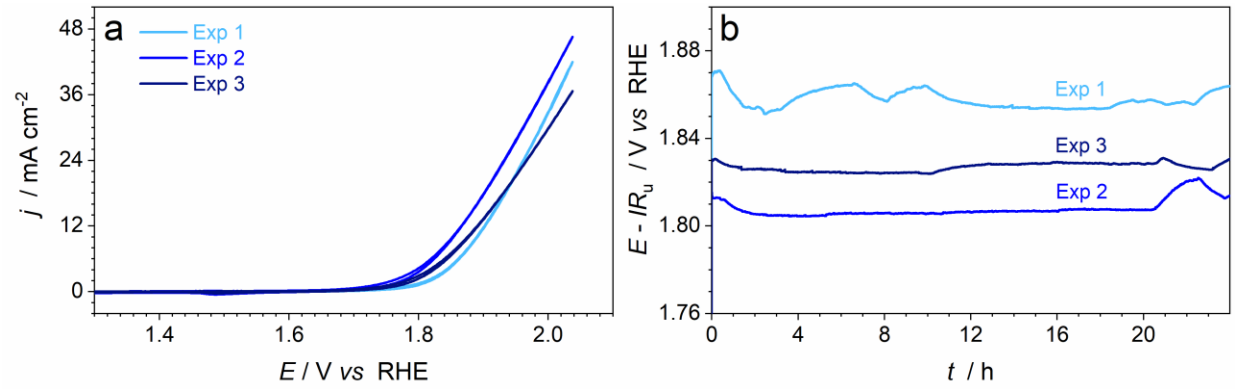

Figure 4.S10. Reproducibility of the electrocatalytic properties of [MnPb+Sb]O_x demonstrated for three independent samples tested in stirred 0.5 M H_2SO_4 at 24 ± 2 °C: (a) initial cyclic voltammetry (scan rate 0.020 V s^{-1}; potentials are not corrected for ohmic losses; currents are normalized to the geometric surface area), and (b) IR_u-corrected chronopotentiograms (current density 10 mA $cm^{-2}_{geom.}$).

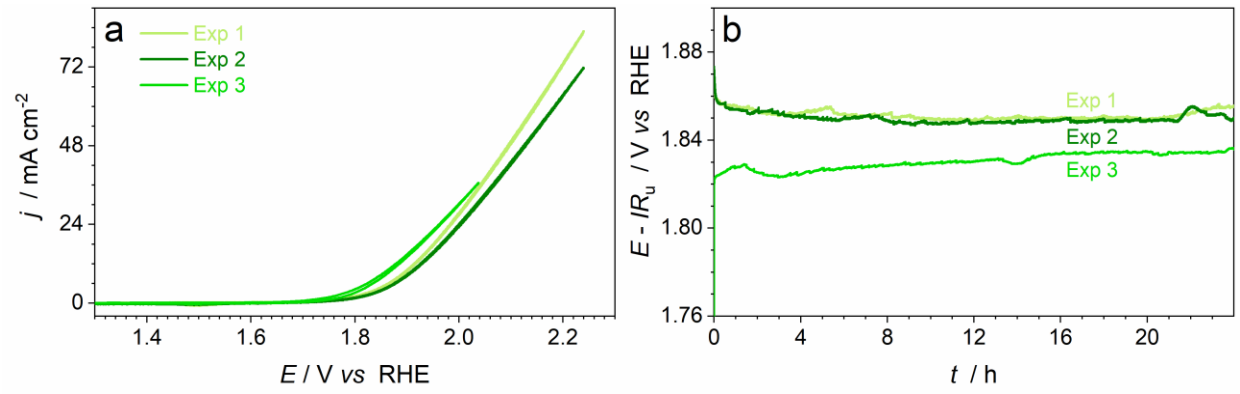

Figure 4.S11. Reproducibility of the electrocatalytic properties of [MnCoPb+Sb]O_x demonstrated for three independent samples tested in stirred 0.5 M H_2SO_4 at 24 ± 2 °C: (a) initial cyclic voltammetry (scan rate 0.020 V s^{-1}; potentials are not corrected for ohmic losses; currents are normalized to the geometric surface area), and (b) IR_u-corrected chronopotentiograms (current density 10 mA $cm^{-2}_{geom.}$).

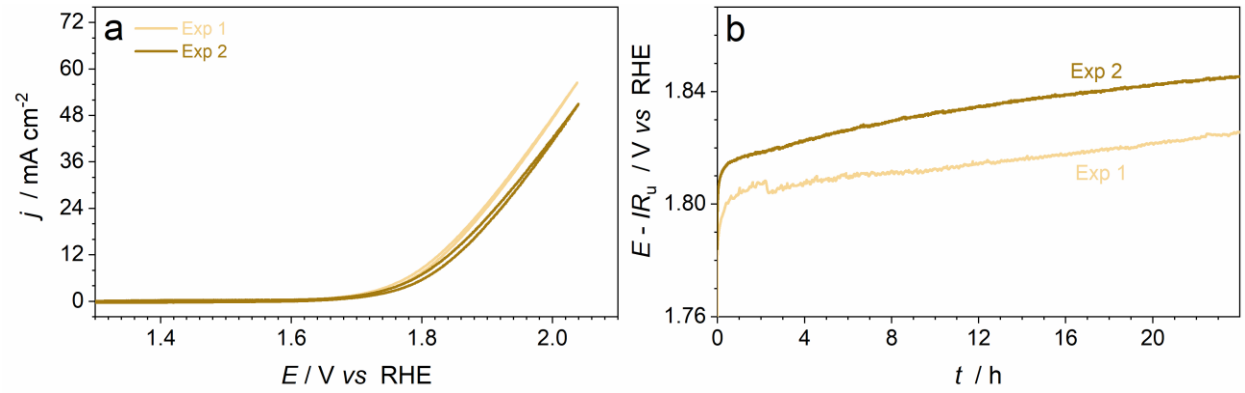

Figure 4.S12. Reproducibility of the electrocatalytic properties of [MnCr+Sb]O_x demonstrated for two independent samples tested in stirred 0.5 M H_2SO_4 at 24 ± 2 °C: (a) initial cyclic voltammetry (scan rate 0.020 V s^{-1}; potentials are not corrected for ohmic losses; currents are normalized to the geometric surface area), and (b) IR_u-corrected chronopotentiograms (current density 10 mA $cm^{-2}_{geom.}$).

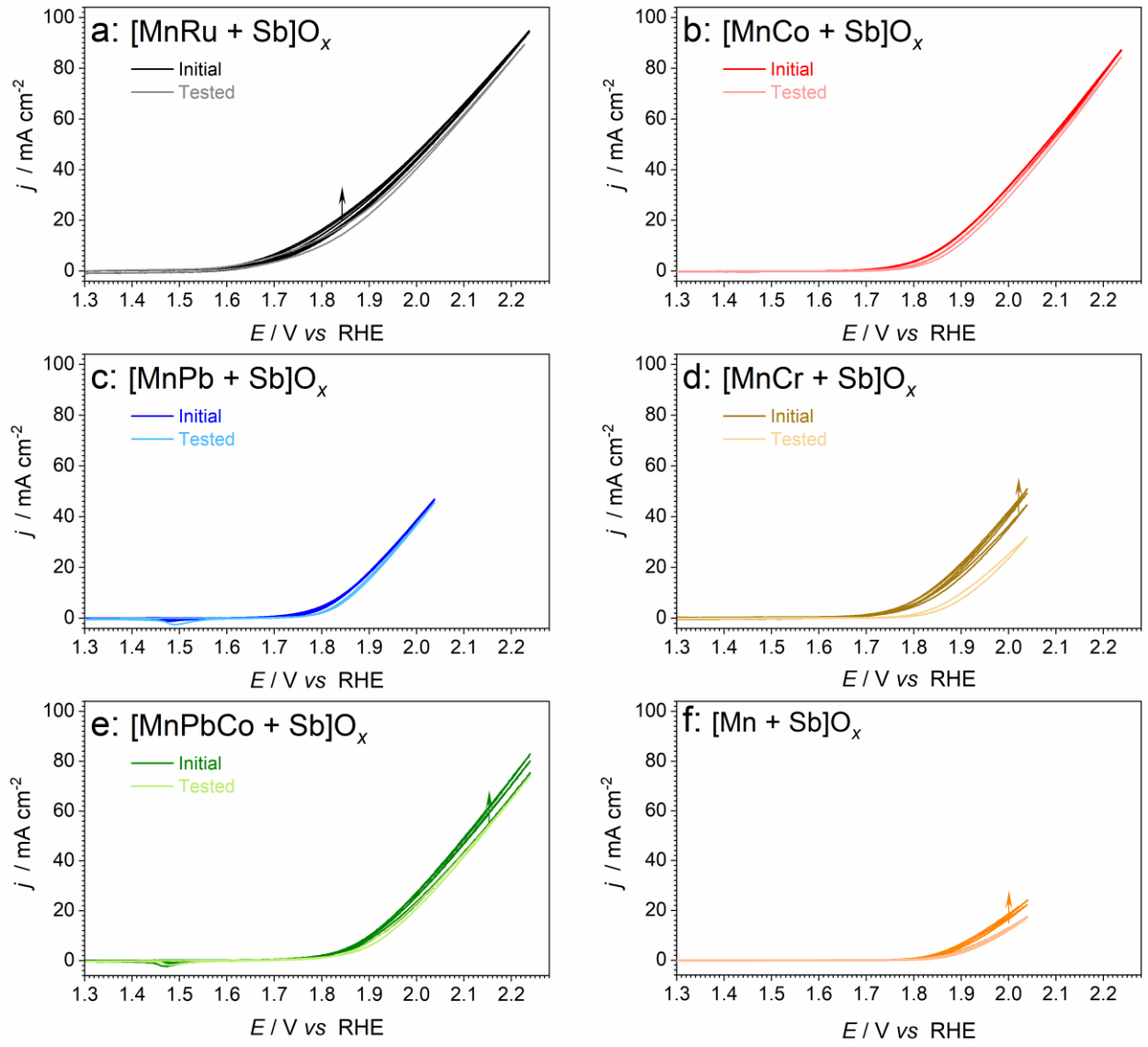

Figure 4.S13. Evolution of cyclic voltammograms (0.020 V s^{-1}; three consecutive cycles shown) of (a) [MnRu+Sb]O_x, (b) [MnCo+Sb]O_x, (c) [MnPb+Sb]O_x, (d) [MnCr+Sb]O_x, and (e) [MnPbCo+Sb]O_x in stirred 0.5 M H_2SO_4 at 24 ± 2 °C. Arrows show the evolution of the current density with cycling. Currents are normalized to the geometric surface area of the electrode; potentials are not corrected for the iR_u-drop.

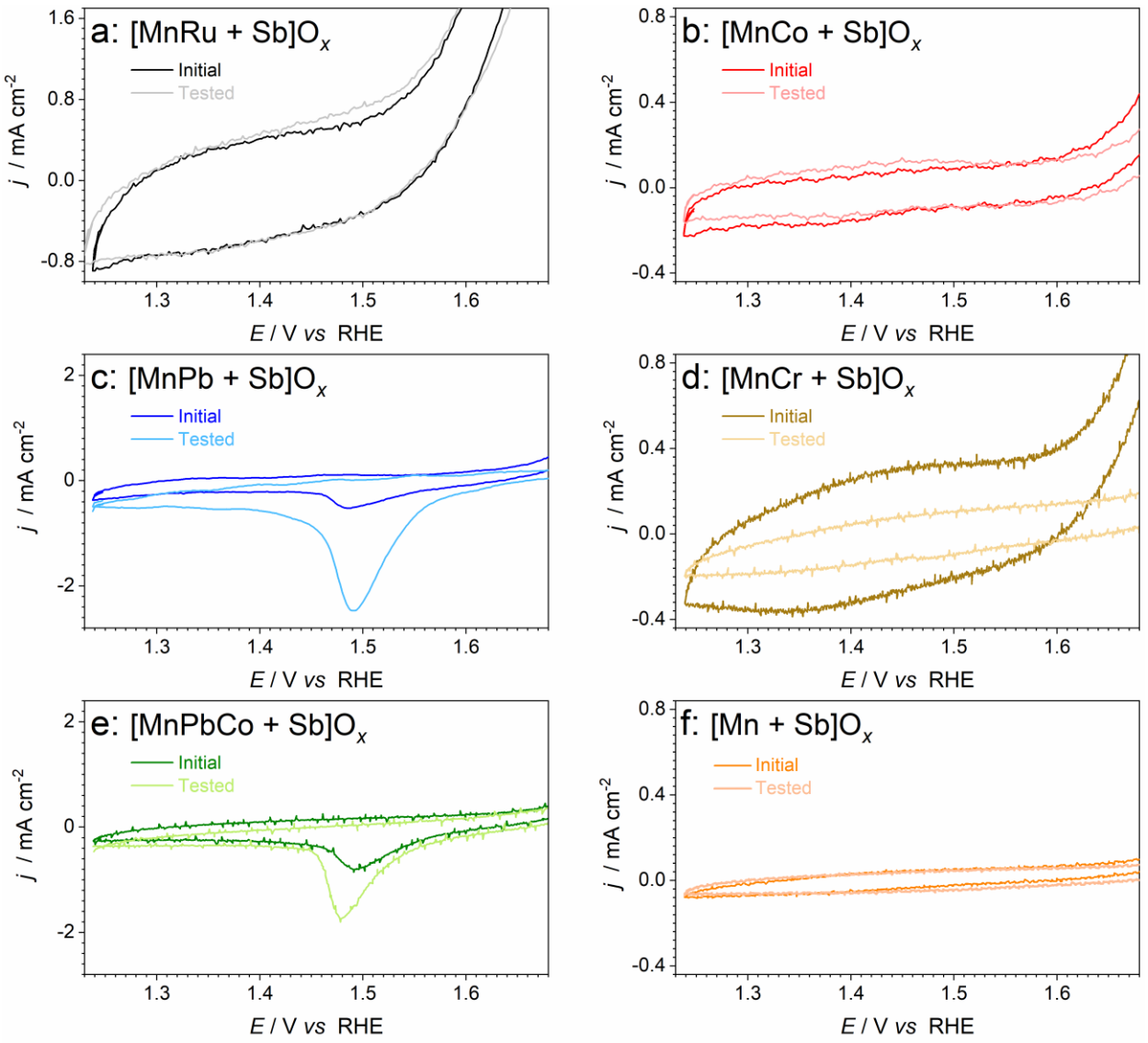

Figure 4.S14. Comparison of the pre-catalytic regions of the quasi-stabilised cyclic voltammograms (0.020 V s^{-1}) of (a) [MnRu+Sb]O_x, (b) [MnCo+Sb]O_x, (c) [MnPb+Sb]O_x, (d) [MnCr+Sb]O_x, and (e) [MnPbCo+Sb]O_x, in stirred 0.5 M H_2SO_4 at ambient temperature before (pale traces) and after (vivid traces) 25 h durability tests (24 h at 10 mA cm^{-2}; 0.5 h at 2.03 V *vs.* RHE; 0.5 h at 1.93 V *vs.* RHE) under the same conditions. Currents are normalized to the geometric surface area of the electrode; potentials are not corrected for the IR_u-drop.

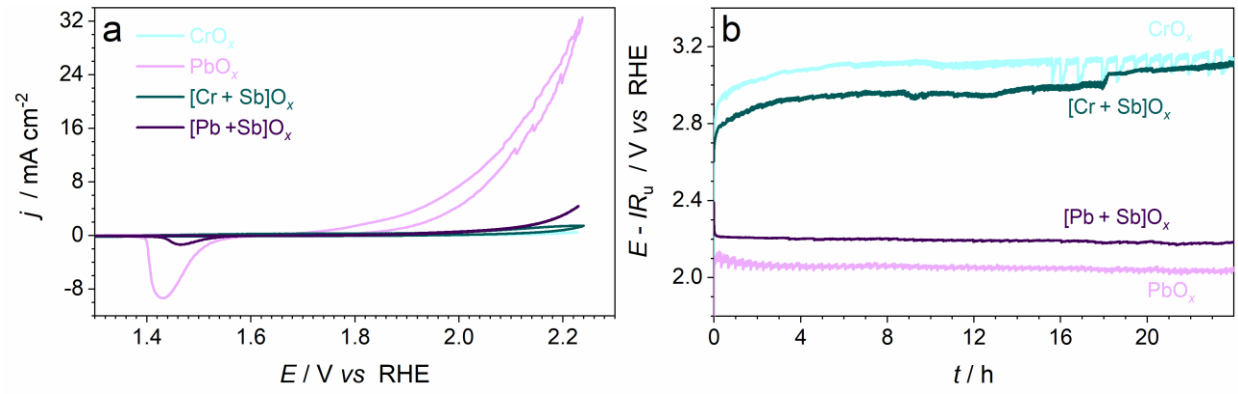

Figure 4.S15. (a) Cyclic voltammetry (0.020 V s^{-1}; potentials are not corrected for the IR_u-drop; currents are normalized to the geometric surface area), and (b) IR_u-corrected chronopotentiograms (current density 10 mA $cm^{-2}_{geom.}$) recorded for FTO electrodes modified with CrO_y, PbO_y, $[Cr+Sb]O_x$, and $[Pb+Sb]O_x$ in contact with stirred 0.5 M H_2SO_4 at 24 ± 2 °C.

Table 4.S1. Relative concentration of metals on the catalysts surface[a] before and after OER tests[b].

	As prepared		Tested at 24 ± 2 °C	
Catalyst	**Mn**	**M**	**Mn**	**M**
$[MnRu+Sb]O_x$	9	2	0.04	n.a [c]
$[MnCr+Sb]O_x$	41	16	3.2	2.5
$[MnCo+Sb]O_x$	29	7	0.16	0.09
$[MnPb+Sb]O_x$	13	34	0.2	0.06
$[MnPbCo+Sb]O_x$	15	6 (Pb) 37 (Co)	2.27	1.18 (Pb) 4.63 (Co)
$[Mn+Sb]O_x$	23	---	0.16	---

[a] Determined by XPS and normalised to the total amount of metals and antimony present on the surface. [b] Determined by XPS and normalised to the amount of antimony present on the surface. [c] Determination of the Ru concentration is not possible due to the overlap with C 1s.

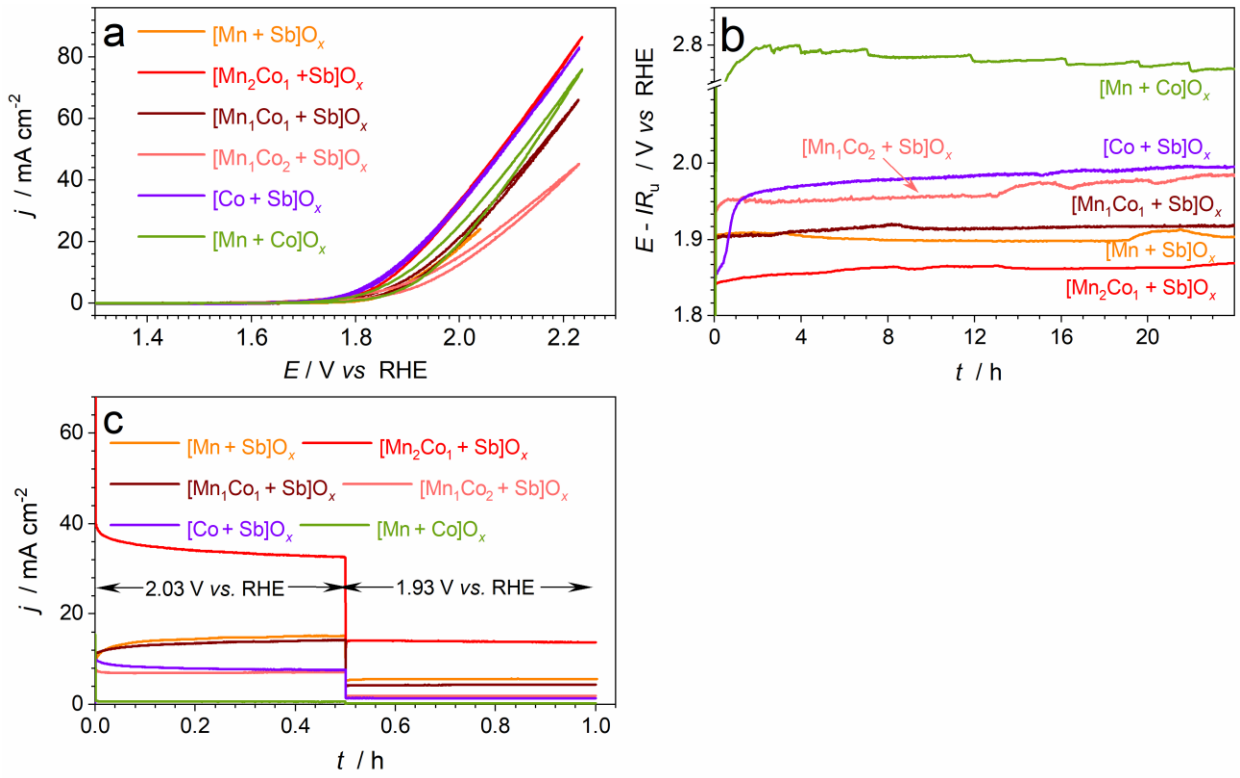

Figure 4.S16. Effect of the Mn : Co initial ratio (see figure) on the performance of the [MnCo+Sb]O_x catalysts in stirred 0.5 M H_2SO_4 at 24 ± 2 °C: (a) cyclic voltammetry (0.020 V s^{-1}; potentials are not IR_u-corrected; currents are normalized to the geometric surface area), (b) IR_u-corrected chronopotentiograms (10 mA $cm^{-2}_{geom.}$), and (c) chronoamperograms at 2.03 and 1.93 V *vs.* RHE. Data for the similarly synthesized [Mn+Sb]O_x, [Co+Sb]O_x, and [Mn+Co]O_x are provided for comparison. As reported previously,[5] [Co+Sb]O_x contains a notable amount of Co_3O_4 admixture enabling reasonable initial performance, which is rapidly lost during constant current tests, and the resulting performance is ascribed to the actual OER catalytic activity of $CoSb_2O_6$ – major phase of [Co+Sb]O_x.

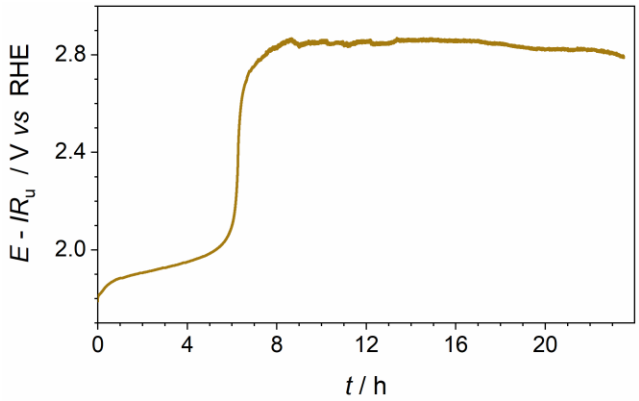

Figure 4.S17. IR_u-corrected chronopotentiogram (current density 10 mA $cm^{-2}_{geom.}$) for $[MnCr+Sb]O_x$ tested in stirred 0.5 M H_2SO_4 at 60 °C.

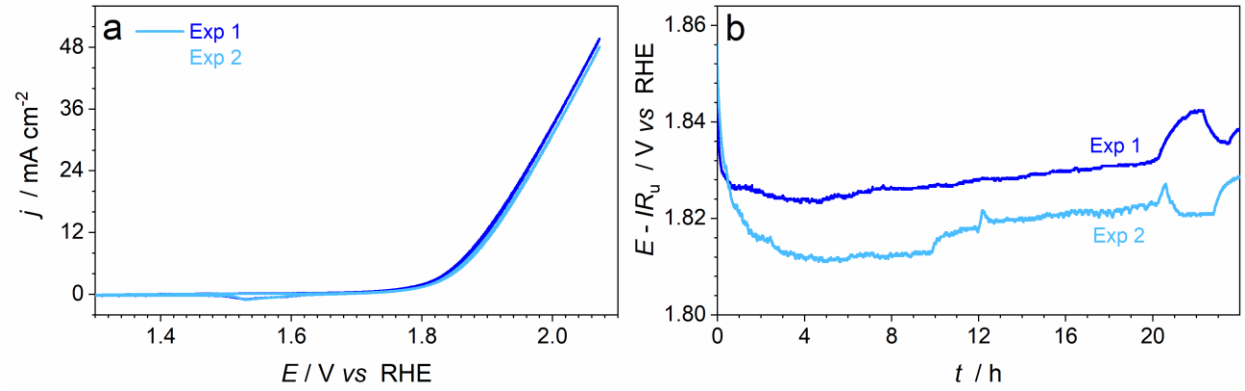

Figure 4.S18. Reproducibility of the electrocatalytic properties of $[MnPb+Sb]O_x$ demonstrated for two independent samples tested in stirred 0.5 M H_2SO_4 at 60 °C: (a) initial cyclic voltammetry (0.020 V s^{-1}; potentials are not IR_u-corrected; currents are normalized to the geometric surface area), and (b) IR_u-corrected chronopotentiograms (current density 10 mA $cm^{-2}_{geom.}$).

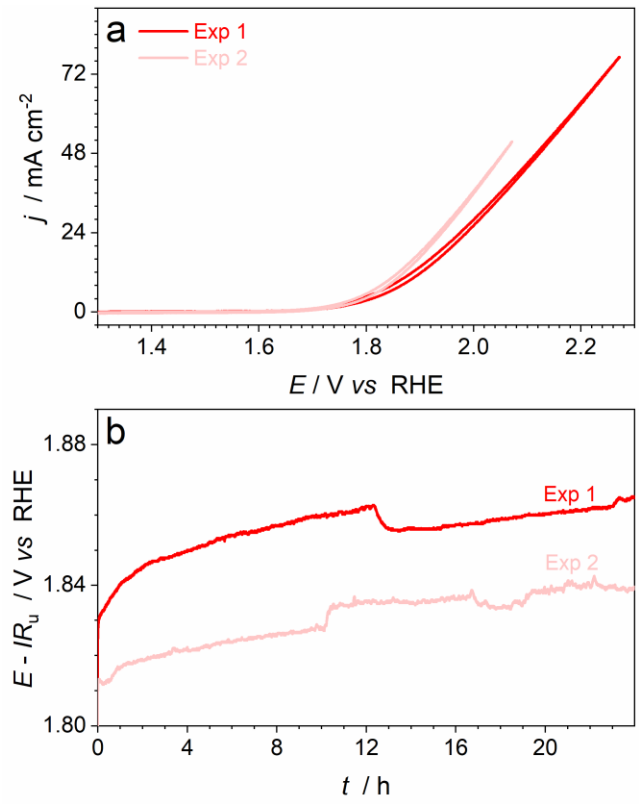

Figure 4.S19. Reproducibility of the electrocatalytic properties of [MnCo+Sb]O_x demonstrated for two independent samples tested in stirred 0.5 M H_2SO_4 at 60 °C: (a) initial cyclic voltammetry (0.020 V s^{-1}; potentials are not IR_u-corrected; currents are normalized to the geometric surface area), and (b) IR_u-corrected chronopotentiograms (current density 10 mA $cm^{-2}_{geom.}$).

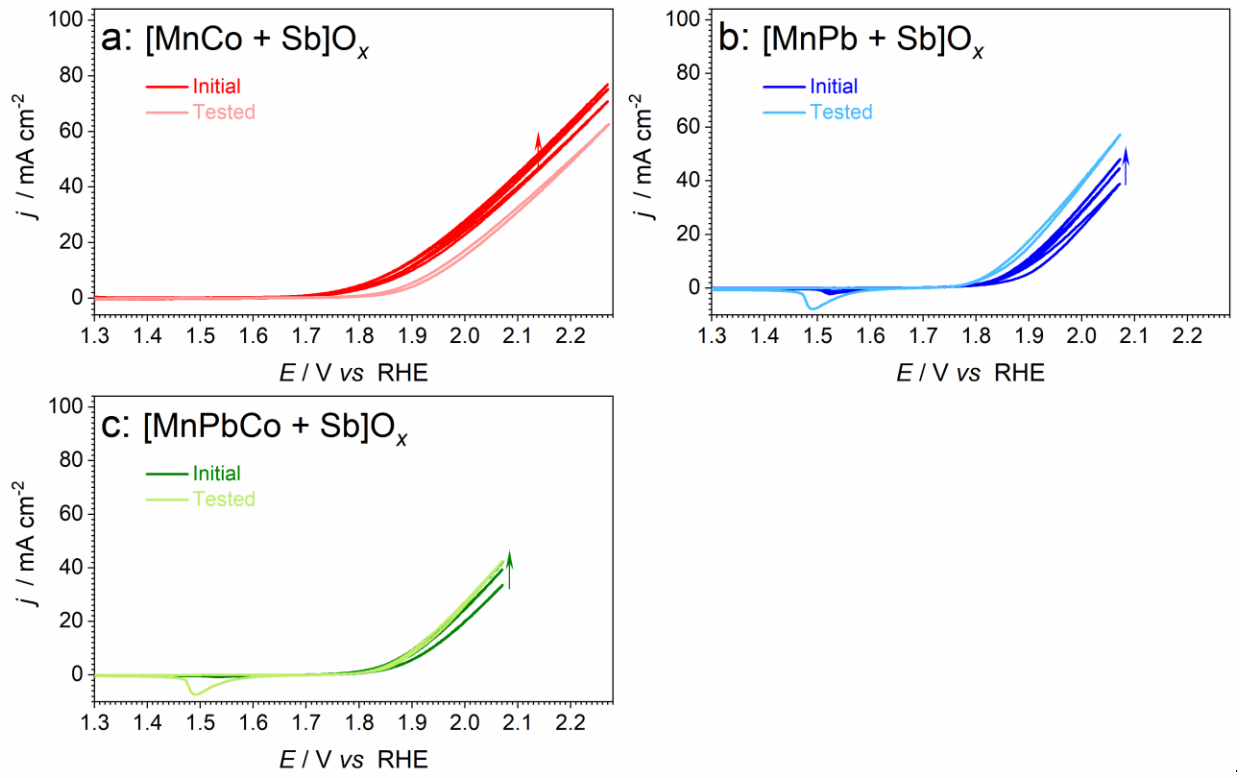

Figure 4.S20. Evolution of cyclic voltammograms (scan rate, v = 0.020 V s^{-1}; three consecutive cycles shown) of (a) [MnCo+Sb]O_x, (b) [MnPb+Sb]O_x, and (c) [MnPbCo+Sb]O_x in 0.5 M H_2SO_4 at 60°C. Arrows show the evolution of the current density with cycling. Currents are normalized to the geometric surface area of the electrode; potential values were not corrected for the IR_u-drop.

4.6 REFERENCES

(1) Zhou, L.; Shinde, A.; Montoya, J. H.; Singh, A.; Gul, S.; Yano, J.; Ye, Y.; Crumlin, E. J.; Richter, M. H.; Cooper, J. K.; Stein, H. S.; Haber, J. A.; Persson, K. A.; Gregoire, J. M. Rutile Alloys in the Mn-Sb-O System Stabilize Mn^{3+} to Enable Oxygen Evolution in Strong Acid. *ACS Catal.* **2018**, *8* (12), 10938–10948. https://doi.org/10.1021/acscatal.8b02689.

(2) Moreno-Hernandez, I. A.; Macfarland, C. A.; Read, C. G.; Papadantonakis, K. M.; Brunschwig, B. S.; Lewis, N. S. Crystalline Nickel Manganese Antimonate as a Stable Water-Oxidation Catalyst in Aqueous 1.0 M H_2SO_4. *Energy Environ. Sci.* **2017**, *10* (10),

2103–2108. https://doi.org/10.1039/c7ee01486d.

(3) Evans, T. A.; Choi, K. S. Electrochemical Synthesis and Investigation of Stoichiometric, Phase - Pure $CoSb_2O_6$ and $MnSb_2O_6$ Electrodes for the Oxygen Evolution Reaction in Acidic Media. *ACS Appl. Energy Mater.* **2020**, *3* (6), 5563–5571. https://doi.org/10.1021/acsaem.0c00526.

(4) Shinde, A.; Jones, R. J. R.; Guevarra, D.; Mitrovic, S.; Becerra-Stasiewicz, N.; Haber, J. A.; Jin, J.; Gregoire, J. M. High-Throughput Screening for Acid-Stable Oxygen Evolution Electrocatalysts in the (Mn–Co–Ta–Sb)O_x Composition Space. *Electrocatalysis* **2015**, *6* (2), 229–236. https://doi.org/10.1007/s12678-014-0237-7.

(5) Sibimol Luke, Manjunath Chatti, Asha Yadav, Brittany V. Kerr, Jiban Kangsabanik, Tim Williams, Pavel V. Cherepanov, Akshat Tanksale, Bernt Johannessen, Douglas R. MacFarlane, Rosalie K. Hocking, Aftab Alam, Aswani Yella, A. N. S. Mixed Metal-Antimony Oxides: High-Durability Catalysts for Low PH Water Oxidation at Ambient and Elevated Temperatures. *Chemrxiv* **2021**.

(6) Mondschein, J. S.; Callejas, J. F.; Read, C. G.; Chen, J. Y. C.; Holder, C. F.; Badding, C. K.; Schaak, R. E. Crystalline Cobalt Oxide Films for Sustained Electrocatalytic Oxygen Evolution under Strongly Acidic Conditions. *Chem. Mater.* **2017**, *29* (3), 950–957. https://doi.org/10.1021/acs.chemmater.6b02879.

(7) Yang, J.; Shao, Q.; Huang, B.; Sun, M.; Huang, X. PH-Universal Water Splitting Catalyst: Ru-Ni Nanosheet Assemblies. *iScience* **2019**, *11*, 492–504. https://doi.org/10.1016/j.isci.2019.01.004.

(8) Forgie, R.; Bugosh, G.; Neyerlin, K. C.; Liu, Z.; Strasser, P. Bimetallic Ru Electrocatalysts for the OER and Electrolytic Water Splitting in Acidic Media. *Electrochem. Solid-State Lett.* **2010**, *13* (4). https://doi.org/10.1149/1.3290735.

(9) Laha, S.; Lee, Y.; Podjaski, F.; Weber, D.; Duppel, V.; Schoop, L. M.; Pielnhofer, F.; Scheurer, C.; Müller, K.; Starke, U.; Reuter, K.; Lotsch, B. V. Ruthenium Oxide Nanosheets for Enhanced Oxygen Evolution Catalysis in Acidic Medium. *Adv. Energy Mater.* **2019**, *9* (15), 1–8. https://doi.org/10.1002/aenm.201803795.

(10) Clancy, M.; Bettles, C. J.; Stuart, A.; Birbilis, N. The Influence of Alloying Elements on the Electrochemistry of Lead Anodes for Electrowinning of Metals: A Review. *Hydrometallurgy*. 2013, pp 144–157. https://doi.org/10.1016/j.hydromet.2012.11.001.

(11) Chen, B.; Wang, S.; Liu, J.; Huang, H.; Dong, C.; He, Y.; Yan, W.; Guo, Z.; Xu, R.; Yang, H. Corrosion Resistance Mechanism of a Novel Porous Ti/Sn-Sb-RuO_x/β-PbO_2 Anode for Zinc Electrowinning. *Corros. Sci.* **2018**, *144* (July), 136–144. https://doi.org/10.1016/j.corsci.2018.08.049.

(12) Bonke, S. A.; Abel, K. L.; Hoogeveen, D. A.; Chatti, M.; Gengenbach, T.; Fournier, M.; Spiccia, L.; Simonov, A. N. Electrolysis of Natural Waters Contaminated with Transition-Metal Ions: Identification of A Metastable FePb-Based Oxygen-Evolution Catalyst Operating in Weakly Acidic Solutions. *Chempluschem* **2018**, *83* (7), 704–710.

https://doi.org/10.1002/cplu.201800020.

(13) Chatti, M.; Gardiner, J. L.; Fournier, M.; Johannessen, B.; Williams, T.; Gengenbach, T. R.; Pai, N.; Nguyen, C.; Macfarlane, D. R.; Hocking, R. K.; Simonov, A. N. For Long-Term Oxidation of Acidic Water At Up. *Nat. Catal.* **2019**, *2* (May), 457–465.

(14) Lin, Y.; Tian, Z.; Zhang, L.; Ma, J.; Jiang, Z.; Chen, L.; Deibert, B. J.; Ge, R. Reaction in Acidic Media. *Nat. Commun.* **2019**, *10* (2019), 162.

(15) Biesinger, M. C.; Payne, B. P.; Grosvenor, A. P.; Lau, L. W. M.; Gerson, A. R.; Smart, R. S. C. Resolving Surface Chemical States in XPS Analysis of First Row Transition Metals, Oxides and Hydroxides: Cr, Mn, Fe, Co and Ni. *Appl. Surf. Sci.* **2011**, *257* (7), 2717–2730. https://doi.org/10.1016/j.apsusc.2010.10.051.

(16) Szafraniak, I.; Połomska, M.; Hilczer, B.; Talik, E.; Kepiński, L. Characterization of $PbTiO_3$ Nanopowders Obtained by Room Temperature Synthesis. *Ferroelectrics* **2006**, *336*, 279–287. https://doi.org/10.1080/00150190600697939.

(17) Morgan, D. J. Resolving Ruthenium: XPS Studies of Common Ruthenium Materials. *Surf. Interface Anal.* **2015**, *47* (11), 1072–1079. https://doi.org/10.1002/sia.5852.

(18) Li, X.; Pletcher, D.; Walsh, F. C. Electrodeposited Lead Dioxide Coatings. *Chem. Soc. Rev.* **2011**, *40* (7), 3879–3894. https://doi.org/10.1039/c0cs00213e.

(19) Lin, C. C.; McCrory, C. C. L. Effect of Chromium Doping on Electrochemical Water Oxidation Activity by $Co_{3-X}Cr_xO_4$ Spinel Catalysts. *ACS Catal.* **2017**, *7* (1), 443–451. https://doi.org/10.1021/acscatal.6b02170.

(20) Gou, W.; Zhang, M.; Zou, Y.; Zhou, X.; Qu, Y. Iridium-Chromium Oxide Nanowires as Highly Performed OER Catalysts in Acidic Media. *ChemCatChem* **2019**, *11* (24), 6008–6014. https://doi.org/10.1002/cctc.201901411.

(21) Xu, D.; Stevens, M. B.; Rui, Y.; DeLuca, G.; Boettcher, S. W.; Reichmanis, E.; Li, Y.; Zhang, Q.; Wang, H. The Role of Cr Doping in Ni–Fe Oxide/(Oxy)Hydroxide Electrocatalysts for Oxygen Evolution. *Electrochim. Acta* **2018**, *265*, 10–18. https://doi.org/10.1016/j.electacta.2018.01.143.

(22) Lin, Y.; Tian, Z.; Zhang, L.; Ma, J.; Jiang, Z.; Chen, L.; Deibert, B. J.; Ge, R. Chromium-Ruthenium Oxide Solid Solution Electrocatalyst for Highly Efficient Oxygen Evolution Reaction in Acidic Media. *Nat. Commun.* **2019**, *10* (2019), 162.

Chapter 5

Modification of Manganese Antimonate Low-pH Water Electrooxidation Catalyst with Interfacial Oxide Layers for the Enhanced Performance

5.1 INTRODUCTION

Among the catalysts reported for water oxidation at low pH, manganese antimonates emerged as the most promising noble-metal free electrocatalyst with its long-term stable operations at ambient conditions.[1–3] This is further confirmed by the extensive manganese antimonate studies in the previous two chapters which even showed its operation at elevated temperatures by quasi-stabilization. Although mixing with other oxides showed an enhancement in the electrocatalytic performance of manganese antimony oxide, the activity of antimonate catalysts is still not in par with state-of-the-art iridium and ruthenium-based catalysts.

In general, extensive research efforts have focused on the enhancement of the performance of the water oxidation electrocatalysts through doping, structural modifications, alloying and creation of mixed metal oxide systems.[1,4–8] Another strategy is to alter the surface structure of the catalyst, which obviously plays a key role for the interfacial catalytic processes.[9,10] Surface engineering can increase the concentration of the active sites and/or fundamentally change their chemical nature to enhance the intrinsic catalytic activity. This can be done by synthesizing

nanostructured catalysts or by depositing other layers on the top of the existing catalytic material. Another possible method to improve the electrocatalytic performance of the catalyst is by modifying the support which increases the active surface area and improves the dispersion of the catalytic particles.[11–14] The interfacial effects between the support, catalyst and the electrolyte determine the energetics of the adsorption of intermediates, the charge-transfer pathways, and the electrochemical stability.[10] Of particular interest herein are the interfacial effects induced by the introduction of an additional thin oxide layer either over the catalytic surface or over the support. Such modifications can alter the surface charge density of the composite and also between the layers.[15,16] This synergistic interaction can contribute to the improved electrocatalytic activity by increasing the active sites with more favorable binding energies for the water oxidation intermediates.[17] Several specific examples of such effects are briefly surveyed below.

A significant body of work on the positive effect of oxide overlayers on the performance of the photoelectrocatalysts has been reported. For example, density functional theory calculations on the introduction of ab Al_2O_3 overlayer on the Fe_2O_3 water oxidation photocatalyst reduces the OER overpotential because of the decrease in the work function.[18] Turner *et al.* reported that amorphous TiO_2 and MoS_x deposited on $GaInP_2$ showed significant improvement in its catalytic activity and stability as a photocathode for the hydrogen evolution reaction (HER).[19] SnO_2 overlayer was demonstrated to improve the stability of the cuprous oxide HER photoelectrocatalysts by preventing the photocorrosion.[20] C.Scheu established that SnO_2 layer over Fe_2O_3 as a photoanode reduced the overpotential by surface passivation and better charge separation because of band bending at the semiconductor/electrolyte interface.[21] ALD of thin SiO_2 interfacial layer is established to act as surface passivation layer in metal-insulator-semiconductor photoelectrodes.[22,23] TiO_2 overlayers by atomic layer deposition (ALD) on

different OER photoanodes were demonstrated to both increase the stability and the catalytic activity.[24–27] This positive effects arise from the passivation of the surface states, improved charge separation, lower recombination of the photogenerated charges and band bending.[26,27] Overpotential reduction was also observed with alumina overlayers on hematite and WO_3 water oxidation photoanodes.[28,29] This approach has also been successfully applied in the design of a core-shell catalysts for the water splitting.[30–32]

In the classical electrocatalytic water oxidation domain, only a few reports on the positive effects of interfacial layers exist, though all of them indicate the promise of this strategy. Hoffman *et al.* demonstrated that atomic layer deposition of TiO_2 onto IrO_2 resulted in a 9-fold increase in the OER activity in 1 M H_2SO_4 and suggested that the titania overlayer facilitates the charge transfer within the catalytic system.[15] Additionally, it was demonstrated that modification of RuO_2 with TiO_2 enables this material to operate as an OER selective catalysts in the presence of Cl^-, which is an important achievement from the perspective of the development of the anodes for splitting sea water.[15,33] TiO_2 is also known as a highly advantageous support for the OER catalysts, which provides excellent stability along with enhancement in the activity because of the electronic interaction between the titania substrate and the catalyst.[34–36] Enhancement in activity by synergistic interactions between Ce oxide with the CoO_x, $NiFeO_x$ and FeOOH water oxidation catalysts was also demonstrated for the OER under alkaline conditions.[17,37–39] These improvements were attributed to the multivalence, good ionic conductivity and high oxygen storage capacity of cerium oxide overlayers.[40,41] Though CeO_x itself is not catalytically active, these peculiar properties were suggested to generate strong electron interactions and quick absorption of oxygen during the reaction which improves the electrocatalytic performance by increasing the charge transfer efficiency.[42] SiO_2 oxide mixed with TiO_2 and RuO_2 exhibited

enhanced electrocatalytic activity because of the mutual interactions, more favorable intermediate adsorption and generation of the new catalytically active sites.[43–45] Recent computational study by Gono and Pasquarello on the bifunctional mechanism for oxygen evolution reaction draws further attention to the effects over/underlayers on the water oxidation electrocatalysts through the explanation of the changes in the reaction overpotential upon creation of the bilayer oxide materials.[46]

Thus, modification of the water oxidation electrocatalysts and especially photoelectrocatalysts is known to positively alter their activity and stability. However, only one work focusing on the model noble-metal IrO_2 catalyst and only one type of the overlayer (TiO_2) has been reported for the acidic OER.[15] The present work aims to fill this existing gap through the exploration of how different oxides such as TiO_2, Al_2O_3, SiO_2, SnO_2 and CeO_2 introduced as overlayers and underlayers affect the electrocatalytic activity of a manganese-antimony oxide water oxidation catalyst designed for the operation at low pH. If the electrocatalytic activity of $[Mn+Sb]O_y$ can be improved, it has the potential to become a cost-effective alternative for noble metal electrocatalysts that are currently used for water oxidation in acidic conditions.

5.2 RESULTS AND DISCUSSION

$[Mn+Sb]O_y$ with the initial manganese : antimony ratio of 1 : 1 mol. was used herein as a reference material as a highly reliable electrocatalyst for water oxidation in acidic medium as discussed in Chapters 3 and 4. As previously, the catalyst was synthesized as a thin film on FTO electrodes by annealing of its precursor salts drop cast from the dimethylformamide and dimethylsulfoxide solution. For the synthesis of the overlayer-modified catalysts, deposition of

the desired material was achieved by spin-coating the corresponding precursor solution by the following procedure.

SnO_2 layer: Tin (IV) oxide (15% in H_2O colloidal dispersion liquid) diluted to 2% by adding deionized water. 50µl of this solution is spincoated once on [Mn+Sb]O_y at 2000 rpm for 30 sec and further annealed at 200^{o}C for 1 h on a hot plate in air.

SiO_2 layer: 50µl of Chlorotrimethylsilane and Hexane in 1:20 vol/vol ratio is spincoated once on [Mn+Sb]O_y at 2000 rpm for 30 sec. Then it is annealed at 200^{o}C for 1 h on a hot plate in air.

CeO_2 layer: 50µl of 0.1mmol of Cerium (III) chloride anhydrous dissolved in 2ml of deionized water is spincoated once at 2000 rpm for 30 sec and further it is annealed at 450^{o}C for 0.5 h at a ramp rate of 5°C/min in air.

Mesoporous TiO_2 layer: 50µl of TiO_2 paste and Ethanol in 1:4 wt/wt ratio is spincoated at 2000 rpm for 30 sec. Then it is annealed at 450^{o}C for 0.5 h at a ramp rate of 5°C/min in air.

Mesoporous Al_2O_3 layer: 50µl of Al_2O_3 paste and Ethanol in 1:6 wt/wt ratio is spincoated at 2000 rpm for 30 sec. Then it is annealed at 450^{o}C for 0.5 h at a ramp rate of 5°C/min in air.

The SEM images of the [Mn+Sb]O_y catalyst with different overlayers are shown in Figure 5.S1 and 5.S2. For the underlayer-modified catalysts, the same deposition procedures were applied to an unmodified FTO substrate prior to the creation of the [Mn+Sb]O_y catalytic layer on top. Extended details on the fabrication procedures are described in the experimental section in Chapter 2. All electrochemical tests were carried out using 0.5 M H_2SO_4 as an electrolyte with a measured pH of 0.3 at ambient temperature (24 ± 2 °C). Compensation for the ohmic losses was applied manually to all galvanostatic data presented below after calculating the uncompensated

(R_u) values from the electrochemical impedance spectroscopy. Since the current in cyclic voltammograms cannot be always confidently attributed to the stationary catalytic OER process alone, these data are presented without compensating for ohmic losses.

The performance of the unmodified [Mn+Sb]O_y material, in particular stabilized OER overpotential of 0.677 ± 0.008 V at a current density of 10 mA cm^{-2} after 24 h of tests, was used as a reference for comparisons with that of the catalysts modified with SnO_2, SiO_2, CeO_2, Al_2O_3 or TiO_2 overlayers or underlayers. When deposited on blank FTO electrodes, neither of these oxides demonstrated any reasonable catalytic activity for the OER (Figure 5.S3), as expected. Therefore, all improvements in the performance discussed below cannot be ascribed to the intrinsic catalytic activity of the over/underlayers.

5.2.1 Tin(IV) oxide

The electrocatalytic performance of [Mn+Sb]O_y with SnO_2 overlayers was analyzed first. It was expected that the thickness of the overlayers would significantly affect the activity of the electrocatalyst and was therefore optimized to achieve in the best result. To this end, the 15 wt.% SnO_2 colloidal dispersion used to deposit the tin oxide overlayers was diluted to 1, 2 and 3 wt.% before deposition to vary the thickness of this oxide layer and its coverage of the surface. Cyclic voltammograms recorded for SnO_2/[Mn+Sb]O_y irrespective of the amount of tin oxide deposited all showed enhanced electrocatalytic activity for the OER with respect to the unmodified material (Figure 5.1), and the best results were achieved for the catalyst prepared with the 2 wt.% SnO_2 dispersion (Figure 5.S4).

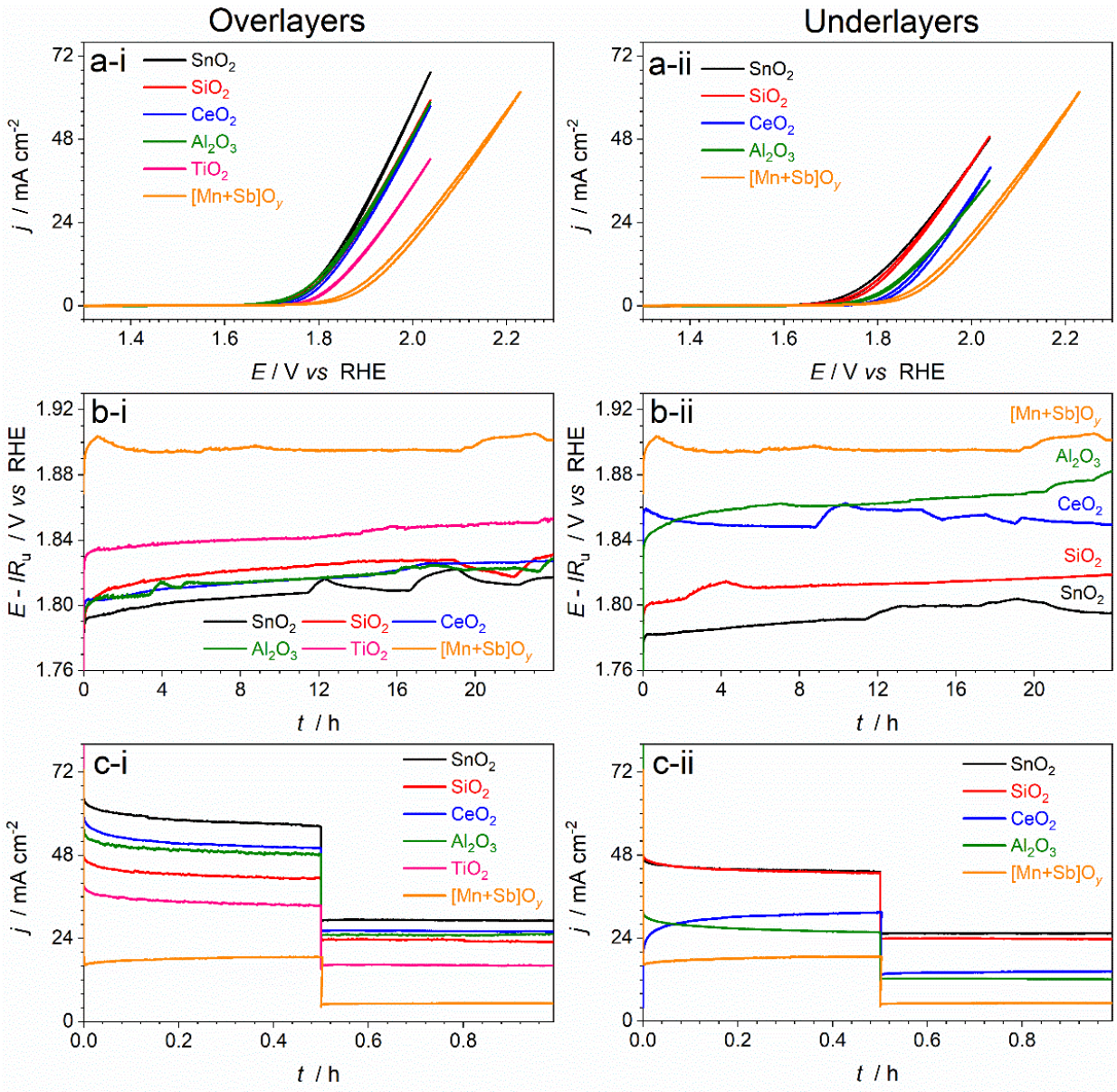

Figure 5.1. Subsequently recorded (a) cyclic voltammetry (scan rate, v = 0.020 V s^{-1}; potentials are not corrected for the IR_u-drop), (b) IR_u-corrected chronopotentiograms (current density 10 mA $cm^{-2}_{geom.}$), and (c) chronoamperograms at 2.03 and 1.93 V *vs.* RHE in 0.5 M H_2SO_4 at 24 ± 2 °C for $[Mn+Sb]O_y$ without (*orange*) and with SnO_2 (*black*), SiO_2 (*red*), CeO_2 (*blue*), Al_2O_3 (*green*), or TiO_2 (*pink*) deposited either as (i) overlayers, or (ii) underlayers. Currents are normalized to the geometric surface area.

A possible explanation of these observations can be that the lower amount of SnO_2 does not allow for the formation of a continuous layer and does not provide enough interactions with the underlying catalyst. On the contrary, the exceedingly thick layer produced with the 3 wt.% dispersion might block the catalytically active sites and thereby suppress the performance of the $[Mn+Sb]O_y$ catalyst. The SnO_2 layer formed with the 2 wt.% dispersion might be providing the close to optimal thickness with some free spaces on the surface of the catalyst and was therefore used for further detailed assessment.

In fact, the enhancement in the performance of $[Mn+Sb]O_y$ provided by 2 wt.% SnO_2 overlayer was the highest among all the other layers examined herein (Figure 5.1) and discussed further in the text (*vide infra*). The overpotential required to achieve the OER rate of 10 mA cm^{-2} with the 2 wt.% $SnO_2/[Mn+Sb]O_y$ after 24 h durability test was only *ca* 0.580 V and reasonably reproducible (exemplified in Figure 5.S5 for two independent samples). While the initial voltammetry was stable (Figure 5.S6a), the galvanostatic measurements revealed a slow initial degradation in the performance, which however still remained notably better than that of the unmodified manganese-antimony oxide after stabilization (Figure 5.S5). The comparison of the precatalytic regions of this catalyst before and after the experiment showed no significant differences (Figure 5.S7a).

No major shifts in the binding energies and changes in the shapes of the peaks were noted in the X-ray photoelectron spectra upon electrochemical tests. Comparisons of the experimental to the published data[47–49] suggests that the major oxidation states of the key elements at the surface are Mn^{3+}, Sb^{5+} and Sn^{4+} (Figure 5.S8a-b and Figure 5.S9a). Another important observation from XPS is the notable suppression of the corrosion of manganese during the operation. Indeed, the

surface of unmodified [Mn+Sb]O_y was notably depleted with Mn, while introduction of the SnO_2 layer decreased this loss substantially (Table 5.1). At the same time, a substantial part of SnO_2 was removed from the surface during the OER, though detectable overlayer still remained on the catalyst surface after 24 h of test.

Table 5.1. Relative concentrations of manganese and overlayer with respect to antimony on the catalysts surface before and after OER tests.[a]

	As prepared		Tested	
Overlayer	**Mn**	**Overlayer**	**Mn**	**Overlayer**
Unmodified	0.30	---	0.14	---
SnO_2	0.20	0.59	0.13	0.37
SiO_2	0.19	0.92	0.19	0.62
CeO_2	0.29	0.39	0.30	0.21
Al_2O_3	0.22	1.36	0.08	0.88
TiO_2	0.29	1.30	0.13	0.97

[a] Determined by XPS; tests were undertaken in 0.5 M H_2SO_4 at 24 ± 2 °C for 24 h.

Analysis of the as-prepared and tested unmodified [Mn+Sb]O_y catalyst by soft X-ray absorption spectroscopy (XAS) at the Mn L-edge revealed that the initially mixed Mn^{2+}+Mn^{3+} states, dominated by manganese(II), were essentially completely converted to Mn^{3+} (Figure 5.2). This is consistent with previous observations from hard XAS at the Mn K-edge as described in Chapter 3 and in Ref.[50] However, analysis of the 2 wt.% SnO_2/[Mn+Sb]O_y catalyst after 24 h galvanostatic followed by 1 h potentiostatic OER tests revealed a presence of notable amounts of Mn^{2+}. Thus, the introduction of the tin(IV) oxide overlayer appears to protect the manganese antimonate from oxidation, which is likely to support the observed suppressed corrosion (Table 5.1) and might also positively affect the electrocatalytic activity of the material.[3]

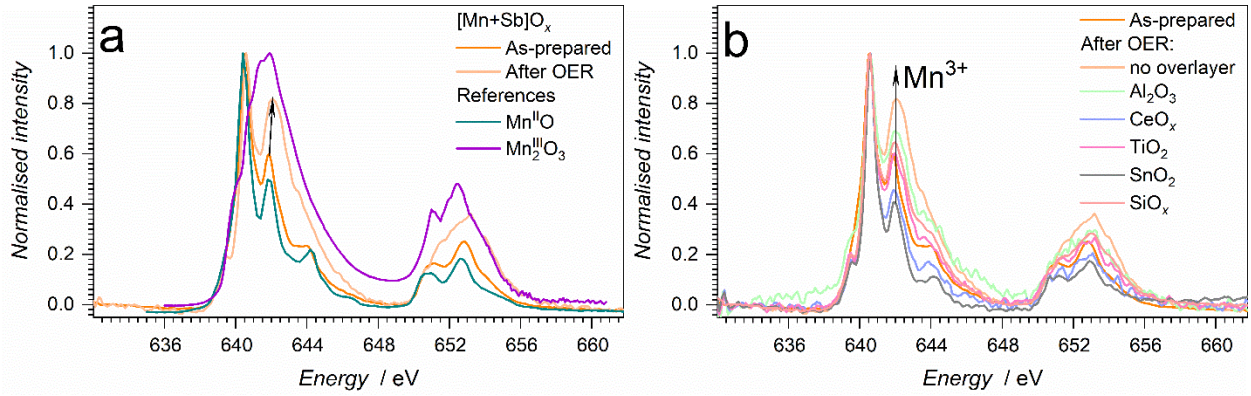

Figure 5.2. X-ray absorption spectra collected at Mn L-edge for the [Mn+Sb]O_x catalysts (a) without and (b) with overlayers present. Panel (a) compares the spectra of the unmodified material before (*dark orange*) and after (*light orange*) the OER tests to those of the MnO (*turquoise*) and Mn_2O_3 (*purple*) reference powders; arrow indicates the significantly increased contribution of Mn^{3+} after galvanostatic water oxidation experiments. Panel (b) shows the data for the catalysts modified with Al_2O_3 (*green*), CeO_x (*blue*), TiO_2 (*cyan*), SnO_2 (*grey*) and SiO_x (*red*) after the OER in comparison with the spectra for the unmodified [Mn+Sb]O_x before (*dark orange*) and after tests (*light orange*). Catalytic tests were undertaken at 24 ± 2 °C and 10 mA $cm^{-2}_{geom.}$ for 24 h in 0.5 M H_2SO_4.

Further, the same 2 wt.% SnO_2 dispersion was used to prepare the underlayer for the subsequent deposition of [Mn+Sb]O_y on the top. Interestingly, such a modification also enhanced the electrocatalytic activity of the material notably. The [Mn+Sb]O_y/2 wt.% SnO_2 catalyst remained stable with minimum drop in the potential over the 24 h galvanostatic tests at ambient temperature with a reproducible potential of approximately 0.565-0.577 V at a current density of 10 $mAcm^{-2}$ (Figure 5.S10), which is even better than with the tin(IV) oxide overlayer (Figure 5.1a). Similar to the case of the SnO_2 overlayer, no changes in the initial cyclic voltammograms are observed, but the stability under the constant current conditions is better (Figure 5.1b).

The key distinction between the [Mn+Sb]O_y/2 wt.% SnO_2 overlayer and [Mn+Sb]O_y/2 wt.% SnO_2 underlayer materials is found in the intensity of the precatalytic current in cyclic voltammetry, which was significantly, *ca* 2-fold, higher for the latter as compared to the former (Figure 5.S7a). This likely reflects a significantly higher electrocatalytically active surface area provided by the deposition of the manganese-antimonate on top of the tin(IV) oxide underlayer and most probably is the major reason for the enhanced stabilized OER catalytic performance. It is noted that the initial activity of 2 wt.% SnO_2/[Mn+Sb]O_y is higher than that of [Mn+Sb]O_y/2 wt.% SnO_2 (Figure 5.1a), which is probably associated with the effects of SnO_2 on the oxidation state of manganese and other potential electronic effects (Figure 5.2).

Table 5.2. Relative concentrations of manganese and underlayer with respect to antimony on the catalysts surface before and after OER tests.[a]

	As prepared		Tested at 24 ± 2 °C	
Underlayer	**Mn**	**Underlayer**	**Mn**	**Underlayer**
Unmodified	0.30	---	0.14	---
SnO_2	0.34	0.01	0.21	0.05
SiO_2	0.26	0.01	0.16	0.03
CeO_2	0.29	0.01	0.18	0.01
Al_2O_3	0.13	0	0.11	0.02

[a] Determined by XPS; tests were undertaken in 0.5 M H_2SO_4 at 24 ± 2 °C for 24 h.

However, this advantage provided by the overlayer is progressively lost, though to a not very significant extent, during the longer-term tests (Figure 5.1b) possibly due to the corrosion of SnO_2 (Table 5.1). As a result, [Mn+Sb]O_y/2 wt.% SnO_2 with a significantly higher active surface area turns out to be more advantageous after the durability tests, notwithstanding a significantly more pronounced level of surface corrosion of manganese (Table 5.2). We also note that there

were no meaningful changes in the XP spectra of manganese and antimony for [Mn+Sb]O_y/2 wt.% SnO_2 before and after tests, and with respect to the material modified with the SnO_2 overlayer (Figure 5.S11a and Figure 5.S12a-b).

5.2.2 Silicon oxide

Further studies focused on the modification of [Mn+Sb]O_y with SiO_x over- and underlayers. In this case, the oxide layers were produced by thermal decomposition of chlorotrimethylsilane. The thickness of the SiO_x overlayer was optimized by varying the volume ratio of this precursor to the hexane solvent; specifically examined ratios were 1:10, 1:20 and 1:30 vol (Figure 5.S4b). Similar to SnO_2 overlayers, the performance of [Mn+Sb]O_y was improved with all examined thicknesses of the silicon oxide overlayers, and the Cyclic voltammetric analysis revealed that the intermediate 1:20 vol. value is the best ratio for depositing the SiO_x overlayer (Figure 5.S1b). Two independent 1:20 SiO_x/[Mn+Sb]O_y samples showed highly consistent performance with the stabilised overpotential of 0.601 at 10 $mAcm^{-2}$ after 24 h of tests (Figure 5.S13). Though the manganese spectra remained the same, there is a shift to higher binding energy for antimony by 0.25 eV and silicon by 1 eV (Figure 5.S8c-d and Figure 5.S9b). The significant shift in the binding energy for silicon shows the presence of organics from the precursor in the freshly prepared electrode which was not removed after heating at 200°C but later the silicon is in +4 state after the experiment. While the loss of SiO_x layer is evident during the operation, the manganese concentration on the surface has no change (Table 5.1). This shows that SiO_x is very efficient in minimizing the manganese dissolution into the electrolyte. Importantly, soft XAS analysis at the Mn L-edge again demonstrated suppressed oxidation of manganese after the OER provided by the protection with the SiO_x overlayer (Figure 5.2b).

SiO_x as an underlayer also induced a notable improvement in the electrocatalytic performance of $[Mn+Sb]O_y$. The $[Mn+Sb]O_y$/1:20 SiO_x catalysts attained a current density of 10 mA cm^{-2} at an overpotential of 0.6 ± 0.02 V with a steady performance during the entire 24 h of operation (Figure 5.1b and Figure 5.S14). Similar to SnO_2, the intensity of precatalytic current of $[Mn+Sb]O_y$/1:20 SiO_x catalysts is almost twice that of 1:20 SiO_x/$[Mn+Sb]O_y$ possibly due to increased surface area (Figure 5.S7b). Although the initial higher activity provided by SiO_x overlayer is not maintained due to possible leaching of SiO_x (Table 5.1), the performance of these catalysts are similar inspite of manganese dissolution observed in $[Mn+Sb]O_y$/1:20 SiO_x catalyst during the electrochemical tests (Table 5.2).

5.2.3 Cerium oxide

CeO_2 which is widely reported as a cocatalyst and an overlayer with different materials[17,37–39] is tested here for its ability for improving the electrocatalytic properties of $[Mn+Sb]O_y$. The galvanostatic measurements for CeO_x/$[Mn+Sb]O_y$ showed reproducible stability for 24 h of testing with an overpotential of 0.59 ± 0.02 V for the current density of 10 mA cm^{-2} (Figure 5.1 and Figure 5.S15). Although the initial cyclic voltammetry was stable, CeO_x/$[Mn+Sb]O_y$ catalyst suffered slow degradation in the electrochemical tests. No notable changes were observed in the precatalytic region of CeO_x/$[Mn+Sb]O_y$ catalyst (Figure 5.S7c). XPS analysis proved that CeO_x can prevent manganese dissolution by sacrificing itself in the reaction like SnO_2 and SiO_x (Table 5.1). Any major variations in the elemental spectrum of this catalyst were not detectable in the XPS analysis before and after the experiments (Figure 5.S8e-f and Figure 5.S9c).

CeO_x can also be used as a possible underlayer as it could reduce the overpotential required to 0.62 ± 0.02V for obtaining a current density of 10 mA cm^{-2} with a stable and reproducible performance (Figure 5.1 and Figure 5.S16). There was a major improvement in the catalytic activity in the initial cyclic voltammogram with the increase in cycles and it led to comparatively stable performance throughout the operation compared to $[Mn+Sb]O_y$ modified with other underlayers (Figure 5.S6c). Manganese corrosion in $[Mn+Sb]O_y/CeO_x$ catalyst is confirmed from the changes in precatalytic region and XPS surface analysis (Figure 5.S7c and Table 5.2). XP spectra for Mn^{3+}, Sb^{5+} and Ce^{4+} oxidation states of the fresh catalysts were same after the long duration stability tests (Figure 5.S11c and 5.S12e-f).

5.2.4 Aluminium oxide

Further studies were performed with mesoporous alumina which has been extensively used as a catalyst support because of its high surface area and thermal stability to modify $[Mn+Sb]O_y$ catalyst. The m-Al_2O_3/$[Mn+Sb]O_y$ recorded a reproducible overpotential of 0.591 – 0.599 V after a 24 h of chronopotentiometry for a current density of 10 mA cm^{-2} (Figure 5.1 and Figure 5.S17). Although the initial voltammetry showed a stable performance, the catalyst showed slow degradation during the galvanostatic test (Figure 5.S6d). But the stabilized performance is still better than unmodified $[Mn+Sb]O_y$ catalyst. However, the precatalytic region showed leaching of manganese into the electrolyte (Figure 5.S7d). This is further confirmed by the XPS analysis. Compared to other overlayers, remarkably higher corrosion of m-Al_2O_3 was observed during the test along with manganese which deterioration of the stability of the catalyst in the operation (Table 5.1). In spite of the dissolution, no significant changes in peak and position are not

observed for Mn^{3+}, Sb^{5+} and Al^{3+} after the electrochemical tests (Figure 5.S8g-h and Figure 5.S9d).

m-Al_2O_3 underlayer also could reduce the overpotential of unmodified [Mn+Sb]O_y and showed a steady performance at an overpotential of 0.61 ± 0.02 V for a current density of 10 mA cm^{-2} (Figure 5.1 and Figure 5.S18). Two out of three independent tests could not show a significant improvement in the catalytic activity with m-Al_2O_3 underlayer (Figure 5.S18). Unlike SnO_2 and SiO_x, the current intensity in the precatalytic region of [Mn+Sb]O_y/m-Al_2O_3 is lower than that of m-Al_2O_3/[Mn+Sb]O_y (Figure 5.S7d). Although no major changes were observed for manganese and antimony XP spectra, the aluminium peaks could not be determined because of its low intensity (Figure 5.S8g-h and Figure 5.S9d). Interestingly, no notable dissolution of manganese is observed for [Mn+Sb]O_y/m-Al_2O_3 catalyst (Table 5.2). XPS analysis also confirms that manganese concentration on the surface of [Mn+Sb]O_y/m-Al_2O_3 catalyst is relatively less compared to other underlayer modified [Mn+Sb]O_y. So, possibly the mesoporous structure of the underlayer reduces the active surface area of the catalyst involved in reaction and the observed enhancement in the activity of the catalyst can be the result of other positive effects with an underlayer.

5.2.5 Titanium(IV) oxide

Finally, m-TiO_2 was also tested as an interfacial layer for [Mn+Sb]O_y. As an overlayer, m-TiO_2 was successful in reducing the overpotential to 0.607 and 0.622 V for two independent experiments after 24 h of chronopotentiometry for a current density of 10 mA cm^{-2} (Figure 5.1 and Figure 5.S19). But the studies showed that there was a significant degradation of the

performance of m-TiO_2/[Mn+Sb]O_y catalyst although the stabilized performance is better than the unmodified catalyst. The study of the precatalytic region showed high manganese dissolution in the process which is further confirmed by the XPS analysis (Figure 5.S7e and Table 5.1). m-TiO_2 failed to protect underlying manganese unlike other overlayers which led to remarkable degradation observed with m-TiO_2/[Mn+Sb]O_y. But it was not successful as an underlayer since it led to more inactivity of [Mn+Sb]O_y catalyst as shown in Figure 5.S20.

5.3 SUMMARY OF THE OBSERVED EFFECTS

Thus, all metals oxides examined herein as interfacial layers to modify the manganese-antimony electrocatalyst induced notable enhancements in the performance of [Mn+Sb]O_y during the OER, notwithstanding their negligible individual catalytic activity for this process. Deposition of oxide overlayers was found to suppress complete oxidation of manganese to the 3+ state during the OER as well as the decrease of the concentration of Mn with respect to Sb on the surface of the catalyst. These observations were true for all examined materials (except for Al_2O_3 where Mn L-edge XAS data were not meaningful due to a very significant thickness of the mesoporous overlayer). Such lack of the dependence of the promoting effect on the chemical nature of the overlayer suggests that the key catalytic species are still manganese antimonate in all cases, but with an altered oxidation states provided by the surface modification, which is probably the major cause of the enhanced catalytic activity. Although we cannot rule out the electronic effects of the oxide overlayers on the catalytic performance, we do not have any evidence, including from XPS, to support this possibility. It is also observed that mesoporous overlayers failed to

prevent underlying manganese dissolution unlike other overlayers, that led to slow degradation of these catalysts.

In the case of the underlayers, a notable enhancement in the electrochemically active surface area of $[Mn+Sb]O_y$ was found and was likely providing the enhanced activity despite of manganese dissolution during the tests. The one exception was the TiO_2-based material, which did not allow for any improvements and also, it is noted that the enhancement with Al_2O_3 layer was not very significant. Therefore, it can be assumed that mesoporous layers likely to reduce the active surface area available for reaction on $[Mn+Sb]O_y$ and has a detrimental effect on the catalyst performance because of its thickness and mesoporous structure.

5.4 CONCLUSIONS

Surface and substrate engineering of the catalyst by modifying it with an additional oxide layer produced an enhancement in the overall performance of the catalyst though it could not show a notable improvement in the stability. The testing of these oxides without the $[Mn+Sb]O_y$ catalyst proved that these oxides are electrochemically inactive for water oxidation. So, it is quite interesting to observe the positive effect of these layers on the catalyst. The interplay of altered surface charge densities, active surface area, effective resistance, and the availability of an additional adsorption site for the intermediates can be speculated as possible reasons for the observation though the actual mechanism is uncertain except for the altered oxidation states of active species with overlayers. More detailed investigation is necessary to understand the mechanism that is promoting better activity with these layers which will possibly lead to design and choose the right oxide layer with optimized thickness required for each catalyst. Since low-

cost electrochemical systems are essential to meet the global energy demands, techniques to improve the activity of the catalyst with low-catalyst loading for earth-abundant stable catalysts will bring a major breakthrough in water electrolysis for hydrogen production.

5.5 SUPPLEMENTARY INFORMATION

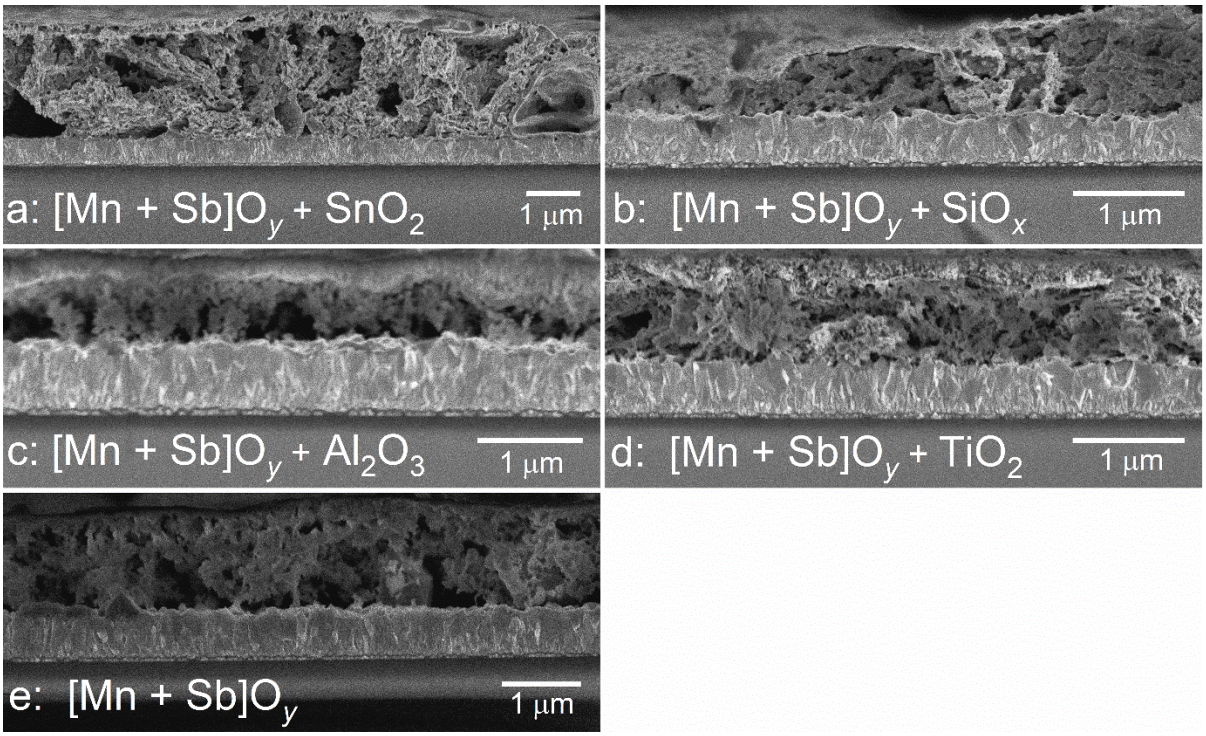

Figure 5.S1. Cross-sectional scanning electron micrographs of [Mn+Sb]O_y with different overlayers (a) SnO_2, (b) SiO_x, (c) Al_2O_3, (d) TiO_2 and (e) none for catalysts before testing for operation in stirred 0.5 M H_2SO_4 at ambient temperature.

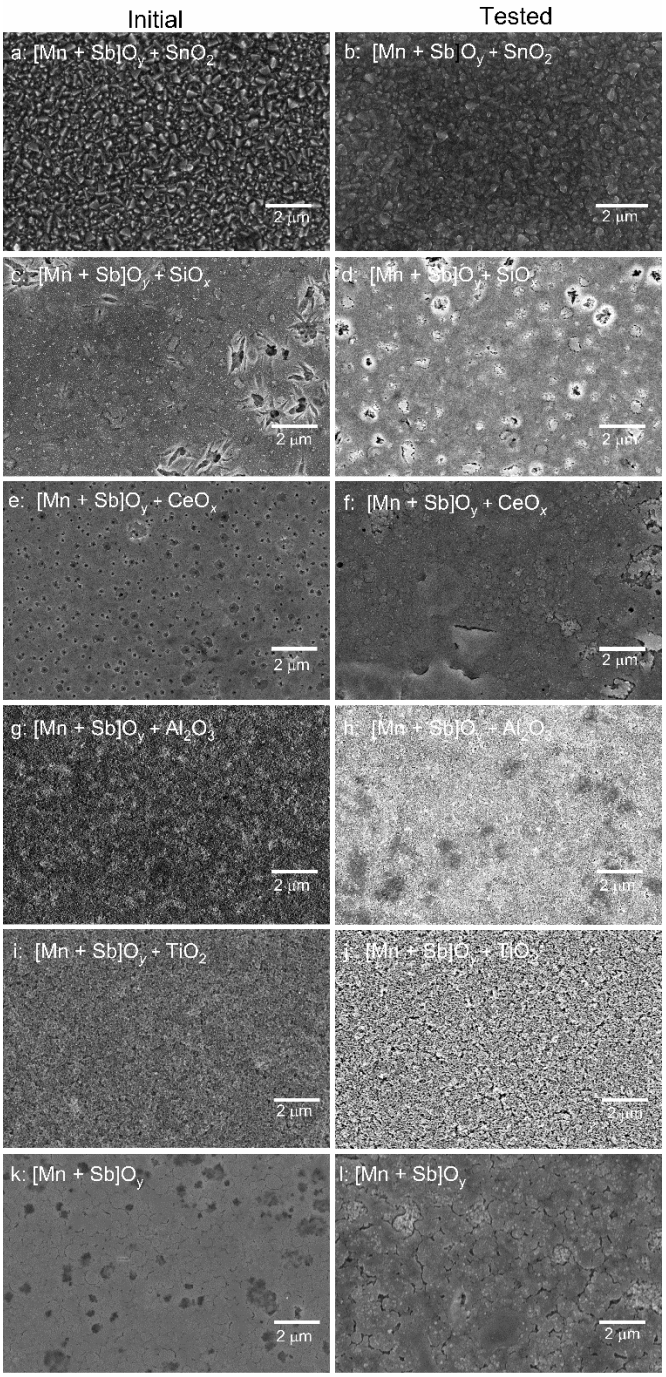

Figure 5.S2. Topview scanning electron micrographs of [Mn+Sb]O_y with different overlayers (a-b) SnO_2, (c-d) SiO_x, (e-f) CeO_x, (g-h) Al_2O_3, (i-j) TiO_2 and (k-l) none for catalysts (a, c, e, g, i, k) before and (b, d, f, h, j, l) after 24 h galvanostatic tests (at 10 mA $cm^{-2}_{geom.}$) and subsequent 1 h potentiostatic (at 2.03 and 1.93 V *vs.* RHE for 0.5 h at each potential) operation in stirred 0.5 M H_2SO_4 at ambient temperature.

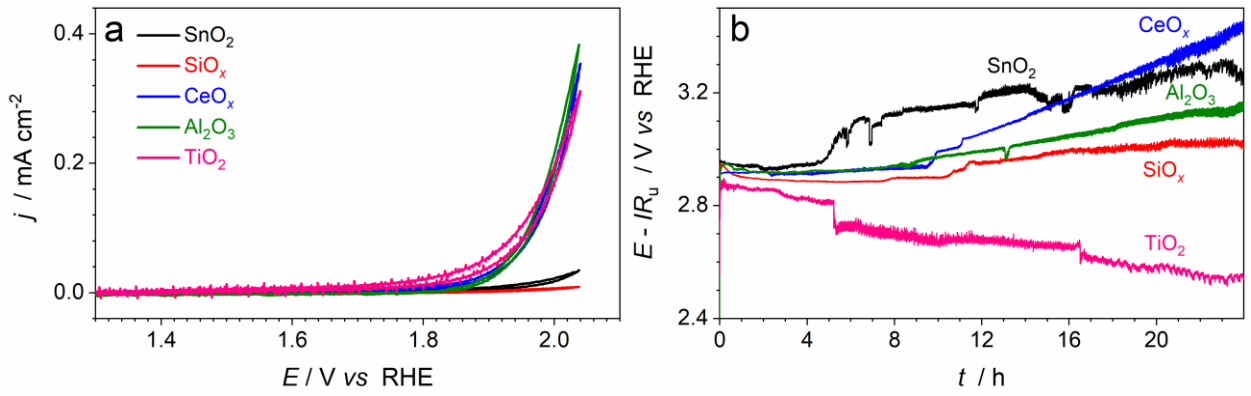

Figure 5.S3. (a) Cyclic voltammetry (potentials are not corrected for the IR_u-drop), and (b) Chronopotentiograms (current density 10 mA $cm^{-2}_{geom.}$) corrected for ohmic losses, recorded for FTO electrodes modified with SnO_2 (*black*), SiO_x (*red*), CeO_x (*blue*), Al_2O_3 (*green*), and TiO_2 (*pink*) in contact with 0.5 M H_2SO_4 at 24 ± 2 °C. Currents are normalized to the geometric surface area.

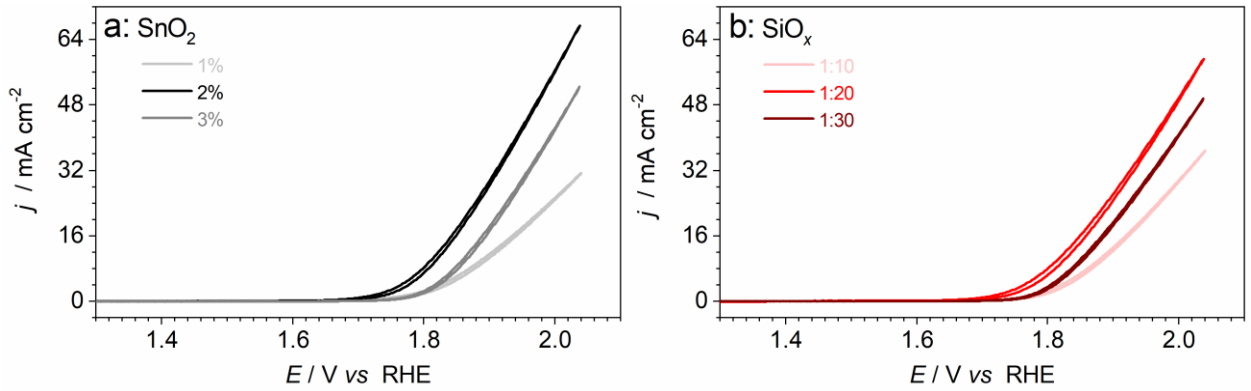

Figure 5.S4. (a) Cyclic voltammetry (potentials are not corrected for the IR_u-drop) recorded for FTO electrodes modified with (a) SnO_2 for SnO_2 dispersion liquid diluted to different percentages, and (b) SiO_x for different Chlorotrimethylsilane and Hexane vol/vol ratio in contact with 0.5 M H_2SO_4 at 24 ± 2 °C. Currents are normalized to the geometric surface area.

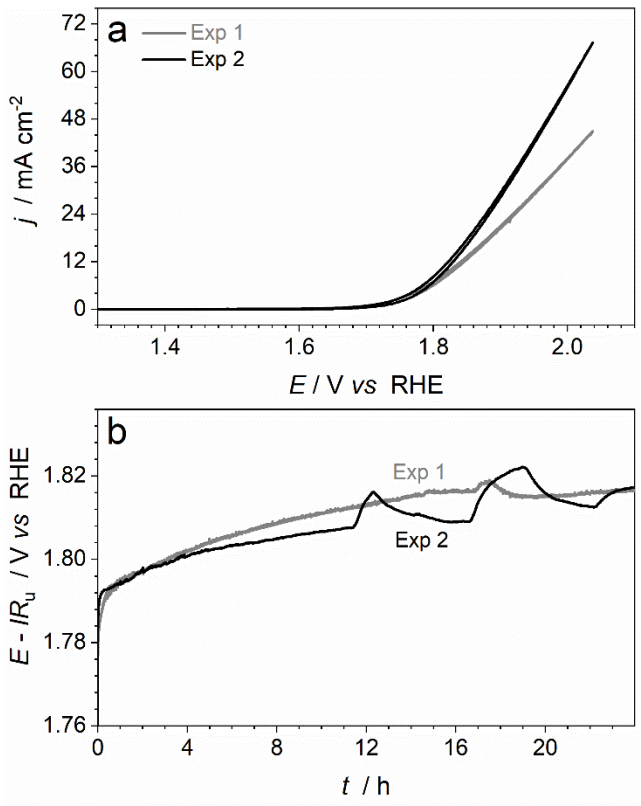

Figure 5.S5. Reproducibility of the electrocatalytic properties of [Mn+Sb]O_y with SnO_2 overlayer demonstrated for two independent samples tested at 24 ± 2 °C in 0.5 M H_2SO_4: (a) initial cyclic voltammetry (potentials are not corrected for ohmic losses), and (b) IR_u-corrected chronopotentiograms for a current density 10 mA $cm^{-2}_{geom.}$).

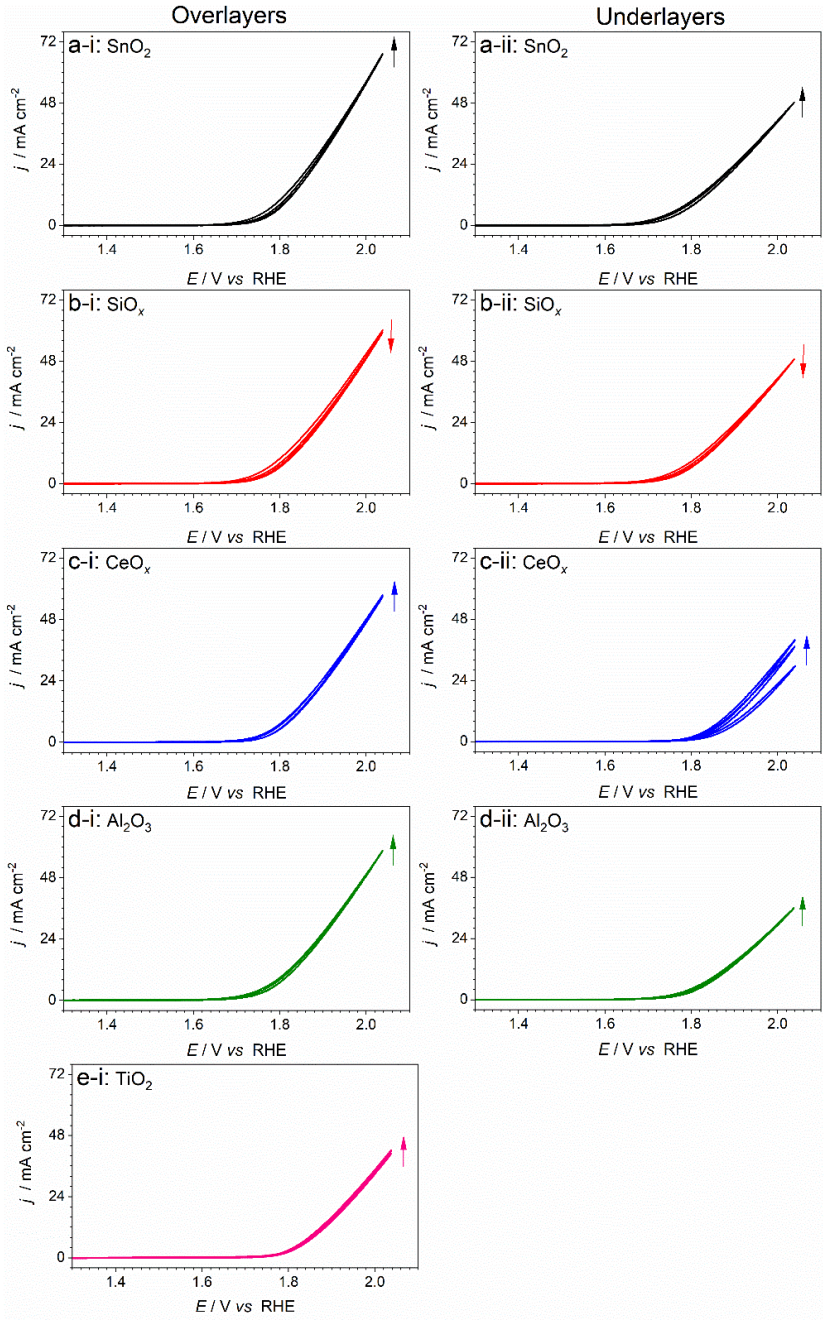

Figure 5.S6. Evolution of cyclic voltammograms (scan rate, v = 0.020 V s^{-1}; three consecutive cycles shown) of [Mn+Sb]O_y with (a) SnO_2, (b) SiO_x, (c) CeO_x, (d) Al_2O_3, and (e) TiO_2 deposited either as (i) overlayers, or (ii) underlayers tested in 0.5 M H_2SO_4 at ambient temperature. Arrows show the evolution of the current density with cycling. Currents are normalized to the geometric surface area of the electrode; potential values were not corrected for the iR_u-drop.

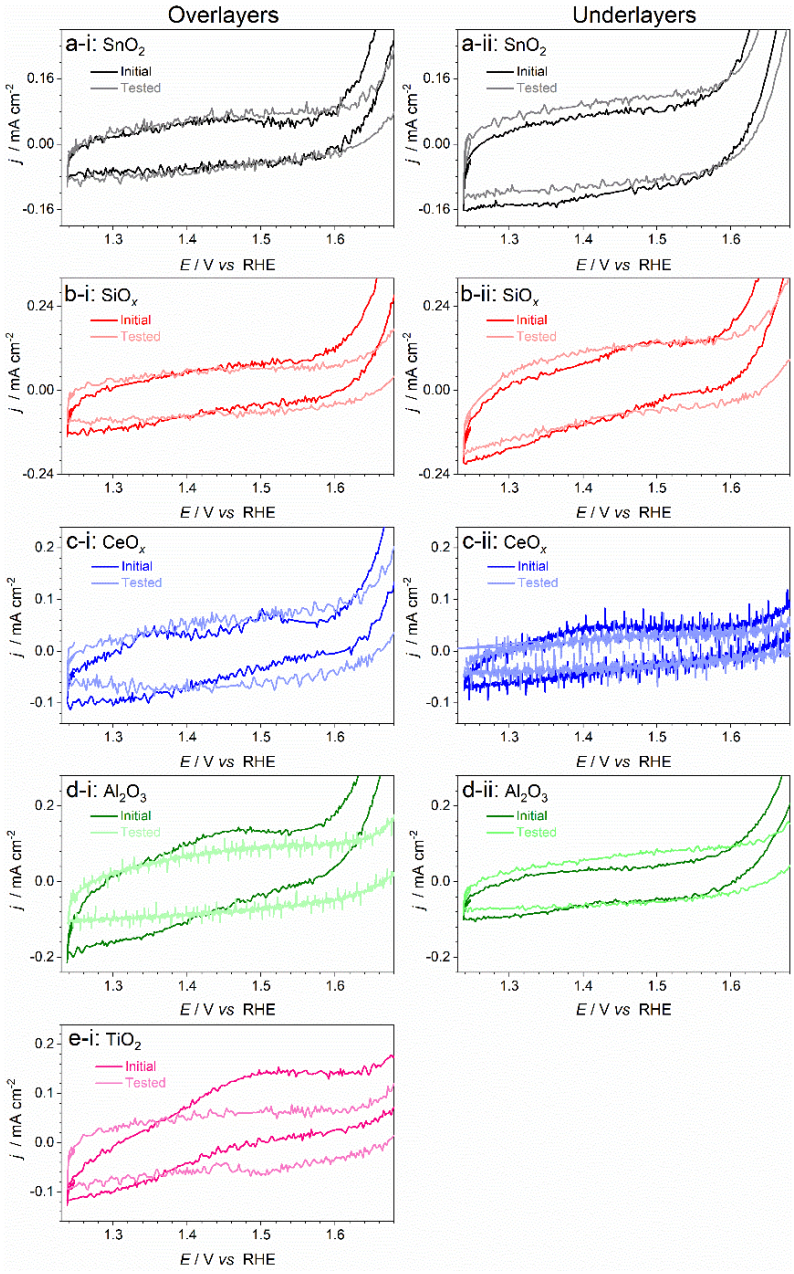

Figure 5.S7. Comparison of the pre-catalytic regions of the quazi-stabilized cyclic voltammograms (scan rate, v = 0.020 V s-1) of $[Mn+Sb]O_y$ with (a) SnO_2, (b) SiO_x, (c) CeO_x, (d) Al_2O_3, and (e) TiO_2 deposited either as (i) overlayers, or (ii) underlayers tested in 0.5 M H_2SO_4 at ambient temperature before (pale traces) and after (vivid traces) 25 h durability tests (24 h at 10 mA cm^{-2}; 0.5 h at 2.03 V vs. RHE; 0.5 h at 1.93 V vs. RHE) under the same conditions. Currents are normalized to the geometric surface area of the electrode; potentials were not corrected for the IR_u-drop.

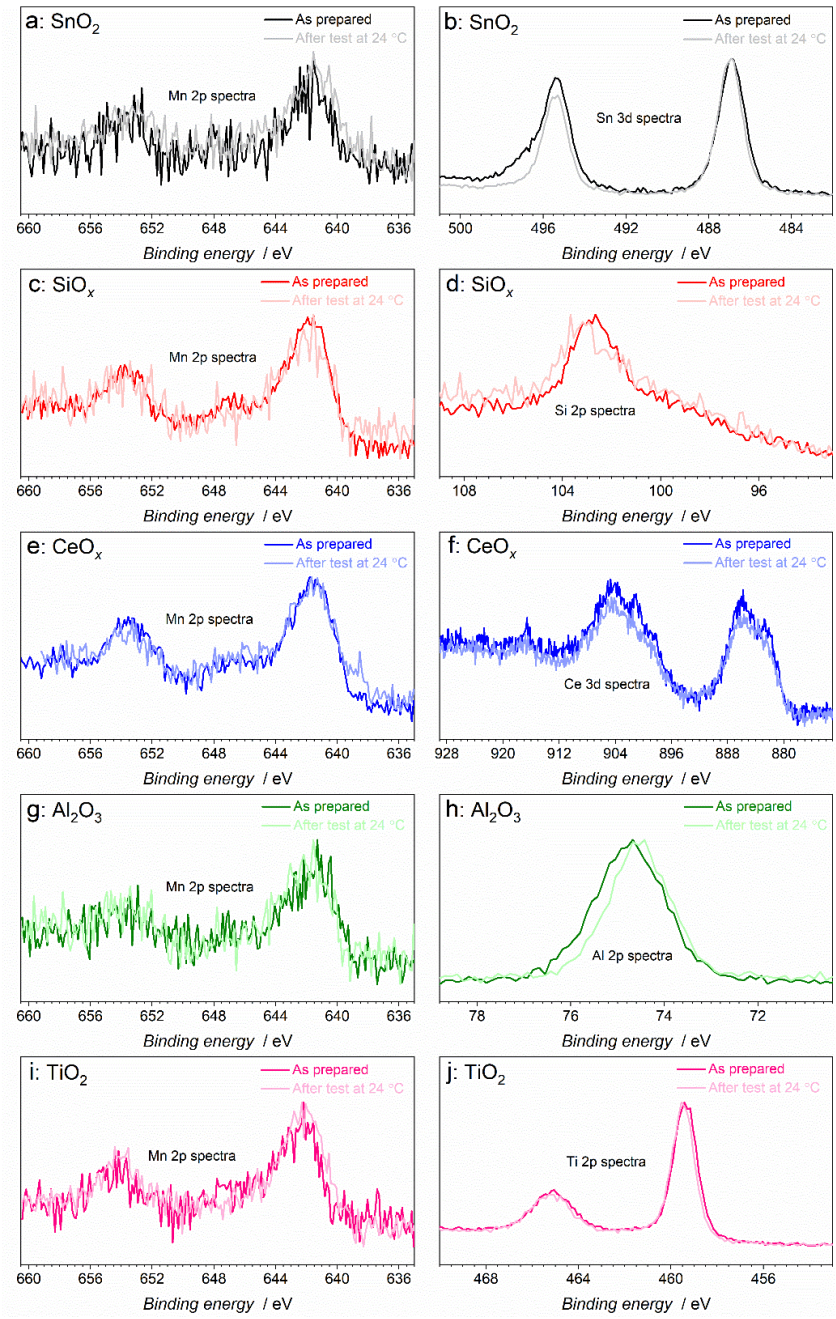

Figure 5.S8. XPS of [Mn+Sb]O_y with different overlayers: (a,c,e,g,i) Mn 2p spectra, and (b) Sn 3d spectra with SnO_2; (d) Si 2p spectra with SiO_x; (f) Ce 3d spectra with CeO_x; (h) Al 2p spectra with Al_2O_3; (j) Ti 2p spectra with TiO_2; before (pale traces) and after (vivid traces) electrocatalytic tests in 0.5 M H_2SO_4. The catalysts were tested for 24 h galvanostatic (at 10 mA $cm^{-2}_{geom.}$) and subsequent 1 h potentiostatic (at 2.03 and 1.93 V *vs.* RHE for 0.5 h at each potential) operation at ambient temperature.

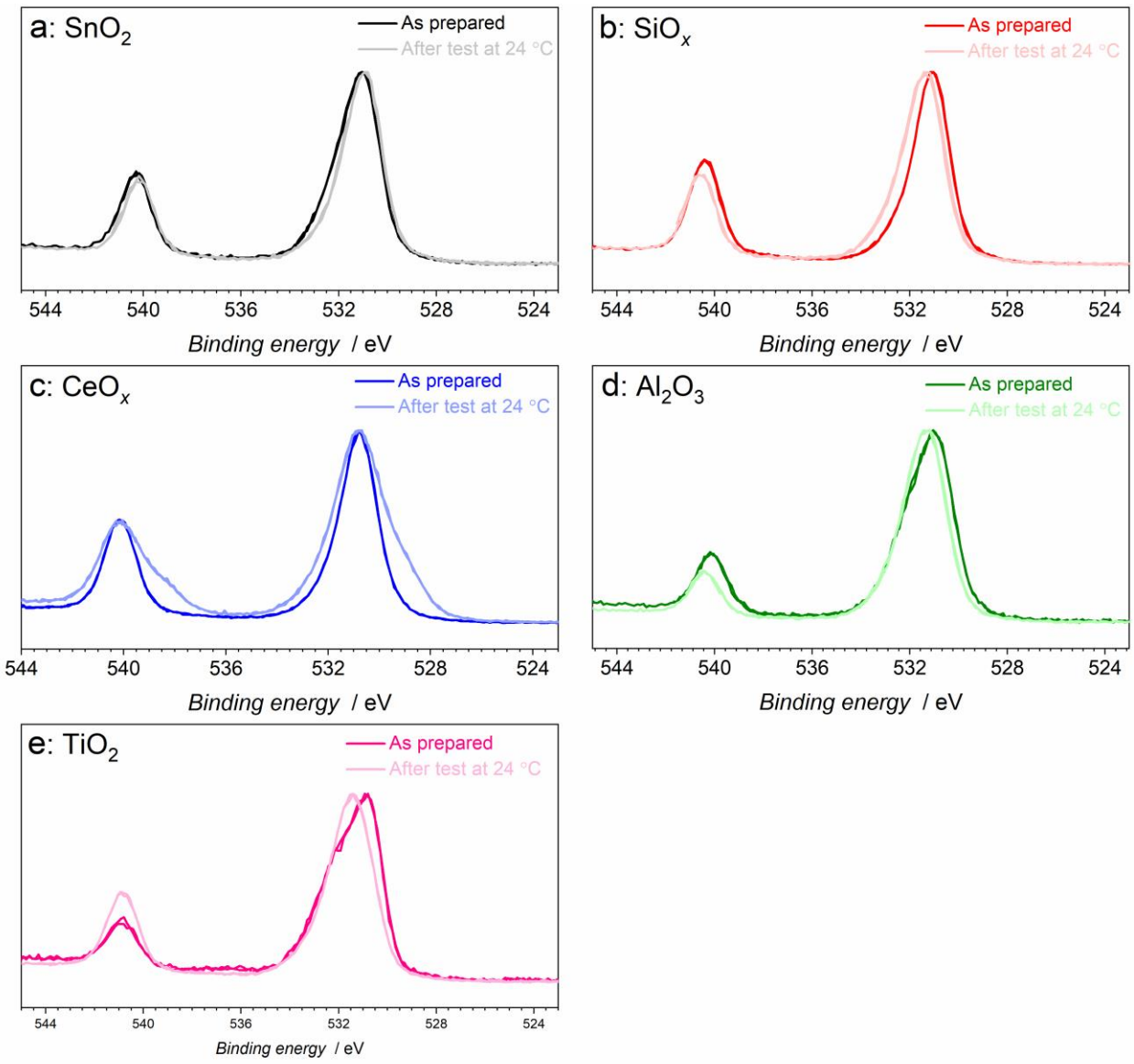

Figure 5.S9. Sb 3d + O 1s spectra for [Mn+Sb]O_y with different overlayers of (a) SnO_2, (b) SiO_2, (c) CeO_2, (d) Al_2O_3, and (e) TiO_2 before (pale traces) and after (vivid traces) electrocatalytic tests in 0.5 M H_2SO_4. The catalysts were tested for 24 h galvanostatic (at 10 mA $cm^{-2}_{geom.}$) and subsequent 1 h potentiostatic (at 2.03 and 1.93 V *vs.* RHE for 0.5 h at each potential) operation at ambient temperature.

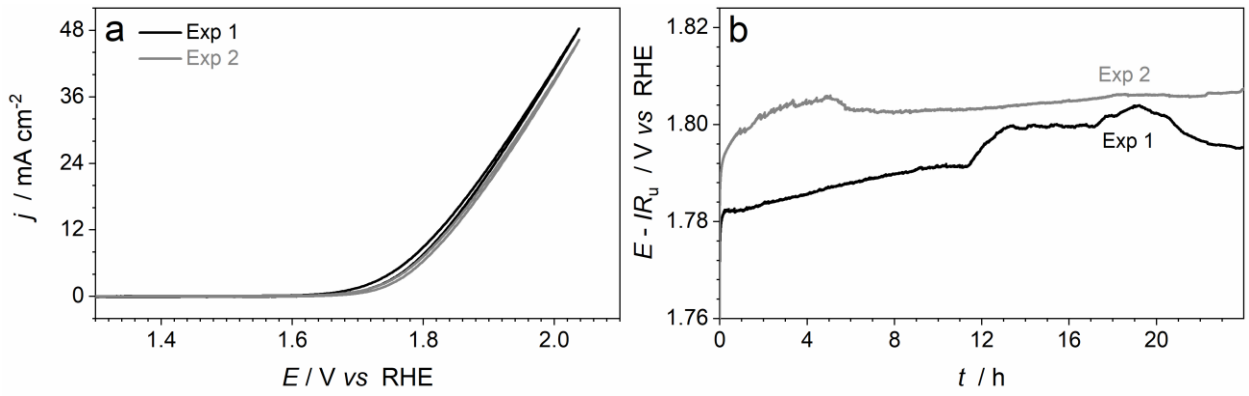

Figure 5.S10. Reproducibility of the electrocatalytic properties of [Mn+Sb]O_y with SnO_2 underlayer demonstrated for two independent samples tested at 24 ± 2 °C in 0.5 M H_2SO_4: (a) initial cyclic voltammetry (potentials are not corrected for ohmic losses), and (b) IR_u-corrected chronopotentiograms (current density 10 mA $cm^{-2}_{geom.}$).

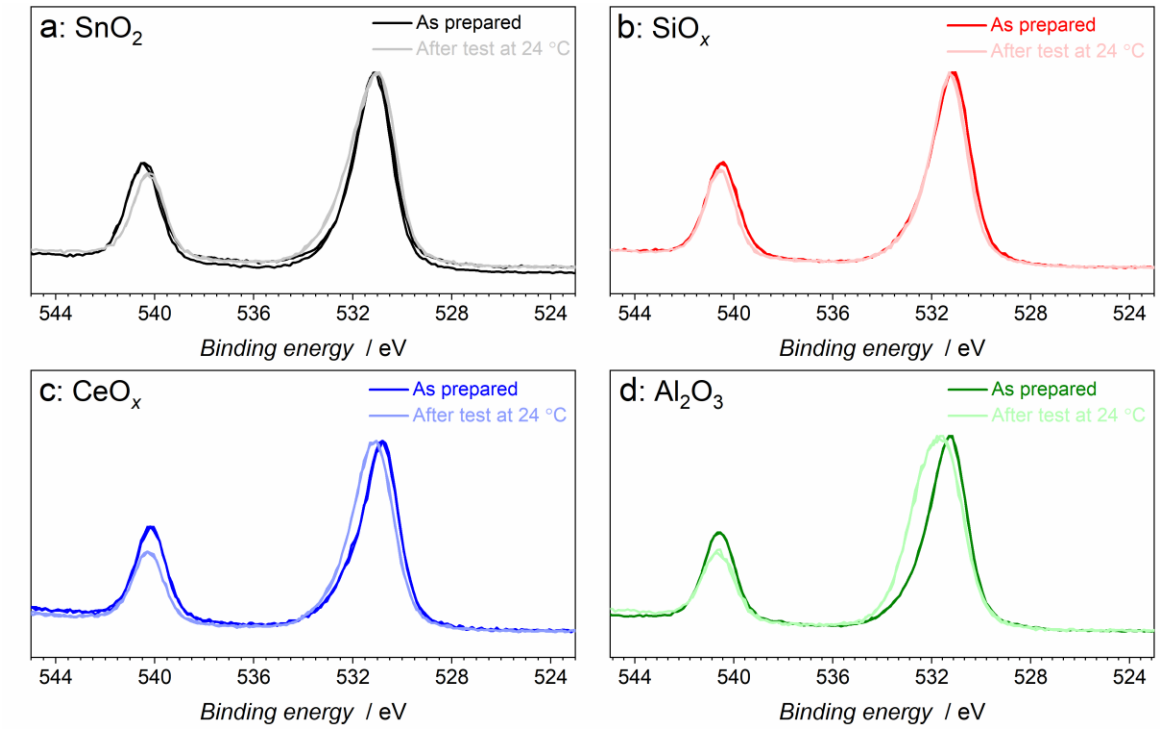

Figure 5.S11. Sb 3d + O 1s spectra for [Mn+Sb]O_y with different underlayers of (a) SnO_2, (b) SiO_x, (c) CeO_x, and (d) Al_2O_3, before (pale traces) and after (vivid traces) electrocatalytic tests in 0.5 M H_2SO_4. The catalysts were tested for 24 h galvanostatic (at 10 mA $cm^{-2}_{geom.}$) and subsequent 1 h potentiostatic (at 2.03 and 1.93 V *vs.* RHE for 0.5 h at each potential) operation at ambient temperature.

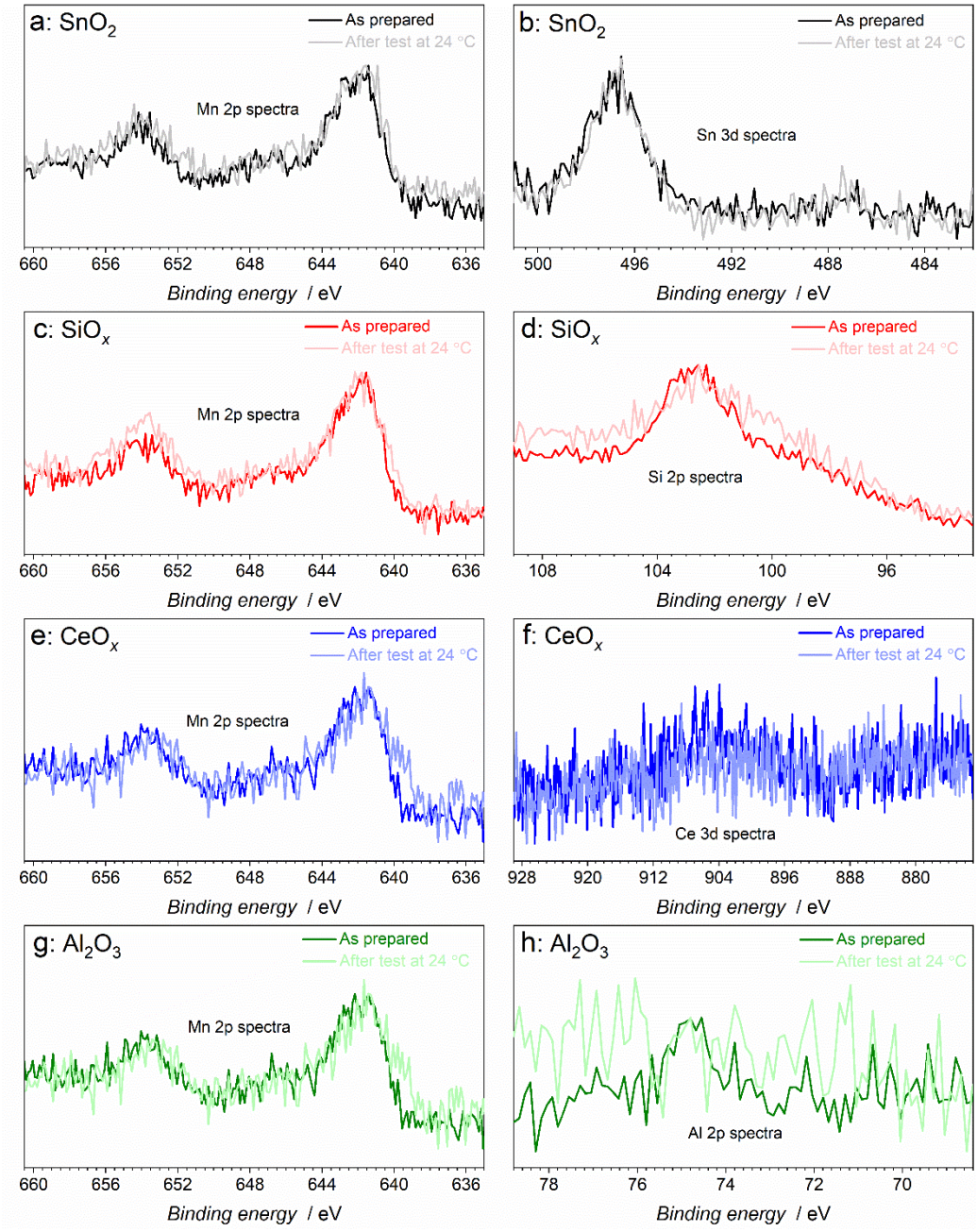

Figure 5.S12. XPS of [Mn+Sb]O_y with different underlayers: (a,c,e,g) Mn 2p spectra, and (b) Sn 3d spectra with SnO_2; (d) Si 2p spectra with SiO_x and (f) Ce 3d spectra with CeO_x; and (h) Al 2p spectra with Al_2O_3; before (pale traces) and after (vivid traces) electrocatalytic tests in 0.5 M H_2SO_4. The catalysts were tested subsequently 24 h galvanostatic (at 10 mA $cm^{-2}_{geom.}$) and subsequent 1 h potentiostatic (at 2.03 and 1.93 V *vs.* RHE for 0.5 h at each potential) operation at ambient temperature.

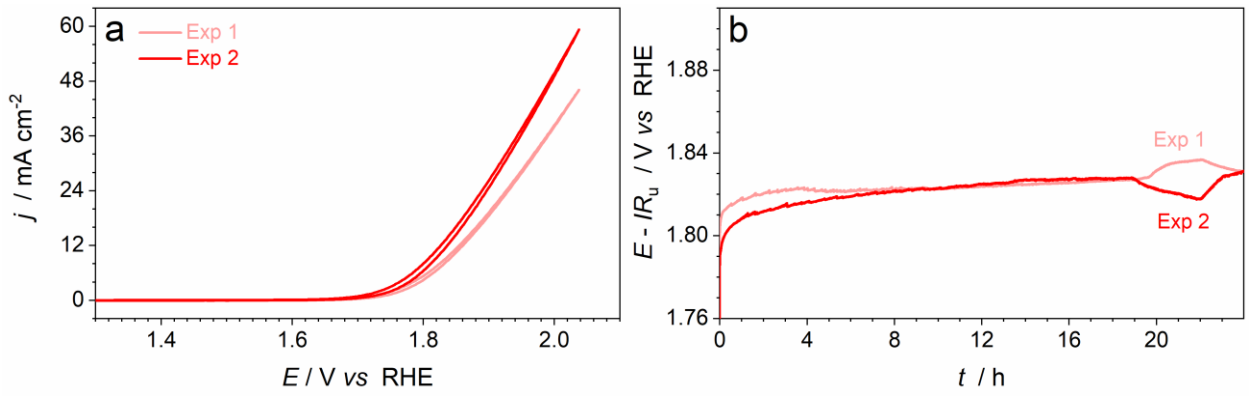

Figure 5.S13. Reproducibility of the electrocatalytic properties of [Mn+Sb]O_y with SiO_x overlayer demonstrated for two independent samples tested at 24 ± 2 °C in 0.5 M H_2SO_4: (a) initial cyclic voltammetry (potentials are not corrected for ohmic losses), and (b) IR_u-corrected chronopotentiograms (current density 10 mA $cm^{-2}_{geom.}$).

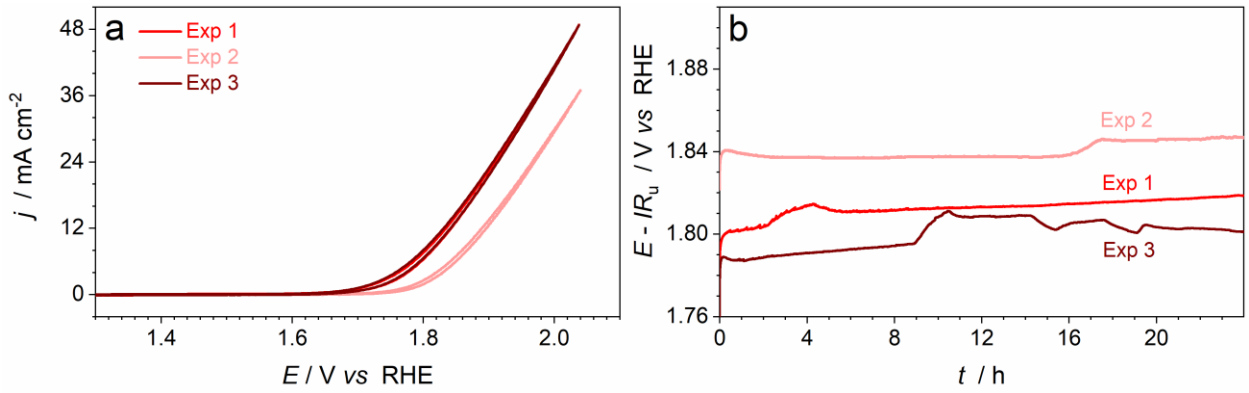

Figure 5.S14. Reproducibility of the electrocatalytic properties of [Mn+Sb]O_y with SiO_x underlayer demonstrated for three independent samples tested at 24 ± 2 °C in 0.5 M H_2SO_4: (a) initial cyclic voltammetry (potentials are not corrected for ohmic losses), and (b) IR_u-corrected chronopotentiograms (current density 10 mA $cm^{-2}_{geom.}$).

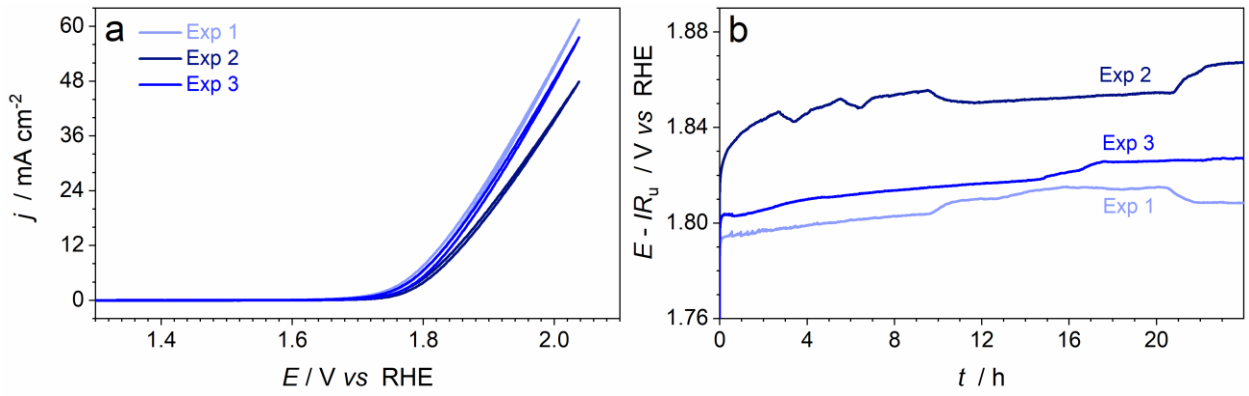

Figure 5.S15. Reproducibility of the electrocatalytic properties of [Mn+Sb]O_y with CeO_x overlayer demonstrated for three independent samples tested at 24 ± 2 °C in 0.5 M H_2SO_4: (a) initial cyclic voltammetry (potentials are not corrected for ohmic losses), and (b) IR_u-corrected chronopotentiograms (current density 10 mA $cm^{-2}_{geom.}$).

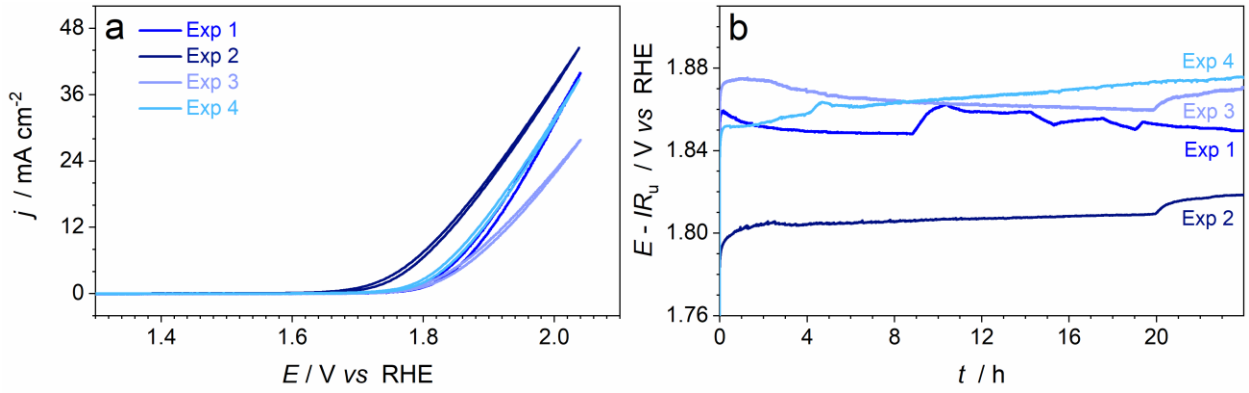

Figure 5.S16. Reproducibility of the electrocatalytic properties of [Mn+Sb]O_y with CeO_x underlayer demonstrated for four independent samples tested at 24 ± 2 °C in 0.5 M H_2SO_4: (a) initial cyclic voltammetry (potentials are not corrected for ohmic losses), and (b) IR_u-corrected chronopotentiograms (current density 10 mA $cm^{-2}_{geom.}$).

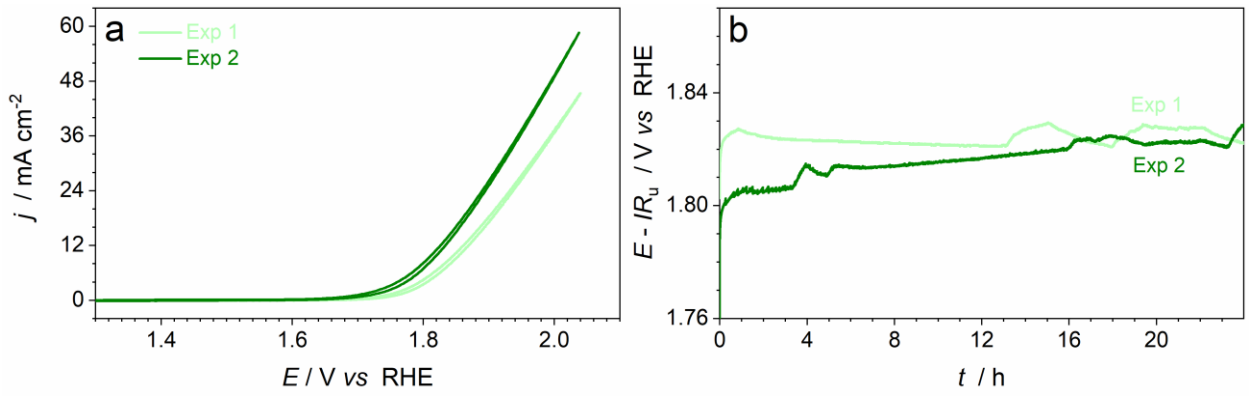

Figure 5.S17. Reproducibility of the electrocatalytic properties of [Mn+Sb]O_y with Al_2O_3 overlayer demonstrated for two independent samples tested at 24 ± 2 °C in 0.5 M H_2SO_4: (a) initial cyclic voltammetry (potentials are not corrected for ohmic losses), and (b) IR_u-corrected chronopotentiograms (current density 10 mA $cm^{-2}_{geom.}$).

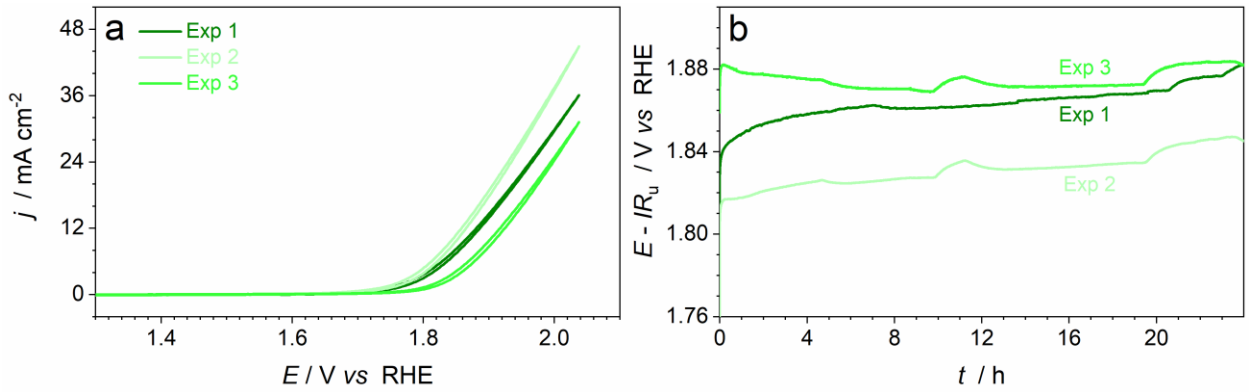

Figure 5.S18. Reproducibility of the electrocatalytic properties of [Mn+Sb]O_y with Al_2O_3 underlayer demonstrated for three independent samples tested at 24 ± 2 °C in 0.5 M H_2SO_4: (a) initial cyclic voltammetry (potentials are not corrected for ohmic losses), and (b) IR_u-corrected chronopotentiograms (current density 10 mA $cm^{-2}_{geom.}$).

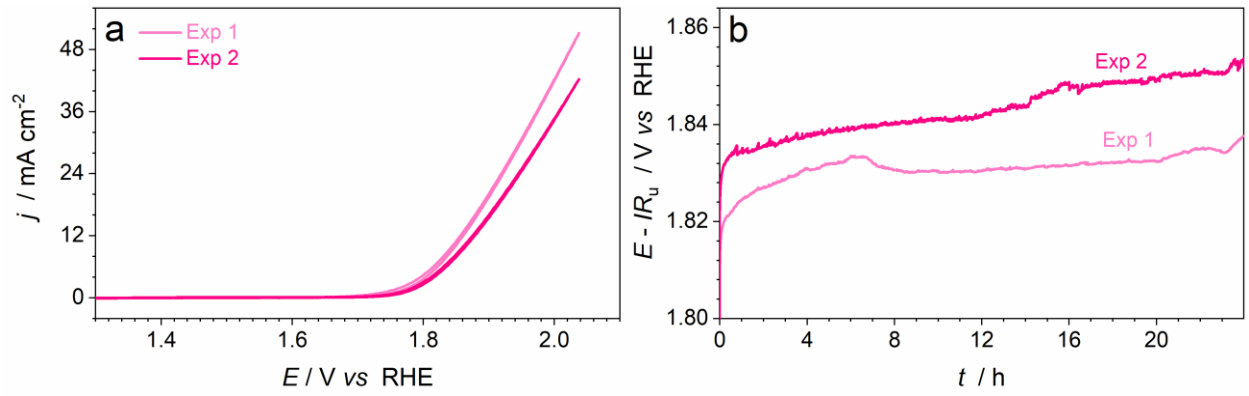

Figure 5.S19. Reproducibility of the electrocatalytic properties of [Mn+Sb]O_y with TiO_2 overlayer demonstrated for two independent samples tested at 24 ± 2 °C in 0.5 M H_2SO_4: (a) initial cyclic voltammetry (potentials are not corrected for ohmic losses), and (b) IR_u-corrected chronopotentiograms (current density 10 mA $cm^{-2}_{geom.}$).

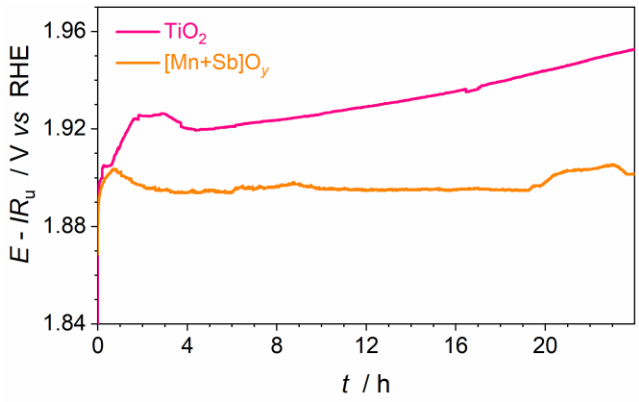

Figure 5.S20. IR_u-corrected chronopotentiogram at a current density 10 mA cm^{-2}_{geom} with TiO_2 underlayer for [Mn+Sb]O_y.

5.6 REFERENCES

(1) Moreno-Hernandez, I. A.; Macfarland, C. A.; Read, C. G.; Papadantonakis, K. M.; Brunschwig, B. S.; Lewis, N. S. Crystalline Nickel Manganese Antimonate as a Stable Water-Oxidation Catalyst in Aqueous 1.0 M H_2SO_4. *Energy Environ. Sci.* **2017**, *10* (10), 2103–2108. https://doi.org/10.1039/c7ee01486d.

(2) Shinde, A.; Jones, R. J. R.; Guevarra, D.; Mitrovic, S.; Becerra-Stasiewicz, N.; Haber, J. A.; Jin, J.; Gregoire, J. M. High-Throughput Screening for Acid-Stable Oxygen Evolution Electrocatalysts in the (Mn–Co–Ta–Sb)O_x Composition Space. *Electrocatalysis* **2015**, *6* (2), 229–236. https://doi.org/10.1007/s12678-014-0237-7.

(3) Zhou, L.; Shinde, A.; Montoya, J. H.; Singh, A.; Gul, S.; Yano, J.; Ye, Y.; Crumlin, E. J.; Richter, M. H.; Cooper, J. K.; Stein, H. S.; Haber, J. A.; Persson, K. A.; Gregoire, J. M. Rutile Alloys in the Mn-Sb-O System Stabilize Mn3+ to Enable Oxygen Evolution in Strong Acid. *ACS Catal.* **2018**, *8* (12), 10938–10948. https://doi.org/10.1021/acscatal.8b02689.

(4) Kim, B.; Park, I.; Yoon, G.; Kim, J. S.; Kim, H.; Kang, K. Atomistic Investigation of Doping Effects on Electrocatalytic Properties of Cobalt Oxides for Water Oxidation. *Adv. Sci.* **2018**, *5* (12). https://doi.org/10.1002/advs.201801632.

(5) Liu, X.; Zhang, L.; Zheng, Y.; Guo, Z.; Zhu, Y.; Chen, H.; Li, F.; Liu, P.; Yu, B.; Wang, X.; Liu, J.; Chen, Y.; Liu, M. Uncovering the Effect of Lattice Strain and Oxygen Deficiency on Electrocatalytic Activity of Perovskite Cobaltite Thin Films. *Adv. Sci.* **2019**, *6* (6), 1–9. https://doi.org/10.1002/advs.201801898.

(6) Guo, F.; Wu, Y.; Chen, H.; Liu, Y.; Yang, L.; Ai, X.; Zou, X. High-Performance Oxygen Evolution Electrocatalysis by Boronized Metal Sheets with Self-Functionalized Surfaces. *Energy Environ. Sci.* **2019**, *12* (2), 684–692. https://doi.org/10.1039/c8ee03405b.

(7) Zhang, B.; Zheng, X.; Voznyy, O.; Comin, R.; Bajdich, M.; García-Melchor, M.; Han, L.; Xu, J.; Liu, M.; Zheng, L.; De Arquer, F. P. G.; Dinh, C. T.; Fan, F.; Yuan, M.; Yassitepe, E.; Chen, N.; Regier, T.; Liu, P.; Li, Y.; De Luna, P.; Janmohamed, A.; Xin, H. L.; Yang, H.; Vojvodic, A.; Sargent, E. H. Homogeneously Dispersed Multimetal Oxygen-Evolving Catalysts. *Science (80-.).* **2016**, *352* (6283), 333–337. https://doi.org/10.1126/science.aaf1525.

(8) Shi, Q.; Zhu, C.; Du, D.; Lin, Y. Robust Noble Metal-Based Electrocatalysts for Oxygen Evolution Reaction. *Chem. Soc. Rev.* **2019**, *48* (12), 3181–3192. https://doi.org/10.1039/c8cs00671g.

(9) Xu, W.; Bai, Y.; Yin, Y. Surface Engineering of Nanostructured Energy Materials. *Adv. Mater.* **2018**, *30* (48), 1–7. https://doi.org/10.1002/adma.201802091.

(10) Li, H.; Chen, C.; Yan, D.; Wang, Y.; Chen, R.; Zou, Y.; Wang, S. Interfacial Effects in Supported Catalysts for Electrocatalysis. *J. Mater. Chem. A* **2019**, *7* (41), 23432–23450. https://doi.org/10.1039/c9ta04888j.

(11) Hayden, B. E. Particle Size and Support Effects in Electrocatalysis. *Acc. Chem. Res.* **2013**, *46* (8), 1858–1866. https://doi.org/10.1021/ar400001n.

(12) Zhao, D.; Zhuang, Z.; Cao, X.; Zhang, C.; Peng, Q.; Chen, C.; Li, Y. Atomic Site Electrocatalysts for Water Splitting, Oxygen Reduction and Selective Oxidation. *Chem. Soc. Rev.* **2020**, *49* (7), 2215–2264. https://doi.org/10.1039/c9cs00869a.

(13) Yang, Y.; Luo, M.; Zhang, W.; Sun, Y.; Chen, X.; Guo, S. Metal Surface and Interface Energy Electrocatalysis: Fundamentals, Performance Engineering, and Opportunities. *Chem*. 2018, pp 2054–2083. https://doi.org/10.1016/j.chempr.2018.05.019.

(14) Zheng, X.; Li, L.; Deng, M.; Li, J.; Ding, W.; Nie, Y.; Wei, Z. Understanding the Effect of Interfacial Interaction on Metal/Metal Oxide Electrocatalysts for Hydrogen Evolution and Hydrogen Oxidation Reactions on the Basis of First-Principles Calculations. *Catal. Sci. Technol.* **2020**, *10* (14), 4743–4751. https://doi.org/10.1039/d0cy00960a.

(15) Finke, C. E.; Omelchenko, S. T.; Jasper, J. T.; Lichterman, M. F.; Read, C. G.; Lewis, N. S.; Hoffmann, M. R. Enhancing the Activity of Oxygen-Evolution and Chlorine-Evolution Electrocatalysts by Atomic Layer Deposition of TiO_2. *Energy Environ. Sci.* **2019**, *12* (1), 358–365. https://doi.org/10.1039/c8ee02351d.

(16) Giordano, L.; Cinquini, F.; Pacchioni, G. Tuning the Surface Metal Work Function by Deposition of Ultrathin Oxide Films: Density Functional Calculations. *Phys. Rev. B - Condens. Matter Mater. Phys.* **2006**, *73* (4), 1–6. https://doi.org/10.1103/PhysRevB.73.045414.

(17) Kim, J. H.; Shin, K.; Kawashima, K.; Youn, D. H.; Lin, J.; Hong, T. E.; Liu, Y.; Wygant, B. R.; Wang, J.; Henkelman, G.; Mullins, C. B. Enhanced Activity Promoted by CeO_x on a CoO_x Electrocatalyst for the Oxygen Evolution Reaction. *ACS Catal.* **2018**, *8* (5), 4257–4265. https://doi.org/10.1021/acscatal.8b00820.

(18) Neufeld, O.; Yatom, N.; Caspary Toroker, M. A First-Principles Study on the Role of an Al_2O_3 Overlayer on Fe_2O_3 for Water Splitting. *ACS Catal.* **2015**, *5* (12), 7237–7243. https://doi.org/10.1021/acscatal.5b01748.

(19) Gu, J.; Aguiar, J. A.; Ferrere, S.; Steirer, K. X.; Yan, Y.; Xiao, C.; Young, J. L.; Al-Jassim, M.; Neale, N. R.; Turner, J. A. A Graded Catalytic-Protective Layer for an Efficient and Stable Water-Splitting Photocathode. *Nat. Energy* **2017**, *2* (2), 1–8. https://doi.org/10.1038/nenergy.2016.192.

(20) Azevedo, J.; Tilley, S. D.; Schreier, M.; Stefik, M.; Sousa, C.; Araújo, J. P.; Mendes, A.; Grätzel, M.; Mayer, M. T. Tin Oxide as Stable Protective Layer for Composite Cuprous Oxide Water-Splitting Photocathodes. *Nano Energy*. 2016, pp 10–16. https://doi.org/10.1016/j.nanoen.2016.03.022.

(21) Hufnagel, A. G.; Hajiyani, H.; Zhang, S.; Li, T.; Kasian, O.; Gault, B.; Breitbach, B.; Bein, T.; Fattakhova-Rohlfing, D.; Scheu, C.; Pentcheva, R. Why Tin-Doping Enhances the Efficiency of Hematite Photoanodes for Water Splitting—The Full Picture. *Adv. Funct. Mater*. **2018**, *28* (52), 1–10. https://doi.org/10.1002/adfm.201804472.

(22) Satterthwaite, P. F.; Scheuermann, A. G.; Hurley, P. K.; Chidsey, C. E. D.; McIntyre, P. C. Engineering Interfacial Silicon Dioxide for Improved Metal-Insulator-Semiconductor Silicon Photoanode Water Splitting Performance. *ACS Appl. Mater. Interfaces* **2016**, *8* (20), 13140–13149. https://doi.org/10.1021/acsami.6b03029.

(23) Chymo, F.; Fröhlich, K.; Kundrata, I.; Hušeková, K.; Harmatha, L.; Racko, J.; Breza, J.; Mikolášek, M. Characterization of MIS Photoanode with a Thin SiO_2 Layer for Photoelectrochemical Water Splitting. *AIP Conf. Proc.* **2019**, *2131* (July), 3–7. https://doi.org/10.1063/1.5119473.

(24) Hu, S.; Shaner, M. R.; Beardslee, J. A.; Lichterman, M.; Brunschwig, B. S.; Lewis, N. S. Amorphous TiO_2 Coatings Stabilize Si, GaAs, and GaP Photoanodes for Efficient Water Oxidation. *Science (80-.).* **2014**, *344* (6187), 1005–1009. https://doi.org/10.1126/science.1251428.

(25) Guo, Z.; Ambrosio, F.; Pasquarello, A. Hole Diffusion across Leaky Amorphous TiO_2 Coating Layers for Catalytic Water Splitting at Photoanodes. *J. Mater. Chem. A* **2018**, *6* (25), 11804–11810. https://doi.org/10.1039/c8ta02179a.

(26) Yang, X.; Liu, R.; Du, C.; Dai, P.; Zheng, Z.; Wang, D. Improving Hematite-Based Photoelectrochemical Water Splitting with Ultrathin TiO_2 by Atomic Layer Deposition. *ACS Appl. Mater. Interfaces* **2014**, *6* (15), 12005–12011. https://doi.org/10.1021/am500948t.

(27) Ahmed, M. G.; Kretschmer, I. E.; Kandiel, T. A.; Ahmed, A. Y.; Rashwan, F. A.; Bahnemann, D. W. A Facile Surface Passivation of Hematite Photoanodes with TiO_2 Overlayers for Efficient Solar Water Splitting. *ACS Appl. Mater. Interfaces* **2015**, *7* (43), 24053–24062. https://doi.org/10.1021/acsami.5b07065.

(28) Kim, W.; Tachikawa, T.; Monllor-Satoca, D.; Kim, H. Il; Majima, T.; Choi, W. Promoting Water Photooxidation on Transparent WO3 Thin Films Using an Alumina Overlayer. *Energy Environ. Sci.* **2013**, *6* (12), 3732–3739. https://doi.org/10.1039/c3ee42151a.

(29) Le Formal, F.; Tétreault, N.; Cornuz, M.; Moehl, T.; Grätzel, M.; Sivula, K. Passivating Surface States on Water Splitting Hematite Photoanodes with Alumina Overlayers. *Chem. Sci.* **2011**, *2* (4), 737–743. https://doi.org/10.1039/c0sc00578a.

(30) Zhuang, Z.; Sheng, W.; Yan, Y. Synthesis of Monodispere Au@Co_3O_4 Core-Shell Nanocrystals and Their Enhanced Catalytic Activity for Oxygen Evolution Reaction. *Adv. Mater.* **2014**, *26* (23), 3950–3955. https://doi.org/10.1002/adma.201400336.

(31) Bu, L.; Zhang, N.; Guo, S.; Zhang, X.; Li, J.; Yao, J.; Wu, T.; Lu, G.; Ma, J. Y.; Su, D.; Huang, X. Biaxially Strained PtPb/Pt Core/Shell Nanoplate Boosts Oxygen Reduction Catalysis. *Science (80-.).* **2016**, *354* (6318), 1410–1414. https://doi.org/10.1126/science.aah6133.

(32) Alibabaei, L.; Sherman, B. D.; Norris, M. R.; Brennaman, M. K.; Meyer, T. J. Visible Photoelectrochemical Water Splitting into H_2 and O_2 in a Dye-Sensitized Photoelectrosynthesis Cell. *Proc. Natl. Acad. Sci. U. S. A.* **2015**, *112* (19), 5899–5902.

https://doi.org/10.1073/pnas.1506111112.

(33) Exner, K. S.; Anton, J.; Jacob, T.; Over, H. Controlling Selectivity in the Chlorine Evolution Reaction over RuO_2-Based Catalysts. *Angew. Chemie - Int. Ed.* **2014**, *53* (41), 11032–11035. https://doi.org/10.1002/anie.201406112.

(34) Vadakkekara, R.; Illathvalappil, R.; Kurungot, S. Layered TiO_2 Nanosheet-Supported $NiCo_2O_4$ Nanoparticles as Bifunctional Electrocatalyst for Overall Water Splitting. *ChemElectroChem* **2018**, *5* (24), 4000–4007. https://doi.org/10.1002/celc.201801107.

(35) Tahira, A.; Ibupoto, Z. H.; Mazzaro, R.; You, S.; Morandi, V.; Natile, M. M.; Vagin, M.; Vomiero, A. Advanced Electrocatalysts for Hydrogen Evolution Reaction Based on Core-Shell MoS_2/TiO_2 Nanostructures in Acidic and Alkaline Media. *ACS Appl. Energy Mater.* **2019**, *2* (3), 2053–2062. https://doi.org/10.1021/acsaem.8b02119.

(36) Oakton, E.; Lebedev, D.; Povia, M.; Abbott, D. F.; Fabbri, E.; Fedorov, A.; Nachtegaal, M.; Copéret, C.; Schmidt, T. J. IrO_2-TiO_2: A High-Surface-Area, Active, and Stable Electrocatalyst for the Oxygen Evolution Reaction. *ACS Catal.* **2017**, *7* (4), 2346–2352. https://doi.org/10.1021/acscatal.6b03246.

(37) Obata, K.; Takanabe, K. A Permselective CeO_x Coating To Improve the Stability of Oxygen Evolution Electrocatalysts. *Angew. Chemie - Int. Ed.* **2018**, *57* (6), 1616–1620. https://doi.org/10.1002/anie.201712121.

(38) Myeong Chang Sung, Gwang Hee Lee, D.-W. K. CeO_2_$Co(OH)_2$ Hybrid Electrocatalysts for Efficient Hydrogen and Oxygen Evolution Reaction. Journal of Alloys and Compounds **2019**, pp 450–455.

(39) Feng, J. X.; Ye, S. H.; Xu, H.; Tong, Y. X.; Li, G. R. Design and Synthesis of FeOOH/CeO_2 Heterolayered Nanotube Electrocatalysts for the Oxygen Evolution Reaction. *Adv. Mater.* **2016**, *28* (23), 4698–4703. https://doi.org/10.1002/adma.201600054.

(40) Wang, J.; Xiao, X.; Liu, Y.; Pan, K.; Pang, H.; Wei, S. The Application of CeO_2-Based Materials in Electrocatalysis. *J. Mater. Chem. A* **2019**, *7* (30), 17675–17702. https://doi.org/10.1039/c9ta04804a.

(41) Friedrich Esch, Stefano Fabris, Ling Zhou, Tiziano Montini, Cristina Africh, Paolo Fornasiero, Giovanni Comelli, R. R. Electron Localization Determines Defect Formation On Ceria Substrates. *Science (80-.).* **2005**, *309*, 752–755. https://doi.org/10.1210/jcem-10-10-1361.

(42) Zheng, Y. R.; Gao, M. R.; Gao, Q.; Li, H. H.; Xu, J.; Wu, Z. Y.; Yu, S. H. An Efficient $CeO_2/CoSe_2$ Nanobelt Composite for Electrochemical Water Oxidation. *Small* **2015**, *11* (2), 182–188. https://doi.org/10.1002/smll.201401423.

(43) Lo, C.; Ramani, V. SiO_2-RuO_2 : A Stable Electrocatalyst Support. *ACS Appl. Mater. Interfaces* **2012**, *4*, 6109−6116.

(44) Zhou, L.; Yan, S.; Tian, B.; Zhang, J.; Anpo, M. Preparation of TiO_2-SiO_2 Film with High

Photocatalytic Activity on PET Substrate. *Mater. Lett.* **2006**, *60* (3), 396–399. https://doi.org/10.1016/j.matlet.2005.08.065.

(45) Venkatkarthick, R.; Davidson, D. J.; Ravichandran, S.; Vengatesan, S.; Sozhan, G.; Vasudevan, S. Eco-Friendly and Facilely Prepared Silica Modified Amorphous Titania (TiO_2-SiO_2) Electrocatalyst for the O_2 and H_2 Evolution Reactions. *Catal. Sci. Technol.* **2015**, *5* (11), 5016–5022. https://doi.org/10.1039/c5cy00805k.

(46) Gono, P.; Pasquarello, A. Oxygen Evolution Reaction: Bifunctional Mechanism Breaking the Linear Scaling Relationship. *J. Chem. Phys.* **2020**, *152* (10). https://doi.org/10.1063/1.5143235.

(47) Luo Jie, X. C. XPS Examination of Tin Oxide on Float Glass Surface. *J. Non. Cryst. Solids* **1990**, *119*, 37–40.

(48) Garbassi, F. XPS and AES Study of Antimony Oxides. *Surf. Interface Anal.* **1980**, *2* (5), 165–169. https://doi.org/10.1002/sia.740020502.

(49) Biesinger, M. C.; Payne, B. P.; Grosvenor, A. P.; Lau, L. W. M.; Gerson, A. R.; Smart, R. S. C. Resolving Surface Chemical States in XPS Analysis of First Row Transition Metals, Oxides and Hydroxides: Cr, Mn, Fe, Co and Ni. *Appl. Surf. Sci.* **2011**, *257* (7), 2717–2730. https://doi.org/10.1016/j.apsusc.2010.10.051.

(50) Luke Sibimol, Manjunath Chatti, Asha Yadav, Brittany Kerr, Jiban Kangsabanik, Tim Williams, Pavel V. Cherepanov, Akshat Tanksale, Bernt Johannessen, Douglas Macfarlane, Rosalie K. Hocking, Aftab Alam, Aswani Yella, A. S. Mixed Metal-Antimony Oxide Nanocomposites: Low PH Water Oxidation Electrocatalysts with Outstanding Durability at Ambient and Elevated Temperature. *Chemrxiv* **2021**.

Chapter 6

Conclusions and Outlook

Hydrogen is a critically important commodity chemical and will likely become a key vehicle for energy storage and transportation in the nearest future to support the global shift to the renewable energy as a major energy resource of humanity. Sustainable and pollution-free electrochemical water splitting powered by renewable electricity is one of the promising alternatives to replace the current heavily polluting H_2 production technologies, as required to reach the targeted climate change goals. Therefore, development of the efficient and cost-effective electrochemical water splitting technologies is an important goal for researchers around the world. One of the key technological problems to be solved before water electrolysis becomes an economically viable large-scale industrial process is the design of effective electrocatalysts to promote the cathode hydrogen evolution and anode oxygen evolution half-reactions, the latter being the most problematic at the current stage. An ideal catalyst should be of low cost with high activity, and equally importantly, should be durable on a sufficiently long timescale. Particularly problematic from this perspective are the water oxidation electrocatalysts for the proton exchange membrane electrolyzers, which are required to operate in strongly acidic conditions and elevated temperatures.

This dissertation presents three studies on the design and detailed investigation of novel low-cost antimony-based electrocatalysts for water oxidation at low pH. One core feature of the work is the rigorous assessment of the stability of the catalysts in operation at ambient and industrially

relevant elevated temperatures. This study also introduces a facile solution processable strategy to synthesize mono- and multimetallic antimony oxide-based catalysts that can be easily scaled up and enables an intimate intermixing of different oxides at the nanoscale. The specific conclusions of each study are summarized below, followed by the suggestions of the PhD candidate on the possible future developments that can further advance the sustainable technology of H_2 production through the PEM water electrolysis.

6.1 CONCLUSIONS

Active studies of antimonates and antimony-oxide-based materials as low-pH electrocatalysts for water oxidation have commenced only recently, and our current knowledge on the electrochemical behavior of these materials is very limited. Each research chapter of this thesis aims to address this through the systematic investigation of different types of the Sb-based OER catalysts.

Chapter 3 presents an in-depth study of the transition metal-antimony oxides as a highly promising family of electrocatalysts for water oxidation at low pH and introduces a new synthesis strategy of such and related materials. Initial durability tests indicated that iron-antimony and nickel-antimony mixed oxides do not exhibit any reasonable stability in operation as OER catalysts at low pH even at ambient temperature, but promising stability was found for the $[Co+Sb]O_y$, $[Mn+Sb]O_y$ and $[Ru+Sb]O_y$ systems. Comprehensive physical characterization of the latter materials suggests that the metal-antimony oxide structure within these catalysts cannot be described by a single phase, except for the case of the cobalt-antimony system, which adopts a trirutile antimonate phase and exhibits the lowest catalytic activity. Comprehensive

assessment of the durability of the best performing [Mn+Sb]O_y and [Ru+Sb]O_y catalysts revealed that the former slowly and irreversibly degrades at elevated temperatures of 60 and 80 °C, while the latter exhibits outstanding stability for at least one week at 80 °C. Density functional theory analysis along with in-depth structural characterization suggest that the enhanced stability of the metal-antimony oxide systems during the OER at low pH can be achieved through either the formation of the new antimonate phase, as found for [Co+Sb]O_y and [Mn+Sb]O_y, or by the mixing of the discrete metal and antimony oxide crystallites at the nanoscale, as applies to the top-performance [Ru+Sb]O_y catalytic system. This new ruthenium-antimony oxide system discovered in this work demonstrates very high electrocatalytic activity for the OER and excels over previously reported low-pH water oxidation catalysts in terms of durability. This finding presents a new approach to the design of robust anode catalysts for the PEM water electrolyzers.

Building upon the breakthrough findings in Chapter 3, the study described in Chapter 4 aimed to explore the effects of mixing different metal oxides with the antimony oxide matrix on their electrocatalytic activity. As a base system, a non-noble-metal [Mn+Sb]O_x catalyst described in the previous chapter was considered and was modified with oxides of Co, Pb, Cr and low amounts of Ru. This approach aimed to combine the beneficial properties of the individual constituent oxides in a synergistic manner to form new materials with improved characteristics, *viz.* catalytic activity, and stability during the OER at low pH at ambient and elevated temperatures. The anticipated improvement in the initial activity was indeed achieved upon modification with all considered metal oxides, which could be explained either by the enhanced electrochemically active surface area (Cr), synergistic catalytic effect (Ru, Co, and Co+Pb), and/or formation of a distinct antimonate phase (Ru and Pb). The ease of tuning of the catalytic properties of the antimony-oxide-based catalysts highlights the potential of the employed

approach and synthesis procedure for the development of high-performance water oxidation electrocatalysts. Although significant improvements in the stability of [Mn+Sb]O_x upon introduction of other metal oxides at elevated temperatures was generally not achieved, all materials except for [MnCr+Sb]O_x were highly robust at ambient temperature, while the mixed manganese cobalt antimony oxide demonstrated an outstanding stability at 80 °C after initial partial corrosion on a timescale of a week. In the latter case, the catalyst operated in a so-called 'self-healing' regime, meaning that its stable operation was supported by an equilibrium between continuous dissolution/redeposition to/from the electrolyzed solution. In contrast to the previous work demonstrating a similar mode of operation for the Co-Fe-Pb oxide system, [MnCo+Sb]O_x required significantly lower concentrations of the dissolved precursors, which is a notable advantage and also clearly suggests that further improvements should be possible through the optimization of the self-healing conditions.

The final research chapter 5 investigates techniques other than mixed metal oxide in a stable matrix strategy to improve the electrocatalytic activity of the catalyst without deteriorating its stability. The promising [Mn+Sb]O_y OER catalysts was functionalized with a thin layer of an oxide such as SnO_2, SiO_2, CeO_2, Al_2O_3 and TiO_2, which are catalytically inactive on its own for water oxidation. The best performance is obtained with SnO_2 as it recorded an overpotential of *ca* 0.58 V (overlayer), and 0.57-0.58 V (underlayer) at a current density of 10 mA $cm^{-2}_{geom.}$ over 24 h of stable operation. It was found that an overlayer suppresses the complete oxidation of manganese to 3+ state and reduces the manganese dissolution during the OER, which possibly led to an enhanced performance compared to unmodified catalyst. The significant improvement with an additional oxide layer on top or bottom of the electrocatalyst proves that altering the

interfacial effects is promising strategy in designing a catalyst. It can dramatically affect the physical, chemical, and electronic properties of the catalyst and can direct the adsorption properties of different reaction intermediates, alter the oxidation states of key active species, and vary the active surface area. Choosing the right oxide layer, thickness and surface coverage of these materials are the major factors to be considered and optimized in implementing this strategy to obtain the maximum possible enhancement. More detailed studies are required to understand the mechanism of bifunctional catalyst and the interfacial effects for designing a suitable catalyst for water electrooxidation.

Table 6.1 Summary of the performance of the catalysts developed in this work to the reported catalysts.

Catalyst	Substrate	Electrolyte	Overpotential at 10 mA cm^{-2} / mV	T / °C	Stability / h	Ref.
$IrO_x/SrIrO_3$	$SrTiO_3$	0.5M H_2SO_4	270	23	<30	[1]
$[Ru+Sb]O_y$	FTO	0.5M H_2SO_4	390 ± 30	23	>>>25	This work
$[Ru+Sb]O_y$	FTO	0.5M H_2SO_4	340 ± 10	80	>>>25	This work
$Ni_xMn_{1-x}Sb_{1.6}O_y$	ATO	1M H_2SO_4	672	23	<168	[2]
Co_3O_4	FTO	0.5M H_2SO_4	570	23	<<12	[3]
$[MnRu+Sb]O_x$	FTO	0.5M H_2SO_4	530 ± 30	23	>25	This work
$[MnCo+Sb]O_x$	FTO	0.5M H_2SO_4	640 ± 10	23	>>>25	This work
$[MnCo+Sb]O_x$	FTO	0.5M H_2SO_4	690	80	>145	This work
$2\%SnO_2/[Mn+Sb]O_y$	FTO	0.5M H_2SO_4	580	23	>25	This work
$[Mn+Sb]O_y/2\%SnO_2$	FTO	0.5M H_2SO_4	570	23	>25	This work

6.2 OUTLOOK

In general, improvements in the performance of the catalysts can be achieved through four major factors. (i) Composition: catalysts with two or more metals can give better performance because of the synergistic effects and electronic interactions. (ii) Morphology: nanostructured or nanosized catalysts increase the density of active sites available for the reactants per unit mass. (iii) Surface engineering: targeted modification of the surface structure can lead to the enhancement in the intrinsic activity of the catalyst. (iv) Catalyst support: design and selection of the high surface area mesoporous provides enhanced area for the immobilization of highly dispersed catalyst particles and might also enhance the activity through the strong catalyst-support interactions. The research chapters 3 and 4 aimed to use the first two strategies in designing the catalyst while the chapter 5 aimed to employ the last two strategies for developing better performing catalysts.

Although the overpotentials reported for noble-metal-free low-pH OER catalysts in this study are higher than those of the state-of-the-art iridium- and ruthenium-based electrocatalysts, their stability is comparable or even better than that of many recently reported catalytic materials. Development of earth-abundant catalysts with performance comparable to noble-metal oxides is essential to replace these catalysts and for building economical hydrogen production systems. As a solution, new materials need to be explored broadly and intentionally. However, a common oversight of the studies in the field is the lack of rigor in the assessment of the technologically relevant stability of new materials and the focus on the initial rather than actual stabilized activity.

As a continuation of these studies, the following research work can be done to enable deeper insights and further development of the high-performance antimonate electrocatalysts.

(1) In-depth investigation of the mechanism of operation of the presented and related catalysts using advanced *in situ* spectroelectrochemical and online electrochemical mass-spectrometry techniques to gain deeper and quantitative insights into the key role of self-healing mechanism and identification of the key catalytically active state of the catalysts.

(2) Based on 1, provision of the optimized self-healing conditions to enable even better stability, in particular at 80° C.

(3) Design of the highly dispersed antimony-oxide-based catalysts supported on suitable high-surface area conductive materials.

(4) Tests of the materials in the PEM water electrolysis prototypes to prove the durability under real conditions.

It can be concluded that the long-term performance of the catalysts studied in this dissertation suggests that these can be used in electrolyzers and integrated solar fuel devices in combination with suitable acid-stable light absorbers and membranes. Focusing on acquiring in-depth fundamental understanding of the water oxidation reactions, the operation and degradation mechanisms of electrocatalysts in acidic medium will open new pathways in the development of efficient and low-cost electrode materials for water oxidation reactions in strongly acidic conditions. The author hopes that the catalysts developed and the research findings in this dissertation will make a significant contribution to the field of electrocatalysis and in achieving the goal of global power transition to sustainable energy and making it available for all.

6.3 REFERENCES

(1) Seitz, L. C.; Dickens, C. F.; Nishio, K.; Hikita, Y.; Montoya, J.; Doyle, A.; Kirk, C.; Vojvodic, A.; Hwang, H. Y.; Norskov, J. K.; Jaramillo, T. F. A Highly Active and Stable $IrO_x/SrIrO_3$ Catalyst for the Oxygen Evolution Reaction. *Science (80-.).* **2016**, *353* (6303), 1011–1014. https://doi.org/10.1126/science.aaf5050.

(2) Moreno-Hernandez, I. A.; Macfarland, C. A.; Read, C. G.; Papadantonakis, K. M.; Brunschwig, B. S.; Lewis, N. S. Crystalline Nickel Manganese Antimonate as a Stable Water-Oxidation Catalyst in Aqueous 1.0 M H_2SO_4. *Energy Environ. Sci.* **2017**, *10* (10), 2103–2108. https://doi.org/10.1039/c7ee01486d.

(3) Mondschein, J. S.; Callejas, J. F.; Read, C. G.; Chen, J. Y. C.; Holder, C. F.; Badding, C. K.; Schaak, R. E. Crystalline Cobalt Oxide Films for Sustained Electrocatalytic Oxygen Evolution under Strongly Acidic Conditions. *Chem. Mater.* **2017**, *29* (3), 950–957. https://doi.org/10.1021/acs.chemmater.6b02879.